Surface detection of alkaline ultramafic rocks in semi-arid and arid terrains using spectral geological techniques

Thesis

SURFACE DETECTION OF ALKALINE ULTRAMAFIC ROCKS IN SEMI-ARID AND ARID TERRAINS USING SPECTRAL GEOLOGICAL TECHNIQUES

A thesis submitted for the degree of Doctor of Philosophy

By

Michael Charles Hussey
B.Sc. (Hons) Southampton

Department of Earth Sciences
The Open University
June, 1998

VOLUME 1 of 2

To the memory of my Father

Ron Hussey

and

Geoffrey Trollope

who inspired my interest in Remote Sensing in Angola, during 1972

ACKNOWLEDGEMENTS

This thesis has resulted from a project I completed while employed at Stockdale Prospecting Limited, a subsidiary of the De Beers Group of companies. Therefore, I acknowledge and thank the senior geological staff in De Beers for permission to complete this thesis and the use of proprietary data presented within it. In particular, I would like to thank:

- Mr Roy Edwards, De Beers Director and Manager of Diamond Exploration for his approval.
- Dr Bobby Danchin, until recently Managing Director of Stockdale Prospecting, for his support and persuasive powers which gained approval for this thesis from the company.
- Ronnie Hazell, Joe Joyce and Bruce Wyatt of Stockdale Prospecting for their permission to balance my other duties with completing this study.

I am of course indebted to my supervisors, Dave Rothery of the Open University and Jon Huntington of the CSIRO Sydney for their patience and understanding of the time required to complete this study. Their support and advice has been invaluable.

Since she has shown more patience than anyone else, I especially thank Vera, my wife, who has been a thesis widow for many weeks. She has also made a major contribution by typing and proof reading the manuscript. Thanks also to Graham Lawrence, Mike Hornibrooke and Anne Becker for proof reading the draft and final manuscript.

Special thanks are also due to Terry Cocks, Managing Director of Integrated Spectronics, who made this study possible by developing the PIMA and HyMap scanners. I also thank him for obtaining permission from ESSI for the use of the HyMap data. Thanks also to Frank Honey whose development of the GEOSCAN scanners demonstrated the maturity of this technology in the 1980s. This interested Stockdale Prospecting in the technology, and furthered my involvement in applying it within De Beers.

Lillo de Gasparis, whose unrivalled ability to persuade management to fund the project from which this thesis developed, deserves thanks as a colleague and a friend. Thanks also to Neil Pendock who widened my interest in image processing techniques.

I also appreciate the help and advice of my current and past colleagues at Stockdale Prospecting: Anne Becker, Brian Bennett, Gavin Hunt, Michele Karakasch, Dorrie Jurisic, Shelagh Brigg and Martyn Friend who have assisted in many ways. Nick Merry made a significant contribution to our development of spectral geology within the company during the pioneering days with the PIMA. His assistance with the fieldwork at the test sites was invaluable as well as entertaining.

Many others at Stockdale and at CSIRO encouraged and assisted me and are too numerous to mention, though Tom Cudahy's help with laboratory studies using the GER IRIS is acknowledged.

To all of you, named or not, I cannot thank you enough.

TABLE OF CONTENTS

VOLUME 1

VOLUME 2

LIST OF FIGURES

CHAPTER 1

CHAPTER 3

CHAPTER 4

CHAPTER 5

CHAPTER 6

CHAPTER 7

CHAPTER 8

CHAPTER 9

CHAPTER 10

CHAPTER 11

LIST OF TABLES

ABSTRACT

Studies have been completed into the spectral response of alkaline and other ultramafic rocks from arid and semi-arid regions. To date these rocks have not been investigated spectrally in a systematic fashion using the latest field and airborne imaging spectrometers. The objective was to determine how spectral geological techniques could be used to locate these rock types when they are exposed, weathered and reduced to residual soil. The data used in this study were spectra obtained from field spectrometers (PIMA and GER IRIS MkIV) and airborne scanners (GEOSCAN MkII, GER IS and HyMap). These data were gathered at four sites within Australia. The data processing software packages used for the analyses were commercially available image processing systems (I^2S S600 and ENVI) and a modified version of PIMAVIEW for processing spectra.

Spectra were measured, in the field and the laboratory, of alkaline and other ultramafic rocks to determine if they had diagnostic spectral absorption features. These studies demonstrated that there are diagnostic spectral absorption features common to alkaline and other ultramafic rocks including dunite, peridotite and serpentinite. The diagnostic spectrum in the SWIR2 region (2000nm to 2500nm) has absorption features located near 2300nm and 2380nm and results from Mg-OH bearing minerals including serpentine, talc and phlogopite.

The VNIR spectra of these rocks also have distinct absorption features, but since these are caused by minerals that are common to a variety of rocks and soils, they have not been considered in this study. When weathered under arid and semi-arid conditions, ultramafic rocks break down into smectite clays, primarily saponite. Saponite has a similar spectral signature to the primary Mg-OH bearing minerals. Further weathering and removal of magnesium results in saponite altering to kaolinite and then to opaline silica. These minerals may occur in residual soils derived from ultramafic rocks. Spectral investigation of mixtures of saponite and other minerals showed that there are linear changes the absorption features of spectra, depth, wavelength and shape, as the proportion of saponite to other minerals varies.

The ability to identify ultramafic rocks from the distribution of their diagnostic spectra was confirmed by analysing data obtained from surface samples and airborne scanners. The coincidence of results obtained from field studies and airborne scanner data signifies that

data acquired remotely are as useful as spectra obtained in the field, for mapping the extent of ultramafic rocks.

Present and past imaging systems have been investigated to determine the specifications required to suit this application. These investigations included sampling the spectra of ultramafic and background rocks with the band pass characteristics of various instruments. The signal-to-noise ratio that is required of scanner data to ensure it is useable was also studied. These studies indicated a specification for data of at least eight and preferably, thirty two channels in the SWIR2 (between 2000nm and 2500nm) obtained with a signal-to-noise ratio in excess of 200:1, ideally 400:1 at 2200nm. Scanners producing data with these specifications can be used to locate ultramafic rocks from their spectral signature, whether exposed or covered by residual soils in a variety of geological environments.

The success of applying these techniques will however depend on the spectral contrast between ultramafic rocks and their backgrounds. Rocks that produce Mg-OH bearing minerals or have near 2300nm absorption can result in areas being mistakenly identified as containing alkaline and other ultramafic rocks. However, in this study it was demonstrated that carbonate soils and rocks that have a near 2300nm absorption feature can be spectrally distinguished from alkaline ultramafic derived saponite using HyMap scanner data. In South Australia dolomite appears to have altered to saponite at surface but kimberlites in the area can still be detected by processing HyMap scanner data with spectral as opposed to conventional image processing techniques.

ACKNOWLEDGEMENTS

This thesis has resulted from a project I completed while employed at Stockdale Prospecting Limited, a subsidiary of the De Beers Group of companies. Therefore, I acknowledge and thank the senior geological staff in De Beers for permission to complete this thesis and the use of proprietary data presented within it. In particular, I would like to thank:

- Mr Roy Edwards, De Beers Director and Manager of Diamond Exploration for his approval.
- Dr Bobby Danchin, until recently Managing Director of Stockdale Prospecting, for his support and persuasive powers which gained approval for this thesis from the company.
- Ronnie Hazell, Joe Joyce and Bruce Wyatt of Stockdale Prospecting for their permission to balance my other duties with completing this study.

I am of course indebted to my supervisors, Dave Rothery of the Open University and Jon Huntington of the CSIRO Sydney for their patience and understanding of the time required to complete this study. Their support and advice has been invaluable.

Since she has shown more patience than anyone else, I especially thank Vera, my wife, who has been a thesis widow for many weeks. She has also made a major contribution by typing and proof reading the manuscript. Thanks also to Graham Lawrence, Mike Hornibrooke and Anne Becker for proof reading the draft and final manuscript.

Special thanks are also due to Terry Cocks, Managing Director of Integrated Spectronics, who made this study possible by developing the PIMA and HyMap scanners. I also thank him for obtaining permission from ESSI for the use of the HyMap data. Thanks also to Frank Honey whose development of the GEOSCAN scanners demonstrated the maturity of this technology in the 1980s. This interested Stockdale Prospecting in the technology, and furthered my involvement in applying it within De Beers.

Lillo de Gasparis, whose unrivalled ability to persuade management to fund the project from which this thesis developed, deserves thanks as a colleague and a friend. Thanks also to Neil Pendock who widened my interest in image processing techniques.

I also appreciate the help and advice of my current and past colleagues at Stockdale Prospecting: Anne Becker, Brian Bennett, Gavin Hunt, Michele Karakasch, Dorrie Jurisic, Shelagh Brigg and Martyn Friend who have assisted in many ways. Nick Merry made a significant contribution to our development of spectral geology within the company during the pioneering days with the PIMA. His assistance with the fieldwork at the test sites was invaluable as well as entertaining.

Many others at Stockdale and at CSIRO encouraged and assisted me and are too numerous to mention, though Tom Cudahy's help with laboratory studies using the GER IRIS is acknowledged.

To all of you, named or not, I cannot thank you enough.

CHAPTER 1

1 INTRODUCTION

1.1 STATEMENT OF OBJECTIVES

The primary objective of the research presented in this thesis is to determine the extent to which spectral geological techniques can be used to locate and delineate alkaline ultramafic rocks. This includes locating them when exposed, weathered and covered by residual soil. A secondary objective was to complete this study by using data acquired from commercially available instruments and processing systems. The research utilised techniques that did not involve extended periods of image correction and calibration, but was rather focussed on operational techniques.

This study was undertaken because there is a dearth of published research into the application of using spectral geological, and other remote sensing, techniques for the detection of alkaline and other ultramafic rocks. In particular no detailed research has been reported on diagnostic spectral signatures of alkaline ultramafic rocks obtained from laboratory and field studies. Trials using multi-channel imaging scanners for this application have also been limited. As field spectrometers and hyperspectral scanner image data are now becoming routinely available an investigation into the potential of these techniques to locate such economically significant rocks is warranted.

1.2 SPECTRAL GEOLOGICAL DEVELOPMENT

Geological remote sensing in its broadest sense can trace its origins to before the Second World War with the interpretation of stereo aerial photographs. This may be termed conventional geological remote sensing. This continued into the era of satellite imagery which became available with the advent of the Landsat multi-spectral scanners that were first launched in 1972 under the acronym ERTS by NASA. The impact of these satellite data was to stimulate the field of digital image enhancement. During this time (mid to late 1970s) digital image processing was directed primarily at enhancing the data to improve it for photo-geological analysis. The primary aim of much of the interpretation was directed at structural analysis with the synoptic overview provided by Landsat MSS imagery resulting in a new understanding of regional tectonics and structure. This was of particular

interest to oil exploration companies (Sanders, 1980 and Everett and Prucha, 1980). Lithological interpretation was addressed by interpreting black and white and various colour composites of the imagery that had been contrast and texturally enhanced. Band ratios were also applied to emphasise the presence of iron minerals and classification techniques were applied to map general variations in lithologies (Rowan et al., 1974, Abrams et al., 1983 and Rothery, 1982). However, the introduction of digital image processing techniques and enhanced imagery, particularly to geophysical data and other geological data sets, established remote sensing comprehensively as a tool for application in mineral exploration and geological mapping. This acceptance was recognised when conferences organised by the Environmental Research Institute of Michigan (ERIM), from 1982 onwards, were specifically directed towards the geological and mineral exploration applications of remote sensing.

Spectral geology, as a sub-discipline of remote sensing, has its origins in studies carried out in the 1960s which were part of the NASA space program for planetary mapping. Landmark studies in this area were published by Lyon (1964) describing the potential of thermal infrared spectrometry for the analysis of the composition of lunar and planetary soils. Though previous work had been carried out (Lyon, Tuddenham and Thompson, 1959) into the infrared spectra on rocks, these were from an analysis viewpoint rather than the development of remote sensing. NASA funded Lyon for some of this research and these findings contributed to the decision to develop the Landsat (ERTS) system. The interest in remote sensing stimulated by satellite imagery resulted in investigations into spectral geology during the 1970s, though the term itself did not become generally used until the late 1980s. The work by Hunt and Salisbury published between 1970 and 1980, mainly in Modern Geology, into the visible and near infrared spectra of minerals and rocks can be regarded as the foundation for later developments in spectral geology. As stated in a paper in 1976 (Hunt and Salisbury, 1976) "with the advent of the ERTS program a definite need had developed for a complete study of rock spectra". By the late 1970s there was a growing body of literature and conference proceedings that had awakened the geological and exploration communities to the possibilities of spectral image data for geological mapping and its potential in mineral exploration. During the late 1970s various mining and oil companies in the USA set up the Geosat Committee. Geosat's function was to lobby the US government to fund remote sensing systems, primarily satellite borne, which would directly benefit mineral exploration. This Committee succeeded in motivating funding for the addition of the seventh band to the Landsat TM scanner. The addition of this band, imaging the 2200nm-2350nm (Short Wave Infrared, SWIR) spectral region, to

the Landsat thematic mapper in the early 1980s, expressed this increase in the awareness of the importance of spectral image data for geological applications. To further these developments in geological remote sensing, particularly the development of higher spectral resolution instruments Geosat commissioned a number of test site surveys. These surveys (Abrams et al., 1984) were carried out in the western USA and clearly demonstrated the potential of this technology in geological mapping and applications to exploration for mineral deposits characterised by hydrothermal alteration and resultant phyllosilicate mineral assemblages.

During the late 1970s Dr A. Greene returned to Australia from Stanford University where he undertook graduate research with Dr R. Lyon into infrared spectrometry of rocks. He joined the CSIRO, and together with Dr. J. Huntington initiated research into digital image processing of Landsat (MSS) data in Australia. This work was funded partly by the mining industry, through the Australia Mineral Industry Research Association (AMIRA) a mining industry based group which raises funds for research, and was the initial project in a program of research that continues until the present time. The second research project, into the interpretation of Landsat at the start of the 1980s, drew on Hunt and Salisbury's work and commenced investigation into the SWIR spectra of rocks and minerals. These spectral studies initially used a spectrometer that had been developed for studying the infrared spectra of clouds. During this period (1982) the author commenced investigations into the spectral signature of alkaline ultramafic rocks including kimberlites and associated rocks.

During the late 1970's, in the United States, the Geophysical Environmental Research (GER) Company developed the first field portable spectrometer capable of recording spectra from 400nm to 2500nm in the field. This instrument was followed by an airborne profiling spectrometer and investigations with these instruments (Collins, et al., 1981 and Marsh and McKeon, 1983) demonstrated the full potential of remotely sensed spectra to map differences in geology and soil mineralogy. In 1983 CSIRO acquired a GER field spectrometer (Infra-red Intelligent Spectroradiometer - IRIS MkIV) and brought the profiling instrument to Australia. Data collected in Australia with the profiler proved that these techniques were applicable in the deeply weathered terrains occurring in Australia (Gabell et al., 1983 and 1984). Previous studies had mainly been conducted in the outcrop rich areas of the western United States. In the USA, during the 1980s, NASA JPL and the USGS had ongoing programs investigating the spectra of rocks. NASA developed plans for a series of aircraft and spaceborne imaging spectrometers that would record spectra from pixel arrays collected as images of the earth's surface. The first of these instruments,

the Airborne Imaging Spectrometer (AIS), was flown with other scanners in a C130 Hercules aircraft during the mid-1980s; these trials included a campaign of data acquisition in Australia. At the end of the 1980s this research by NASA resulted in the development of the Airborne Visible/Infrared Imaging Spectrometer (AVIRIS) instrument which was the first truly hyperspectral scanner produced (Potter et al., 1990).

During the 1980s a number of commercial companies, including GER and Daedalus, started manufacturing imaging spectrometers which were tested over a number of mineral deposits of which the Cuprite area in Nevada (Figure 1.1) is a type locality. At the same time other airborne scanners that emulated Landsat TM with much reduced pixel sizes had become available, for example, the Daedalus 1268. However, these instruments did not produce the increment in information that is gained from hyperspectral and imaging spectrometers.

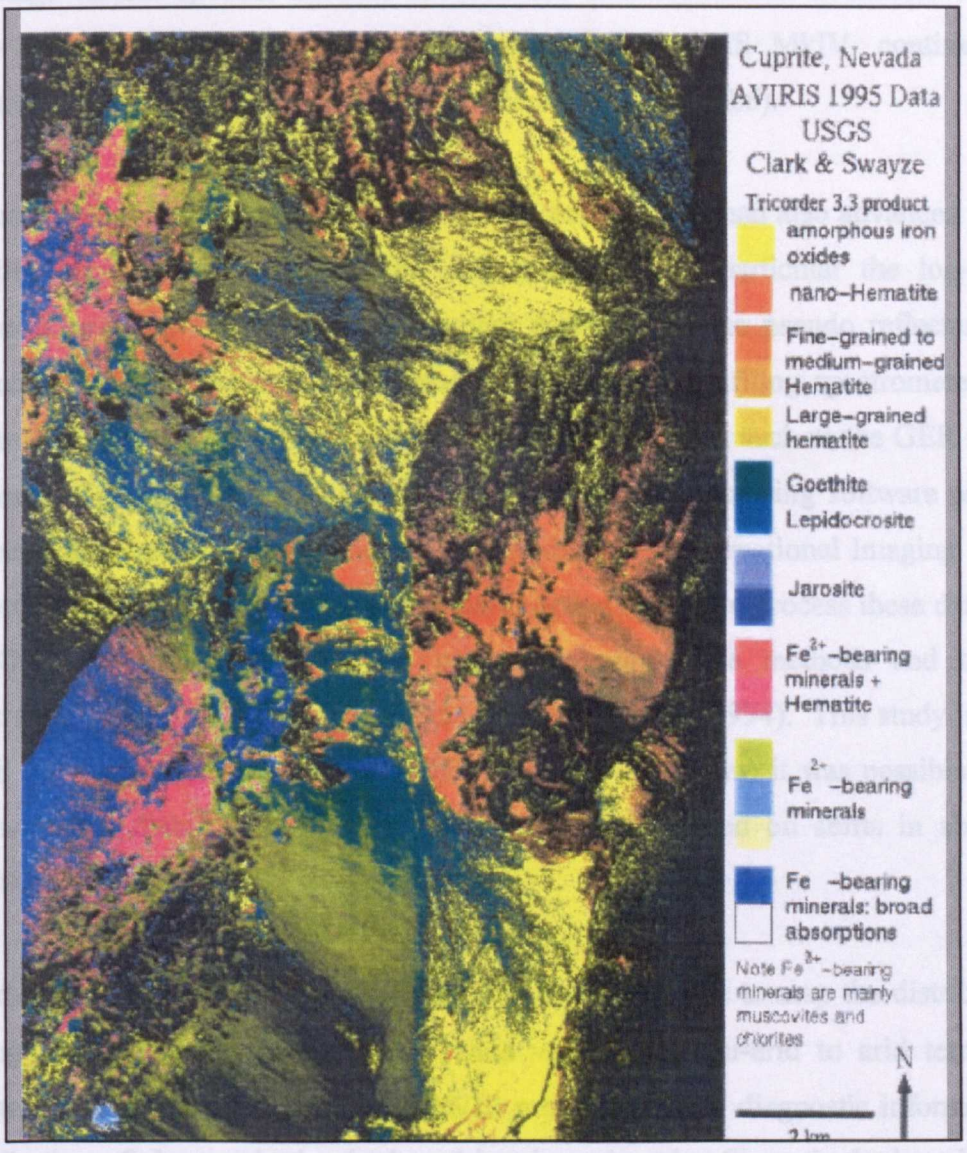

Figure 1.1: Mineral map derived from AVIRIS data obtained over Cuprite, Nevada, in 1995. The scene is 10.5 km wide. Source Clarke and Swayze (1995).

In Australia the GEOSCAN Company which was founded Dr F. Honey, developed the GEOSCAN MkI and MkII scanners. These instruments had specifications between those of multi-spectral scanners and imaging spectrometers. The approach taken by GEOSCAN to process the data from these instruments was only partially directed at spectral evaluation (Honey and Daniels, 1986). These data were not atmospherically corrected; at the time no commercially available image processing package had the capability to correct such data for atmospheric affects and reduce it from radiance to reflectance, or to carry out more advanced spectral analyses.

In parallel with airborne developments investigations with field spectrometers, particularly the GER IRIS MkIV, continued and techniques for processing spectra were refined so that spectral features could be more clearly identified, particularly by applying a hull quotient. At this stage various spectral libraries of rocks and minerals became available. Research into the signature of various minerals, using the GER IRIS MkIV, continued and techniques for processing these data were developed (Gabell, 1986).

By the late 1980s software for processing of airborne imagery had also advanced with the availability of programs such as SIPS and GENASIS. In particular the log-residual technique (Craig and Green, 1985) to convert radiance data to pseudo reflectance was developed. Originally developed for processing the GER profiling spectrometer data it also permitted spectral analysis of data produced from scanners, such as the GER imaging spectrometer (GER IS), using standard commercial image processing software packages. Commercial processing systems, such as that produced by International Imaging Systems (I^2S), could easily be modified with additional functions added to process these data. Even the GEOSCAN MkII data could be processed using these methods and this was demonstrated by a CSIRO research project (Huntington et al., 1994). This study indicated that with only eight channels in the SWIR2 (2000nm - 2500nm) it was possible to map variations in the distribution of phengite and muscovite based on shifts in absorption feature wavelengths.

By the start of the 1990s it was established that it was possible to map the distribution of mineralogy using spectral imagery in a wide variety of semi-arid to arid terrains. In particular the absorption features in the SWIR produced highly diagnostic information on the distribution of clays and other hydroxyl bearing minerals. Since the hydroxyl bearing minerals are characteristic of hydrothermal alteration this was of interest to mineral

explorationists. Hence, the discipline of spectral geology became recognised and was allocated sessions at international conferences and the term mineral mapping, meaning the derivation of maps of mineral distribution using spectral geological techniques, became accepted. To a certain extent the understanding and potential of these techniques had exceeded the ability of available instruments to gather the required data. Existing airborne instruments, including the early AVIRIS and GER IS, lacked the number of spectral channels and/or the signal-to-noise ratio to produce data that could be reliably processed and interpreted spectrally, except under ideal conditions. The only field instrument commercially available at the time was the GER IRIS MkIV which was slow and cumbersome to use. This was demonstrated to the author in South Africa during 1984 when the dependence on cloud free conditions severely limited the amount of information that could be collected during a day's field work. It was this experience that resulted in my using a lamp to illuminate the sample while collecting spectra in the field with a GER IRIS MkIV spectrometer. This testing was carried out in South Australia during 1985. This established that using a lamp in the field resulted in significantly more, and therefore statistically analysable, data being collected.

Experience with the GER IRIS MkIV at the CSIRO and a widening interest in industry, indicated by the support of AMIRA funded research, led to the development and manufacture of the PIMA spectrometer by Dr T. Cocks (an employee of CSIRO at that time). The author was involved in field trials of the prototype of the PIMA and purchased the first production model in 1990. The advent of the PIMA instrument stimulated research not only into the spectral signature of minerals but also into processing sets of data in statistically meaningful ways. This resulted in the determination of spectral differences and associations from these data that are not apparent from mineral identification of a single spectrum.

Research into spectral techniques, using AVIRIS data (the JPL annual workshops edited by Robert O. Green documenting a wide range of investigations including geological applications), continued in the 1990s and there has been a proliferation of airborne and planned spaceborne instruments. However, advances in field instrument design and availability have not developed at the same pace as scanner systems.

These developments are not solely to satisfy the needs of geological and exploration communities; environmental monitoring is also a major factor along with defence and agricultural requirements. The growing availability of these data sets and instruments will

result in the continual development of this technology for geological mapping and mineral exploration.

1.3 ALKLINE ULTRAMAFIC ROCKS

This study has been primarily directed towards alkaline ultramafic rocks (kimberlites and lamproites); although the spectral features diagnostic of these rocks are common to other ultramafic rocks that have a high magnesium percentage (see Tables 1-2 and 1-3). According to Mitchell (1986), Mitchell and Bergman (1991) and Mitchell (1995) kimberlites and lamproites are clans of rocks that maybe classified as alkaline or potassic ultramafic rocks. Alkaline rocks being those in which either Al_2O_2 or SiO_2 are deficient with an excess of Na_2O and/or K_2O (Shand, 1922).

As mentioned above, most of the investigations into the applications of spectral geology published and presented at conferences cover the mapping of hydrothermal alteration in semi-arid to arid terrains. In this respect the Cuprite, Oatman and Silver Bell sites in the southwestern USA are typical. These sites having been flown with many of the imaging spectrometers available since the late 1970s (GEOSCAN MkII, AIS, AVIRIS, GER IS, HyMap, HyDice). Examination of Figure 1.2 shows that the distribution of AVIRIS test sites confirms this bias towards the arid southwest of the United States.

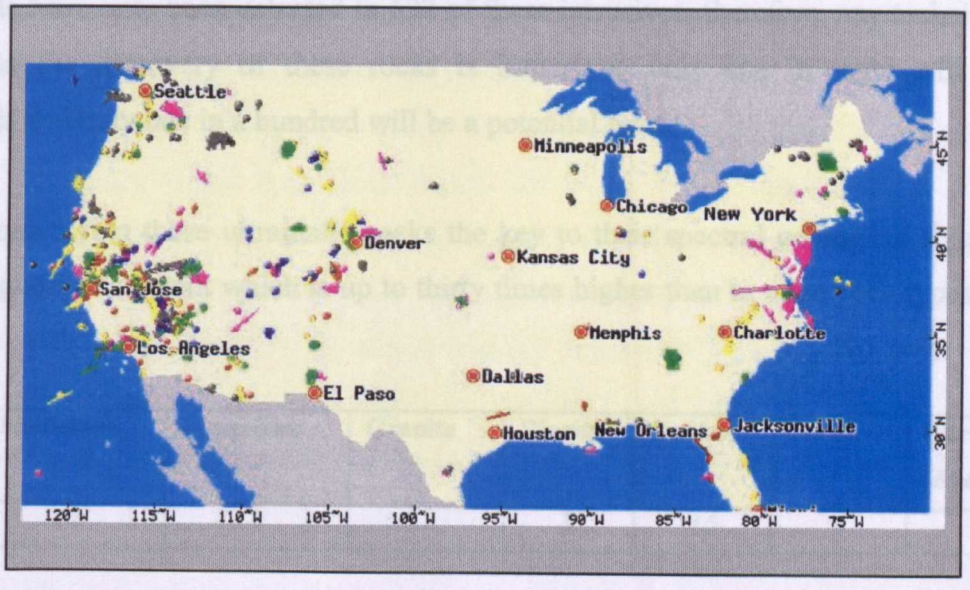

Figure 1.2: AVIRIS sites from the JPL web page showing the preponderance of surveys in the SW USA. Source Chovit (1997). The coloured dots show different test sites flown in different years.

A literature search that I have carried out using the Georef database (covering the period from 1980 to January 1998) has revealed that of 28,184 references to remote sensing and

spectral geology only 78 involve ultramafic rocks. This is evidence of the dearth of research into the application of spectral geological techniques to detect and delineate ultramafic, let alone, alkaline ultramafic rocks.

Ultramafic rocks as group are important as they have various types of ore deposits associated with them (Table 1.1).

Rock Type	Deposit Type	Geological Environment
Kimberlite	Diamond	Archaean Cratonic Areas
Lamproite	Diamond	Proterozoic Mobile Belts
Dunite-Peridotite	Ni Sulphide	Archaean Greenstone Belts
Serpentinised Peridotite	Lateritic Ni	Lateritically Weathered Terrain
Serpentinised Peridotite	Au	Archaean Greenstone Belts
Komatiite	Au	Archaean Greenstone Belts
Pyroxenite/Dunite/Peridotite	Cr and Platinoids	Layered Mafic Intrusives
Serpentinite	White Asbestos	Major Ultramafic Dykes

Table 1.1: Mineral deposits associated with ultramafic rocks. Sources Edwards & Atkinson (1986), and Stanton (1972).

Of these deposit types diamond bearing alkaline ultramafic rocks, kimberlite and lamproite, are probably the most valuable. The significance of detecting these with remote sensing techniques is reinforced by the fact that of the 5940 known kimberlitic intrusives in the world only 51 have been or are being mined for diamonds (Skinner, 1987). In fact diamonds have only been detected in 692 of these intrusives, therefore, any technique that facilitates the discovery of these rocks is important; only one in eight will contain diamonds and only one in a hundred will be a potential mine.

When considering these ultramafic rocks the key to their spectral geological signature is their magnesium content which is up to thirty times higher than in other rock types (Table 1.2).

Shale	Sandstone	Limestone	Granite	Diorite	Gabbro	Basalt	Ultramafic (Average)
2.5	1	8	1	3	7.5	6	30

Table 1.2: Magnesium percentage content of common rocks compared to ultramafic rocks. Source Spock (1961).

The percentage of magnesium varies in ultramafic rocks. However, in the alkaline ultramafic rocks it can reach ~36 percent (Table 1.3). It is this high magnesium content that

results in the association of spectrally distinct Mg-OH bearing minerals with these rocks.

Komatiite	Pyroxenite	Peridotite	*Lamproite (Olivine)	*Kimberlite	Dunite	Serpentinite
12	24	36	11-26	28-36	46	32

*Table 1.3: Magnesium percentage content of ultramafic rocks. Sources Wyllie (1967), Mitchell (1986) and Jaques et. al (1986). * Alkaline ultramafic rocks.*

The surface expression of these ultramafic rocks can range from distinct high relief outcrops to areas of lower relief depending on their weathering history and environment. In humid environments, such as tropical rain forests, they may be preserved with distinctly different topographic expression to surrounding rocks, often with more intense vegetation cover (Allum, 1982, Edwards and Atkinson, 1986). Where they have been subjected to prolonged lateritic weathering all traces may have been obliterated by the development of kaolinite at the surface or they may have been totally silificified (Butt, 1981). In less severely weathered terrains they may be expressed by changes in soil type and colour.

1.4 REMOTE SENSING APPLIED TO ULTRAMAFIC ROCKS

Allum (1982) stated that it was possible to map and delineate areas of potential for lateritic nickel deposits developed over ultramafic rocks in the Amazon basin using aerial photographs and radar imagery. The diagnostic photogeological signature in this case comprises areas of rounded topography, lack of joints and uniformity of vegetation species compared to surrounding rock units. In Pontual's (1990) research into mapping of the Oman Ophiolite, TM imagery was found highly effective in delineating the ultramafic rocks. That study found that decorrelation stretching of TM bands 7, 5 and 4 and combining these bands into red, green and blue colour composite images could be used to distinguish the various ultramafic rocks and map variations within them. These variations could be understood spectrally by examining full resolution spectra taken from the rock types present and convolving them to the TM spectral bands. However, these are examples of geographically extensive rock units whereas the alkaline ultramafic rocks often occur as intrusives, dykes or sills of limited spatial extent.

Apart from the extreme situations of tropical rain forest and total outcrop in desert, the ability to map ultramafic rocks with imagery using conventional remote sensing data processing and interpretation techniques is limited. Edwards and Atkinson (1981) pointed out that to use multi-spectral scanning techniques to locate kimberlites requires 'rigorous

preliminary field spectral studies over known intrusions under specific climate conditions ... ... to obtain significant spectral signatures". This is the focus of my thesis.

The primary difference in using spectral geological techniques as opposed to conventional remote sensing processing and interpretation is as follows:

- In conventional interpretation the multi-spectral imagery is enhanced and then interpreted visually with geological boundaries annotated. Applying various digital enhancement procedures, some of which may involve a prior knowledge, may assist determination of these boundaries. The spectra for the different units can then be determined from the imagery and some estimate made of the mineralogical meaning of the spectra and the units that they represent; this step is often omitted.

- Applying spectral geological techniques requires imagery that has sufficient spectral resolution. This permits meaningful comparisons between high-resolution (1nm to 5nm) laboratory and field spectra of minerals with those obtained from the imagery. The data required need to be collected with either imaging spectrometers or hyperspectral scanners. Processing of data is then directed at determining the distribution of areas of spectrally distinct units within the image; that is mineral mapping. This uses more sophisticated processing techniques than conventional remote sensing although of course hyperspectral scanner data can also be processed using the conventional methods. It also requires an in-depth knowledge of the spectra, not only of individual minerals but also spectra resulting from mixtures of minerals, as well as minerals mixed with green and dry vegetation. To obtain this knowledge requires both laboratory and field measurements of the spectra of rocks and soils.

Field measurements can be used as a spectral geological method for mapping the extent of various lithologies particularly in areas where residual soil cover obscures the surface exposure of the rocks.

The critical issues when applying spectral techniques to geological studies are the wavelength resolution of the instruments used and how the spectra obtained relate to the area from which the data is recorded. In field and laboratory studies, this tends not to be a major concern with most spectrometers having adequate spectral resolution, though not all have sufficient signal-to-noise ratio. However, when comparing pixels from scanners this is more significant and instrument characteristics will determine how reliable systems are in meeting the objective of mapping target materials.

1.5 GEOGRAPHIC RANGE OF INVESTIGATIONS

In this thesis research has been confined to regions that are semi-arid to arid. Semi-arid is defined as an area that receives less than 50cm of rainfall per year and arid areas less than

25cm (Jackson, 1997). How these terms relate to vegetation cover is important from a remote sensing perspective. Gentille (1977) presented a map (Figure 1.3), that shows the phytohydroxic contours for Australia, which is an indication of the vegetation potential. The contour level five on this map coincides closely with the 50cm rainfall contour. The following vegetation cover types occur within the contour levels up to 5:

- 0-1 Sand or stony desert ie. bare soil
- 1-3 Seasonal grassland or arid scrub
- 3-5 Grassland and open woodland

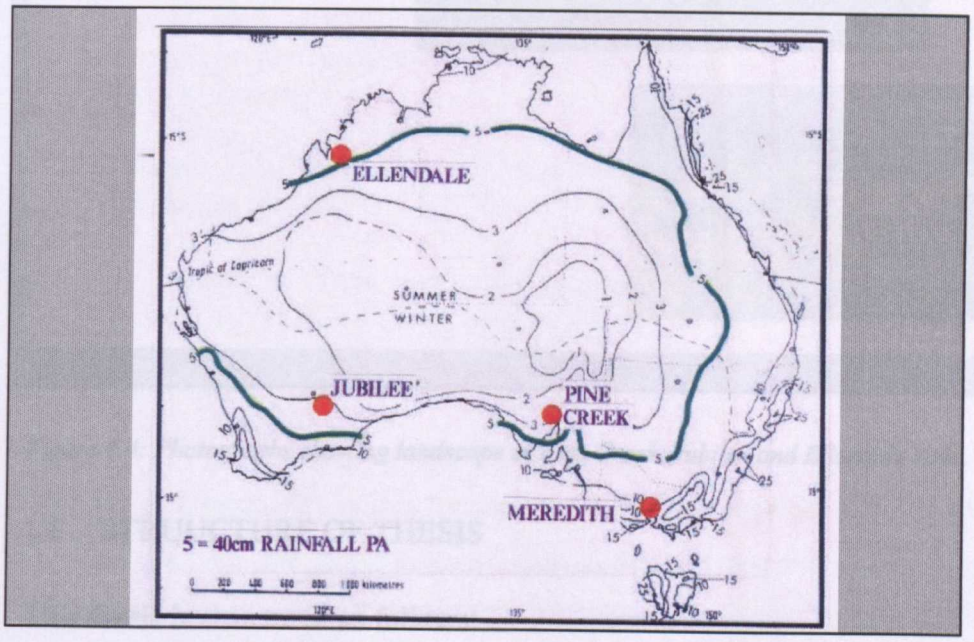

Figure 1.3: Phytohydroxic index map of Australia. Source Gentilli (1977). This map delineates climatic boundaries that are close to natural vegetation boundaries and shows the location of the image and field test sites discussed in this thesis. All the image test sites referred to in this study fall on or below the level 5 contour. Only the Meredith field test site referred to in Chapter 9, is located above the level 5 contour.

As can be seen in the photographs taken at the image test sites they show vegetation cover typical of dry-land regions (Figure 1.4). Tree cover is sparse and ground cover is variable. The Jubilee (centre photograph) site has the least vegetation and the Ellendale (bottom) the most. This however, is deceptive, the dry grass in the Ellendale photograph is not as extensive as it appears and can almost vanish as the dry season (May-September) progresses.

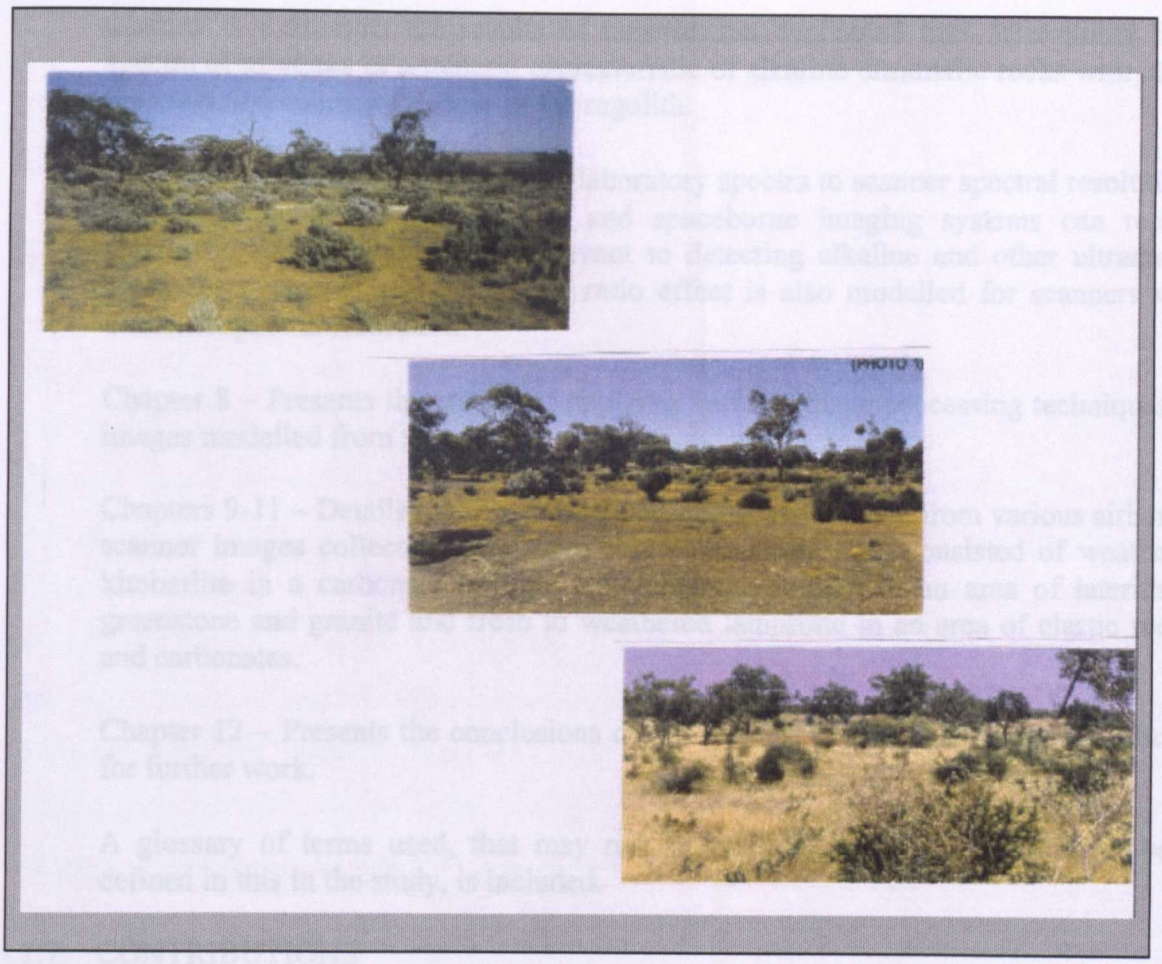

Figure 1.4: Photographs showing landscape at Pine Creek, Jubilee and Ellendale sites.

1.6 STRUUCTURE OF THESIS

This thesis is structured as follows:

Chapter 2 - Reviews previous studies relevant to this research. It is based on literature searches, checking conference/seminar proceedings (mainly ERIM Geological Thematic Conferences and NASA AVIRIS workshops) and unpublished Ph.D. theses.

Chapter 3 – Provides information on the range of systems investigated, the techniques used to process the data and a brief discussion on the physics of spectral geology.

Chapter 4 – Discusses the mineralogy of the rocks investigated and their weathering and breakdown products that can be preserved in the regolith.

Chapter 5 – Details the results of field and laboratory spectral studies of alkaline and other ultramafic rocks. The spectra of other rocks, minerals and materials that may be confused with those of ultramafic rocks or occur as background to these rocks are also presented.

Chapter 6 – Presents the results of experiments conducted into determining the spectra of mixtures of a mineral characteristic of alkaline ultramafic rocks with other minerals that commonly occur in the regolith.

Chapter 7 – Examines, by sampling laboratory spectra to scanner spectral resolution, the extent to which different air and spaceborne imaging systems can record diagnostic spectral information relevant to detecting alkaline and other ultramafic rocks. The issue of signal-to-noise ratio effect is also modelled for scanners with different spectral resolution.

Chapter 8 – Presents the results of applying various image-processing techniques to images modelled from spectra.

Chapters 9-11 – Details the results obtained on the ground and from various airborne scanner images collected from three test sites. These sites consisted of weathered kimberlite in a carbonate background, fresh serpentinite in an area of lateritised greenstone and granite and fresh to weathered lamproite in an area of clastic rocks and carbonates.

Chapter 12 – Presents the conclusions drawn from this study and recommendations for further work.

A glossary of terms used, that may not be generally familiar or that have been defined in this in the study, is included.

1.7 CONTRIBUTIONS

The research presented in this thesis is based on my activities while working for De Beers in Australia. All the studies comprising this thesis are the result of my own work. A colleague, Dr A. Becker, wrote the software developed to simulate noise in scanner imagery and spectra at my request. Dr Becker also modified the software supplied by GEOSCAN to apply the corrections to the data discussed in Chapter 10.

The image processing software I used is commercially available. The Microsoft Windows NT/95 version of PIMAVIEW used in this study incorporates techniques that I suggested, including the ability to parse values obtained from spectra into various processing algorithms. The latest version of PIMAVIEW (for Microsoft Windows NT/95) is similar in functionality to the in-house software I used for this thesis.

CHAPTER 2

2 PREVIOUS INVESTIGATIONS

2.1 INTRODUCTION

The extent of previous investigations into the application of spectral geological and remote sensing techniques for locating ultramafic rocks has been investigated. I conducted a literature search through the GEOREF and GEOBASE databases, using a search engine that combines these data bases, supplemented with the Anglo American Research Laboratory library database in Johannesburg. A collection of papers, conference proceedings and Ph.D. theses I have collected or to which colleagues referred me were also examined. Relevant papers not brought to light by the database searches were also located in copies of the JPL airborne geoscience workshop summaries, specifically those volumes dealing with the AIS and AVIRIS. The Environmental Research Institute of Michigan thematic conferences on geology and mineral exploration provided many of the most relevant papers located; many of these were found by the database search but others were located by manually checking the volumes.

Set	Term Searched	Items
S1	remote sensing or spectral geology or spectra or image processing or rock signature or satellite image or Landsat or imaging spectrometry	36994
S2	S1 and ultrabasic or ultramafic or serpentinite or kimberlite or dunite or peridotite or harzburgite or pyroxenite	78

Table 2.1: Keywords and results of GEOBASE/GEOREF database search.

As Table 2.1 shows, the results of the combined GEOBASE/GEOREF search indicated 78 unique publications linking spectral geology and/or remote sensing to the ultramafic rock and associated terms. Elimination of non-English papers, those duplicated in different publications and others which examination of their abstracts showed were irrelevant resulted in only eight papers being sought. Of these, seven were obtained as re-prints. Checking of other sources mentioned identified a further thirteen publications and theses as relevant, bringing the total considered to 21 documents. These documents are discussed below as they are considered relevant to this study. It cannot be guaranteed that this is an exhaustive search. There are bound to be some publications where the titles and keywords do not highlight relevant documents in searches. This may occur when the material of

relevance is found in the body of the text. For example, de Souza's 1995 thesis (Remote Sensing and the Tectonic Evolution Northern Eritrea) discusses ultramafic rocks in Chapter 4 but this was not located by the database search. Reading the documents located, including their reference lists, and the conformity of their findings suggests, however, that no major investigation into the topic of this thesis has been overlooked.

It is also of interest to note that of the 36,994 publications on remote sensing that are in the GEOBASE/GEOREF data bases only 78 relate to ultramafic rocks. This indicates that this is an area requiring further study. For example, when linking S1 (see Table 2.1) to hydrothermal alteration and metasomatism 216 items are produced, three times the number of publications on ultramafic rocks.

For convenience I have split the papers into scanner type investigated and listed them by date.

2.2 REVIEWS

Field Studies

Mustard and Pieters, (1988)

In the paper the authors recorded that serpentinite and talc horizons in an ophiolite melange, located in east central California, have spectral signatures that show a diagnostic absorption feature, near 2300nm. The area investigated was grass covered and dry grass spectra were also measured. The dry grass spectra also have near 2300nm absorption features but they have an additional feature at 2150nm, not observed in the mineral spectra.

The authors concluded that AVIRIS SWIR2 scanner data, with sufficient signal-to-noise ratio, appropriately processed should be able to map the ultramafic components within this ophiolite melange. The results of such a study would be a comprehensive view of the melange's ultramafic constituents and their relationship to crustal fracture zones.

Landsat MSS

Bouchect, Cervelle and Chorowicz (1984)

In this paper attempts to map the distribution of serpentinites in Morocco using the VNIR spectral channels of the Landsat MSS scanner were unsuccessful. The authors concluded that not enough spectrally diagnostic information is available from this scanner for its data to be used in this application.

Hardy & Bird 1984

This study was based on Landsat MSS data and was aimed at mapping the distribution of an ultramafic complex (Josephine peridotite consisting of peridotite and serpentinite) that has been thrust over sediments, volcanics and gabbros. In this case the ultramafic rocks show superficial colour differences which are attributed to variations in their iron oxide content. This was confirmed by examining visible to near infrared spectra.

From the spectra analyses it was determined that Landsat MSS 5/7 ratio would differentiate between the main rock types that are collectively referred to as peridotite (hartzburgite, serpentinite and intrusive (sic – peridotite?)). Compositing the MSS 5/7, 6/5 ratios and the first principle component (colour assignments not documented) produced an image in which the ultramafic complex could be distinguished the background rocks.

Landsat TM

Rivand (1989)

Rivand applied a linear un-mixing procedure, based on a linear mixing model, that he considered would permit Landsat TM imagery to be used to map the distribution of serpentinised ultramafic rocks in a melange. The area investigated is situated in the eastern Egyptian desert, near the Red Sea. The author determined that the melange consists of four distinct lithological units, serpentinite, granitoid, talc-carbonate rocks and iron bearing alumino silicates (gabbros and pillow basalts). It was established that the Landsat TM pixel's spectral signature is a linear combination of the convolved spectra that characterised these rock units. The spectral variations are distinguished by differences in overall spectral shape and radiance levels. Spectral variation was established by collecting

spectra from field samples and convolving them to Landsat TM bands. Un-mixing the Landsat TM data resulted in images that gave an approximation of the relative contribution of these rock end-member's spectra to each pixel's spectrum. This permitted mapping of the distribution of these rocks within the melange.

Rivand concluded that Landsat TM data obtained in arid areas and processed using un-mixing, based on linear mixing models, mapped the variations of rock types within the melange investigated. He also concluded that the distribution of serpentinites is more widespread than shown on the existing geological maps of the area. Specifically areas mapped as meta-volcanic and meta-basic rocks are, usually, in part serpentinite.

Chaturvedi (1990)

In this thesis Landsat based TM studies of kimberlite located in the Minas Gerias state of Brazil were investigated. Spectra were measured for the wavelength range 400nm and 2200nm (missing the diagnostic Mg-OH spectral features at 2300nm) of soils collected from the kimberlites. Chaturvedi concluded that applying a modified tasselled capped transform to Landsat TM data determines a redness index for the soils from the region. In this index image some of the known kimberlites are discriminated from the background rocks and soils. This result was related to variation in iron oxide content by analysing the spectra collected from the kimberlite soils. By converging the analysis of aeromagnetic data with the red-soil index anomalies, to rank them, Chaturvedi demonstrated it is possible to locate un-exposed kimberlites in this region.

Pontual (1990)

Pontual demonstrated in this thesis that variations in the composition and type of ultramafic rocks in the Oman ophilites can be mapped by applying de-correlation stretches to Landsat TM data and by producing colour composite images from selected bands. This result was attributed to the changes in the overall spectral shape present in pixels located on these rocks. To confirm this, spectra field samples were convolved to Landsat TM bands. These convolved spectra matched those obtained from the reflectance corrected Landsat TM data. Band ratios were also used to determine these lithological variations from the image data.

Weathering enhanced the spectral differences that were apparent in the spectra and image data. The degree of redness, due to iron oxide developed on the rock surfaces, varies with the different mineral composition of the rocks.

Scambos (1991)

Kimberlite diatremes that outcrop as buttes in a 50km long corridor in central Montana were investigated by Scambos. The image data sets studied were Landsat TM and MSS.

Spectra were taken from the soils collected on the kimberlites, background rocks and the mixed soil zone that fringes the kimberlites. These eight samples were also analysed by X-ray diffraction. Results from studies of soil samples indicate the presence of serpentine, phlogopite and chlorite in the kimberlite outcrop and soils, though no smectite clays were recorded. In the background soils, illite, montmorillonite, quartz with minor kyanite, dolomite and carbonate (calcite) are present. In the mixed soils, from the fringe of the kimberlite, background minerals are present in higher concentrations than those derived from the kimberlite.

Scambos noted the diagnostic significance of the 2300nm absorption feature association with the kimberlite and attempted to map this using Landsat TM data. He concluded that the Landsat MSS data would be unable to differentiate between the kimberlite and the background soils because of its lack of SWIR bands. Band ratios were selected as a method of mapping the extent of the 2300nm absorption feature from the Landsat TM data. The ratio chosen was band 5 divided by band 7, based on spectra from the soil samples convolved to the Landsat TM bands. The values for this ratio obtained from the convolved spectra were 0.875 for the kimberlite and mixed soils and 0.81 for background rocks. These band 5/7 ratio images showed some of the kimberlites as darker areas as well as many other areas of bare soil and grass.

The conclusion of this investigation was that Landsat TM data cannot be used to find kimberlites reliably in this region. He suggested that imaging spectrometer data with more SWIR channels, to enable discrimination between the areas showing the occurrence of the 2300nm and 2200nm absorption feature, might be useful for locating kimberlites.

Macias (1995)

In this paper Landsat TM and spectrometer investigations into mafic and ultramafic complexes in the arid Pilbara and the semi-arid monsoonal Kimberley regions of Australia were documented. Macias presented evidence that from the results of weathering:

- ultramafic olivine is transformed to serpentinite and magnetite, further weathering resulting in calcite, talc and saponite
- clinopyroxenes break down into clino-amphiboles, chlorite, epidote, carbonate and eventually saponite

This weathering mineralogy was supported by analysis of spectra obtained using the GER IRIS MkIV spectrometer. The field spectrometer study also indicated that lichen, developed on soil and rock surfaces, does not mask the diagnostic absorption features in the 2100nm-2500nm spectral region.

Processing TM images for the three sites studied showed that the ultramafic rocks appear red/brown in the colour composite produced by assigning band ratios 5/7, 5/3 and 7/1 to RGB. Gabbro and other mafic rocks are green and background areas blue to cyan in these colour ratio composite images.

Simpson, Macias and Moore, 1998

Band ratios 3/2, 6/3, - 5/6 (the minus 5 indicates the value used in the ratio is 255 minus the DN for each pixel in band 5) were applied to the NS001 (TM simulator) scanner data. With these ratio images it was possible to differentiate ultramafic rocks from granite background. These results were compromised when these rocks were heavily covered in lichen. This investigation was carried out in the Pilbara region of Western Australia where the rocks are exposed and sparsely vegetated, apart from lichen.

Sultan & Sturichio, 1986

In this paper the results of applying ratio images to map serpentinite in the eastern Egyptian desert was presented. The author concluded that a band ratio of Landsat TM5/TM7 can be used to delineate the areas of hydroxyl bearing minerals, TM5/TM1 the magnetite content of rocks and the reflectance ratio for band 4 the presence of iron bearing aluminosilicates. The selection of these ratios was based on theoretical considerations

obtained from literature studies. The effectiveness of these ratios was checked by plotting the values obtained from the TM5/TM1 and TM5/TM7 as a scattergram for various lithologies in the study area. This scattergram showed significant separation of the various lithologies by the values obtained from the ratio images.

By producing index images from the ratios images, with the threshold level determined as the mean plus standard deviation of the image data, the ability of these images to map the serpentinite and differentiate it from other rocks was demonstrated.

O'Conner, 1993

In this study the importance of the Mg-OH and $Mg\text{-}CO_3$ minerals in determining short wave infrared spectral features was recognised. It was noted that these diagnostic absorption features are covered by the Landsat TM band 7. These minerals also all show a shoulder or peak centred on Landsat TM band 5. Therefore, it was considered that a Landsat TM5/TM7 ratio image would be the most effective at separating spectral differences between various Mg-OH and $Mg\text{-}CO_3$ minerals and backgrounds. However, careful application of contrast stretching is required to selectively reveal the regions of these minerals within the imagery. A band ratio composite of TM 5/TM7, TM5/TM1 and band 4 in red green and blue respectively was contrast stretched and examined. With this imagery it was possible to discriminate volcanic schist belts from serpentinite, talc and carbonate assemblages in an area of the Arabian–Nubian shield in Egypt.

Marrs, Marks, Hausel and Albert, 1984

Analyses of the spectra of kimberlite obtained from locations on the Wyoming/Colorado border of the USA indicated diagnostic absorption features at 2300nm. These absorption features were attributed to the presence of Mg-OH bearing clays and minerals including montmorillonitic (smectite-saponite?) clays, serpentinite, chlorite and talc. These features were also observed in spectra recorded from soils derived from the kimberlite(s). It was also noted that the serpentinite, chlorite and talc show absorption features between 600-680nm and 900-1100nm due to the presence of iron oxides. It was concluded that these spectral features could be exploited using the NS001 (Landsat TM simulator) scanner to differentiate the kimberlite from the background rocks, granite and anorthosite.

Using principle component analyses (not the Crosta techniuque – see Chapter 8) and band ratios (bands 1650nm /2300nm and bands 660nm/500nm) a number of interesting anomalies were located, however, none could be attributed to previously known kimberlites. Some of these anomalies were reported to have interesting heavy mineral indicators associated with them, suggestive of kimberlite but none were confirmed. This is a report of work in progress.

Landsat TM and JERS-1 OPS

Dennis, Rothery, Ceuleneer & Mamia, 1994

In this paper a study of the ophilites in Oman using JERS-1 OPS data is compared to results from Landsat TM. It was pointed out that the JERS-1 OPS data is noisy, (no estimate of signal-to-noise ratio was provided) and requires noise reduction before further processing.

Rock types investigated were dunite and serpentinite. It was difficult to distinguish these rock types with the TM data, but JERS-1 OPS provides information on the Fe^{2+}, Al-OH and Mg-OH minerals which is not easily obtained from the TM imagery. These JERS-1 OPS data improved the discrimination of all rock types including ultramafics. It was also noted in this study that as serpentinite develops from other ultramafic rock the 2300nm absorption feature increases in prominence.

The image used was a JERS-1 OPS bands 8,5,2 red, green, blue colour composite de-correlation stretch and this was compared to a de-correlation stretched Landsat TM bands 7,5,4 colour composite. In the TM data five lithological units could be distinguished, however, they had better definition in the JERS-1 OPS colour composite. This also delineated areas of dunite not observed in the Landsat TM colour composite. Field checking proved that the JERS-1 OPS 852 image mapped the lithological changes more consistently than was achieved using the TM data. Apparently, the proportion of wehrlite (olivine-clinopyroxene rock) in the sequence is associated with this differentiation.

The conclusion of this study is that even the noisy JERS-1 OPS data can produce more information on ophilites that can be located from TM imagery in extremely arid areas.

De Souza, 1995

This study compared JERS-1 OPS and Landsat TM imagery for mapping serpentinite in Northern Eritrea. Simulated images of Landsat TM band ratios were produced based on laboratory spectra obtained from the field samples. These ratio techniques were then checked on actual Landsat TM data obtained from study area, which were also processed using the Crosta principal component technique. JERS-1 OPS data from the same area was also examined; the importance of the JERS-1 OPS channel 8 that is centred near the 2300nm Mg-OH absorption feature was discussed.

The simulated study showed that the ratio TM5/TM7 produced a good contrast between serpentinite and other lithologies, silicified volcanics and carbonates. However, the serpentinite is not separated from other ultramafic rocks and dark marbles by this ratio. The other ratios tested were Landsat TM5/TM1, TM5/TM4 and TM3/TM4. In all of these images serpentinites are confused with impure marbles. This was confirmed when the actual Landsat TM ratio images were examined. These images showed similar colours (red) for serpentinite, impure marble, chlorite schist and gabbro. The Crosta technique was also applied to the actual image data. Generally, this technique appears to have been better than the ratio images in mapping the serpentinite and pyroxenite but ambiguities remained. Some marbles and acidic metavolcanic were confused with the ultramafic rocks. de Souza concluded that comparing the Crosta colour composite and a de-correlation stretched Landsat TM742 colour composite complemented each other. This led to an improvement in the geological interpretation of the various lithologies from the Landsat TM imagery.

By comparing the spectra of the serpentinite convolved to Landsat TM bands and JERS-1 OPS channels de Souza demonstrated that the JERS-1 OPS data will be superior at differentiating the Al-OH and Mg-OH minerals. Applying the Crosta technique to the JERS-1 OPS data produced better definition of the various lithologies. Units within the ultramafic rocks were more clearly discriminated. The separation of serpentinite and marble was achieved and additional serpentinite occurrences were located that could not be detected with the Landsat TM imagery.

GEOSCAN MkII

Agar, 1994

The processing technique applied to the data in this study was the production of band difference colour composites. Two ultramafic intrusions were discussed in this paper. A kimberlite located in the Kimberley region and a metamorphosed (schistose) ultramafic in the Yilgarn, Western Australia.

The kimberlite is intruded into sandstone and has surface expression as a negative topographic feature. Consequently it is obscured by a cover of surficial material and alluvium. It was not selectively enhanced by the processing techniques applied to these data.

In the Yilgarn ultramafic example the colour composite was produced by the band differences (GEOSCAN MkII bands 11-16, 11-17, 11-18 and 13-14, 13-15, 13-16 displayed in red, green, blue respectively) both of these colour composites highlight the ultramafic intrusive as white in a blue-cyan background. Agar interpreted this result to indicate the weathering of the ultramafic had produced Al-OH clays which are absent elsewhere. This reinforced Agars analyses of the thermal infrared band images. These he interpreted as showing extensive areas of silicification, developed on the background granite, which is absent over the ultramafic.

This study indicates that in lateritically weathered terrains ultramafic rocks intruded into granites, which have been silicified, may produce anomalous concentrations of clay minerals. However, these clays may not be Mg-OH bearing and, therefore, of themselves be diagnostic of ultramafic rocks.

AIS

Mustard and Pieters, (1986)

Mustard and Pieters investigated the Moses Rock kimberlite dyke in southwest Utah. The total ultramafic content of this diatreme/dyke is 13 percent serpentine, classified as kimberlitic in origin. Using end-member processing they were able to recognise gypsum, background soil, illite and kimberlite soil as distinct spectral classes from the AIS data.

However, the kimberlite spectral end-member signature also occurred within lithologies surrounding the diatreme/dyke. This indicated that these data and processing techniques were not able to accurately un-mix this data so that the ultramafic rocks could be reliably identified.

GER IS

van der Meer (1995)

In this study it was determined that serpentinite altered from peridotite can be detected using data acquired with the GER IS hyperspectral scanner in Spain. Field spectrometer studies established that the diagnostic absorption feature was situated at 2300nm. The GER IS data was transformed using the IARR processing technique. Pixels from areas of vegetation were masked out and a hull transform was then applied to the data. These processes permitted the extracted values for depths of the 2300nm absorption feature to be assigned to each pixel. A stochastic statistical technique was then applied to these transformed data values to determine a pixel's serpentine content. Field examination of the areas predicted to contain serpentinite rocks confirmed that it is possible to map the degree of serpentinisation, within the peridotites, using GER IS data. This paper stressed the linear changes that mineral mixing causes to the depth of spectral absorption features.

Fan & Bodechtel, 1996

This paper discusses an evaluation using MAIS scanner, built by the Chinese with similar specifications to the GER IS. The test site discussed is situated over an ultramafic dyke intruded into mafic gneiss, marble and migmatite, situated in northwestern China. The data collected and analysed were from the spectral regions 480nm-960nm (VNIR) and 2030nm-2040nm (SWIR2). Using the IARR processing technique, the data were converted from radiance to reflectance.

Spectra are displayed from a number of pixels to form a spectral profile across the ultramafic and host rocks. The ultramafic rock spectra have absorption features in the NIR and near 2300nm / 2380nm which are absent in the host rock spectra. Using these spectra as targets for the spectral angle-matching program (SAM) it was possible to map the distribution of the ultramafic rock as well as various host rocks with these data.

AVIRIS

Rowan, Bowers, Crowley, Pacheo, Gumiel & Kingston, 1995

AVIRIS data was obtained from a carbonatite-alkali igneous complex in Colorado. These data were calibrated to reflectance using a flat field correction based on laboratory determined reflectance spectra.

Subsequently the spectral angle matching function (SAM) and linear spectral unmixing were used to process these data. Only the SWIR spectra were used with the SAM to map dolomite, sericitised felsite, quartz, granite and hydrothermally altered ash flow. The dominant alkaline igneous rocks, including pyroxenite, were also mapped with the SAM, however, for these rock the full 400nm-2500nm spectra were used. The linear unmixing also used the full range image spectra. This technique gave similar results to the SAM for the carbonates but produced significant improvement in mapping of the Mg-OH minerals; as well as the distribution of the haematite and goethite.

Substituting a spectra of biotite, obtained from the image, for the reference end-member spectra of peridotite (pyroxenite) in the linear un-mixing resulted in significantly better mapping of the pyroxenite unit. It was concluded that the un-mixing techniques gave better results because the non carbonate rocks were vegetated. Therefore, including the vegetation end-member improved the delineation achieved by the linear un-mixing when compared to the results obtained using SAM.

Mustard (1995)

Mustard reported in this paper on the examination of AVRIS data over an area of serpentinite in central eastern California. The area has extensive grass cover and end-member un-mixing techniques established that six end-members could be derived from these data. Two of the end-members could be related to green and dry vegetation and the remainder to variations in soil type. The areas of different soil spectral end-members could not be related to the distribution of ultramafic rocks in the area. However, this paper documents investigations using the VNIR wavelength channels and not those in the SWIR where the diagnostic mineral absorption features occur.

Kruse and Boardman (1997)

These authors investigated the kimberlites that occur in Utah and Wyoming using data from AVIRIS. No ground studies were conducted but they refer to work presented by Mustard (1986), reviewed above. In Wyoming no diagnostic spectral end-members were located associated with the kimberlites; this area has dense vegetation and lacks rock and soil exposure.

In Utah the Moses Rock dyke and nearby kimberlites were investigated. The data were processed using the ATREM package (Gao et al., 1992) to convert the spectra from radiance to reflectance. Analyses of the data located ten VNIR spectral end-members that could be attributed to iron oxides, green vegetation, water and shales. The SWIR2 bands produced thirteen end-members including dolomite, calcite, talc, illite, iron illite, quartz and several with broad 2350nm absorptions which they attributed to weathered serpentinite. Examination of the un-mixed image produced for the 2350nm end-member spectra showed that it occurred in the kimberlite diatreme at Mules Ear, though this end member was also detected in the surrounding sediments. This was a report on work in progress.

2.3 CONCLUSIONS

Those publications that mentioned Landsat MSS stated that its data was of limited use for this application because it lacks SWIR bands.

The papers on Landsat TM conclude that the overall spectral shape and/or iron spectral absorption feature can permit discrimination of exposed ultramafic rocks with these data in extremely arid areas. Scambos (1990) points out that more information is needed from the SWIR2 spectral region if spectral geological techniques are to be used to locate kimberlite and by analogy other ultramafic rocks in soil covered areas. Rivand (1998) demonstrated that un-mixing of Landsat TM imagery could map the distribution of serpentinite within a melange in an arid area. Macias (1995) reported that lichens do not always obscure the SWIR2 diagnostic absorption features. The studies by O'Conner (1993), de Souza (1995) and Dennis et. al (1994) and Sultan et al. (1987) all indicate that ultramafic rocks can be discriminated using Landsat TM imagery in arid areas. However, some of these papers demonstrate that the better spectral resolution of the JERS-1 OPS data in the SWIR2, compared to Landsat TM, improves this discrimination. A significant finding from this literature study is that data from systems such as Landsat TM, that have broad bands with

restricted wavelength coverage, cannot be used to map ultramafic rocks consistently. It appears that the results obtained are area dependent, and processing techniques that works in one region may not work as well in another. This is discussed in detail by de Souza (1995) who found that the techniques developed by Sultan et. al. (1987) for data collected in Egypt did not reliably map serpentinites in Eritrea.

The field studies and papers on hyperspectral scanners (AIS, GER IS and AVIRIS) indicate that the near 2300nm absorption feature is important in locating ultramafic rocks using spectral geological techniques. In none of the papers on hyperspectral scanners were conventional image processing techniques discussed. The papers either refer to statistical methods, spectral angle matching or end-member un-mixing. No papers reviewed reported on augmenting the results obtained from scanner processed imagery and interpretation with detailed ground spectral studies. The specifications of the hyperspectral scanners discussed in these publications have not been linked to their ability to produce data capable of detecting the spectral signature of ultramafic rocks.

From this literature review I conclude that there is recognition of the potential for spectral geological techniques, particularly utilising data from hyperspectral scanners, to detect the spectral signature of ultramafic rocks in areas of exposure and residual soils. However, there does not appear to have been a broad and systematic investigation carried out into this topic to date.

CHAPTER 3

3 SPECTRAL GEOLOGICAL CONCEPTS, INSTRUMENTS, AND TECHNIQUES INVESTIGATED

3.1 INTRODUCTION

In line with the objectives of this thesis, my research has focussed on readily available instruments and commercial software packages. In this section the instruments which provide the data for spectral geological investigation are reviewed. The software packages used to process the data are discussed, particularly those unique to spectral geology. Where appropriate the concepts that underlie the instruments and processing are discussed.

3.2 SPECTRAL REGIONS INVESTIGATED

This research has investigated data derived from the visible near infrared (VNIR) and short wave infrared (SWIR) spectral regions (from 400nm to 2500nm). However, the majority of the investigation has been concentrated in the SWIR2 spectral region from 2000nm-2500nm. It is not considered necessary to detail the physics and concepts of remote sensing in detail as these are well documented in the literature (Drury, 1987 and 1993, Mather, 1989). It is worth noting that at the wavelengths being considered the spectral variations seen in minerals and, therefore, rocks and soils are due to the following interactions of electromagnetic radiation with elements and their bonding within minerals:

- In the visible to near infrared region the absorption features are due to crystal field and charge transitions which affect iron oxide bearing minerals (Figure 3.1). As Drury (1993) pointed out, the charge transfer effects are dominant in spectra collected from natural surfaces and result in broad absorption bands below 500nm. The crystal field effects are less pronounced but also result in absorption features situated between 800nm and 900nm due to iron and other transition metal oxides.

- The SWIR region has absorption features between 1300nm and 2500nm due to the overtone combinations of the fundamental O-H absorption at 2700nm with the band-bending transforms that are due to metal hydroxyl bonding. Results of these combinations and overtones are absorption features near 2200nm that can be attributed to Al-OH, at 2240nm related to Fe-OH and at 2300nm related to Mg-OH (Figure 3.2).

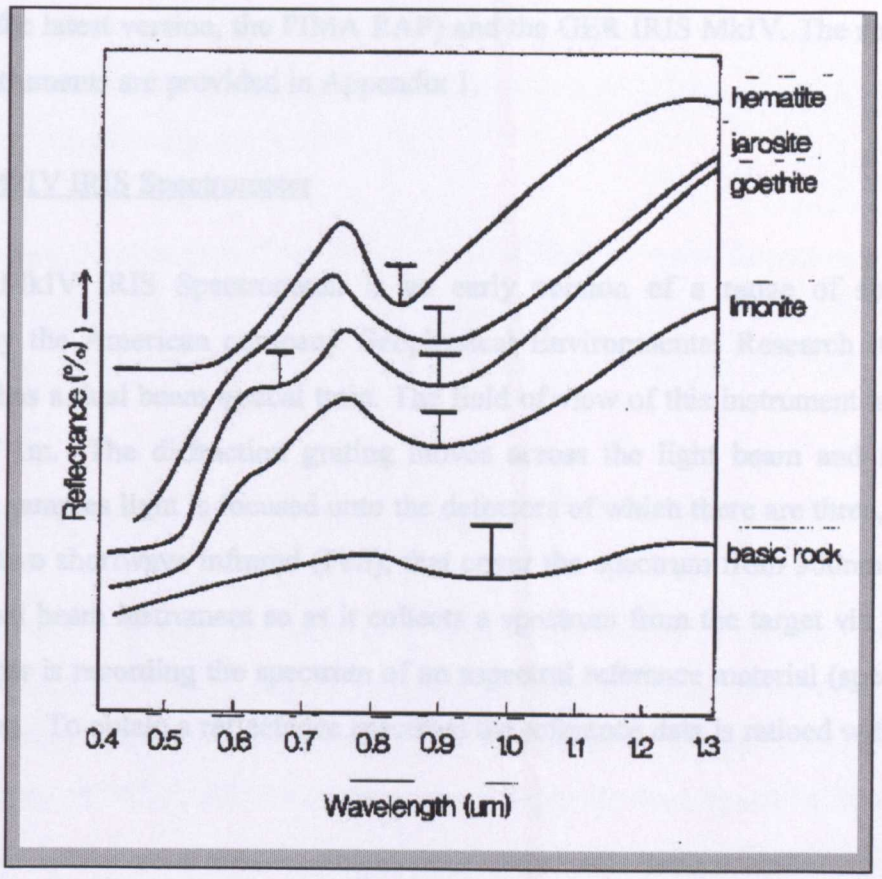

Figure 3.1:VNIR Spectra of Iron Oxide bearing minerals. Note the broad but relatively shallow absorption minima shown by the T and fall off towards 400nm (0.4um). Source Drury (1993).

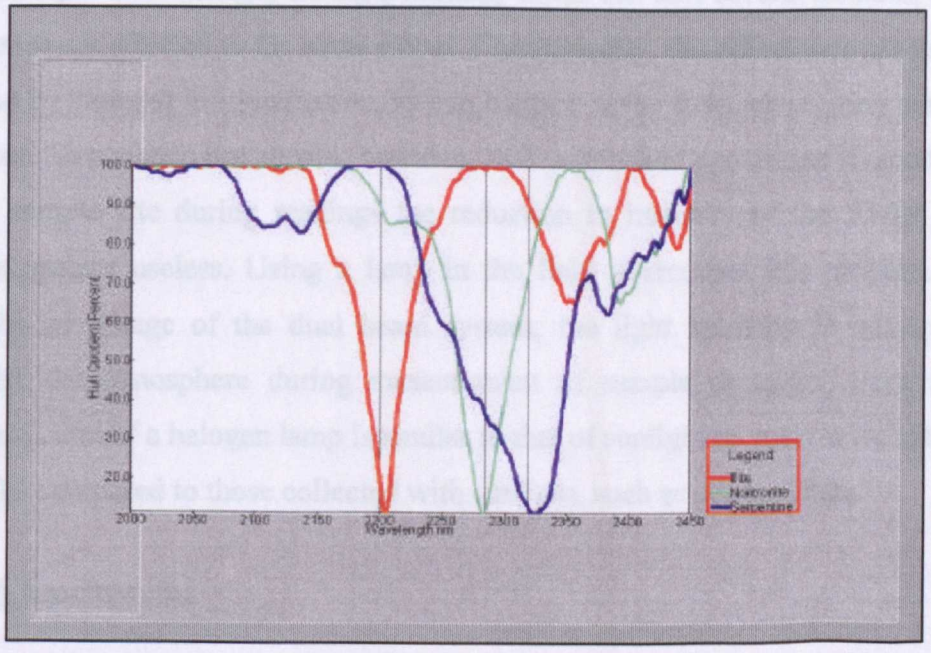

Figure 3.2: Examples of SWIR spectra, illite red (Al-OH), nontronite green (Fe-OH) and Serpentinite blue (Mg-OH). Note the changes in the position of the main absorption features.

3.3 FIELD AND THE LABORATORY SPECTROMETERS

I have made use of two reflectance spectrometers: the Integrated Spectronics PIMA

(including the latest version, the PIMA RAP) and the GER IRIS MkIV. The specifications of these instruments are provided in Appendix 1.

The GER MkIV IRIS Spectrometer

The GER MkIV IRIS Spectrometer is an early version of a range of spectrometers produced by the American company Geophysical Environmental Research (GER). This instrument has a dual beam optical train. The field of view of this instrument is $4cm^2$ at a distance of 1m. The diffraction grating moves across the light beam and for discrete wavelength samples light is focused onto the detectors of which there are three, one visible (SiO_2) and two shortwave infrared (PbS), that cover the spectrum from 300nm - 2600nm. This is a dual beam instrument so as it collects a spectrum from the target via one optical train the other is recording the spectrum of an aspectral reference material (spectrally flat) such as halon. To obtain a reflectance spectrum the reference data is ratioed with the target spectrum.

There are non-dual beam versions of this instrument that measure the sample separately from reference pad, pre-or post-sample. However, the advantage of the dual beam system is that if the light level changes during a reading, which can take several minutes, the target and reference are affected to the same extent. Consequently, the reflectance spectrum is not invalidated by changes in illumination, as can happen in the field when using sunlight for illumination. Experience has shown, however, that under field conditions if cloud shadows cross the sample site during readings the reduction in intensity of the SWIR radiation makes the spectra useless. Using a lamp in the field overcomes this problem and also reduces the advantage of the dual beam system; the light intensity is not appreciably affected by the atmosphere during measurement of sample or target. Fortunately the irradiance spectra of a halogen lamp is similar to that of sunlight so spectra recorded with a lamp can be compared to those collected with sunlight, such as scanner data.

The PIMA Spectrometer

This is also a diffraction grating instrument. However, it has an internal halogen lamp that shines onto a diffraction grating that moves across the beam. The target is, therefore, illuminated by light at unique wavelengths. The light is reflected back via an integrating sphere onto the PbS detector. As PbS is only sensitive to infrared radiation the spectral range of this instrument is in the SWIR only, 1300nm-2500nm. After the target spectrum

has been recorded a gold plate is moved across the field of view and its spectrum is recorded as a standard. The two spectra, target and gold reference, are then ratioed to produce the reflectance spectrum.

This is a contact instrument and the field of view is 2mm by 4mm. Recent models (SP and RAP) permit measuring of samples without recording the gold reference for each target, this halves the measurement time (+/- 15 seconds) as it requires only one reading per sample.

3.4 PROCESSING OF SPECTROMETER DATA

Spectrometer data has been processed over time with a variety of software packages that have evolved considerably during the period covered by this study. However, the spectral data used in this thesis were processed with an in-house developed Microsoft Windows NT/95 version of PIMAVIEW (supplied by Integrated Spectronics with the PIMA). Where values have been extracted from the spectra to produce profiles and contour plots related to spectral variation, Microsoft Excel and Surfer for Windows have been used.

The need to be able to extract parameters of spectra such as the depth of a specific absorption feature or the range of wavelengths associated with an absorption feature was determined early in the processing of PIMA data. I conveyed this need to Integrated Spectronics who used software we developed at Stockdale Prospecting to release an additional software package PIMACALC. This package is run in conjunction with PIMAVIEW to produce files containing spectrally diagnostic information. Integrated Spectronics also supplied the source code for PIMAVIEW to Stockdale Prospecting which formed the basis of the in-house Windows NT/95 program (mentioned above), this also incorporated PIMACALC. The latest release of PIMAVIEW, from Integrated Spectronics, is a Windows 95 version similar to the program I have used in this study.

Spectral Processing Techniques

Visual Analysis and Matching to Libraries

The most basic method of processing and interpreting spectra is to plot them, on paper or a computer monitor, scaled so that the range of the Y-axis matches the data range. Otherwise, the spectral may appear as a nearly featureless line (Figure 3.3).

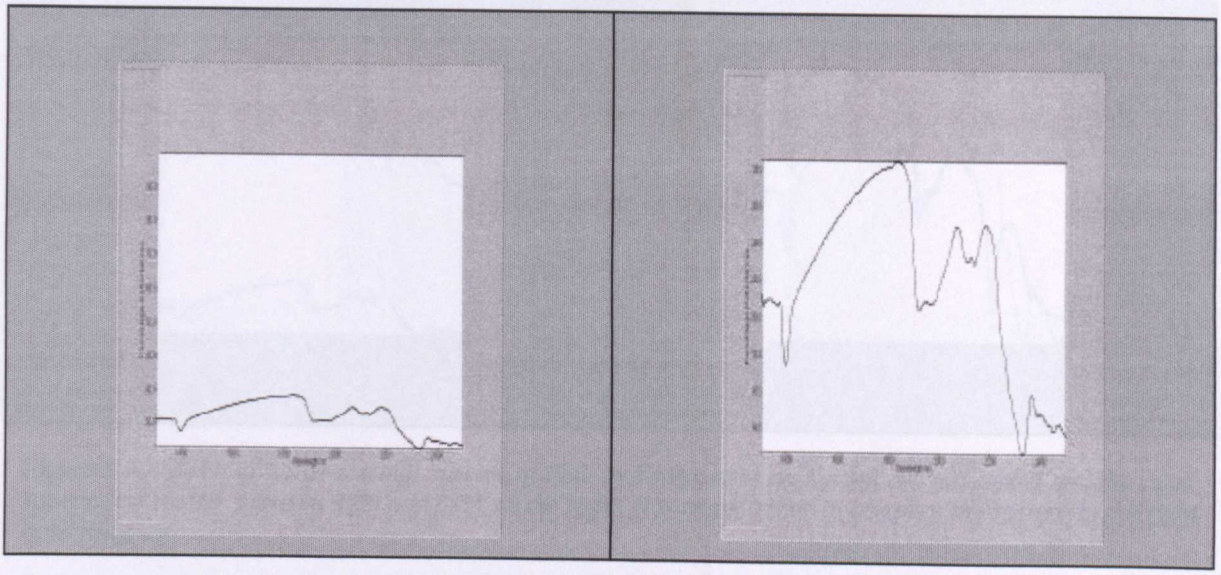

Figure 3.3: Serpentine spectra displayed with Y-Axis at full range (left) and scaled to Y-Axis data range (right).

The spectra (spectrum) being investiagted can then be visually compared to library spectra of known minerals and identification can be made with varying degrees of confidence. Where an exact match occurs this is simple but where the target spectra is from a mineral mixture this can result in ambiguities (Chapter 6). There are several processing techniques that can be applied to spectral data that can assist and improve on the extraction of information from spectra.

Linear Scaling and Stacked Profiles

By taking the maximum Y-Axis range of a spectrum and then scaling it to a fixed range, for example 20% - 100% (Figure 3.4), and applying this scaling to other spectra it becomes much easier to compare spectra. For example, to compare a target with a library spectra, or when a series of spectra are displayed in a stacked plot so that they can be differentiated into different classes (Figure 3.5).

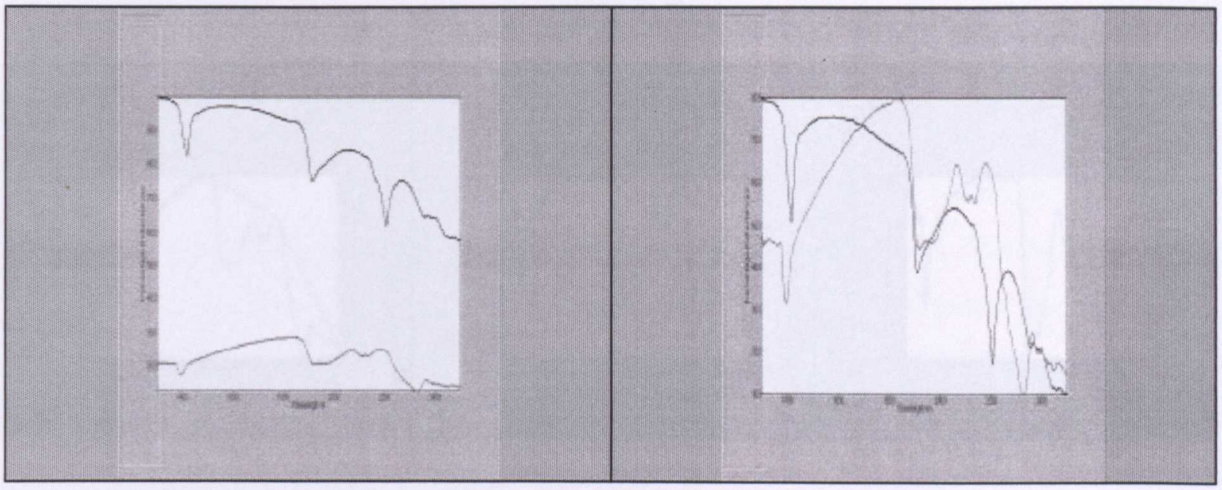

Figure 3.4: Effects of linear scaling: spectra of illite and serpentine on the left are not scaled and the same spectra are scaled between 20% and 80% on the right. It is much easier to compare the spectra in the right hand diagram.

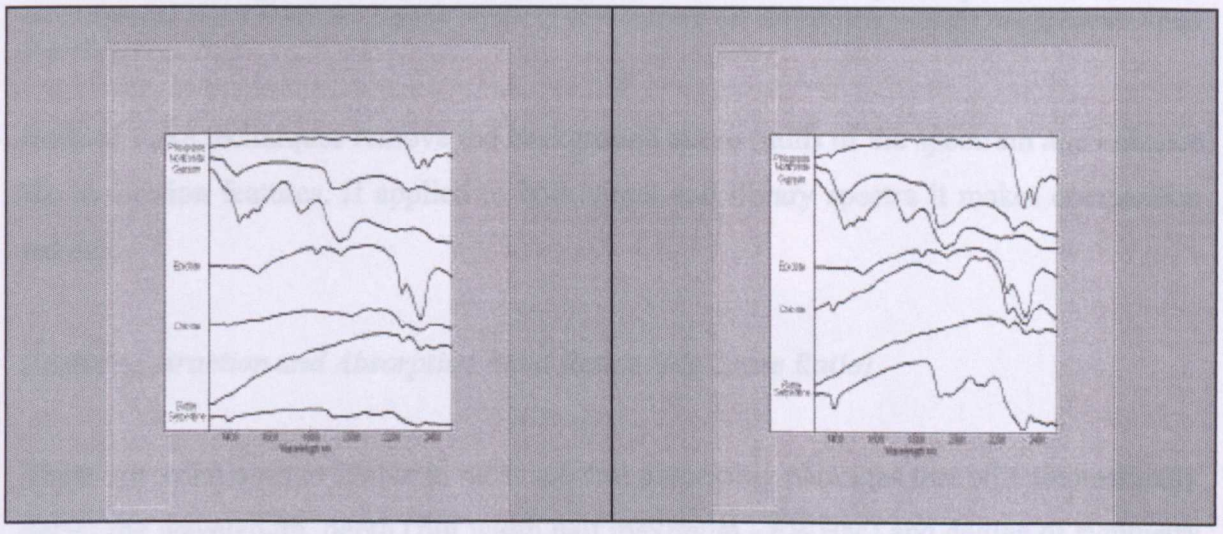

Figure 3.5: Stacked profile spectra. Spectra in the plot on the left have not been linear scaled, while those on right have been scaled from 10% to 100%. Note the greater detail visible in he spectra in the plot on the right.

Hull Quotient and Hull Difference Transforms

These techniques are carried out by simulating a hull line across the spectrum and then dividing (quotient) or subtracting (difference) the Y-axis spectral values with the hull line values (Figure 3.6). This technique was first described by Craig and Green (1985). In either case, the hull spectrum values are expressed as percentages. However, in the hull difference case they actually provide the true depth of an absorption features, so long as the spectrum has not been linearly scaled.

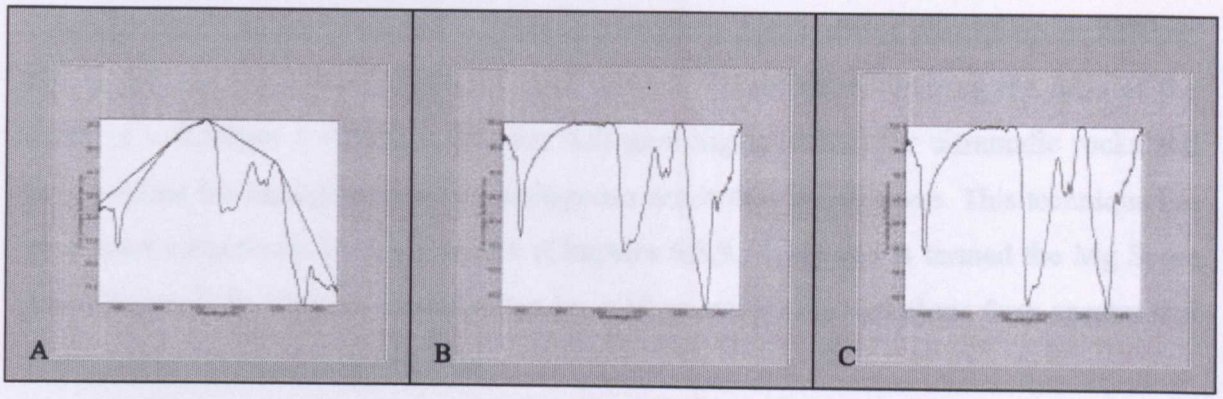

Figure 3.6: Hull quotient and Hull difference spectra. The plot A is a spectrum of serpentine showing the hull line. The B plot is the hull quotient produced by dividing the serpentine Y-axis values into the hull line values and converting the values obtained to percentages. The C plot is the hull difference spectra obtained by subtracting the serpentine Y-axis values from the hull line. In the C plot the Y-axis values range from 100% to 93% showing that the deepest absorption features are 7%. The hull quotient percent values cannot be interpreted in this way; they suggest depths of 40% that are not comparable with the raw spectrum range in plot A.

Both of these techniques remove the background curve (hull) of the spectrum and enhance the absorption features. If applied to both target and library spectra it makes comparison easier.

Feature Extraction and Absorption Band Ratios (Mg Score Ratio)

There are techniques available in most spectral processing packages that will automatically detect the wavelength, depth (full width half maximum - FWHM) and degree of symmetry of absorption features. These values by themselves can be compared to those obtained from library spectra to assist with identification. More importantly they can be extracted from a series of spectra and plotted against data coordinates so that diagnostic changes in a group of spectra can be geographically located. For example, contouring the depth of the 2300nm-absorption feature obtained from spectra collected from a grid over an ultramafic rock should highlight the ultramafic in the contours. In fact, these techniques are arguably the most important method of utilising mineral spectral data, rather than purely identifying the mineral species. Often the subtle changes in the wavelength and relative depths of absorption features reveal significant geological information from what may appear, at first sight, to be a monotonous sequence of mono-mineralic spectra.

These extracted values can also be parsed into a formula that, for example, divides the depths of absorption features by one another. This is useful, if for instance, the background to an ultramafic rock was kaolinite-rich rocks. Since both the kaolinite and ultramafic rock

spectra have absorptions at ~2300nm contouring the depth of this feature alone may not uniquely highlight the ultramafic. However, kaolinite has a strong absorption at 2200nm that is not seen in a pure ultramafic rock spectra. Therefore, contouring the ratio of the depth of ~ 2200nm / ~2300nm features will give higher values for ultramafic rocks and lower values for background; a less ambiguous result than depth alone. This technique has been used extensively in this research (Chapters 6,8,9,10,11) and is termed the Mg Score ratio (Figure 3.7). Various formulae can be used to extract the variations from spectra that reveal subtle changes in mineralogy.

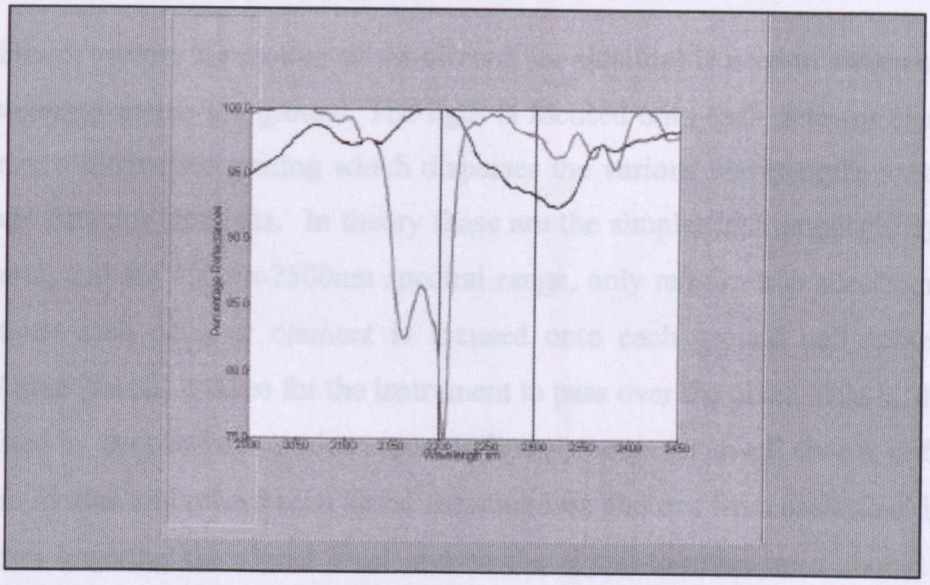

Figure 3.7: Spectra of kaolinite (grey) and serpentine (black), vertical lines at 2200nm and 2300nm. The depth of the 2300nm feature in serpentine is 6.4% and kaolinite 4%. Dividing the depth of the >2200nm feature by the depth of the >2300nm feature gives the values of 6% for serpentine and 1% for kaolinite.

Profiling, Contouring and Image Data Cubes

When dealing with multiple spectra there are a variety of methods that can be applied to present analysis results. In this study, spectra obtained from samples collected on grids have had the Mg Score ratio applied to them and these values contoured. Where the spectra have been obtained from a single traverse a profile has been plotted.

However, for grid samples it is possible to convert the spectra into an image cube such that the X, Y dimensions are the grid location and the Z-axis has the spectral values. Such grids can then be treated as a hyperspectral image (or data cube) and image processing techniques can be applied to them. This is the basis for the simulated scanner images discussed in Chapter 8.

3.5 SCANNER IMAGING SYSTEMS

Airborne Scanner Design

There are two principal designs for imaging scanners: the pushbroom and the optical mechanical scanner or line scanning systems. There is copious literature available on the principles and specifications of these instruments, ranging from brief reviews in most remote sensing textbooks (Drury, 1993) to in depth technical descriptions (Kramer, 1994 and Simonett et. al., 1984).

In a pushbroom system the motion of the aircraft (or satellite) is used to sweep an array of detector elements across the ground. The light is focused onto each detector element after passing from a diffraction grating which disperses the various wavelengths spatially onto the different detector elements. In theory these are the simpler instruments, they have no moving parts, and for 400nm-2500nm spectral range, only require two spectrometers. In these systems each detector element is focused onto each ground cell (pixel) for the amount of time (dwell) it takes for the instrument to pass over the pixel. That is, dwell time is determined by the platform motion alone. In line scanners the dwell time is defined both by platform motion and mirror scan speed meaning less photons from each pixel impact on the detectors lowering the signal level and so the signal-to-noise ratio should be lower when compared to pushbroom systems. For simple three band systems such as SPOT the pushbroom system works well. However, as the number of bands increases the electronic complexity rises rapidly. This is because the number of detector elements in the array has to equal the number of pixels across track (swath) multiplied by the number of spectral bands. For example a 512 pixel system with three bands would require 1,536 detector elements in the array. For 32 channels this would increase to 16,384 detector elements which results in complex multiplexing of the wiring on the back-plane of the array. This is technically challenging when working with InSb (Cocks, pers. com), the material required for infrared imaging, and can result in induction of noise into the data.

In line or optical mechanical scanners (Figure 3.8) a large rotating mirror scans across the path of the platform. The light beam is then focused via a collimator through an aperture (field stop) the size of which defines the field of view and geometry of the each pixel. The light is then focused through a telescope lens system onto beam splitters, they direct specific wavelength ranges to each spectrometer. From the beam splitter the light is focused onto a diffraction grating which disperses the various wavelengths spatially onto

different detectors elements. In such instruments the dwell time of light from each pixel is less than in a pushbroom scanner (for 512 pixel swath systems 1/512). This means the overall signal level is lower, however, with the latest technology in detectors and optics it is still possible to obtain an adequate SNR (see Chapter 7). However, the detector electronic circuitry of these systems is far simpler than for pushbroom scanners, for a 512-pixel swath imaging 96 channels in three spectral regions there will only be three detector arrays of 32 elements each.

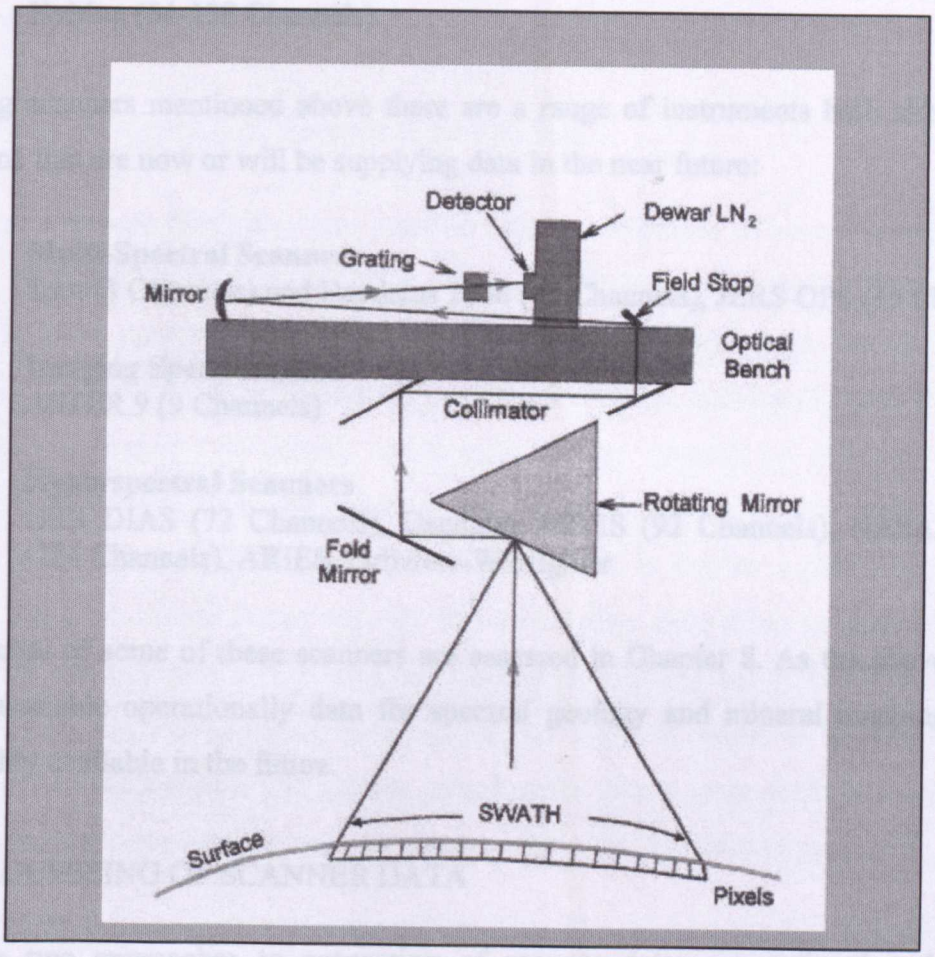

Figure 3.8: Schematic of a modern HyMap type optical mechanical scanner. The motion direction would be out of the page. LN_2 indicates that the infrared InSb detector array is cooled by liquid nitrogen.

All of the data used in this study has been supplied by line scan/optical mechanical scanners.

Airborne Scanner Classification

The image bandwidth and number of channels, in the VNIR to SWIR (400nm-2500nm) spectral wavelength regions have been used to classify the scanners from which data has been utilised in this study as follows:

- **Multi-Spectral Scanners**
  Bandwidth: 60nm to 140nm with non-contiguous bands - Landsat TM (7 Channels)

- **Imaging Spectrometers**
  Bandwidth 20nm-50nm with contiguous bands - GEOSCAN MKII (24 Channels)

- **Hyperspectral Scanners**
  Bandwidth: <20nm with contiguous bands - GER IS (63 Channels), HyMap (64-128 Channels)

Excluding scanners mentioned above there are a range of instruments both airborne and spaceborne that are now or will be supplying data in the near future:

- **Multi-Spectral Scanners**
  Spot (3 Channels) and Daedalus 1268 (15 Channels), JERS OPS (15 Channels)

- **Imaging Spectrometers**
  ASTER 9 (9 Channels)

- **Hyperspectral Scanners**
  GER DIAS (72 Channels), Daedalus MIVIS (92 Channels), NASA AVIRIS (224 Channels), ARIES, Orbview-Warfighter

The potential of some of these scanners are assessed in Chapter 8. As the above systems become available operationally data for spectral geology and mineral mapping will be more readily available in the future.

3.6 PROCESSING OF SCANNER DATA

There are two approaches to processing of scanner data: conventional and spectral processing. Both require knowledge of the spectral properties of the materials in a scene. However, in conventional processing this knowledge is used to select bands that are operated on to highlight the presence of band specific absorption features. For example, the Mg Score ratio divides the >2300nm band by the > 2200nm band, this will highlight areas of >2300nm absorption including Mg-OH minerals in a single band ratio image. In spectral processing the total form of a spectrum, rather than one or two attributes, is utilised to locate the occurrence of pixels that have spectra that match the target spectrum.

In conventional and spectral processing of imagery it is first necessary to make corrections to the raw data. These include removal of system introduced offsets and atmospheric

corrections. For broader channel data, with less than 30 channels, for example Landsat TM and GEOSCAN MkII, it is possible to use offset removal techniques such as dark pixel subtraction (Chavez, 1989), regression line removal (Potter, 1977) and the regression intersection method (Crippen, 1987) for both atmospheric and system corrections (Chapter 8). All these methods require obtaining offset values from within the data for each band and then subtracting these values from each pixel in the corresponding bands. When band numbers increase these methods become very time-consuming. They also require identification of spectrally homogeneous areas within the image from which values for the offset have to be collected.

Conversion of Raw Data to Radiance and Reflectance

The digital numbers (DN) that raw scanner data is comprised of are a measure of the intensity of reflection of the imaged surface at different wavelengths. However, these values also have contributions from light that is scattered back into the scanner from particles in the atmosphere and background voltage, from the systems electronics. The DN values are also reduced in certain wavelength regions (bands) by absorptions due to atmospheric gases, O_2, CO_2 and water vapour. There is also a spatial variation in the intensity levels of pixels from the same material. This is due to a pixel's topographic situation, those on slopes facing the sun will be brighter than those in shadowed areas. Furthermore, the DN values vary with the wavelength position due to the intensity of the sunlight, which has a solar (black body) curve that peaks at 500nm in the visible region and falls off towards longer and shorter wavelengths. For a more detailed review of the physics and remote sensing concepts see Drury (1993) and Simonett et. al. (1984).

These additive and subtractive variations distort the DN values such that a plot of a single pixel from raw scanner data will not produce an easily recognisable spectrum. Such data cannot be processed systematically, nor will the spectra of the same material from different parts of the scene be similar. The raw DN data has to be processed to convert it to reflectance data similar to that obtained from field and laboratory spectrometers. However, with scanners it is not practical to have a large area of spectrally uniform material on the ground to act as a reference target. Therefore, these corrections cannot be made by the ratioing of target to reflectance as is done with laboratory and field spectrometers (see section 3.4).

System Corrections

The system voltage that contributes to the DN is termed the dark current, that is, it is the DN obtained when the system is imaging a totally non-reflecting (black hence dark current) surface. It varies in intensity from band to band and is always additive. In modern scanners this value is recorded for each data line and band during the scan cycle. The dark current value is then subtracted from each band during pre-processing of the data.

After the dark current correction has been applied, if the scanner has been calibrated using a standard light source so that each detector response is kown, then each band can be multiplied by a correction factor. This will result in the data being converted to radiance; so that the DN is then in units expressed in watts per metre squared per steradian per nanometre.

In older scanners such as the GEOSCAN MkII the dark current data was not collected coincidentally with the image data. Therefore, either this data has to be obtained by running the scanner with the aperture blocked off or determined from the data itself, see Chapter 7. Neither of these methods is as reliable as using the dark current values collected during data acquisition.

Atmospheric Correction and Calibration to Surface Reflectance

After the data has had the dark current correction applied, an essential first stage, then the conversion to reflectance can be undertaken. It is not absolutely necessary to convert the data to true radiance values for this.

For multispectral scanners research has been undertaken into various techniques to atmospherically correct the scanner data in order to convert the radiance values recorded by the scanner to reflectance. Results of testing these techniques for simulated Landsat TM and GEOSCAN MKII data are presented in Chapter 7. Some of the techniques used are available in software packages such as ENVI. However, the more sophisticated techniques that are applied to hyperspectral scanner data are not available in commercial processing packages at the present time. These techniques are reviewed in Clarke et. al. (1994) and software to carry out these corrections is available as shareware from NASA, JPL and academic institutions.

The objective of all of these techniques is to remove from the image data the solar irradiance; atmospheric transmittance and atmospheric scattering that are obscuring the surface reflectance data. This is a formidable task according to Clarke et. al., 1994. These techniques, such as the Atmosphere Removal Program (ATREM), all require the development of an atmospheric and solar irradiance spectrum models that are dependent on season, latitude and water vapour content as well as other atmospheric gas concentrations. These models are derived from atmospheric modelling programs such as LOWTRAN 7. Applying these calibration techniques produces a model irradiance spectrum that satisfies the survey condition parameters and this is used to correct the scanner data to reflectance. It removes the effects of scattering, the solar irradiance spectrum and atmospheric gases and water vapour.

However, estimating water vapour is problematic as it can vary significantly within a survey scene both spatially and temporally. For this to be reliably estimated requires that the non-saturated water absorption wavelengths at 950nm and 1150nm are imaged. The depth of these absorption bands can be used as a measure of the water content for each pixel's atmospheric column and will considerably improve the results for the calibration of the image data to reflectance. An additional complication is that the solar irradiance spectrum may fluctuate temporally (Clarke et.al., 1994).

According to Clarke et.al., 1994 the most precise result, for AVIRIS hyperspectral data, is to use the ATREM method, (which is a radiative transfer model) combined with a ground calibration method. The ground calibration method relies on determining the surface spectra from several areas of spectrally uniform material within a scene. The field spectral measurements required for this may take several man weeks and may not be reliable if large topographic variation occurs within the scene (Clarke et. al., 1994).

It should also be noted that these techniques do not correct for topographic effects on spectral brightness (albedo) unless a digital elevation model is integrated into the modelling.

These techniques have not been used in this study. This is because they are time consuming to apply to data that is being used operationally. The log residual technique described below has been found to be an acceptable alternative, at least for SWIR2 data, but this may not be the case for the VNIR hyperspectral data.

Log Residual Correction

Although the log-residual or quick residual programs (Craig and Greene, 1985) are not available in many commercial image-processing systems, they can easily be implemented. The ENVI function IARR (Internal Average Relative Reflectance) is essentially the log residual transform (Kruse and Boardman, 1997).

Before applying the log (and quick) residual program the image data must have been dark current corrected. Other additive offsets, such as atmospheric scattering and instrument offsets must also be removed (Tsuchida et. al, 1994), see Chapter 8. In the SWIR (1300nm-2500nm) the effects of atmospheric scattering are minimal (Drury, 1993) and the atmospheric scattering correction need not be applied to data from these wavelengths prior to carrying out the log residual transform. However, offsets introduced during data collection, as with the GEOSCAN MkII scanner data should be removed (Huntington et. al., 1994). My experience has shown that it is better to apply the log residual transform separately to data from different wavelength regions, except in multispectral scanner data with a limited number of bands (eg. Landsat TM).

The log residual transform removes the solar irradiance, atmospheric transmittance, instrument gain (where the data range is compressed to byte as in the GEOSCAN MkII) and topography/albedo effects from the raw data to produce a pseudo reflectance image. This is achieved by calculating two geometric means from the data, the spectral and spatial means. Each image data value is then divided first by the spectral then by the spatial mean. Geometric means are obtaining using the logarithm of the data values to calculate the means; this is because the transmittance and other effects are considered multiplicative. The spectral mean is the mean of all bands for each pixel and removes topographic effects. Calculating the mean of all pixels for each band gives the spatial mean that accounts for the solar irradiance, atmospheric transmittance and instrument gain. (Greenbaum, et.al., 1994). If the normal arithmetic means are used instead of geometric means the process is termed the quick residual transform (Huntington et.al., 1994).

I have conducted experiments to determine if log-residual processing can be relied upon to convert scanner data into meaningful (pseudo) reflectance spectra. This was done by comparing the spectra derived from pixels of log residual processed imagery with the spectra collected from the location of these pixels in the field. Comparisons were made using GER IS, HyMap and GEOSCAN MkII scanner data. No appreciable differences

were noted in the spectra obtained and this is illustrated in Figure 3.9. It should be noted that the target pixels were collected from areas of spectrally uniform material.

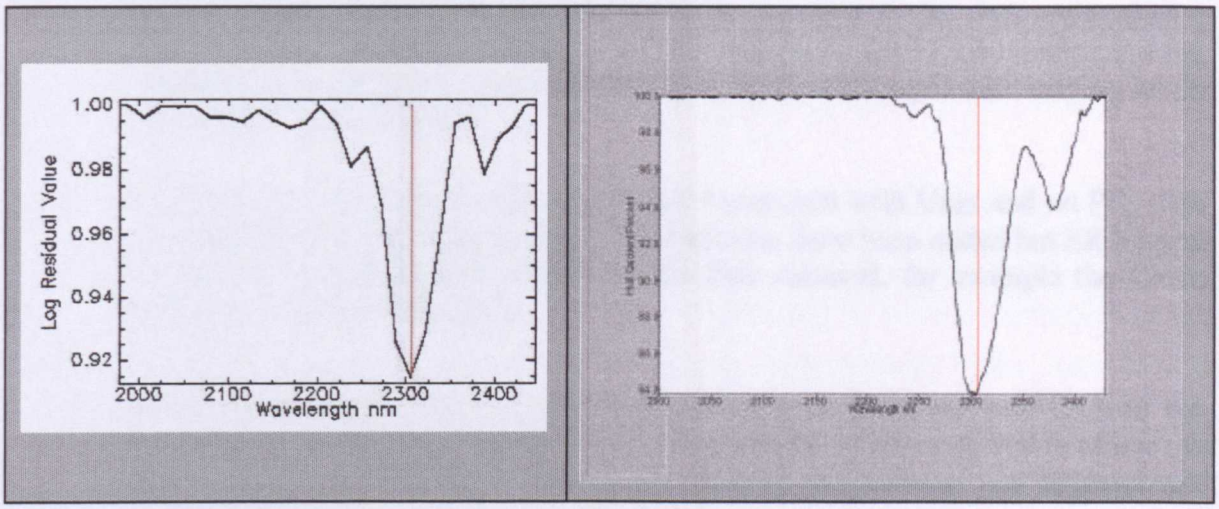

Figure 3.9 Image log residual transformed spectrum left compared to field spectrum (right) from the same area of spectrally uniform material. Field data collected with PIMA and image data from HyMap data at Pine Creek test site (Chapter 9). Vertical red line at 2306nm

The log residual technique was developed to deal with imagery of high spectral resolution though it can also be applied to data such as Landsat TM and Geoscan MkII imagery.

The developers of the log residual processing technique (Huntington, pers. comm.) have cautioned that this technique may be unreliable if the target spectrum sought comprises a statistically significant portion of the image data. This caution is reiterated by Tsuchida et.al., (1994) who found that the log residual data is not similar to reflectance data if the the image area is dominated by one material, usually vegetation. This has not been the case at any site in this study. As might be expected, the examples of alkaline ultramafic rocks investigated at test sites in this study are restricted in extent. This might not be the case where, for example, there are extensive areas of ultramafic rocks covering a large proportion of a scene's extent. In these situations investigations using imaging spectrometer or hyperspectral scanner data may require full correction and calibration of the imagery from raw data via radiance to reflectance.

Image Processing Software

Image processing software used in this research either is or was commercially available and modifications and additions are noted below. The software packages used were:

- **International Imaging Systems (I^2S) System 600.** (Operates on Sun 4 and DEC VAX computers under Unix and VMS operating systems). It was necessary to add functions to this system and modify others to cope with imaging spectrometry data. These functions included a dark current correction (which is the removal of electronically induced currents that contribute a signal to the data even when a scanner is not imaging), a routine to display spectra on the IVAS monitor, the log residual transform and a program to produce simulated images with varying levels of noise (Chapters 8 and 9).

- **ER Mapper.** (Operates on Sun and similar computers with Unix and on PCs with the Windows NT operating system). No functions have been added but ER Mapper algorithms were developed to process the data required, for example the Crosta principle component transform.

- **ENVI.** (Operates on Sun and similar computers with Unix and on PCs with the Windows NT operating system). No modifications have been required to utilise this software, it is customised for processing imaging spectrometer and hyperspectral scanner data.

Conventional Image Processing

Further discussion on the techniques described below is presented in Chapter 8.

Band Ratios

Ratios are calculated by division of one band centred on an absorption feature of interest into a band that acts as a background reference. This will then result in pixels that contain the absorption feature of interest being highlighted as brighter than background.

Band Ratio Colour Composites

By combining several ratios into a red, green and blue composite image it is possible to produce images in which the colours can be interpreted as representing the different materials characterised by their variations in spectral absorption.

Anomaly Residual Prediction Technique

This involved predicting the value of a band from a linear combination of all the other bands and then subtracting the predicted value from the actual value (Pendock and Lamb, 1989). Where the predicted band has an absorption feature the residual value is larger and results in brighter pixels than the non-absorbing background. A simple form of un-mixing, this technique was first developed to produce images from Landsat TM that would identify

pixels containing clay rather than vegetation. TM band 7 has lower values for both clay and vegetation. Therefore, band ratios cannot be used to map the distribution of clay minerals in a scene containing vegetation unambiguously. The residual technique successfully makes this separation (Pendock and Lamb, 1989) because the presence of vegetation can be predicted from the values in the other bands while clay cannot.

Directed Principal Components

This technique is also a form of un-mixing; directed principal component analysis depends on calculating the second principal component of two ratios (Fraser, 1985). One ratio is chosen that has ambiguous results (for example band 5 divided by band 7 in Landsat TM which confuses clay and vegetation) and one in which the result will not be ambiguous (for example Landsat TM band 4 divided by band 5 that discriminates vegetation). The second principal component will then, depending on band ordering and weighting, reveal the distribution of clay-containing pixels in the scene. It has not been utilised in this study as a previous study that I published in 1990 (Hussey and Hunt, 1990) showed that it produced results that were virtually identical to those obtained from the anomaly prediction technique.

Crosta Principal Component Technique

Originally developed and reported by Crosta and Moore (1989) it was documented and described in detail by Loughlin (1991). It relies on calculating the eigen matrix for a selected band combination and then examining the matrix. The bands are selected so that three are background and one represents the maximum spectral (absorption feature) variation in materials sought. The eigen matrix row, that is eigen vector, which shows the bands of interest most differentiated by the weighting values is then used to select the principal component band that will highlight the areas containing the absorption feature of interest. The image data is then transformed into principal component (PC) space using this eigen matrix, and the selected PC band of interest maps the distribution of the material sought. Loughlin (1991) determined that by using Landsat TM bands 1, 4, 5 and 7 this technique can be used to map the distribution of clay (hydroxyl bearing) minerals in a scene.

Log (Kwik) Residual Colour Composites

After raw data have been converted to pseudo-reflectance by either log residual or kwik residual transforms it is possible to obtain spectrally interpretable images by the simple expedient of selecting bands that match the wavelengths with diagnostic absorptions and displaying these as colour composites. If the negatives of these images are used then the absorption features will be brightest in the scene and, therefore, show as the colour to which they are assigned. Where mixing occurs colours will be the intermediate between the colours that have been chosen for these absorption bands. For example if kaolinite is red and vegetation is green then areas where they mix will be yellow.

Compound Colour Composite Images

Useful images can be produced by combining images obtained from different processing techniques into colour composites to enhance the distribution of the colours that represent materials being investigated. For example, with Landsat TM imagery a compound image containing the clay residual image, Crosta iron (haematite) image and a vegetation ratio image can be merged into a red, green and blue image in which clay would be red, iron green and vegetation blue.

Index Images

This takes the combination image a step further and has been used extensively in this study. The images differentiating the materials sought are density sliced by taking the pixels in the image which have values that are equal to or greater than a defined threshold and setting them to a uniform colour. This will highlight anomalous concentrations of the material of interest. The essential aspect of this is the selection of the cut off threshold level.

Where there is a known target in the scene it is simple to apply an X or Y profile across the spectral target and select a value that shows the threshold between target and background (Figure 3.10).

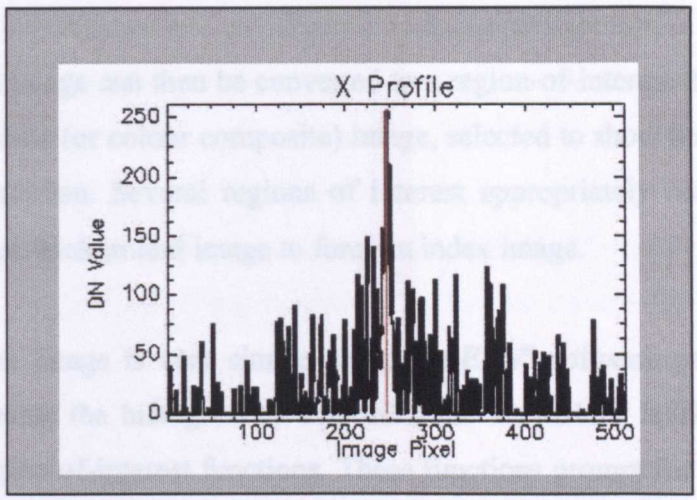

Figure 3.10: X Profile over a Mg-OH anomaly obtained from contrast stretched un-mixed image linearly stretched between 0 to 255 DN. The target straddles pixel 250 (red line) The cut off value for the region-of-interest would be a DN value of 150.

However, when there is no known target a statistical method can be used. In this case, the mean and standard deviation obtained from, for example, the end-member un-mixed image is determined. The threshold level is then set to the mean plus a certain number of standard deviations, my experience has shown that twice the standard deviation usually produces a suitable threshold. This technique is illustrated in Figure 3.11.

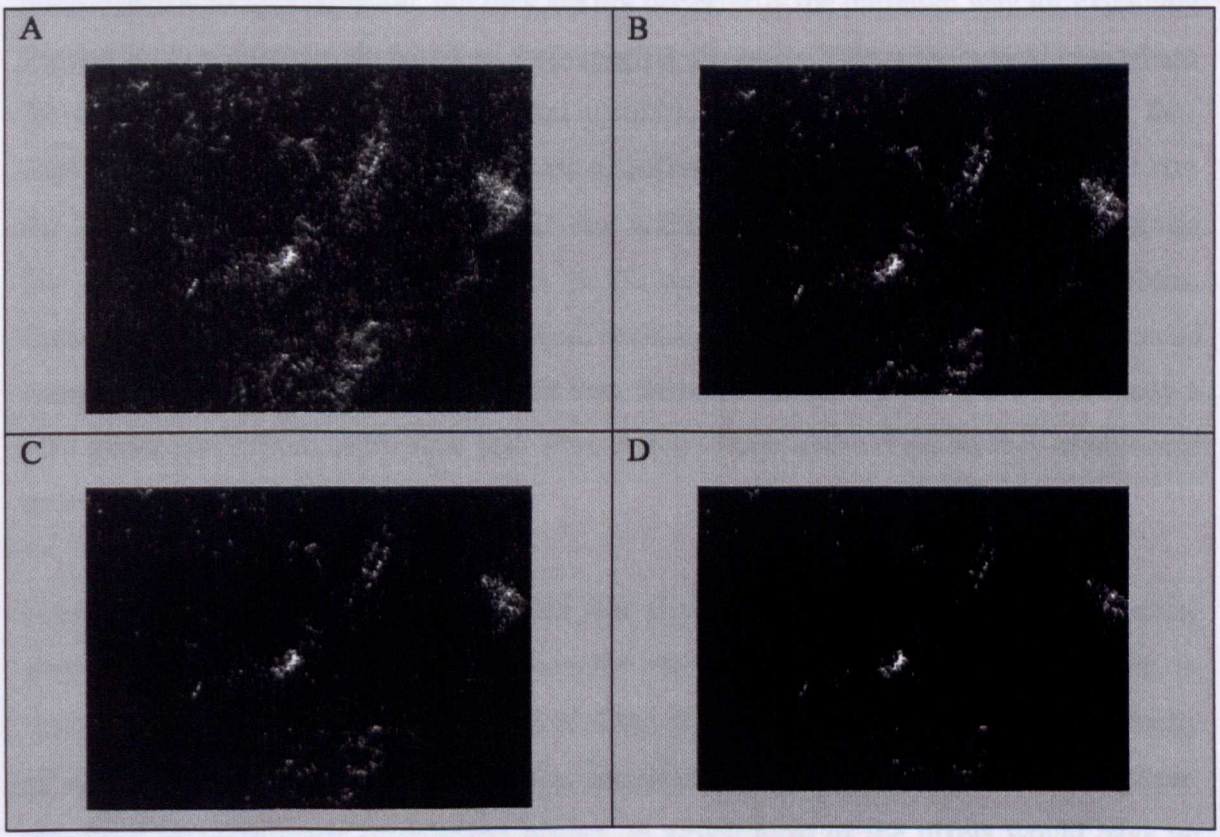

Figure 3.11: Index images produced by thresholding an un-mixed image at : A- the mean value, B- the mean plus 1 standard deviation, C- the mean plus 2 standard deviations, D- the mean plus three standard deviations.

This density sliced image can then be converted to a region-of-interest that can be overlain onto a black and white (or colour composite) image, selected to show the most topographic and location information. Several regions of interest appropriately colour coded can be overlain on the same background image to form an index image.

Producing an index image is very simple using the ENVI software package. All that is required is to examine the histogram to determine the anomalous level and then use the density slice or region-of-interest functions. These functions prompt for the data range and then colour the pixels in this range uniformly. The region-of-interest can be output directly from the processed image onto a background reference image. Median filtering to remove noise, that is isolated individual pixels, can be used to improve the appearance of the output. However, care must be taken when applying filters to ensure that small targets of interest are not eliminated.

Spectral Methods

All the techniques mentioned in the previous section can be applied to any scanner data set, multi-spectral to hyperspectral, but they are not necessarily the optimum way for extracting the distribution of materials based on their spectral signature. This is the typical case where the material of interest has its spectrum combined or mixed with other materials that contribute to the overall spectral signature of individual pixels. The smaller the pixel size the less mixing occurs and it is possible that within any scene there will be a few pixels that cover areas consisting only of a single material, that is spectral end-members. However, this means that the conventional techniques discussed above will have limited success in locating the presence of pixels that, though clustered spatially, are statistically a very minor component of the data set. This is true of ultramafic rocks as they often occur as isolated and discrete occurrences.

Pendock (1997, pers. comm.) has stated that the problem with conventional statistical approaches, for example principal components transforms such as the Crosta technique, is the presumption of a Gaussian distribution of the data. When considering ultramafic rocks of limited distribution within a scene a Gaussian distribution is often rare. In these situations an asymmetric distribution occurs, in which most of the pixels would have no ultramafic rock signature and a few would have a lot, perhaps being almost pure end-members. Such distributions have a large positive kurtosis and are termed super Gaussian

distributions. To address these issues techniques are being developed specifically aimed at identifying the occurrence of these outlier pixels.

The ENVI software package has a number of functions specifically included to carry out spectral analyses of data. Not only does this include algorithms to process the data but also visualisation tools that facilitate interpretation of the resultant spectrally classified data (see index images above).

ENVI Routines

ENVI provides a set of software tools for extracting information on the distribution of materials in an image from their spectral signatures. In this study the approach taken was to use the pixel purity index (PPI) and spectral angle matching (SAM) functions to locate the spectrally distinct but statistically insignificant pixels that are of interest (Kruse and Huntington, 1996), in this case the pixels indicating ultramafic rocks.

The sequence of routines applied to carry out the processing using ENVI functions, named in italics, is as follows:

- *Subset* the image to select the desired sub scene area.
- Produce a log residual (or quick residual) image either with a stand-alone function or by using a combination of *Internal Average Relative Reflectance (IARR)* and *Continuum Removed* functions.
- Transform the log residual image with the *Maximum Noise Fraction (MNF)* function and from the output image *sub-band* out the high order and low noise valid bands.
- Run the *Pixel Purity Index (PPI)* on the MNF valid bands image (this can take several hours with early versions of ENVI even on 400Mhz computers) with iterations set to above 5000.
- Examine the PPI image and threshold *(contrast stretch)* it to produce a *Region of Interest (ROI)* with values two to three times the noise level determined from the MNF transform (a value of around 3 in most cases).
- Use the *nD(*imensional) projection routine to visualise the PPI ROI data. This means input of the PPI ROI data and MNF subset into this routine.

- After selecting the first 3 bands in the *nD* function rotate the data and select the 'corner' points of the data cloud. The log residual image has to be linked to the MNF transform with the *spectral profile (z)* window open. Examine the spectra that are then obtained from each corner point progressively. Successively select out the low interest, that is common, spectra. When these have all been identified use the *collapse by variance* function until only corners with spectra of interest remain. This may take several interactive iterations until the target spectra appear as distinct corners.

- Select the high interest corner clusters (one or more) and produce ROIs for these.

- Apply the *matched filter* function to the log residual image selecting end-members with the ROI option.

- The output of the matched filter is an image that is a grey scale of the spectral means of the ROI and this image has as many bands as ROIs and, therefore, end-member spectra of interest. The image has been un-mixed by this process.

- The final step is to threshold the matched filter bands by *contrast stretching*. To do this the spectra are examined and the data clipped so that the higher values (right) tail of the histogram are set to bright values and lower values zeroed. (Range –1.0 to 1.0 with mean typically below 0.1). Converting the data to byte and then using the image mean plus twice the standard deviation can also be used for the thresholding, see Index images above.

Hybrid Processing

As can be seen the ENVI route for end-member selection and un-mixing is an interactive and time-consuming procedure. Advances in ENVI are streamlining this procedure. For instance, the *PPI* now takes less than an hour to run in the latest version of ENVI. At Stockdale Prospecting in-house software has been developed that reduces this complex process to two stages after the production of the log residual image; spectral end-member selection and un-mixing. These techniques are proprietry and cannot be discussed, however, there is another method that works well and uses a combination of both conventional and spectral processing.

In this, hybrid, method a conventional technique such as band prediction or Crosta principal components is used to map the areas within an image that have a specific absorption. These areas are thresholded and then the ENVI region of interest function is applied to highlight the most anomalous areas of this threshold within a scene. This thresholding leads to the production of an index image (see above).

In ENVI, the image showing the threshold areas can be linked to the log residual (or other image that has been processed to reflectance) and the spectra examined from these regions of interest. It is then possible to select a spectrum from a pixel that matches the target sought; that is it has both the target absorption feature and other characteristics. For example, in the case of ultramafic rocks an ideal Mg-OH spectra would have no features near 2150nm or 2200nm (indicative of dry vegetation and Al-OH clays respectively).

It would, however, have a >2300nm feature that is symmetric and sharp and a minor absorption at >2380nm. In ENVI, it is possible to visually select a characteristic spectrum from regions of interest and input it into the matched filter routine. This matched filter function will un-mix the data producing an image in which the brightest DN's indicate the highest concentration of the target spectra. This image can then be converted to an index image that will give a more reliable mapping of the distribution of the target spectra and, therefore, rock/soil type of interest.

An obvious improvement, not currently available in ENVI, would be to have a software program that isolates each thresholded and discrete area of interest in a scene and produce the average spectra for these. This would considerably reduce the time it takes to search the regions of interest for the target spectra.

3.7 MODELLING OF SCANNER SPECTRA

To test how well various image processing techniques have isolated the spectral information sought from scanner imagery simulated images have been made from spectral data (Chapter 8). This requires sampling of the spectra at the scanner band positions. Spectral sampling has also been applied (Chapter 7) to investigate the potential of different scanners to locate the Mg-OH and other spectral signatures; and to investigate the effects of noise.

For broader band multi-spectral scanner data it is necessary to take account of the shape of the detector responses when convolving spectrometer spectra to simulate scanner spectra. With higher resolution imaging spectrometers and hyperspectral scanners the band passes are usually equally sized with Gaussian distributions (Figure 3.12).

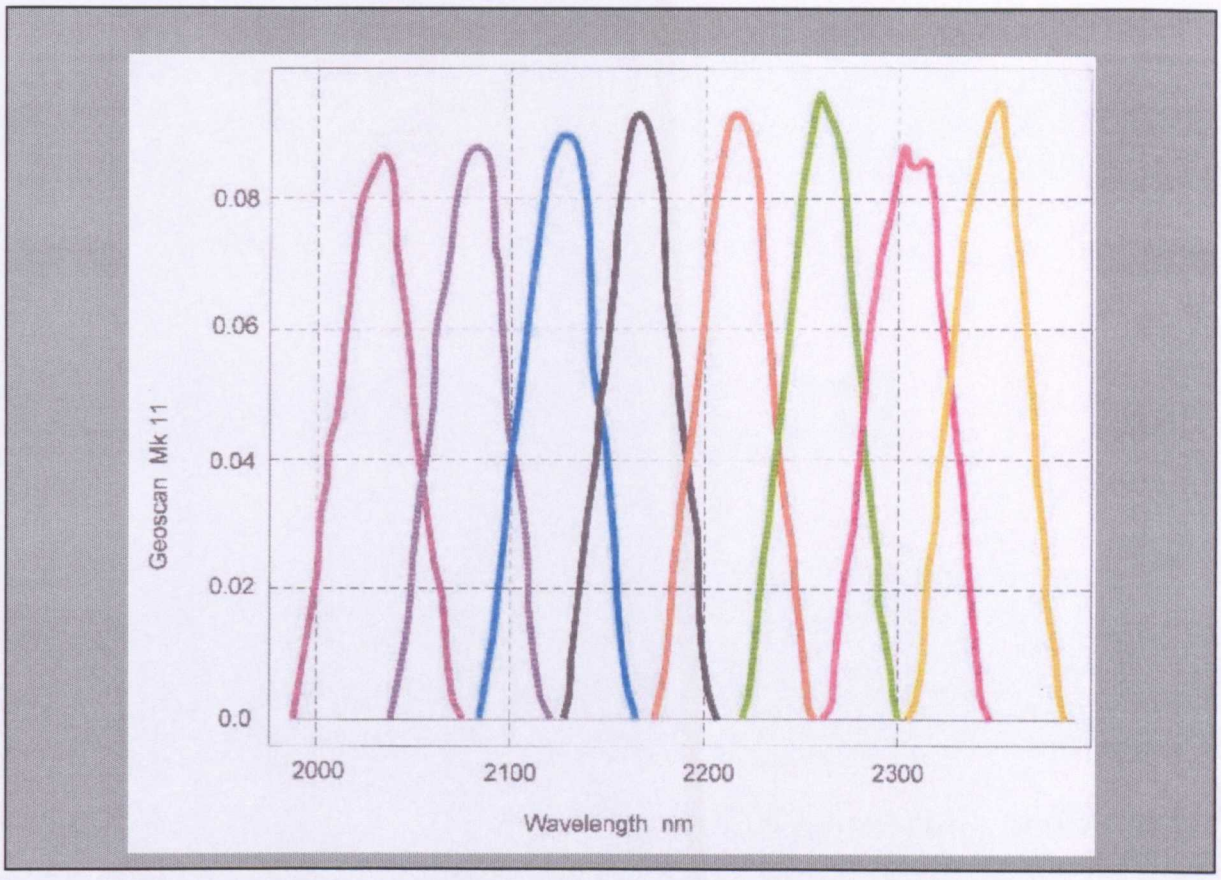

Figure 3.12: Plot showing band passes for GEOSCAN MkII scanner, they are contiguous and Gaussian in shape which is typical of imaging spectrometer and hyperspectral systems.

Therefore, the issue of whether a simple band centred conversion is sufficient or if it is necessary to take into account the band pass shapes when making such conversions has to be considered. To test this I used a PIMA talc spectrum and convolved it to the band passes for AVIRIS using the full width half maximum (FWHM) function available in ENVI that takes into account the band pass shape. The talc spectrum was also converted to an AVIRIS spectra by simple band centre sampling. These two forms of simulated scanner spectra were then compared (Figure 3.13).

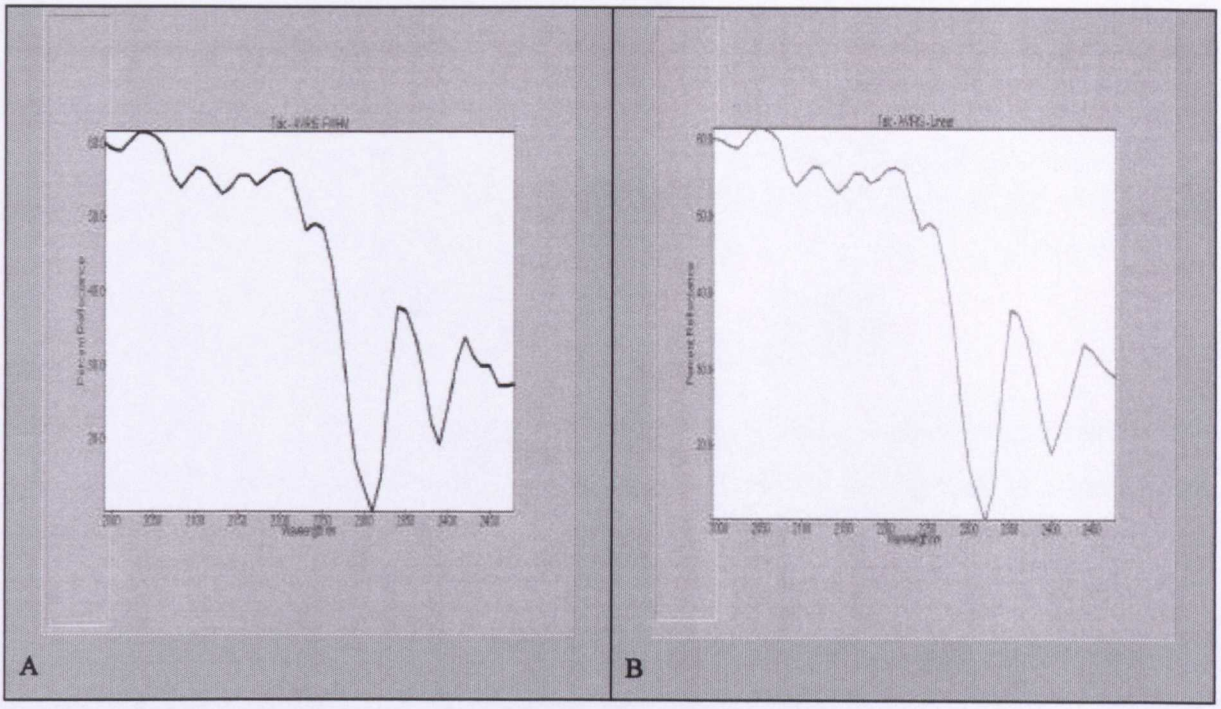

Figure 3.13: Comparison of two methods of re-sampling a talc reflectance spectrum to an AVIRIS SWIR2 spectrum. Convolved by FWHM (A) and band centre sampled (B). The resultant spectra are virtually identical.

These comparisons show no major differences between spectra that have been convolved using the detector response curves (FWHM) and simple band centre sampling. Therefore, the band centre sampling is the technique that I have applied in this research.

CHAPTER 4

4 THE MINERALOGY AND WEATHERING OF ALKALIN OTHER ULTRAMAFIC ROCKS; IMPLICATIONS FOR SURFACE SPECTRAL EXPRESSION

4.1 INTRODUCTION

The primary rock types considered in this study are alkaline ultramafic rocks: and lamproite but other ultramafic rocks that have similar mineralogy such as s pyroxenite, peridotite, and dunite are also considered.

In the regions considered in this study alkaline and other ultramafic rocks are w varying degrees and are commonly covered by residual soil. These catena soi admixtures of the weathering products of the ultramafic and background ro diluted by aeolian quartz. The dominant minerals in the weathered surface derived from ultramafic rocks are, except in areas subjected to extreme leachi rich. Viewed from above, as pixels of, green and dry vegetation are alsc component of the surface.

4.2 CLASSIFICATION AND MINERALOGY OF ULTRAMAFIC ROCKS

In Middlemost (1985), ultramafic rocks are defined as those rocks containing m percent mafic minerals (amphiboles, micas, olivines, pyroxenes and Middlemost divides the ultramafic rocks into twelve classes based primarily Within this classification are the alkaline ultramafic rocks including lamproites, and carbonatites. The definition of alkaline ultramafic rocks being that have a higher proportion of alkali metals (Na_2O and K_2O) than is consid for the group.

This study has focused on kimberlites (alkalic – potassic mica peridotite (Mit and lamproites (ultrapotassic leucite bearing rocks (Mitchell, 1991) which ha genesis to kimberlite and have in the past been confused with them (Mitchell, 1 rocks may contain hypabyssal cores and nodules of other ultramafic roc serpentinite (Middlemost, 1985 and Mitchell, 1970, 1991).

When intruded and preserved as volcanic pipes these rocks have a variety of facies not usually seen in other ultramafic rocks. Kimberlites and lamproites, depending on their preservation, determined by the erosion level, have a core of hypabyssal rock that grades upwards into diatreme and crater facies (Hawthorne, 1975) usually with some dilution of the ultramafic content upwards (Figure 4.1). The hypabyssal core is typically serpentinite rich and talc is a common mineral in all facies. Kimberlite dykes are usually hypabyssal and serpentinite rich.

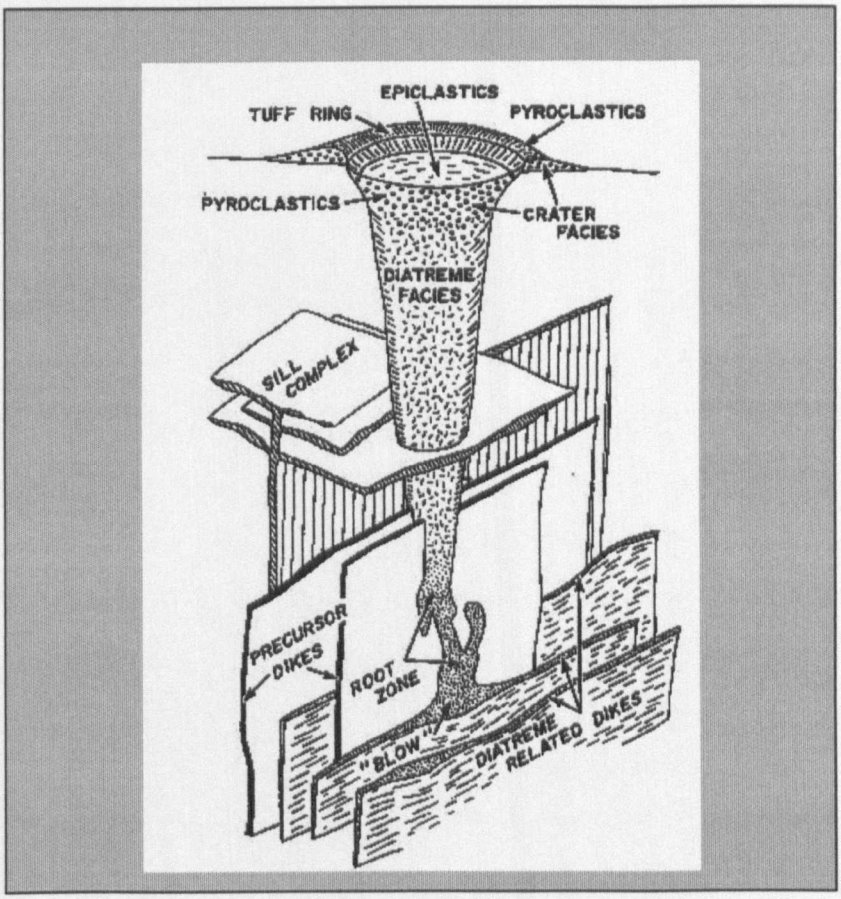

Figure 4.1: Kimberlite model after Hawthorn (1975) showing vertical distribution of main facies units.

When examining these rock spectra it is necessary to consider their mineralogy. Jackson (1997) has defined the typical mineralogy of the ultramafic rock types considered as follows:

- Pyroxenite: nearly mono-mineralic rock which is comprised of pyroxenes (usually bronzite if iron rich or enstatite if magnesium rich). They contain minor amounts of accessory minerals such as hornblende, biotite and olivine.

- Peridotite: olivine-rich rock often containing bronzite and phlogopite as accessory minerals.

- Dunite: peridotite with greater than 90 percent olivine, usually with chromite as a minor accessory mineral.

- Serpentinite: almost entirely serpentine group minerals (antigorite, chrysolite and lizardite) that are formed by the hydration of olivine and pyroxenes; accessory minerals are chlorite and talc. The hydration of dunite, peridotite and pyroxenite often means that these rocks can be converted to serpentine in whole or part.

- Kimberlites: split into two mineralogically distinct groups by Skinner et. al., (1987):

  Group I: olivine, phlogopite and, monticellite, calcite and serpentinite

  Group II: phlogopite dominates over other minerals in both phenocrysts and ground mass and monticellite is absent.

- Lamproites: contain a wide variety of minerals, the olivine (magnesium rich) varieties are dominated by the presence of olivine and phlogopite, leucite content varies (Mitchell, 1991)

From this review, it is apparent that in fresh ultramafic rocks, the following minerals can be expected: olivine, talc, serpentine, phlogopite, monticellite, calcite, pyroxene and leucite. Apart from calcite these minerals have absorption features in the VNIR (Figure 4.2) that result from iron oxides which have only limited diagnostic value due to their occurrence in many rock and soil types. Of these minerals only serpentine, talc, phlogopite and calcite have spectra that show distinctly diagnostic absorption features in the SWIR2 regions (Figure 4.3). The other minerals have potentially diagnostic absorption features in the longer wavelength thermal infrared region (Lyon, 1964) but this has not been investigated in this study.

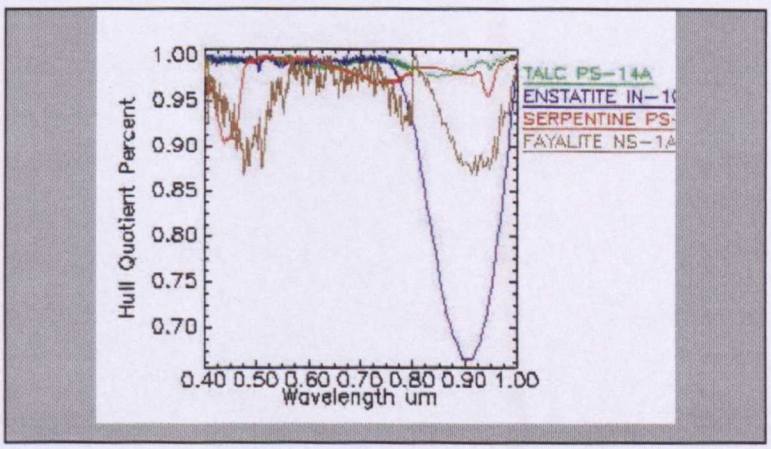

Figure 4.2: VNIR spectra of some typical ultramafic rock minerals, green - talc, blue- pyroxene, red - serpentine and brown –olivine. Note the common absorption feature at .9um (900nm).

Where ultramafic rocks are exposed but have not been affected by intense leaching, a veneer of alteration is often developed on exposed surfaces. In the diatreme and crater facies of kimberlite and lamproite the effects of weathering and alteration are more pronounced. This is due to an admixture of other rocks within these units and the high percentage of volatiles that accompanied their emplacement (Middlemost, 1985). This veneer of alteration minerals coupled with the presence of talc and phlogopite results in the spectra of these rocks showing the diagnostic Mg-OH mineral absorption features at ~2300nm and ~2380nm (Figure 4.3 and Chapter 5).

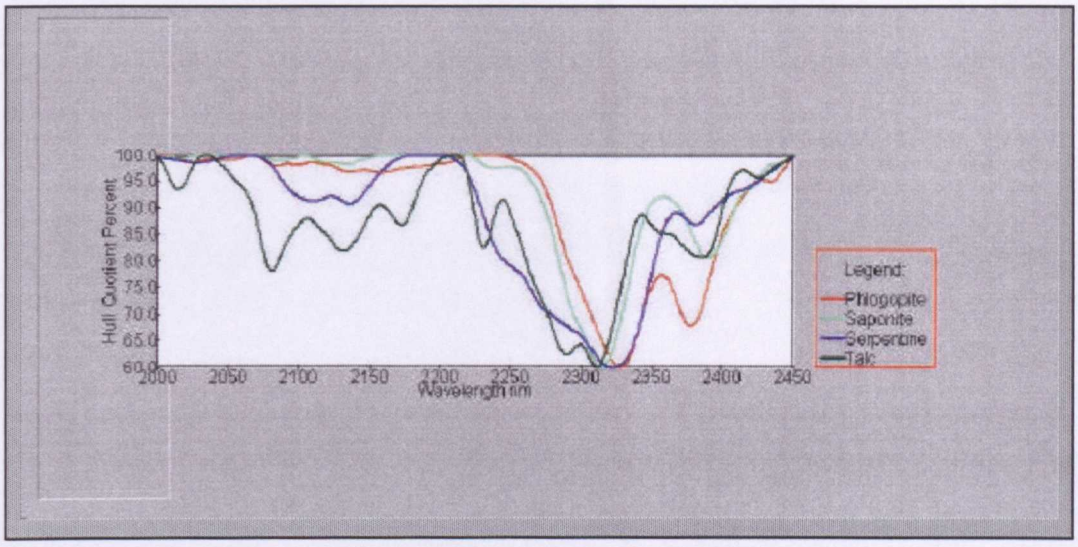

Figure 4.3: SWIR2 spectra of minerals that can occur on the exposed surfaces of alkaline and other ultramafic rocks. Diagnostic absorption features at >2300nm and >2380nm.

4.3 WEATHERING OF ULTRAMAFIC ROCKS

A literature review has been made on the topic of the weathering of ultramafic rocks and the following is a synopsis of the main issues. Reviews by Butt (1981 and 1992), Courtnage (1997), Cudahy (1992) and Ollier and Pain, (1996) and studies by Pontual et. al. (1997) and Kersten (1973) were particularly informative. However, apart from Kersten (1973) the literature lacks any reports on focused research into the weathering products of alkaline ultramafic rocks.

Weathering in Arid Regions

Rock type and the amount of water available determine the type and degree of weathering. Chemical weathering and soil formation is characterised by the progressive loss of mobile cations eg. magnesium, potassium, sodium, calcium and silica resulting in the parent rock

being altered to clays. Initially smectites form and then if leaching continues kaolinite develops and eventually dominates.

In extremely arid desert conditions, there is very little chemical weathering and the breakdown of rocks is primarily by physical processes. However, even in desert conditions there will usually be sufficient moisture at the surface for the development of clay rinds on exposed surfaces and areas of immature soil development. The test sites investigated in this study are in arid areas. These sites either have rainfall that is infrequent and spasmodic in the more temperate latitudes, or seasonal with prolonged dry seasons in lower latitudes.

Wherever rainfall is sufficient clay mineral development will occur. Initially Mg smectites such as saponite and vermiculite will result from the breakdown of ultramafic rocks (Table 4.1). As leaching of magnesium (and other mobile cations), proceeds these Mg-OH bearing clays break down into kaolinite (Ollier and Pain, 1996).

PRIMARY ROCK MINERALS	FIRST STAGE BREAKDOWN	SECOND STAGE BREAKDOWN
Olivine	Serpentine & Vermiculite Calcite	Saponite
Orthopyroxene	Talc & serpentinite	Vermiculite & Saponite
Phlogopite	Chlorite & vermiculite	Saponite

Table 4.1 Weathering products of minerals characteristic of ultramafic rocks in arid soils (adapted from Kersten, 1973).

The proportion of the minerals in the residual weathering products and soils developed from ultramafic rocks will depend on the topography and geomorphic history of the area. In immature stripped landscapes the effects of rainfall and topography will dominate. Courtnage (1997) has pointed out that there will be increased decomposition on shallow slopes and a decreased decomposition on steep slopes in all environments. Therefore, in lower lying areas the build up of clays in residual soils will be greater than on steep slopes. As the minerals that characterise ultramafic rocks are spectrally similar to their clay weathering products, the spectral signature in both of these situations will be similar. However, where steeper slopes have soil developed the outflow of water will accelerate the leaching of the mobile cations so increasing the development of kaolinite. In flat areas the converse is true to some degree, less water flow will reduce the lateral leaching effect.

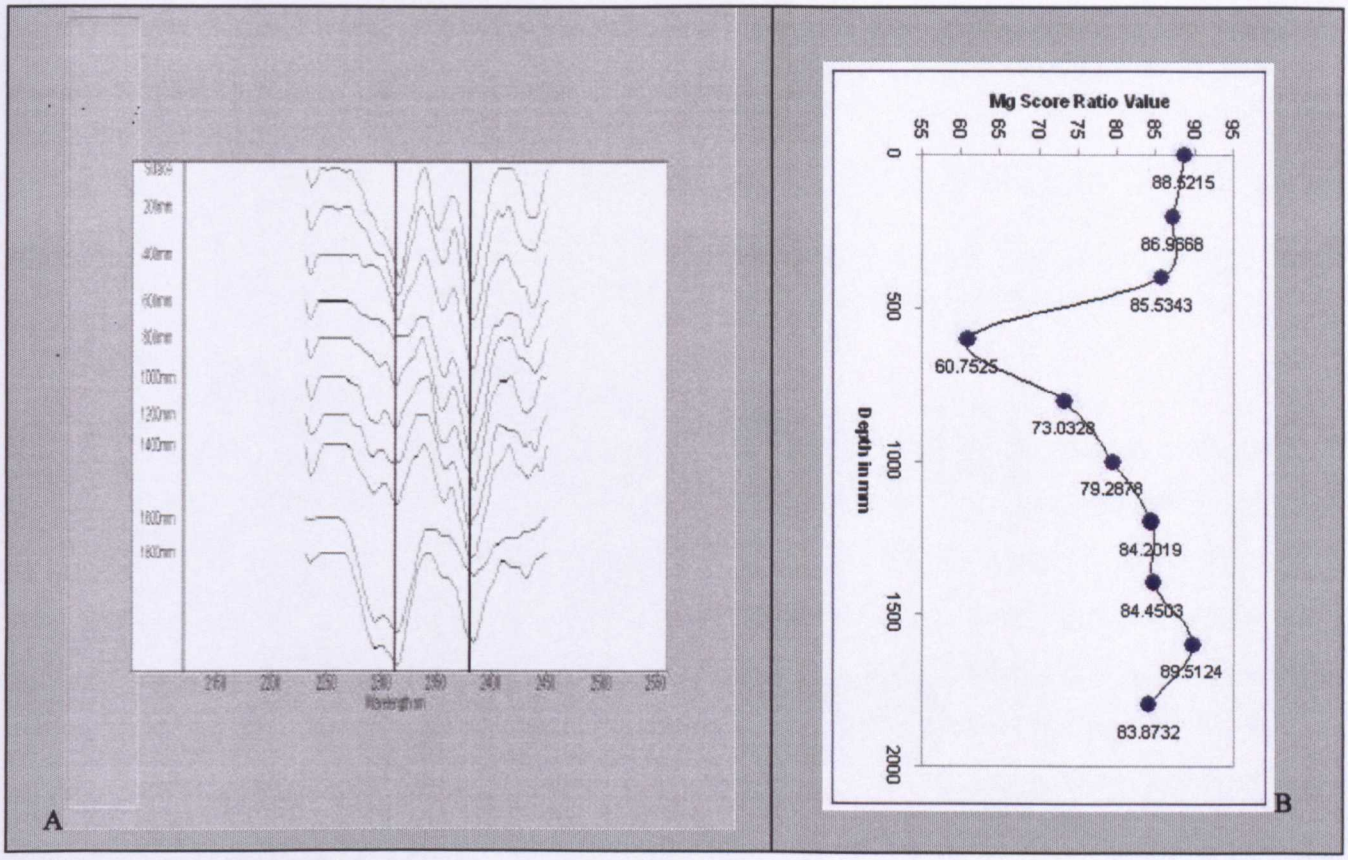

Figure 4.4: Stacked spectra (A) and vertical soil profiles (B) from a kimberlite in Bahia State, Brazil. The stacked hull difference spectra are offset on the Y-axis for clarity and are ordered from surface to the bottom of the pit at 200mm intervals. Vertical lines in stacked profile at 2312nm and 2380nm highlighting the position of the Mg-OH absorption features. The profile is derived from the Mg Score values with higher values to the right indicating elevated Mg-OH content.

Even in flat areas with low rainfall there may be sufficient vertical leaching to promote the development of kaolinite near the surface. Several centimetres below surface there can be an enhanced development of Mg-OH clays, typically saponite. This is not always the case as I discovered from a spectral soil profile recorded from a kimberlite, in the arid Bahia province of Brazil, (Figure 4.4). In this case the spectra indicate change from weathered rock into saponite clays then upward into a zone where kaolinite is the dominant mineral, near to the surface saponite re-occurs mixed with kaolinite. The association of surface saponite-kaolinite soil with the ultramafic rock was confirmed by its disappearance at the margin of the kimberlite, marked by a change to Al-OH clays

Genesis of Saponite

In Velde (1992) the weathering of a generic ultramafic rock consisting of olivine and pyroxenes results in a progressive removal of Ca and Mg and corresponding concentration of Al, Fe and Si. The sequence of minerals produced is:

- Hydrolysis in the parent rock - olivine is converted to serpentine, orthopyroxene is converted to clinopyroxene due to loss of Ca and any iron present is oxidised.
- Saprock - destabilisation of clinopyroxene to form talc and oxides, serpentine remains.
- Saprolite - saponite is formed from the breakdown of serpentine and talc both of which it pseudomorphs.
- Fissures - promote hydrolysis of saponite to nontronite due to loss of Mg and if water flux is sufficient kaolinite and iron oxides form (mottled zone).

Australian Weathering Conditions

Where an arid area has been subjected to tropical or temperate weathering in the past, a more complex situation arises. This is the case in many parts of Australia, particularly in the Yilgarn region of Western Australia, where the lateritic weathering profiles have developed under past tropical conditions. These are now being re-eroded under arid conditions (Cudahy, 1992 and Ollier and Pain, 1996). The typical lateritic profile has been described in detail by Ollier et. al. (1996 and 1988) and Butt (1981 and 1992), this is summarised in Table 4.2 and Figure 4.5. The progression from unweathered parent rock is from coarse (saprock) to fine saprolite, where the texture and mineralogy of the parent rocks is progressively diminished. The saprolite zone is overlain by a mottled zone of clay and iron oxides which is capped by duricrust, that can be composed of iron oxide, silicon hydroxide (silcrete-opaline silica) or carbonate (calcrete). This profile can vary in depth and degree of preservation, while the parent rock composition influences the mineralogy of the weathering products including the duricrust. Carbonates (calcite and dolomite) can occur as primary minerals in some alkaline ultramafic rocks. When lateritically weathered these rocks may produce a carbonate duricrust (calcrete - caliche). Whether there are differences between calcretes derived from alkaline ultramafic rocks and from non-ultramafic rock is a topic that requires further, including spectral, investigation.

WEATHERING ZONE	ARID WEATHERING	TEMPERATE WEATHERING	HUMID/TROPICAL WEATHERING
Soil	Saponite Phlogopite + quartz	Saponite->nontronite Phlogopite->vermiculite	Kaolinite >nontronite >saponite
Saprolite	Talc Saponite Phlogopite	Talc + serpentinite Saponite	Saponite>nontronite Vermiculite Silicon hydroxide(?)
Saprock	Talc Phlogopite Saponite	Pyroxenes->Talc Serpentinite Phlogopite	Talc Saponite Phlogopite
Fresh rock	Olivine Serpentine Phlogopite Pyroxene Etc	Olivine Serpentine Phlogopite Pyroxene Etc	Olivine Serpentine Phlogopite Pyroxene Etc

Table 4.2: Weathering zone minerals produced from ultramafic rocks under different weathering regimes (adapted from Pontual et. al., 1997)

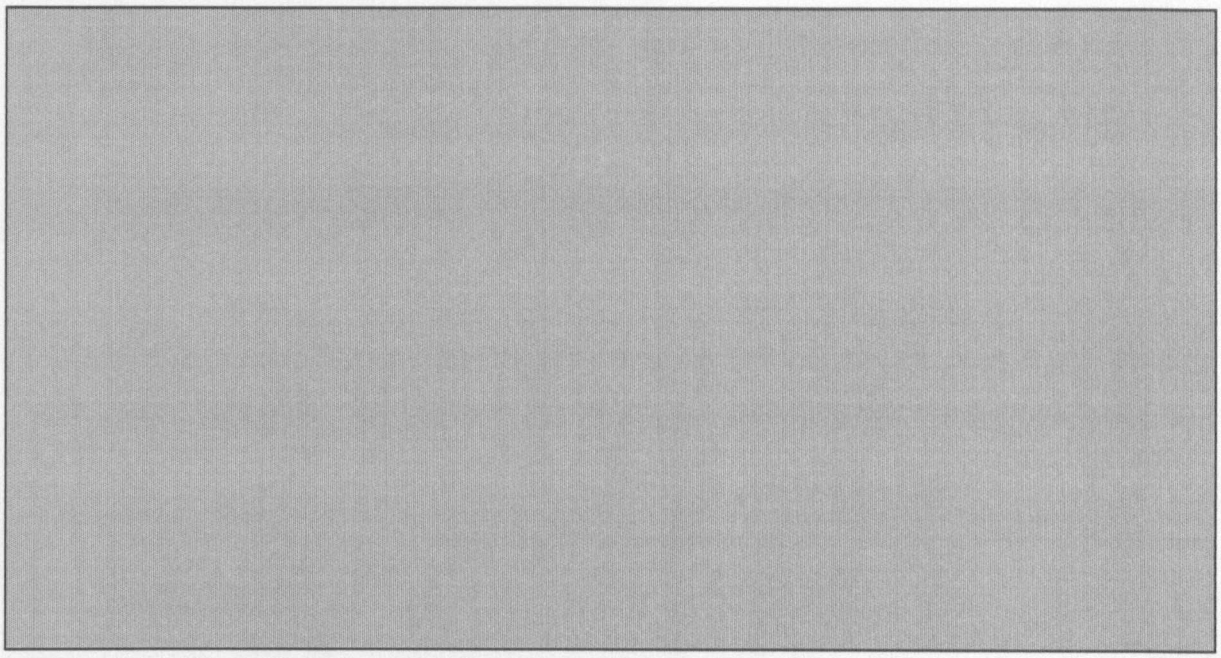

Figure 4.5: Sketch (after Butt, 1981) showing variation in profile type due to differences in parent rock mineralogy that develop under lateritic conditions . Ultramafic rock types are dunite on left and peridotite on right. Centre yellow area names different regolith zones.

Butt (1981) has pointed out that in the lateritic profiles the primary minerals of ultramafic rocks, such as the olivines and pyroxenes (and carbonates which may be present in alkaline ultramafic rocks), are entirely converted to smectites in the saprolite zone. As Kersten (1973) has shown saponite is the typical smectite produced by the chemical breakdown of these minerals and this has been confirmed by studies undertaken by the author (Hussey, various un-published company reports, 1990-1998). Other minerals such as serpentine and chlorite breakdown less readily to smectites and may be preserved along side them in the saprolite and mottled zones. Minerals such as talc (Butt, 1992) and phlogopite (authors observations) may be preserved throughout the profile. Therefore, the nature of the saprolite and mottled zones is dependent on the mineralogy of the parent rock.

Whatever the parent rock, Butt (1992) points out, the profile tends to become ferruginous towards the surface. In intensely weathered serpentinised dunites, in the Yilgarn, Butt (1981) has noted saprolite zones that consist of iron oxides that have been silicified to form an iron rich silcrete, consisting of 90 percent Si-OH. Butt (1981) has concluded that this silicification is characteristic of serpentinised dunite. However, it is possible that other occurrences of serpentinites, such as in hypabyssal alkaline ultramafic rocks, would produce the same weathering product. In Brand et. al. (1997) the equation for the hydrolysis of Mg Olivine (forsterite) indicates that the removal of Mg results in the

formation of silicon hydroxide, this may explain the development of silcrete from these rocks. The presence of ferruginous silcrete over ultramafic rocks, in the Yilgarn, has also been noted by Lyon (1990).

In previously lateritically weathered areas the spectral expression of an ultramafic rock will, therefore, depend on its local situation as well as mineralogy, Figure 4.5. If it is located in an area of active and deep stripping, where the lateritic profile has been removed, the spectral response will be similar to that in other arid regions. Where stripping is less severe only the original lateritic saprolite may be exposed. Depending on the composition of the parent rock this saprock-saprolite will show a mixture of Al-OH dominating over Mg-OH clays, resulting in a mixed spectral response (Cudahy, 1992). The formation of kaolinite results from the desilification (Ollier and Pain, 1996) of the smectite (saponite). Where ultramafic rocks occur in areas of totally preserved and intensely lateritised regolith no Mg-OH minerals will be preserved at surface. The removal of Mg will have resulted in the production of kaolinite and/or ferruginous silcrete, depending on the parent rock mineralogy.

Field observations during this study have supported the fact that nontronite can also be preserved in areas of lateritisation, at the surface.

Mapping of Silicon Hydroxide SiOH (Opaline Silica)

No occurrences of silcrete were noted at any of the test sites investigated in this study. However, this review of the weathering process does indicate that in many arid areas of Australia the alkaline ultramafic rocks may be expressed at surface as areas of ferruginous silcrete. Even where subsequent erosion has removed the lateritic weathering this silcrete would be expected to persist, it is hard and not vulnerable to further chemical change. Silicon hydroxide has a broad shallow absorption feature centred at 2240nm in the SWIR2. Examination of the end-member spectra and un-mixed (Chapter 3) HyMap/Probe 1 scanner image from Cuprite (Nevada, USA) shows that this mineral can be located using SWIR2 imagery (Figure 4.6). Therefore, the occurrence of silcrete (Si-OH) is a potential spectral mineral indicator for the presence of alkaline ultramafic rocks, in regions such as the Yilgarn of Western Australia that have been subjected to intense lateritic weathering. How diagnostic this would be is questionable, silcrete can also be formed from the weathering of granite and other acidic rocks (Butt, 1985).

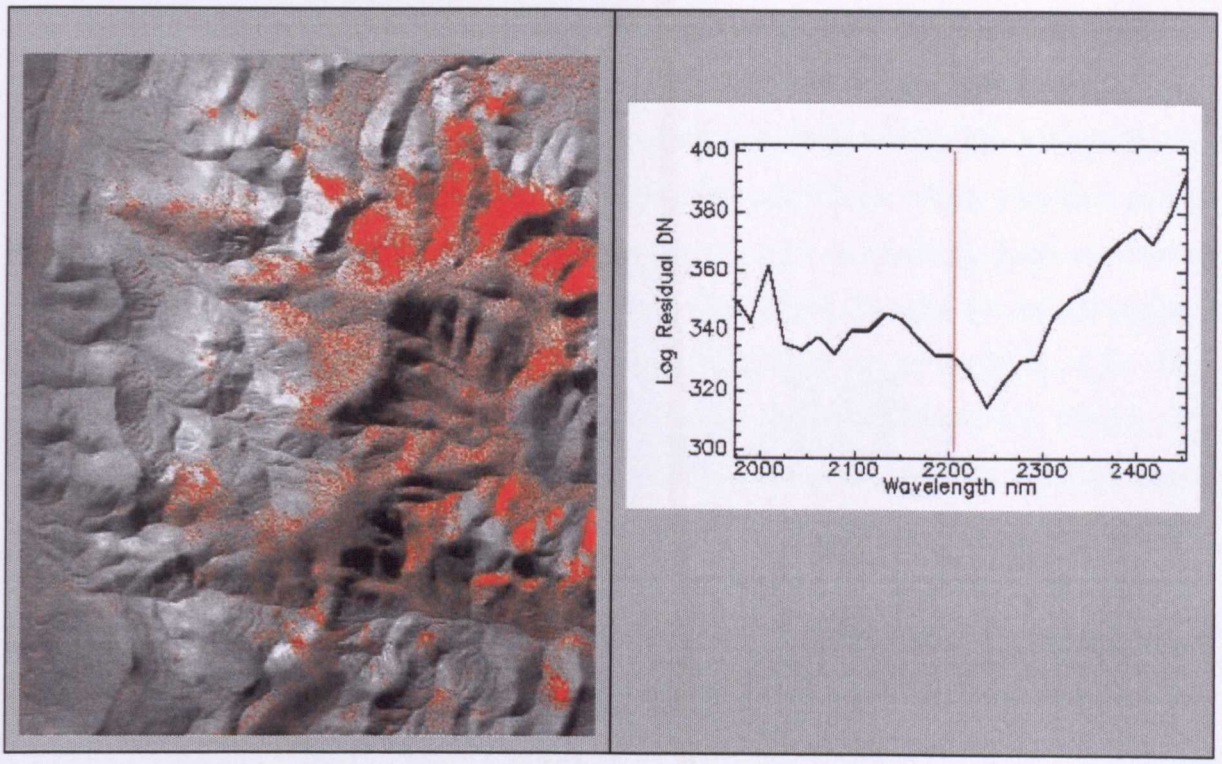

Figure 4.6 HyMap end-member un-mixed image (left) showing the distribution of silcrete (SiOH-opaline silica) in the Cuprite area (Nevada USA) in red. The spectra (right) is that of SiOH extracted from the log residual transformed image data. Image is 5km east west and north is towards top. Vertical red line in spectra at 2200nm.

Weathering In Areas Studied

None of the areas investigated in the field or with scanner imagery, in this study, show the effects of the lateritic weathering that is prevalent over much of Australia. All of these sites are located in arid to semi-arid regions. The main development of lateritic regolith occurred in the early tertiary in Australia and this regolith is well preserved in the Yilgarn area of Western Australia (Butt, 1992). However, uplift and erosion have removed the typical lateritic profile (op sit) in many areas, even within the Yilgarn (Ollier et. al., 1988). This is the case at the Jubilee site, east of Kalgoorlie (Chapter 10), where typical lateritic profiles are present in the immediate area but have been removed, by erosion, near the exposed serpentinite. At the Pine Creek site in South Australia (Chapter 9) there is no trace of an extensive lateritic profile. In the Ellendale area (Chapter 11) laterite regolith is preserved locally, though the lamproites at this site are dated as late Tertiary (Jaques et. al., 1986), that is, post dating the main phase of laterite development.

The presence of Mg-OH smectite clays, particularly saponite, is associated with the weathering of ultramafic rocks in the test site studies documented in Chapters 9 to 11 of this thesis. However, the weathering and alteration of other rocks can produce these clays (Table 4.2 and Chapter 10). Nevertheless, the diagnostic spectral signatures that Mg-OH

bearing clays derived from weathering of ultramafic rocks are reinforced, in field and imaged spectra, by the preservation of phlogopite, talc and serpentinite at the surface. These minerals showing similar spectra to that of saponite (Figure 4.3). The models for the spectral response of weathered ultramafic rocks in arid conditions, where a lateritic profile has never developed or been stripped, can be proposed by considering these weathering products. Where the soil development is immature or minimal, then the minerals at surface will be saponite plus serpentine and phlogopite (if present in the original rock). The spectrum of a mixture of saponite and serpentine is shown in Figure 4.7. Where soil development is more advanced then saponite will be mixed with kaolinite. Aeolian quartz sand is also likely to be present. The spectrum derived from a mixture of saponite, kaolinite and quartz is also shown in Figure 4.7. Spectral data obtained at the test sites discussed in Chapters 9 to 11 (from field work and scanner data) show that these suggested mineral mixtures are produced under natural conditions from the breakdown of ultramafic rocks.

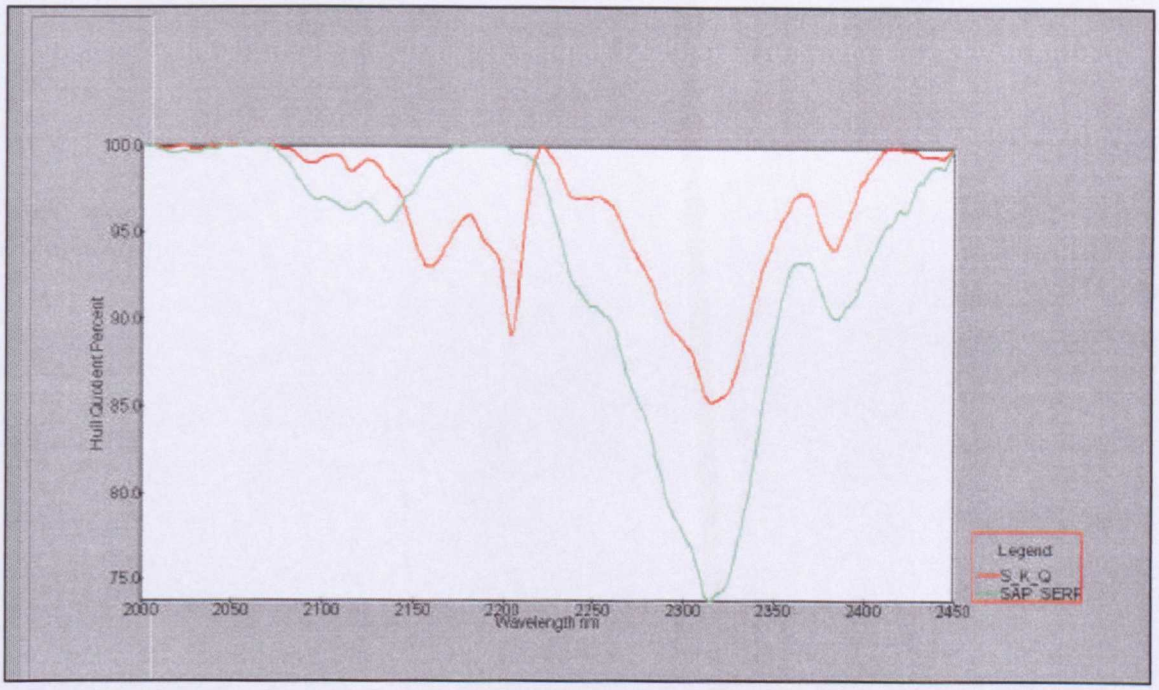

Figure 4.7: Model spectra proposed for weathered ultramafic rocks and derived soils in arid areas. Green spectrum is a saponite and serpentine mixture - outcrop and immature soil. Red spectrum is saponite, kaolinite and quartz - residual soils.

4.4 WEATHERING PRODUCTS OF NON-ULTRAMAFIC ROCKS

Grimm (1968) pointed out that under arid conditions and low relief, magnesium will remain in the soil profile (if present in the original rock) and results in the formation of smectic clays such as saponite. Hence, any non-ultramafic rocks rich in Mg, such as amphibolites, will also produce saponite when weathered. However, if the Mg content of

the rocks is low as in most acidic to basic igneous rocks, quartzites, sandstones and felsic metamorphic rocks then the weathering product is kaolinite. If the weathering conditions in arid areas favour the rapid removal of Mg (see above) then kaolinite will also result though smectites may be preserved mixed with kaolinite.

Calcareous rocks weather to calcium-bearing smectites, such as montmorillonite, and can release any illite that they often contain (Grimm, 1968). Under certain conditions kaolinite rich dolomite, may weather to saponite (Graham, 1967) and this is discussed in Chapter 10. Weathering of shales and other phyllites release illite due to the high content of this mineral in these rocks.

As aridity increases, that is as desert conditions become prevalent, then chemical weathering is less pronounced and the soils are composed of the fragments of the parent rocks usually with an admixture of aeolian quartz sand. Even in extremely arid conditions, previous phases of weathering may have altered the parent rocks chemically to form the clays previously discussed. The spectra of various non-ultramafic rocks that may host alkaline ultramafic rocks are presented in Chapter 5.

4.5 CONCLUSIONS

Where weathering has not advanced to the stage of soil formation then the parent mineralogy and the initial breakdown products will dominate rock surfaces. Under arid conditions it is likely that ultramafic rocks will weather to Mg-OH bearing clays such as saponite, that can be preserved in the soil. As weathering progresses and soil formation matures, these Mg-OH clays will be diluted by the presence of aeolian quartz and Al-OH clays. When weathering is intense desilification can progress until the smectite clays, breakdown into kaolinite. If there is insufficient Al in the parent rock then under intense lateritic weathering the removal of the Mg will result in SiOH formation. This will result in the development of silcrete, that may also be detected by its spectral signature. Physical mixing from surrounding lithologies and soils can also add other clays and minerals to the residual soil such as montmorillonite and illite.

Similarly the spectral response for background rocks may be dominated by the phyllosilicates such as muscovite, chlorite, illite, kaolinite and other Al-OH bearing minerals in immature soils and predominantly Al-OH clays in more developed soils.

CHAPTER 5

5 DETERMINATION OF THE SPECTRA OF ALKALINE, OTHER ULTRAMAFIC AND BACKGROUND ROCKS

5.1 INTRODUCTION

This chapter presents the results I obtained from spectral measurements of alkaline and other ultramafic rocks. Spectra were also measured from a variety of rocks which can be the background to ultramafic intrusives.

The results obtained from measurements made in the field are compared to those made in the laboratory.

5.2 LABORATORY SPECTRAL STUDIES

These laboratory studies were conducted using the GER IRIS MkIV and PIMA spectrometers discussed previously. Samples for these spectral studies were obtained from collections of rocks and minerals held at Stockdale Prospecting, the Anglo American Research Laboratories in Johannesburg and from samples collected by the author during fieldwork. Some GER IRIS MkIV spectra of ultramafic rocks have generously been provided by Dr T. Cudahy of the CSIRO Division of Exploration and Mineralogy in Perth.

When using the GER IRIS MkIV spectrometer the sample is positioned so that it covers a fixed portion of the field of view and a halon pad covers another portion. Measurements are then made simultaneously on both sample and the reference halon pad (Figure 5.1).

With the PIMA the sample is placed against the spectrometer window and a measurement recorded (Figure 5.2). Since it has a small field of view, several measurements may be taken where the sample is a heterogeneous mixture of minerals to ensure that a representative average spectrum is obtained. For soil samples, it has been found that the best method is to up-end the PIMA and place a Petri dish containing the sample on the aperture window. Tests have confirmed that measurement through glass does not affect the spectra. Plastic containers must never be used as they produce spurious absorption features.

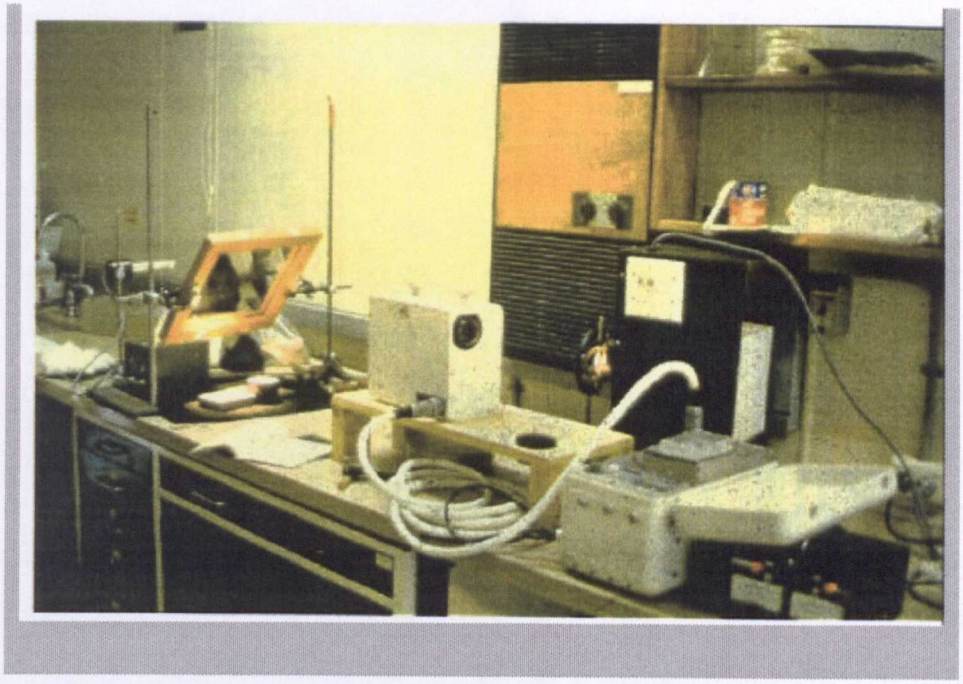

Figure 5.1: GER IRIS MkIV spectrometer set up in a laboratory. The sample is below the mirror to the left next to the white halon reference pad. In the centre is the optics-spectrometer unit linked to the electronics control box by thick white cable. The sample and halon reference pad are illuminated by the lamp held by a clamp to the left of the mirror.

Figure 5.2: PIMA set up in a laboratory with a Petri dish containing the sample on top of the aperture of the spectrometer. To the right is the Laptop PC that controls the instrument and displays a spectrum immediately after it has been recorded.

With the GER IRIS Mk IV, after a spectrum is recorded it needs to be down loaded into a computer and then converted to reflectance by dividing the halon pad spectrum by the sample spectrum. In the PIMA the data are saved directly into the computer. The conversion to reflectance is done at this time when the sample spectrum is divided by the

spectrum of a gold reference standard that is contained in the instrument.

5.3 SURFACE FIELD STUDIES

These field studies were conducted using the GER IRIS MkIV and PIMA spectrometers. Using the GER IRIS MkIV in the field is cumbersome due to the need for a tripod, halon reference pad and the fact that the instrument has two units joined by a cable. In use it was discovered that although it is a dual beam instrument measuring both the sample and the reference pad simultaneously, it is still affected by cloud cover which restricts the number of measurements that can be taken. The number of measurements can be increased if the target is illuminated with a 200watt lamp. Taking a lamp to the field with the GER IRIS MkIV was first done by the author and Dr A Gabell of CSIRO at the Pine Creek test site in 1986. This then became standard practice, however, using a lamp does mean extra equipment has to be carried (Figure 5.3).

Figure 5.3: GER IRIS MkIV in the field during 1986, the first recorded time a lamp was used with this instrument in the field. The optical head is on the tripod pointing at the ground and the halon reference pad. To the right of the spectrometer the lamp is attached to a 12-volt car battery.

Due to a measurement and set-up time of between five and ten minutes (includes moving between sample sites), I have found it is difficult to collect spectra with the GER IRIS MkIV from more than fifty sites per day. Using a PIMA it is possible to record spectra from 100 to 200 sites per day in the field, though battery life and over-heating of the instrument in hot conditions can reduce this number.

My field experience has proven that recording spectra directly in the field is not a cost-effective method of collecting data with these instruments. Recently a modified PIMA has been developed by Integrated Spectronics, in consultation with the author, that overcomes these limitations and makes it possible to record spectra in the field at a rate of up to 50 per hour. Generally, however, returning samples to the laboratory or a field camp, has proved to be an effective method of obtaining spectra. Using a standard PIMA it is possible to record spectra from 300 sites per day in a laboratory environment and over 100 spectra can be recorded with the GER IRIS MkIV in this way.

In Situ versus Laboratory measurements.

The issue of whether laboratory measured spectra truly represent the in situ spectral response has been investigated; there are in fact two issues in this respect:

- Does disturbing the surface by sampling affect its spectra.
- Is the admixture of other surface materials such as green and dry vegetation affecting the soil spectra.

The first of these concerns was investigated by measuring samples in situ in the field and then returning them to the laboratory for measurement. The results of such tests with data I collected using a PIMA at the Pine Creek, Ellendale and Jubilee sites showed that for soils and rocks (weathered surfaces) there are no significant differences between in situ and laboratory measurements (Figure 5.4).

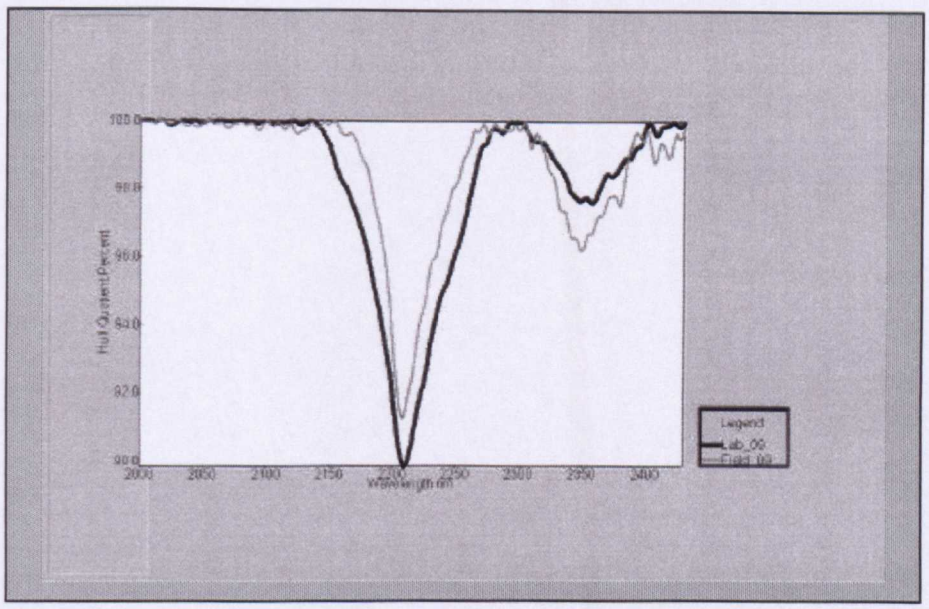

Figure 5.4: Spectra obtained from same sample material in the laboratory (black) and the field (grey). From 2000nm onwards (SWIR2), where main diagnostic features occur, the spectra show only minor differences in intensity(Y-axis) but virtually identical shape.

These field and laboratory studies indicated that where soils are well-developed, that is not immature (consisting mainly of rock fragments), recording a spectrum from a sample collected from 20cm below the surface results in spectra that have better defined features than those recorded from the surface (Figure 5.5).

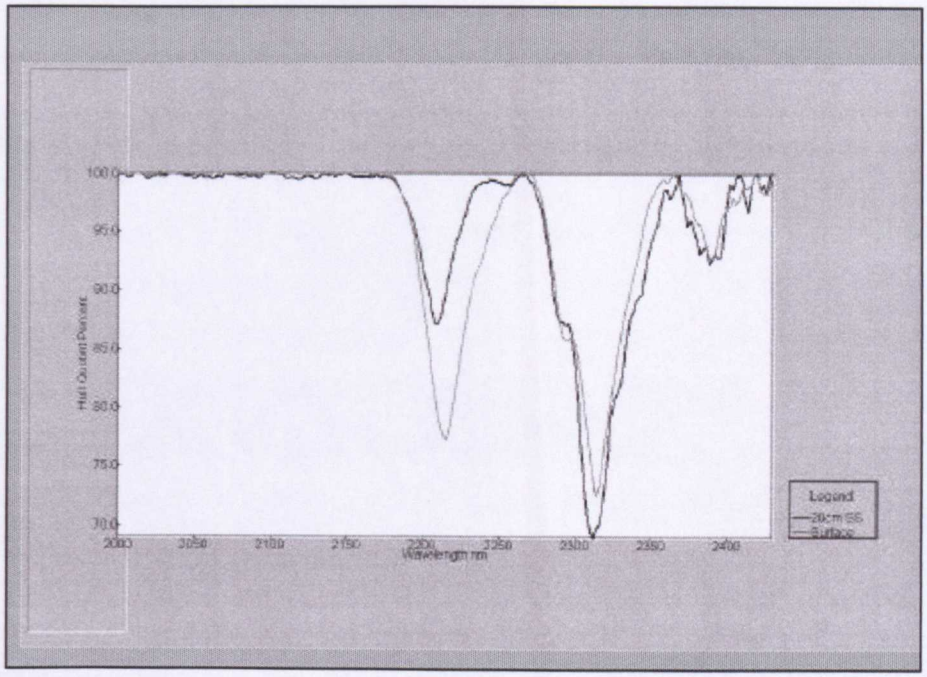

Figure 5.5: Example spectra taken from the surface (grey) and sub-surface (black). Note that the absorption features are more pronounced in the sub-surface spectrum.

This suggests that there is a surface layer from a few mm to a few cm thick where transported material dilutes the spectral signature. I suggest that this dilution is primarily due to quartz particles in the soil that reduce the spectral contrast but do not produce additional absorption features (see Chapter 6).

When the sample size is greater than the few square mm, which is the aperture size of the PIMA, then effects of surface material mixing will affect the spectra. If the investigations being carried out are field based this is not a concern as any material obscuring the surface can be moved and the soil or rock spectra recorded in situ. It is the spectral variation of the soils and rocks that are of interest and not the obscuring material.

5.4 ULTRAMAFIC ROCK SPECTRA

The primary rock types considered in this study are alkaline ultramafic rocks with elevated MgO content: lamproite and kimberlite. However, as these rocks have similar mineralogy to other ultramafic rocks, particularly when weathered (see Chapter 4) spectra of

pyroxenite, dunite, peridotite and serpentinite have been recorded.

Fresh Rock Spectra

Examples are shown (Figure 5.6) of the spectra obtained from the fresh surfaces of peridotite, dunite, pyroxenite, serpentinite and hypabyssal kimberlite, for the Visible Near Infrared (VNIR-600nm-1200nm), Short Wave Infrared 1 (SWIR1- 1200nm-2000nm) and Short Wave Infrared 2 (SWIR2-2000nm-2500nm). These reflectance spectra are typified by a slope towards longer wavelengths, apart from the kimberlite that has a convex form centred at 1600nm. All of the spectra have broad absorption features near 900nm that are typical of iron bearing minerals. The maximum reflectance values in these rocks is in the order of 10 percent to 20 percent which is as expected when rocks are uniformly dark in colour. Kimberlite, however, has a reflectance peak of 25 percent. Numerous hypabyssal kimberlite reflectance spectra that I have examined were characterised by a convex form because fresh kimberlite is rapidly altered on exposure to the air resulting in a surface veneer of clay minerals that are spectrally brighter.

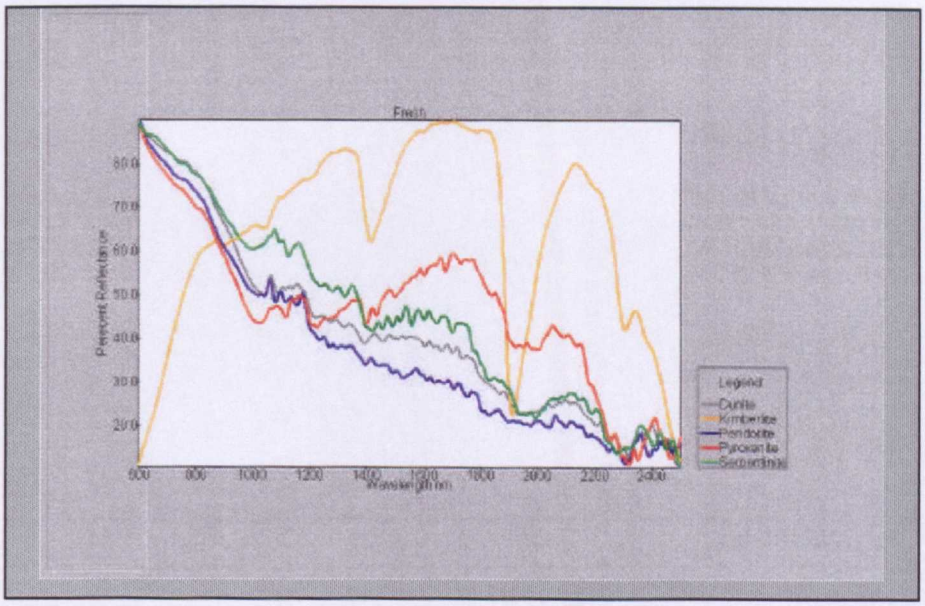

Figure 5.6: VNIR to SWIR2 reflectance spectra of fresh surfaces of ultramafic rocks.

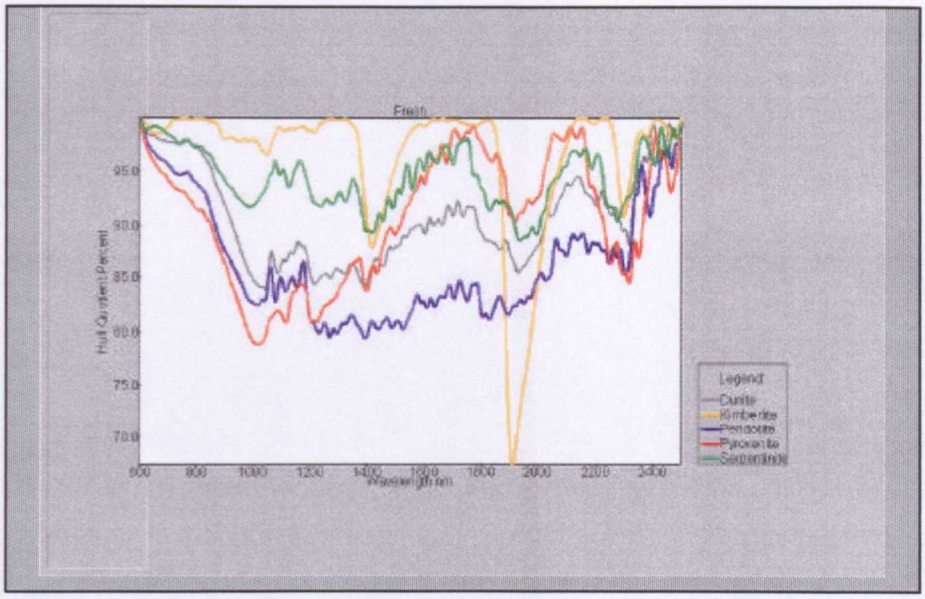

Figure 5.7: VNIR to SWIR2 hull quotient spectra of ultramafic rocks. The hull quotient removes the background spectral curve and emphasises the absorption features (see Chapter 3).

As the hull quotient spectra show (Figure 5.7) these rocks have their most distinct absorption features in the SWIR2 (2000nm to 2500nm) spectral range consequently this spectral interval is considered for the remainder of this study. Note that the non alkaline ultramafic rocks all show an absorption feature at ~900nm that is only weakly developed in the kimberlite spectrum. In kimberlites and lamproites, the facies differences result in spectra that have some variation in their SWIR2 spectra (Figure 5.8).

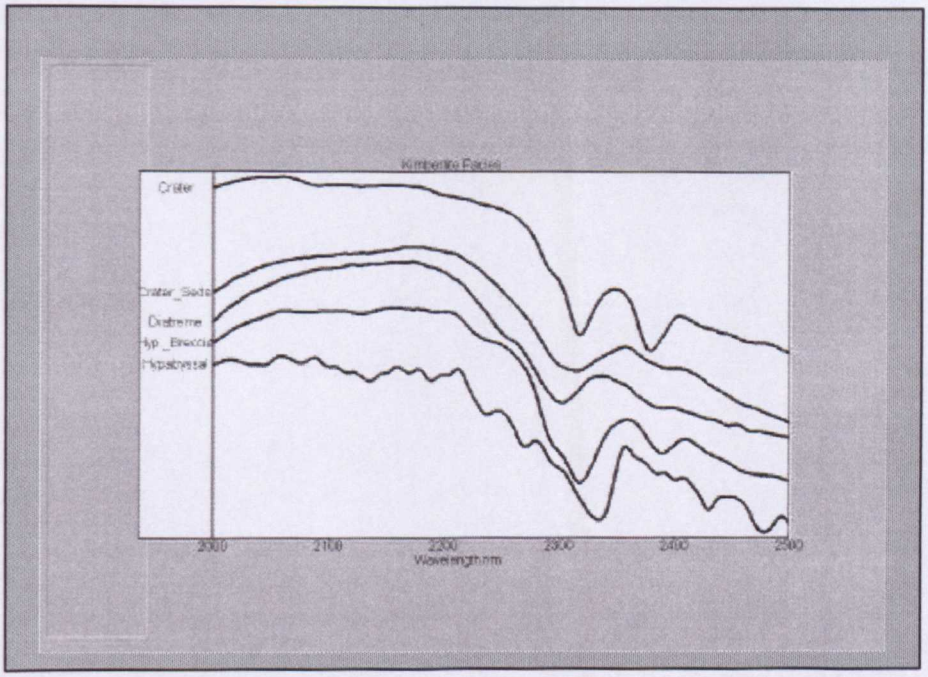

Figure 5.8: Stacked hull quotient spectra of kimberlite facies changes for the SWIR2. The depth of the main Mg-OH absorption feature at 2300nm is markedly deeper in the spectra of the non-hypabyssal facies rocks. Note Y-axis is not scaled and offset for clarity.

The depths of main spectral absorption features (determined from the hull difference transformed version - Chapter 3 - of plots Figures 5.6 and 5.7) of ultramafic rocks are listed in Table 5.1. A null value indicates no absorption feature near the specified wavelength.

ROCK	Near 2100nm	Near 2200nm	Near 2250nm	Near 2300nm	Near 2350nm	Near 2380nm
Dunite	0.05	0.38	0.54	1	-	0.29
Serpentinite	0.04	0.17	0.46	0.57		
Pyroxenite	0.08		1	1.12	0.92	
Peridotite	0.16		0.41	0.57	0.14	0.33
Kimberlite (average)	0.78	0.75	2.18	6.48		0.98
Hypabyssal	0.93	0.3	1.9	22		8.23
Diatreme	0.23			20.85		10.73
Breccia	0.17	0.03		15.9		3.2
Crater-Tuff	0.19			15.72		7.36
Lamproite (Olivine)	0.31	0.41	2.71	17.29		7.21

Table 5.1: Percentage depth of the SWIR2 absorption features derived from the hull difference spectra of fresh rock samples (Figure 5.6 and 5.7).

Examination of numerous SWIR2 spectra of ultramafic rocks shows that the diagnostic absorption feature is located between 2300nm and 2310nm. The hypabyssal kimberlite and lamproite spectra have features similar to each other. An absorption feature near 2300nm wavelength is common to all these rocks; in kimberlite and lamproite these features are deeper.

When reviewing these spectra it is necessary to consider the mineralogy of these rocks. As discussed in Chapter 4, it is apparent that in fresh ultramafic rocks, the following minerals can be expected: olivine, talc, serpentine, phlogopite, monticellite, calcite, pyroxene and leucite. The SWIR2 spectra of these minerals that are hydroxyl bearing are shown in Figure 5.9.

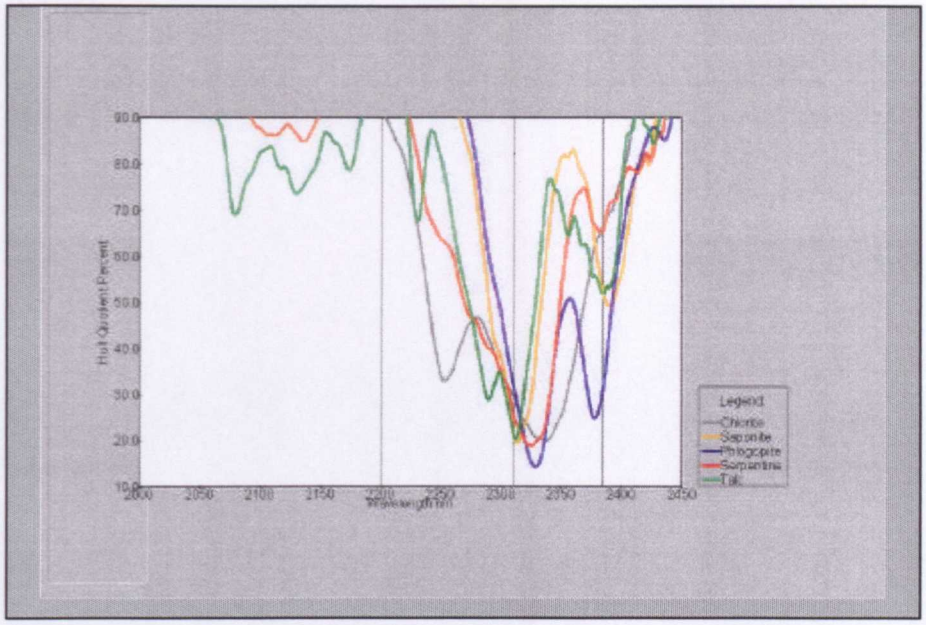

Figure 5.9: SWIR2 spectra of hydroxyl bearing minerals typical of ultramafic rocks. Note the common absorption feature > 2300nm.

Examination of these spectra (Figure 5.9) of Mg-OH bearing minerals: talc, serpentine, phlogopite (and chlorite), shows they are similar to each other. This is due to the diagnostic Mg-OH absorption feature that is common to all of them, > 2300nm in the SWIR2.

Weathered Rock Spectra

When weathered the proportion of hydroxyl minerals on exposed surfaces of ultramafic rocks increases (Chapter 4). Hydration of these rocks whether due to metamorphism or metasomatism will result in their conversion to an assemblage of serpentine, talc, chlorite and Mg-OH bearing clay minerals such as saponite (Velde, 1992, Kersten, 1973 and Pontual et. al., 1997). Phlogopite is more resistant to hydration than any other primary minerals but is itself a Mg-OH bearing mineral with a spectrum similar to other Mg-OH minerals such as talc.

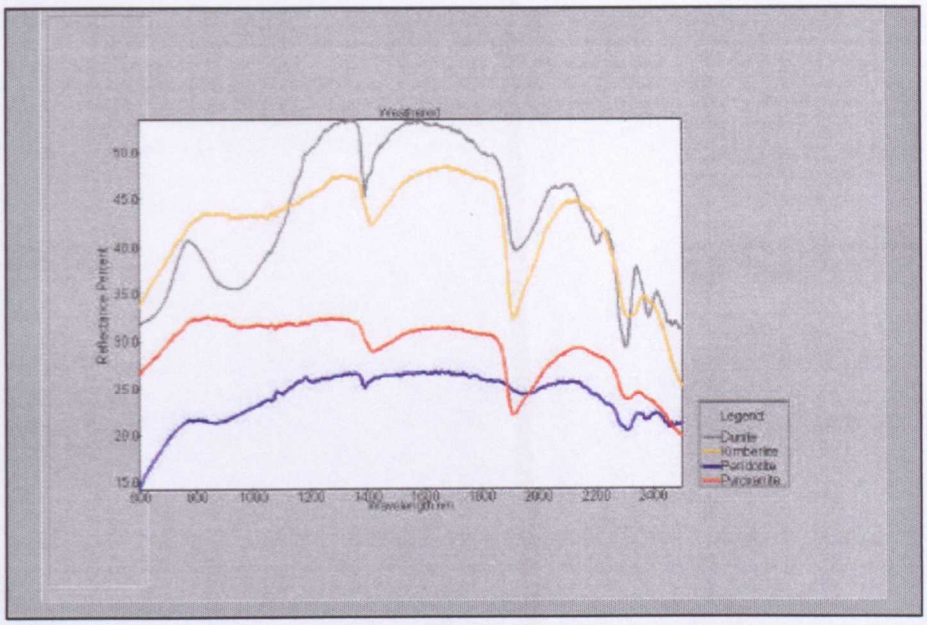

Figure 5.10: VNIR to SWIR reflectance spectra of weathered surfaces of ultramafic rocks. Note the convex form with a maximum at near 1600nm and absorption features at 900nm (iron) and 2300nm(Mg-OH). These spectra are brighter and have more pronounced absorption features than the fresh rock spectra shown in Figure 5.6.

The spectra shown in Figure 5.10 have a different form from those shown in Figure 5.6. They have acquired the convex form centred about 1600nm. All have a pronounced absorption feature >2300nm; dunite and kimberlite have an absorption feature at ~2380nm not apparent in the peridotite spectra. This change in spectral shape with weathering I attribute to the effects of hydration on the minerals in these rocks which results in the development of Mg-OH bearing phyllosilicates. Examination of the spectra of the weathered surfaces shows deeper 1400nm and 1900nm water absorption bands than the fresh rocks surfaces, in addition to the stronger >2300nm features, which is evidence of clay formation.

ROCK	Near 2100nm	Near 2200nm	Near 2250nm	Near 2300nm	Near 2350mn	Near 2380nm
Dunite	0.03	6.69		25.20		9.83
Serpentinite	0.15	2.19		10.69		3.49
Peridotite	0.02	2.68		13.10		5.66
Kimberlite	0.6	0.4		6		1.2
Lamproite (Olivine)	0.61	0.46	8.24	15.3	11.25	

Table 5.2: Percentage depth of the SWIR2 absorption features derived from the hull difference spectra of weathered rock samples (Figure 5.6 and PIMA spectra of weathered kimberlite and lamproite).

The figures presented in Table 5.2 emphasise the development of phyllosilicate minerals on the weathered surface with the main absorption features being deeper than in the fresh rocks. Furthermore, the development of 2200nm absorption features in these samples

indicates the formation of Al-OH minerals that are typical of the weathering process. The development of the 2250nm feature noted from lamproite spectra, collected in the Ellendale field in Western Australia is indicative of the presence of an Fe-OH mineral such as nontronite or chlorite.

It is possible in extremely arid conditions that there is little or no development of clay minerals on the exposed surfaces of ultramafic rocks. Pontual's (1990) study of the ophiolite belt in Oman showed that in extremely dry conditions the extent of weathering of ultramafic rocks is minimal. In Oman, lack of soil and vegetation cover means it is possible to differentiate between ultramafic and background rocks using the spectral contrast apparent from TM imagery. Pontual also demonstrated that it was possible to differentiate between some of the ultramafic units such as pyroxenite and peridotite based on their spectral response in TM data. However, Pontual (1990) determined that alteration of the harzburgite and dunite to serpentinite reduces the ability to discriminate these units using TM imagery, in Oman. This study indicates that discrimination of these rocks types, in such arid areas, would also be achieved from using SWIR2 data alone.

5.5 SPECTRA OF SOILS DERIVED FROM ULTRAMAFIC ROCKS

As discussed in Chapter 4 when alkaline and other ultramafic rocks are weathered the products of this weathering are incorporated into residual soils. Therefore, the spectral response of soil-regolith from an ultramafic rock can be anticipated to be a mixed spectrum with both Mg-OH and non Mg-OH (typically due to Al-OH clays) absorption features. The effects of mineral mixing on spectra are discussed in Chapter 6.

Figure 5.11 shows the spectra obtained from the test sites investigated in this study, Pine Creek (kimberlite), Meredith (melnoite), Jubilee (serpentinite) and Ellendale (lamproite) with the spectra of kimberlite and micaeous shale for comparison. It is clear that both the >2300nm and >2200nm features are developed in these soil spectra.

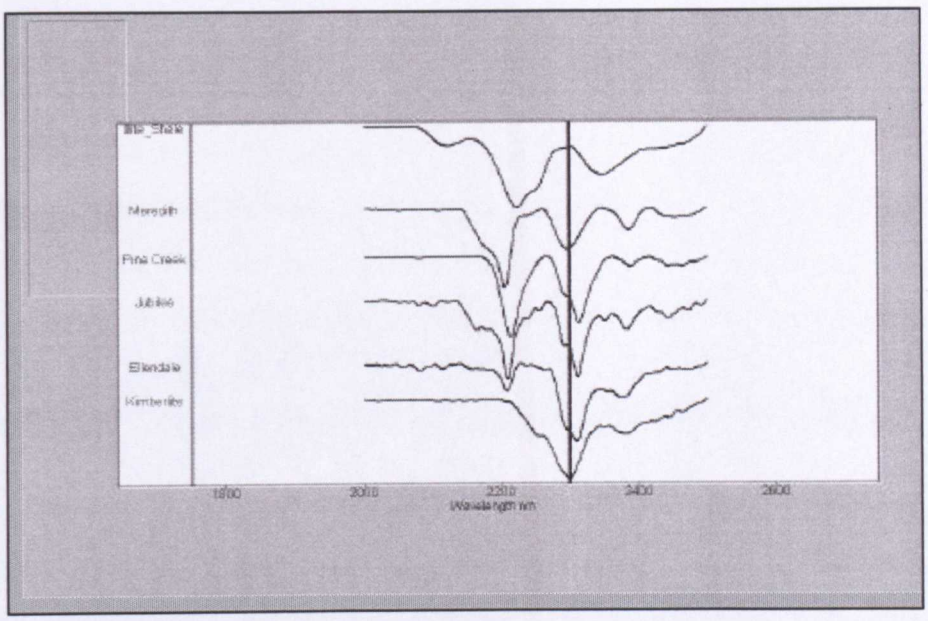

Figure 5.11 Stacked SWIR2 hull quotient spectra of soils derived from alkaline and other ultramafic rocks in Australia. Spectra of kimberlite and illite-shale are shown for reference. Note both >2300nm and >2200nm absorption features in the soil spectra indicating mixed mineralogy. Spectra are offset on Y-axis for clarity. Vertical Line at 2300nm.

5.6 BACKGROUND ROCKS (AND MATERIALS) INCLUDING THOSE SPECTRALLY SIMILAR TO ULTRAMAFIC ROCKS

If spectral geological techniques are to be applied to the detection and mapping of ultramafic rocks then it is essential to determine the degree to which their spectral signatures are unique.

Ultramafic rocks investigated in this study can occur intruded and incorporated into a variety of background rocks (Jackson, 1997). Section 5.4 has shown that the ultramafic rocks are characterised by having diagnostic spectra due to their Mg-OH minerals content, that have significant absorption features near 2300nm. However, these minerals also have a VNIR spectral structure that typifies the presence of iron minerals. Ultramafic rocks share these iron spectral features with numerous other minerals and rocks; it may be diagnostic in some areas to a lesser degree than the SWIR2 features and has not been considered in this study. Therefore, when considering background rocks, minerals, (and other materials) I have concentrated either on those that contain Mg-OH or for other reasons have absorption features developed between 2300nm and 2500nm. It is beyond the scope of this study to determine the spectrum of every rock type that may surround ultramafic rocks; only spectra of the more common rock types are presented.

In Table 5.3 common minerals that contain Mg-OH are listed together with their diagnostic absorption features wavelengths and the non ultramafic rocks in which they can occur. Occurrences of these rocks will, depending on their weathering products, have a spectral signature similar to ultramafic rocks. Using spectral geological techniques in the field means that mis-identification may be reduced by visual inspection, though when dealing with weathered rock this may be difficult. However, spectral analysis of remotely sensed imagery can result in occurrences of these rocks being attributed to ultramafic rock.

MINERALS	SIGNIFICANT SWIR ABSORPTION WAVELENGTHS	ROCKS CONTAINING THESE MINERALS
Talc	2290nm, 2312nm, 2386nm	Low grade metamorphism of rocks such as gabbro and dolomite forming Talc Schist
Chlorite	2254nm, 2332nm Varies with iron : magnesium ratio	Greenschists. Hydrothermal alteration. Andesites. Argillaceous sediments.
Biotite	2254nm, 2340nm , 2389nm	Intermediate - acid intrusives. High-grade hornfels. Marbles and basalts. Hydrothermal alteration.
Amphiboles	2312nm, 2383nm	Amphibolites and tremolite schist.
Clays		
Saponite	2316nm, 2389nm	Evaporites formed in magnesium rich environments. Weathering of dolomite-rare
Vermiculite	2317nm, 2389nm	Hydration of biotite containing rocks.
Hectorite	2306nm	Hydrothermal alteration of dolomite (rare).
Sepiolite	2164nm, 2306nm, 2352nm	Low temperature hydrothermal alteration of carbonates.

Table 5.3: Mg-OH bearing minerals that can occur in non-ultramafic rocks. The deepest and diagnostic absorption features are underlined.

Some minerals and materials do not have any Mg-OH in their crystal lattice but still have absorption features near 2300nm. These are listed in table 5.4. These minerals can also be mistaken for occurrences of ultramafic rocks when relying on spectral identification alone, for example, when interpreting remotely sensed data or spectra from percussion drilling. However, unlike rocks with Mg-OH bearing minerals the overall shape of these minerals and materials spectra is often sufficient to prevent mis-identification occurring.

MINERAL / MATERIAL	2300nm WAVELENGTHS & FEATURE FORM	ROCK TYPES ETC.
Calcite	2332nm broad and asymmetric feature	Limestone and calcrete
Dolomite	2312nm broad and asymmetric feature	Dolomite
Magnesite	2296nm broad and deep symmetric feature	Weathered ultramafic rocks.
Kaolinite	2322nm minor feature that can cause problems when examining mixed spectra	Weathered felspar and white micaceous rocks. End member weathering product of hydrothermal alteration
Cellulose – Plant oils and waxes	2312nm shape of spectra at shorter wavelengths is diagnostic due to 2137nm and 2275nm features	Woody and dry vegetation and litter
Plastic	2314nm in some plastics but spiky spectra and well-developed features at 2266nm and 2354nm are diagnostic.	Sample bags and containers

Table 5.4: Minerals, rocks and other materials that have absorption features near 2300nm.

Figure 5.12 shows example spectra of these minerals/materials compared to a composite spectrum of kimberlite. This illustrates the similarity of these minerals and materials to spectra of ultramafic rock. For comparison, Figures 5.13 to 5.15 show the SWIR2 spectra of some common rock types.

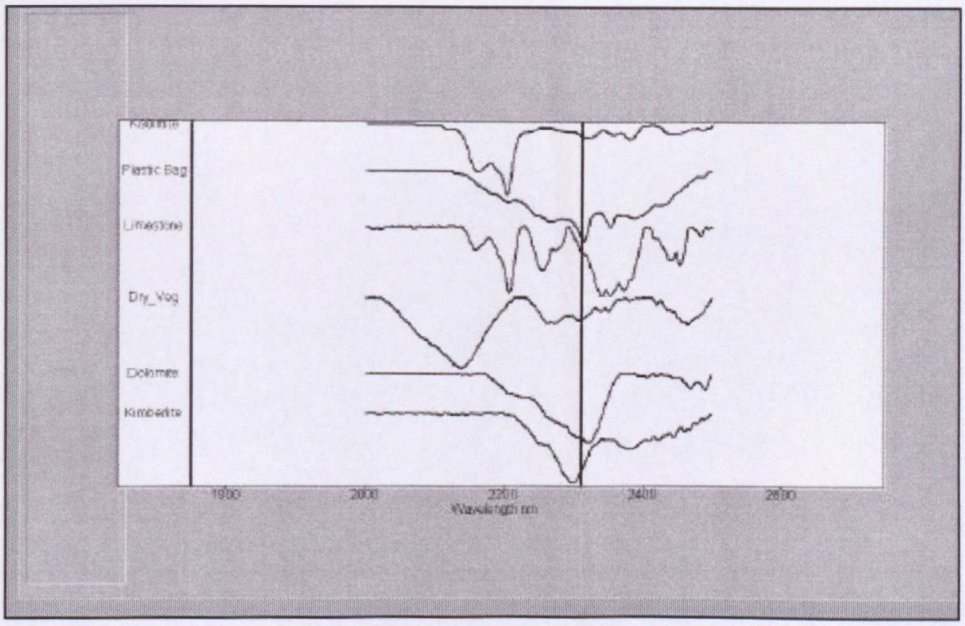

Figure 5.12 Stacked SWIR2 hull quotient spectra of minerals and materials with near 2300nm absorption features and a kimberlite spectrum as an example of a diagnostic alkaline ultramafic rock spectrum. Spectra are offset on the Y-axis for clarity. Note the spectrum of plastic shows why spectra should never be measured of samples through plastic containers/bags. Vertical line at 2312nm.

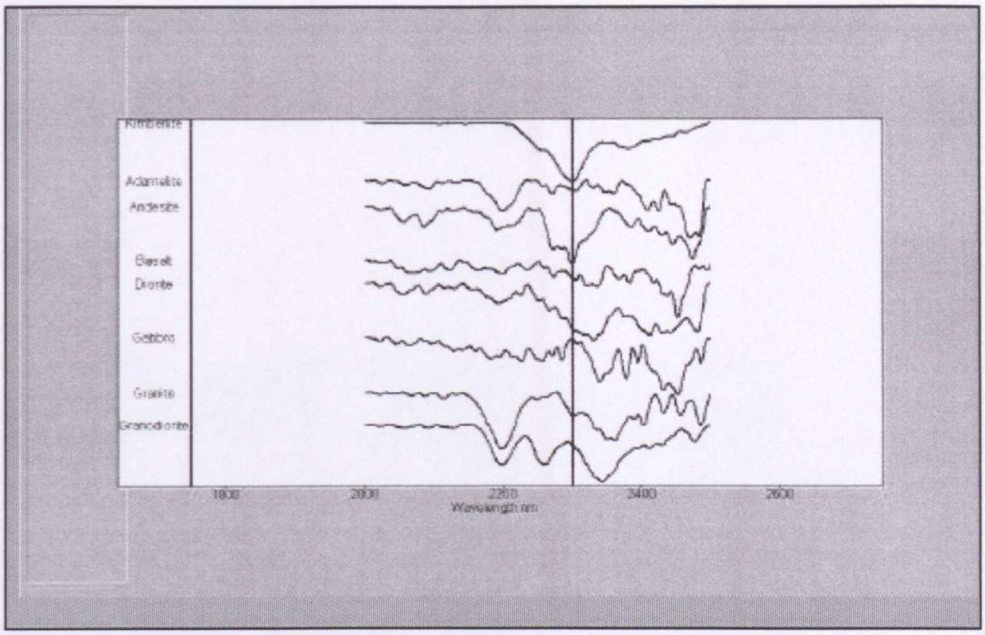

Figure 5. 13: Stacked SWIR2 hull quotient spectra of igneous rocks and kimberlite for comparison. Spectra are offset on the Y-axis for clarity. Vertical line at 2312nm.

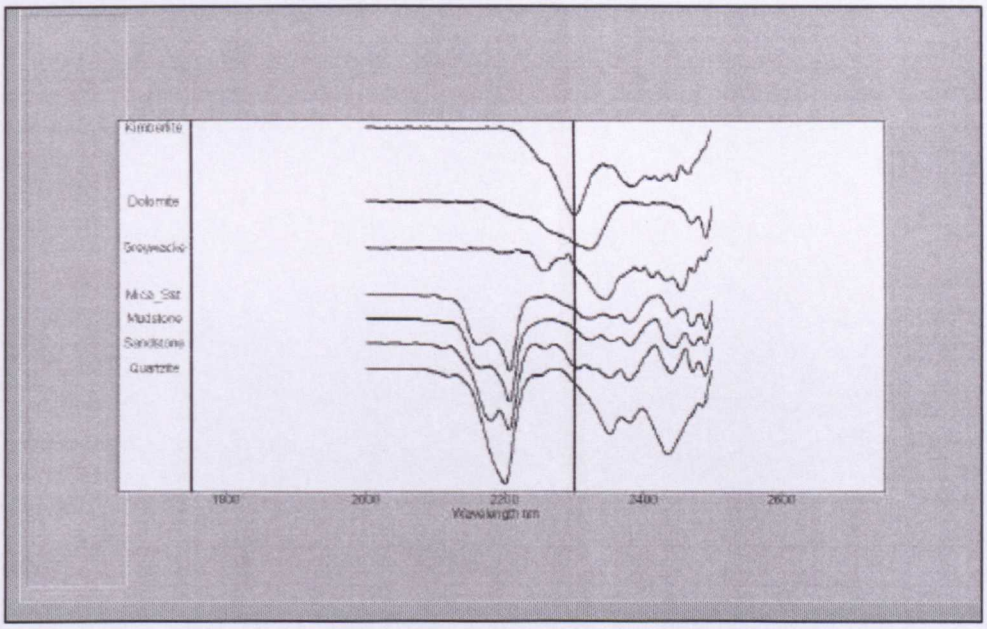

Figure 5.14: Stacked SWIR2 hull quotient spectra of sedimentary rocks and kimberlite for comparison. Spectra are offset on the Y-axis for clarity. Vertical line at 2312nm.

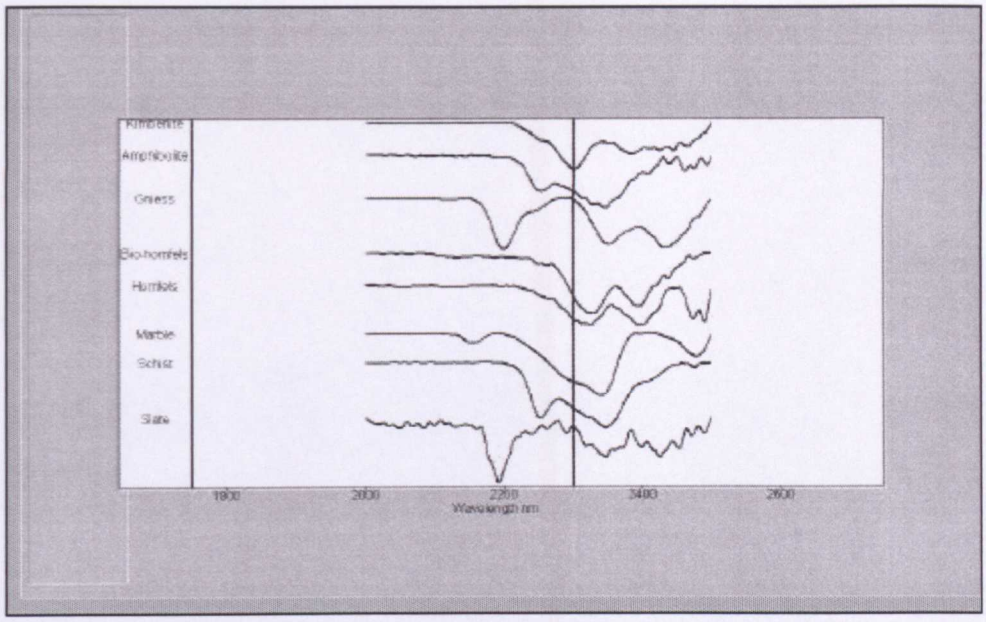

Figure 5.15 Stacked SWIR hull quotient spectra of metamorphic rocks and kimberlite for comparison. Spectra are offset on the Y-axis for clarity. Vertical line at 2312nm.

Of the rock spectra shown in Figures 5.13 to 5.15, only andesite (Figure 5.13) has a spectrum that is similar to that of an ultramafic rock. In fact this andesite spectra can be interpreted as magnesium chlorite a mineral that is not common in ultramafic rocks.

5.7 CONCLUSIONS

Fresh and unaltered ultramafic rocks have uniformly low albedo that reduces spectral contrast. This can be problematic when dealing with field and drill samples. However, only in rare cases will these rocks be fresh. In semi arid and arid regions when exposed they usually show the effects of surface weathering. The alteration mineralogy and weathering means these rock's surfaces contain a high proportions of Mg-OH minerals such as serpentine and saponite. As weathering intensity increases on exposed surfaces, clay mineral formation will intensify and the development of these diagnostic spectral absorption features will be enhanced.

In Table 5.5 the percentage depth of absorption features of the minerals that occur in these rocks at surface are listed and this shows that their absorption features are deeper than in the spectra of fresh rocks (or soils). This is because these are single spectra of pure minerals; mixing of minerals reduces the depth of absorption features. In Table 5.5 where absorption features have wavelengths significantly offset from main absorption bands, this wavelength is noted.

Mineral	Near 2100nm	Near 2200nm	Near 2280nm	Near 2300nm	Near 2350mn	Near 2380nm	Weathering
Serpentine	7.7			36.94		16.95	Low
Phlogopite	5.32			50.16		41.84	Low
Talc	8.17	8.78 2231nm	17.71 2290nm	18.93		12.37	Low
Chlorite	1.93	27.73			28 2330nm		Moderate
Nontronite	0.14	5.5	22.58 2283nm			9.03	Moderate iron>Mg
Saponite	1.91	.7	2.95 2292nm	38.33		21.94	High
Kaolinite	40.83 2168nm	45.76		25.65	22.59	22.50	Extreme

Table 5.5 Distribution and percentage depth of diagnostic absorption features for minerals can occur at the surface of typical ultramafic rocks and the degree of weathering involved in their formation-preservation.

When applying spectral geological methods to ultramafic rocks and their weathering products the most useful diagnostic information is gained from the SWIR2 spectral region, specifically, absorption features centred between 2300nm – 2320nm and 2380-2385nm. It would be rare to find extensive unweathered areas of these rocks when examining remote-sensing imagery. The effects of weathering of ultramafic rocks and soil formation produces mixed mineral spectra. The primary Mg-OH absorption features at >2300nm are preserved but are less pronounced and the spectra typically show Al-OH absorption features (>2200nmn) as well.

When examining data from outcrops, exposure in pits, trenches, drill core and particularly percussion drill chips the recognition of the spectral signatures detailed above, coupled with visual inspection, can greatly assist in the interpretation of the local geology and mineralogy.

The data presented indicate that when dealing with fresh and weathered rock samples, only rocks containing abundant Mg-OH bearing minerals are likely to be confused with ultramafic rocks spectrally. In practice, visual examination of the rocks may clarify their identification, though in the case of highly weathered material and drill chips/powder visual analyses may not be definitive. Differentiation and identification of outcrop areas using remotely sensed spectral data is more problematic. Extensive areas of outcrop may be classifiable due to associations of the rock types and their relationships. In areas of sparse and isolated outcrop, occurrences of the Mg-OH spectral signatures derived from scanner imagery will be more difficult to classify.

Spectra should never be recorded through plastic bottles or bags.

CHAPTER 6

6 MINERAL MIXING AND THE SPECTRAL RESPONSE OF ALKALINE ULTRAMAFIC ROCKS AND DERIVED SOILS

6.1 INTRODUCTION

In this chapter there are several pages with blank areas, this is a result of the constraints imposed in formatting the document so that diagrams and text are kept together.

Mixed spectra can be produced from rocks (which are mineral mixtures) and from a variety of processes both natural and inherent in the recording of the spectra:

- Weathering and soil formation: weathering of rocks usually produces an assemblage of minerals which together with rock fragments can be incorporated into soils by physical mixing. These minerals can undergo further change by chemical evolution within the soil (see Chapter 4). Hence the natural surfaces of rocks and soils frequently have spectra typical of mineral mixtures
- Sampling: physical mixing resulting from the sampling process.
- Pixels: when a scanner (or spectrometer) acquires images, all materials in the extent of a pixel will integrate and contribute to the pixel's spectral response

I have carried out experiments to determine the spectral response that may be expected when alkaline ultramafic rocks and their breakdown products are mixed with other mineral mixtures. As was shown in Chapter 4 though alkaline, other ultramafic rocks and their weathering products consist of a variety of minerals, those containing Mg-OH dominate in their spectra response. Saponite, derived from weathered kimberlite, was used as the ultramafic component in these mixtures as it has the typical Mg-OH spectral absorption features and is a clay produced by the weathering of ultramafic rocks (see Chapter 4). These experiments were carried out in three ways:

- Physical mixtures: minerals were mixed in fixed proportions and their spectra recorded.
- Virtual mixtures: the spectra obtained from the pure minerals (measured for the physical mixtures) were added together, weighted to produce the different proportions.
- Virtual library mixtures: virtual mixtures derived from spectra supplied with the PIMAVIEW software.

The results obtained from these methods were compared to determine if the virtual method is reliable.

Physical mineral mixtures investigated were:

- saponite with kaolinite
- saponite with illite
- saponite with dolomite
- saponite with limestone (calcite)

Virtual mineral mixtures examined were:

- saponite with kaolinite
- saponite with illite
- saponite with dolomite

Virtual library mixtures examined were:

- saponite with kaolinite
- saponite with illite
- saponite with quartz sand
- saponite with quartz sand and kaolinite
- saponite with dolomite
- saponite with chlorite

Dry vegetation has absorption features near 2300nm due to waxes and oils (Lewis,1997 pers. comm. and in press) and is a common component of an image pixel in arid areas. Therefore, physical and virtual mixtures of saponite and dry vegetation were also investigated.

The physical mixing process involved grinding in a mortar and pestle both the sample materials together, measured in required proportions, until they appeared to be of uniform size and well mixed. The proportions used were 33 percent-66 percent, 50 percent-50 percent and 66 percent-33 percent. For these physical mixtures graphs were produced of diagnostic parameters obtained from their spectra to determine the degree of linearity expressed as an effect of mixing. When sufficiently linear these mixing plots can be used as look-up tables to estimate the percentages of the component minerals in a mixture from the parameters derived from a spectrum. Linearity in spectral variation of mineral mixtures is supported by studies carried out by Yang and Huntington (1997) and Ramsey and Christensen (1998).

For virtual mixing the two spectra were added to each other, weighted by the same values as the physical mixtures. Spectra were output as stacked plots for each type of mixing, with a hull quotient transform applied to emphasise the characteristic absorption features.

Virtual spectra were also produced of a mixture of saponite-kaolinite-quartz spectra as the review of the weathering of ultramafic rocks (Chapter 4) has indicated that this would be a typical mineral assemblage for soil derived from ultramafic rocks in arid conditions.

6.2 KAOLINITE – SAPONITE

Physical Mixtures

The "pure" saponite sample used obviously has minor contamination with an Al-OH clay, which is depicted by a minor absorption feature at 2200mm (Figure 6.1).

In the stack plot (Figure 6.1) the main effect of mixing is expressed by a reduction in the 2200nm feature depth as the proportion of saponite increases. This decrease is most dramatic between 33 percent kaolinite and the pure saponite, after which there is a progressive decrease in the depth of the feature, though not as pronounced. There is also a progressive shift towards shorter wavelengths of the near 2300nm feature from 2320nm in the kaolinite to 2312nm in saponite. Similarly, the kaolinite features at 2350nm and ~2390nm become shallower as the proportion of saponite increases.

The Mg Score ratio is calculated by dividing the hull quotient reflectance value at 2200nm by the hull quotient reflectance value at 2312nm. Plotting these values for the saponite-kaolinite physical mixture (Figure 6.2) shows a linear trend, indicated by the second order regression line (derived using the Microsoft Excel chart function: Linear). This plot (Figure 6.2) may be used as a look-up-table to determine the proportion of kaolinite and saponite in a spectrum that represents this mixture by determining the Mg Score ratio value.

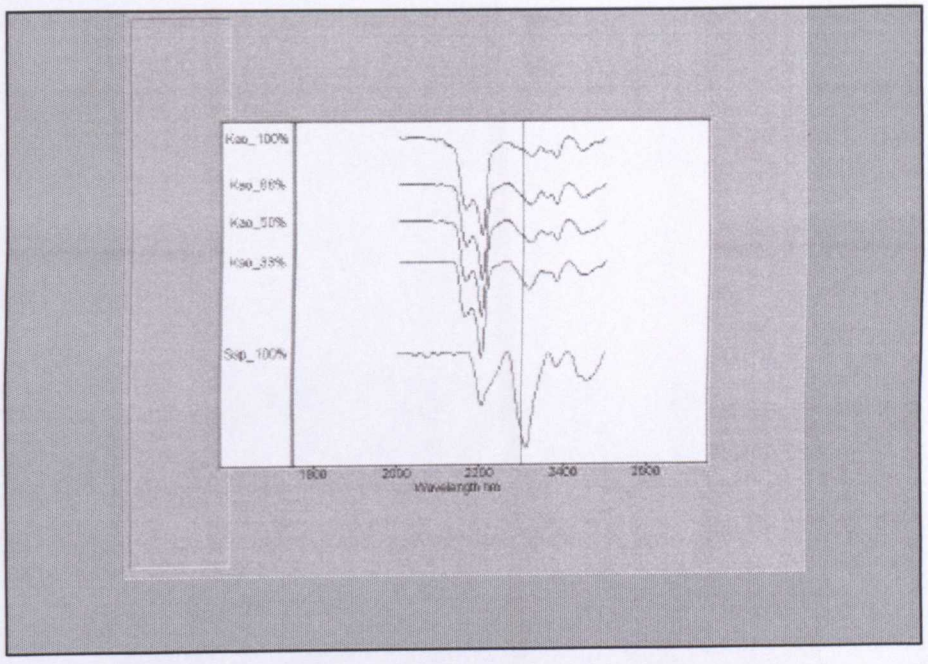

Figure 6.1: Stacked hull quotient spectra of physical mixtures of saponite and kaolinite. Spectra are offset on the Y-axis by 5 percent for clarity. The Y-axis labels are the abbreviated spectral file names and indicate the percentages of the end-member in each spectral sample. Vertical bar at 2312nm.

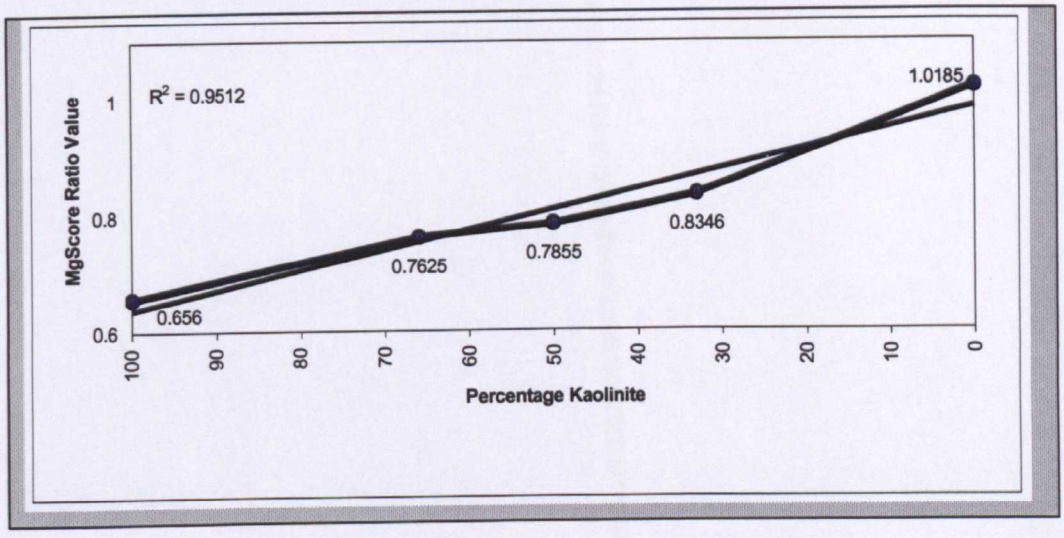

Figure 6.2: Plot of Mg Score ratio values calculated from the saponite-kaolinite spectra shown in Figure 6.1. The thin line is the second order regression line. This plot shows a linear increase in ratio values as the proportion of saponite increases.

Virtual Mixtures

When comparing the stacked profiles of spectra for the virtual mixtures (Figure 6.3) with the physical spectra (Figure 6.1) no apparent difference is observed. This virtual saponite-kaolinite mixture can also be regarded as linear.

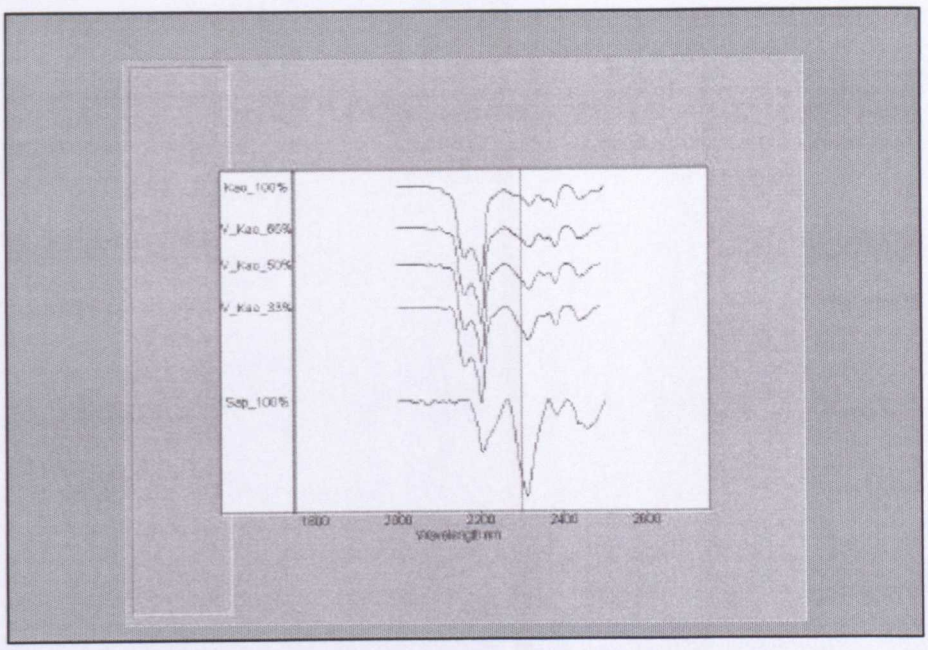

Figure 6.3: Stacked hull quotient spectra of virtual mixtures of saponite and kaolinite. Spectra are offset on the Y-axis by 5 percent for clarity. The Y-axis labels are the spectra file names that indicate the percentages of the end-member in each spectral sample. Vertical bar at 2312nm for reference.

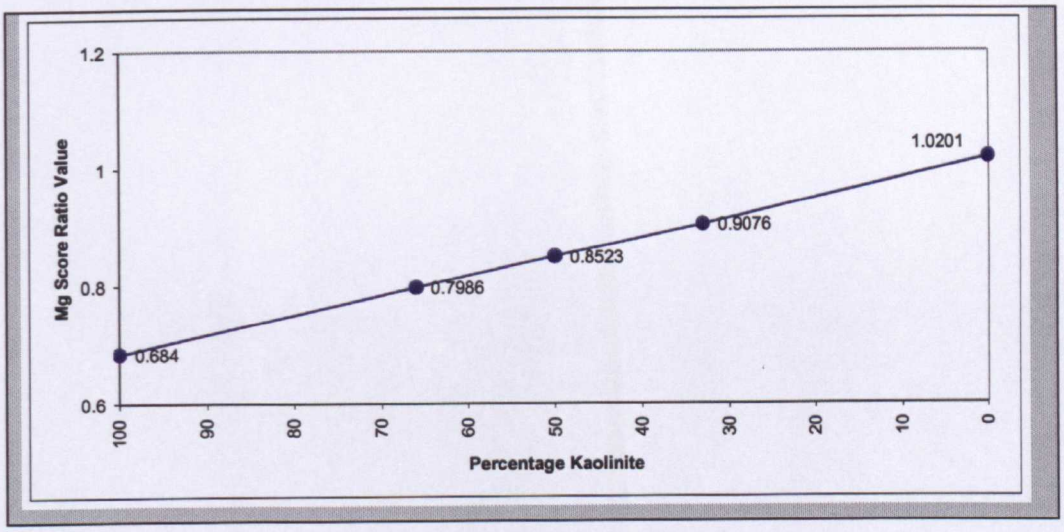

Figure 6.4: Plot of Mg Score ratio values calculated from the saponite-kaolinite spectra shown in Figure 6.3. The second order regression line is covered by ratio value plot. This plot shows a linear increase in ratio values as the proportion of saponite increases.

Virtual Library Mixtures

In Figure 6.5 the stacked profiles show that the 100 percent saponite spectrum has much deeper 2312nm and 2385nm features than in the previous examples (Figures 6.1 and 6.3) and the 2200nm feature is absent in this spectrum. However, the same reduction in the depth of 2200nm feature as the proportion of saponite relative to kaolinite increases, is apparent. There is a decrease in the intensity of the 2312nm and 2380nm features between 100 percent saponite and 33 percent kaolinite.

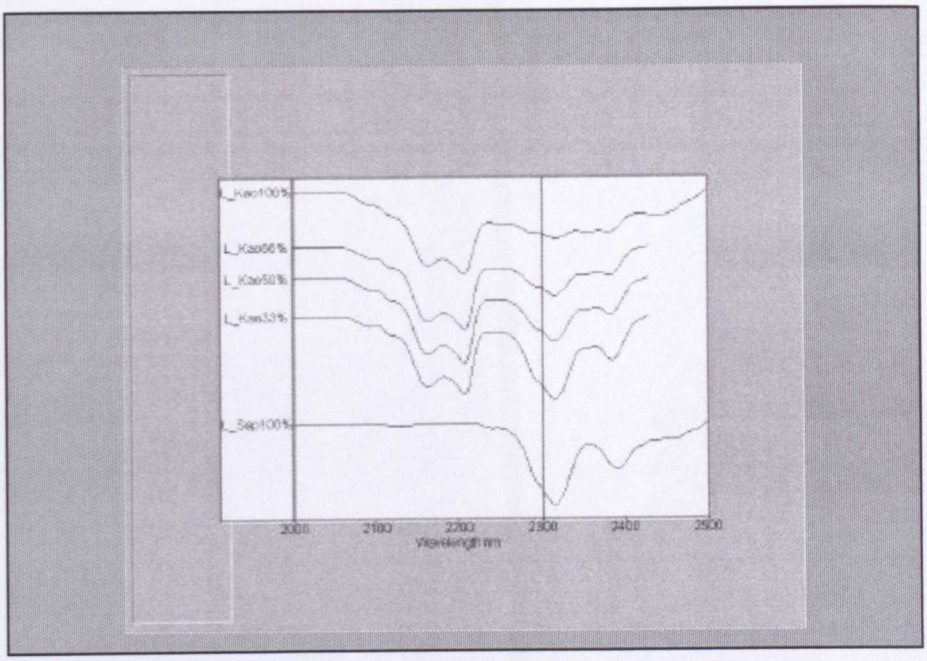

Figure 6.5: Stacked hull quotient spectra of virtual library mixtures of saponite and kaolinite. Spectra are offset on the Y-axis by 5 percent for clarity. The Y-axis labels are the spectra file names and indicate the percentages of the end-member in each spectral sample. Vertical bar at 2312nm for reference.

The Mg Score ratio plot derived from these spectra is similar to that obtained in the plots of the physical and virtual mixtures (Figure 6.2 and 6.4). Below 33 percent kaolinite, however, the gradient steepens that is towards higher saponite content. This is due to the lack of any 2200nm absorption feature in the pure library saponite.

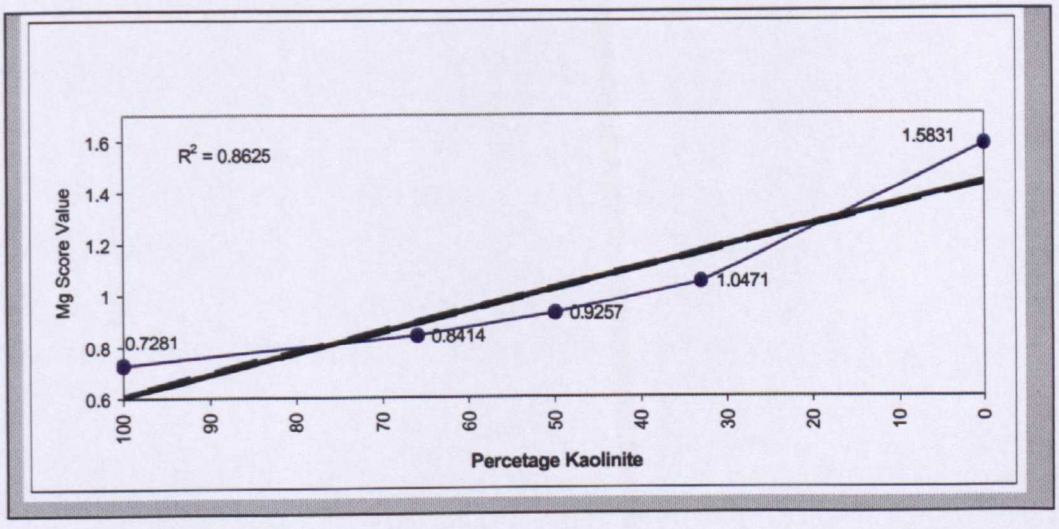

Figure 6.6: Plot of Mg Score ratio values calculated from saponite-kaolinite spectra shown in Figure 6.5 The thicker line is the second order regression line. This plot shows a linear increase in ratio values as the proportion of saponite increases until 66 percent then an increase in gradient to 100 percent saponite.

Comments

Evaluating virtual library spectra and plots suggests that a small admixture of kaolinite with saponite (amount not determined but less than 33 percent) results in the most marked reduction in the depth of the 2312nm absorption feature. Further increase in kaolinite content has less effect and the spectral changes are then proportional to the ratio of saponite to kaolinite in the mixture. As the saponite used in both the physical and virtual mixtures was contaminated with kaolinite, or another Al-OH bearing mineral (weak 2200nm-absorption feature), this may explain why the change in gradient is less marked in the physical and virtual mixture Mg Score ratio plot. Using the virtual library Mg Score ratio plot as a look-up-table and taking the ratio value of the pure saponite (1.2 from the physical mixture) indicates the percentage of kaolinite (or some other Al-OH mineral) in this saponite end-member mineral is approximately 22 percent.

These deductions indicate that care should be taken when carrying out mixing experiments to ensure that the minerals used as spectral end-members are pure. This was not the case in these experiments but the objective was to determine if virtual mixtures represent physical mixtures which appears to be the case.

6.3 SAPONITE - ILLITE

Physical Mixtures

In the case of saponite and illite (Figure 6.7) the stacked profile indicates a uniform trend in spectral changes as the proportion of the end-members varies. As saponite increases, the 2200nm feature reduces. Similarly the 2300nm absorption becomes shallower and shifts towards longer wavelengths as illite content in the mixture increases as follows:

- 100 percent Illite 2349nm
- 66 percent Illite 2339nm with 2317nm shoulder
- 50 percent Illite 2314nm & 2344nm
- 33 percent Illite 2317nm with 2344nm shoulder
- 0 percent Illite 2311nm.

The profile from the Mg Score ratio (Figure 6.8) is almost linear with a steepening in gradient towards the 100 percent illite end member.

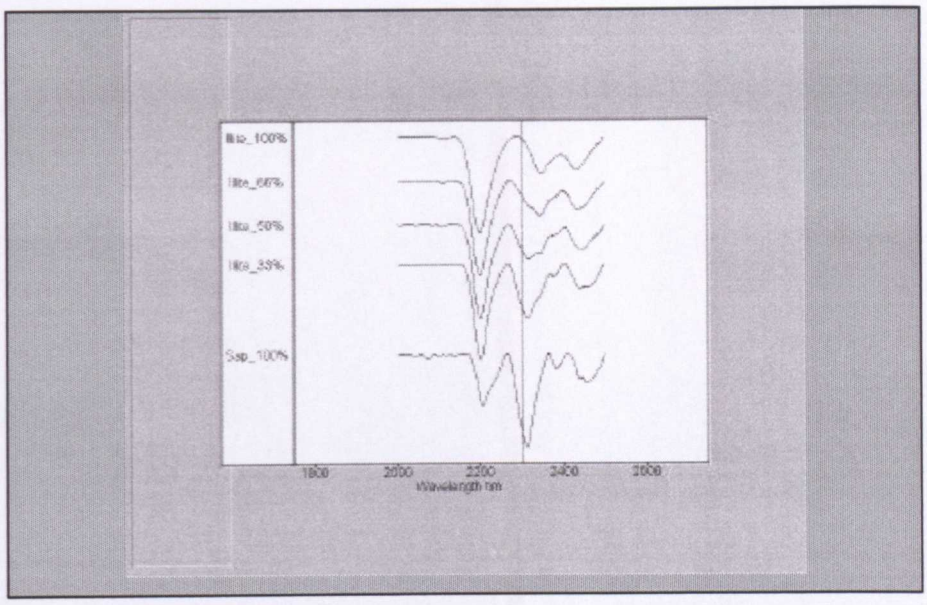

Figure 6.7: Stacked hull quotient spectra of physical mixtures of saponite and illite. Spectra are offset on the Y-axis by 5 percent for clarity. The Y-axis labels are the spectrum file names and indicate the percentages of the end-member in each spectral sample. Vertical bar at 2312nm for reference.

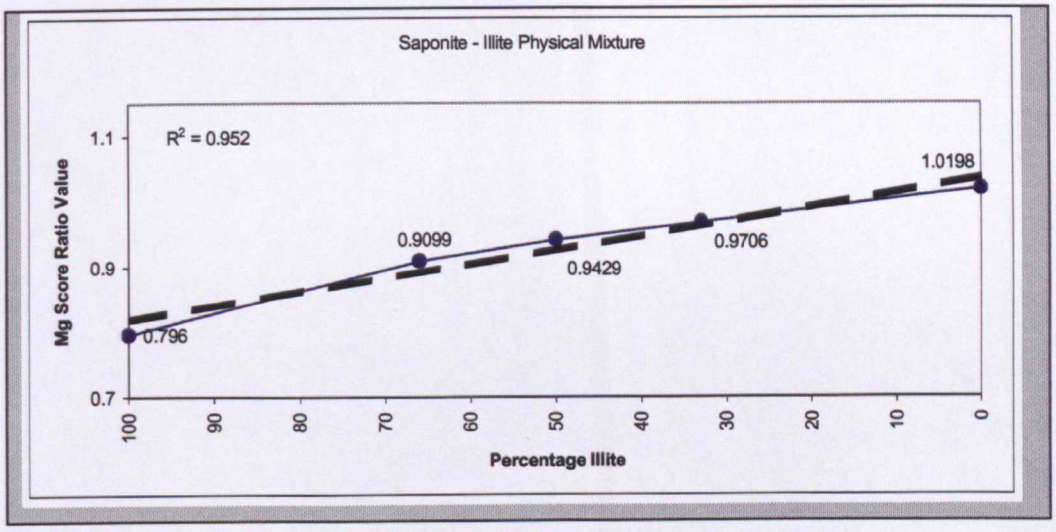

Figure 6.8: Plot of Mg Score ratio values calculated from saponite-illite spectra shown in Figure 6.7 The dashed line is the second order regression line. This plot has a linear increase in ratio values as the proportion of saponite increases.

Virtual Mixtures

The stacked plot for the virtual mixture (Figure 6.9) is visually indistinguishable from the physical saponite-illite mixture (Figure 6.7).

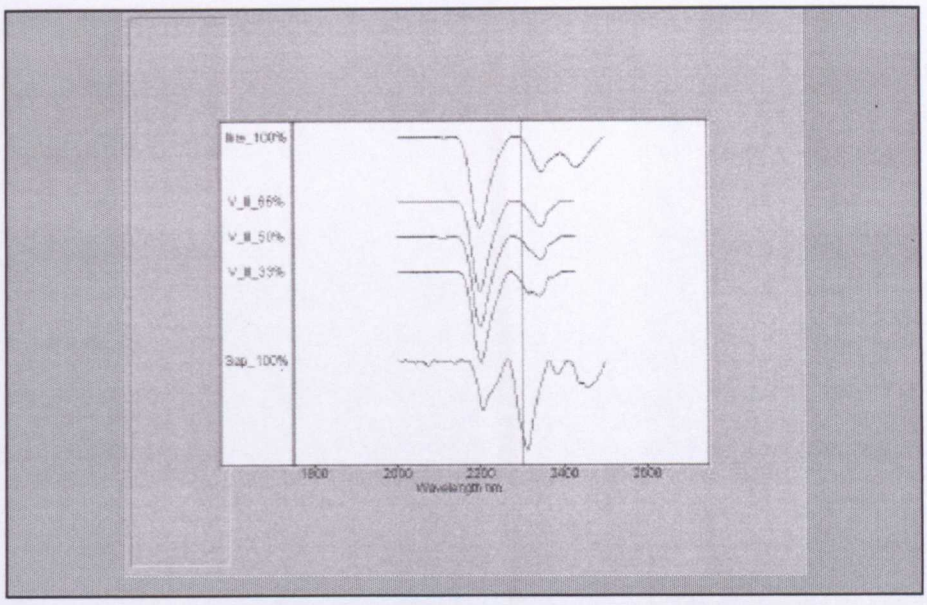

Figure 6.9: Stacked hull quotient spectra of virtual mixtures of saponite and illite. Spectra are offset on the Y-axis by 5 percent for clarity. The Y-axis labels are the spectrum file names and indicate the percentages of the end-member in each spectral sample. Vertical bar at 2312nm for reference.

The Mg Score plot for the virtual mixture has greater linearity than the physical mixture; it does not show the change in gradient towards the 100 percent illite. (Figure 6.10). However, as in the case of saponite-kaolinite, it shows an increase in gradient towards 100 percent saponite, from 66 percent saponite.

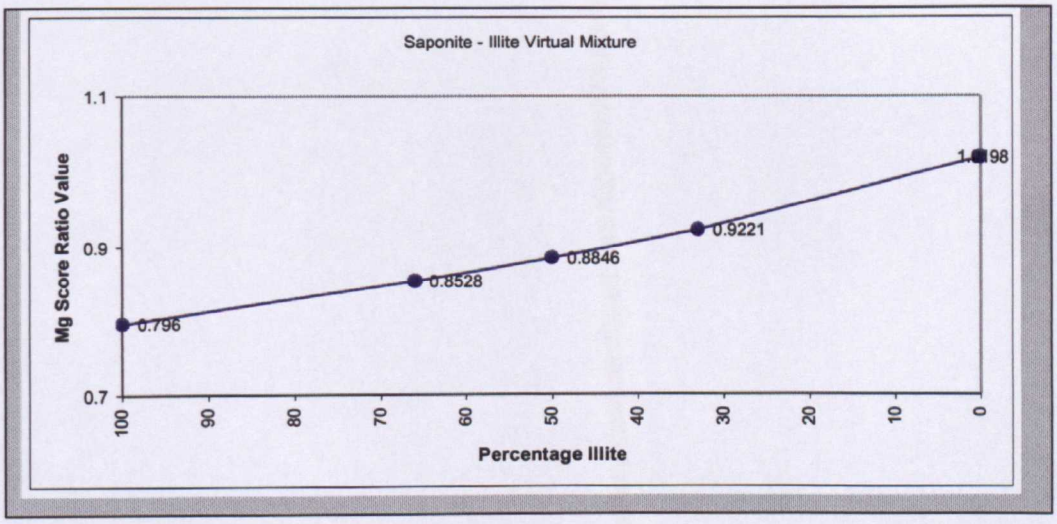

Figure 6.10: Plot of Mg Score ratio values calculated from the virtual saponite-illite spectra shown in Figure 6.9. This plot has a linear increase in ratio values as the proportion of saponite.

Virtual Library Mixtures

The stacked plot of the spectra created from the library saponite and illite end-members (Figure 6.11) shows the same pattern of progressive change in absorption features as the

proportion of saponite increases as seen in Figures 6.5 and 6.7. However, the 100 percent saponite shows the same abrupt change in form as noted for the saponite-kaolinite virtual library mixture (Figure 6.5).

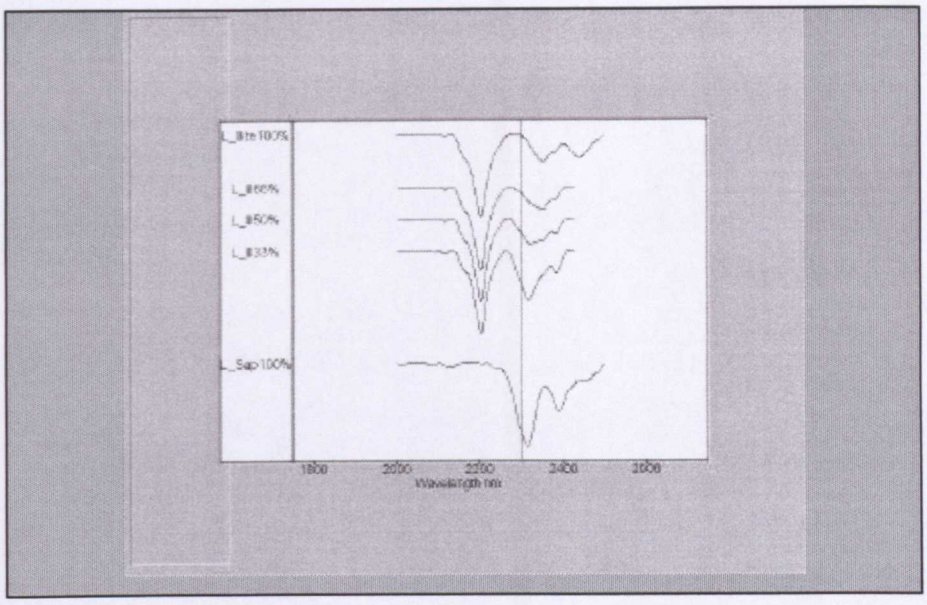

Figure 6.11: Stacked hull quotient spectra of virtual library mixtures of saponite and illite. Spectra are offset on the Y-axis by 5 percent for clarity. The Y-axis labels are the spectra file names and indicate the percentages of the end-member in each spectral sample. Vertical bar at 2312nm for reference.

In the Mg Score ratio plot (Figure 6.12) derived from these spectra the steepening in the gradient of the ratio values line beyond 66 percent saponite is pronounced. Below 66 percent saponite, however, the ratio values plot linearly, increasing towards higher saponite content.

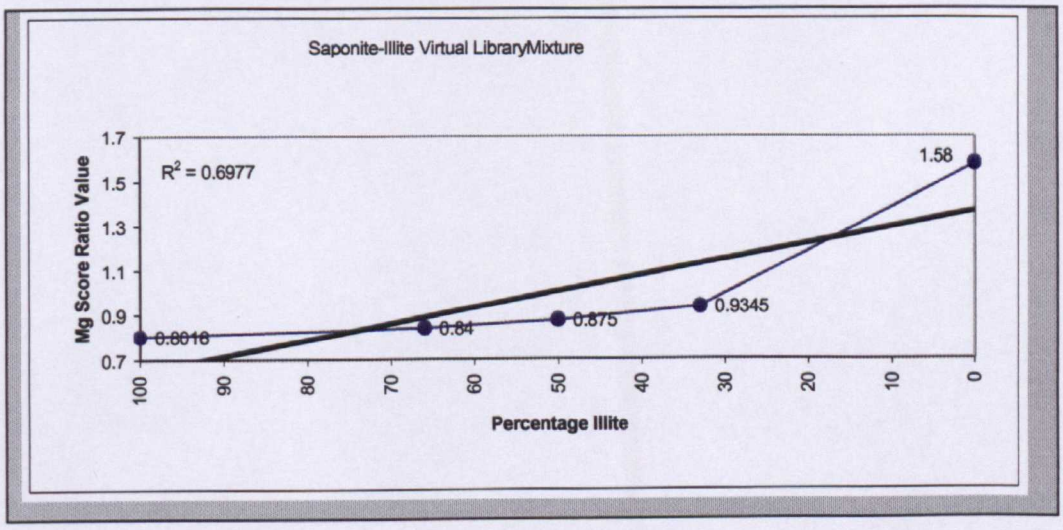

Figure 6.12: Plot of Mg Score ratio values calculated from saponite-illite spectra shown in Figure 6.11. The thick line is the second order regression line This plot has a linear increase in ratio values as the proportion of saponite increases until 66 percent then there is a distinct increase in gradient to 100 percent saponite.

Comments

Repeating the procedures discussed in the preceding saponite-kaolinite section also determines a value of 22 percent contamination of the saponite sample, used in these experiments, with Al-OH bearing clay.

6.4 SAPONITE-DOLOMITE

Physical Mixtures

For saponite and dolomite mixtures the major change in the spectra (ignoring the 2200nm feature which is due to the contamination of the saponite) is a change in the asymmetry and wavelength of the main absorption feature situated immediately beyond 2300mm. This absorption feature becomes more asymmetric and shifts towards longer wavelengths as the proportion of dolomite increases. These features are shown in the stacked profile plot of the saponite-dolomite physical mixture spectra (Figure 6.13). Change in the gradient of the shorter wavelength slope of this absorption feature quantifies this asymmetry, calculated by dividing the hull quotient reflectance values at 2300nm by the value at 2269nm.

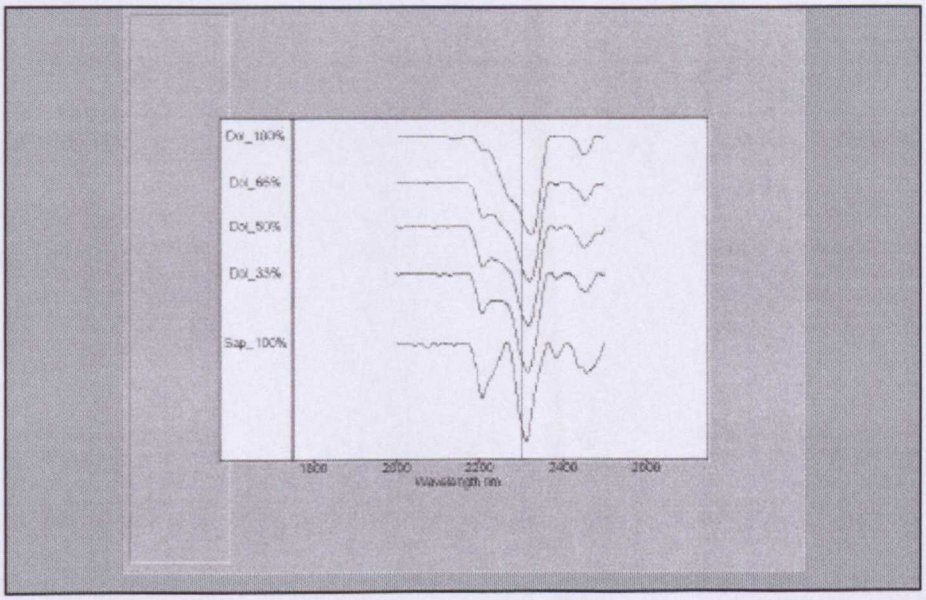

Figure 6.13: Stacked hull quotient spectra of physical mixtures of saponite and dolomite. The spectra are offset on the Y-axis by 5 percent for clarity. The Y-axis labels are the spectra file names and indicate the percentages of the end-member in each spectral sample. Note the change in asymmetry in the 2300nm absorption feature and the shift of its wavelength towards shorter wavelengths. A reference line at 2312nm has been added to emphasise this wavelength shift.

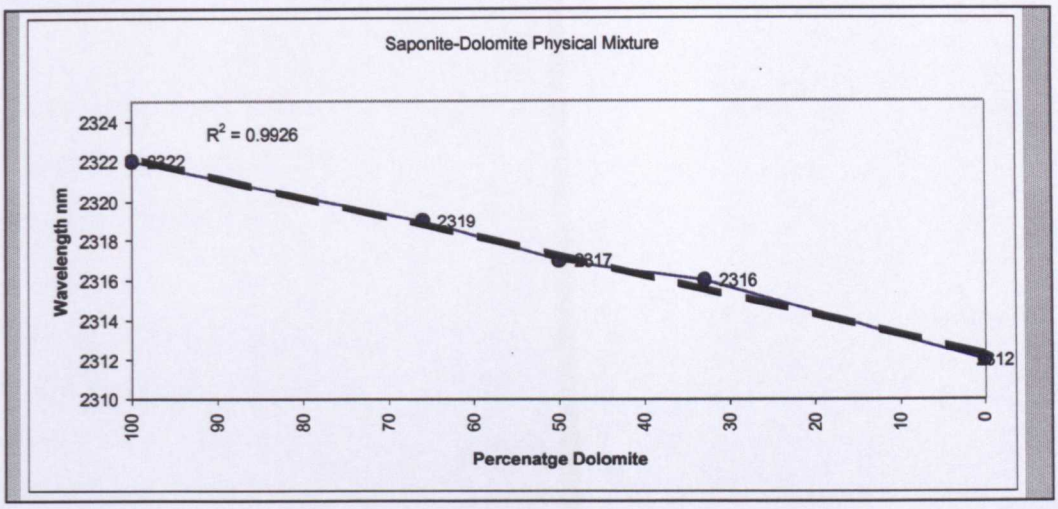

Figure 6.14: Plot of the saponite-dolomite physical mixture spectral wavelengths of the absorption features beyond 2300nm. There is a linear trend to shorter wavelengths as the percentage of saponite increases. Regression line dashed.

In Figure 6.14, a plot of the wavelengths of the absorption minima has a linear trend towards shorter values as the percentage of saponite increases.

Plotting the values for the ratio of the depth of the 2300nm and 2269nm values (Figure 6.15) shows a generally linear decrease in these values, indicating steepening of these spectral slopes (gradient) as the proportion of saponite increases.

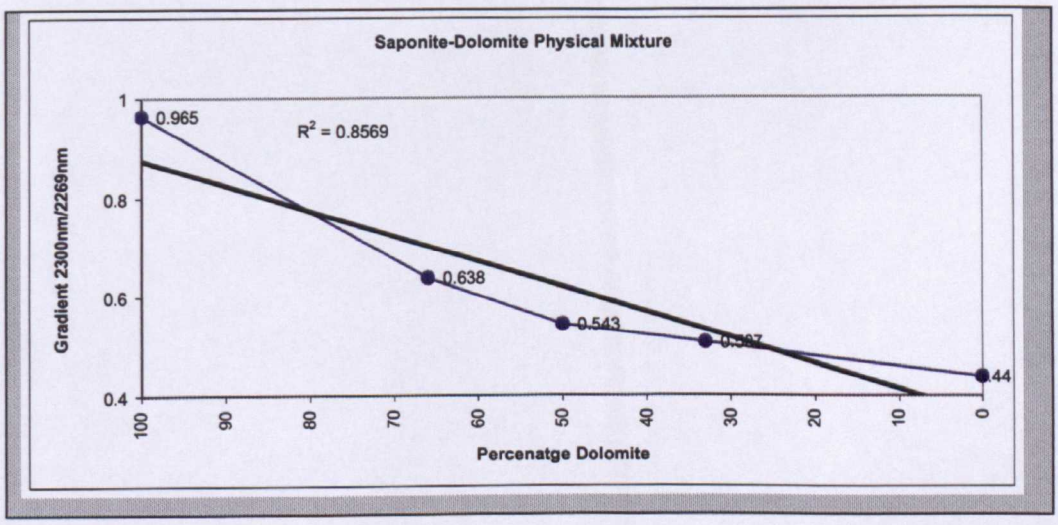

Figure 6.15: Plot for the saponite-dolomite physical mixture spectral gradient values obtained by dividing the hull quotient values at 2300nm and 2269nm. Regression line thicker .

Virtual Mixtures

The same pattern of spectral variation is observed in the stacked profile plot of the saponite-dolomite virtual spectral mixtures (Figure 6.16) that was observed in the physical mixture plot (Figure 6.11).

In this case plotting the change in wavelength values (Figure 6.15), shows a linear decrease in the wavelength minimum from 2322nm (100 percent dolomite) to 2312nm (100 percent saponite). Plotting the values for the slope of the absorption feature between 2269nm and 2300nm (Figure 6.16) also shows a linear decrease in these values, indicating a steeper slope as the proportion of saponite increases.

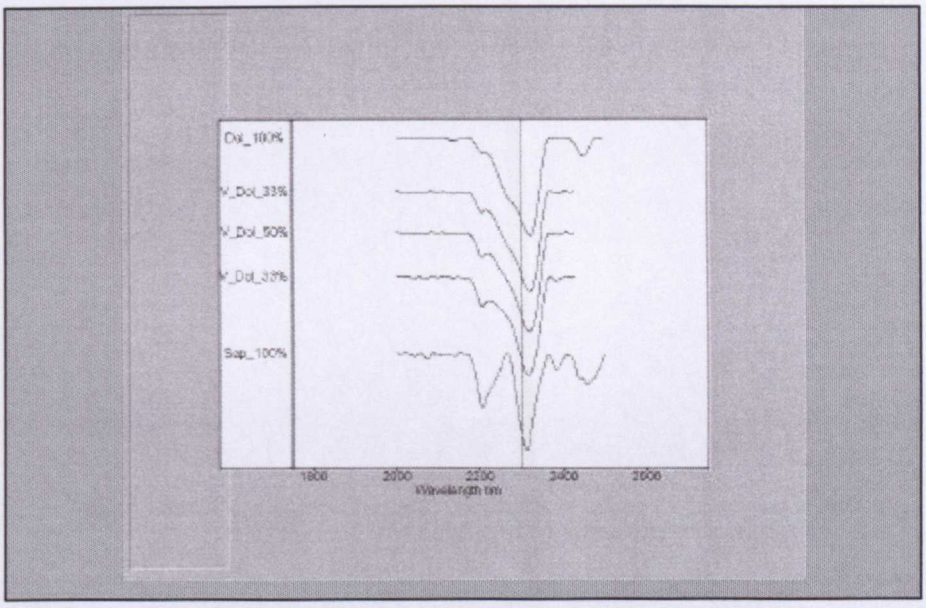

Figure 6.16: Stacked hull quotient profile of spectra for virtual mixtures of saponite and dolomite. Spectra are offset on the Y-axis by 5 percent for clarity. The Y-axis labels are the spectra file names and indicate the percentages of the end-member in each spectral sample. Note the change in asymmetry in the 2300nm-absorption feature and the shift of its wavelength towards shorter wavelengths. A reference line at 2312nm has been added to emphasise this wavelength shift.

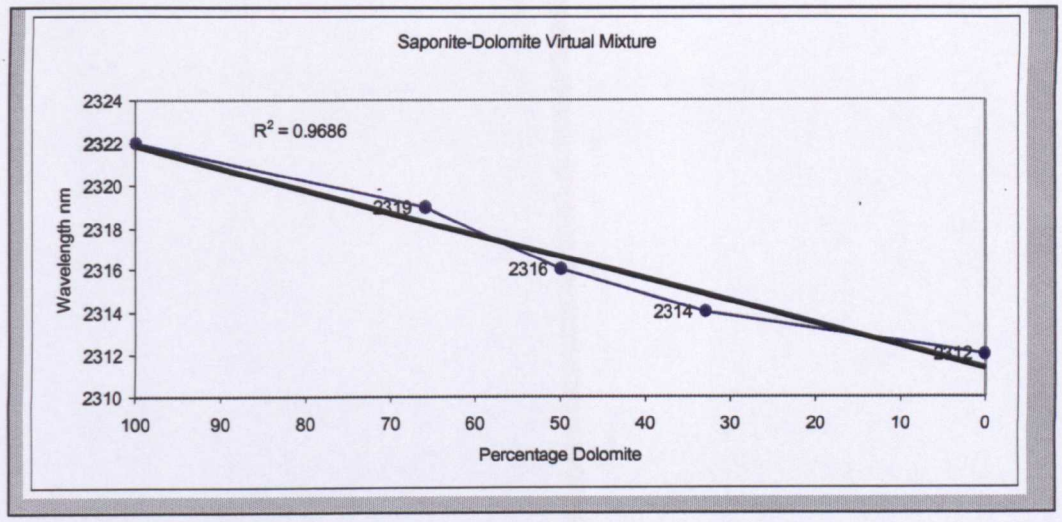

Figure 6.17: Plot of saponite-dolomite virtual mixed spectra for the wavelengths of the absorption features beyond 2300nm. Regression line darker. There is a trend to shorter wavelengths as the percentage of saponite increases.

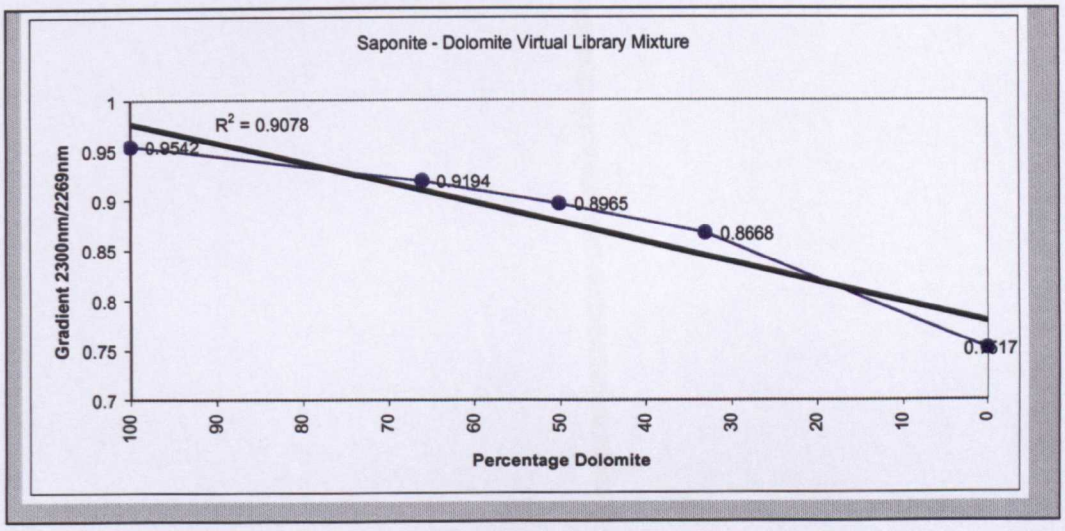

Figure 6.18: Plot oft the saponite-dolomite virtual mixture spectral gradient values obtained by dividing the hull quotient values at 2300nm and 2269nm. Regression line thicker.

Library Virtual Mixtures

In the stacked spectral plot shown in Figure 6.19 the absorption feature situated beyond 2300nm appears to be deeper than in the physical and virtual mixture plots (Figures 6.13 and 6.16). This is very distinct in the 100 percent saponite spectrum that also shows no absorption feature at 2200nm, though in this case this feature is developed in the dolomite containing mixtures. The stacked profile plot shows the trend towards shorter wavelengths as the saponite percentage increases (2322nm to 2312nm). The plot of the slope gradient values (Figure 6.20) between 2269mn and 2300nm shows a linear decrease as the proportion of saponite increases.

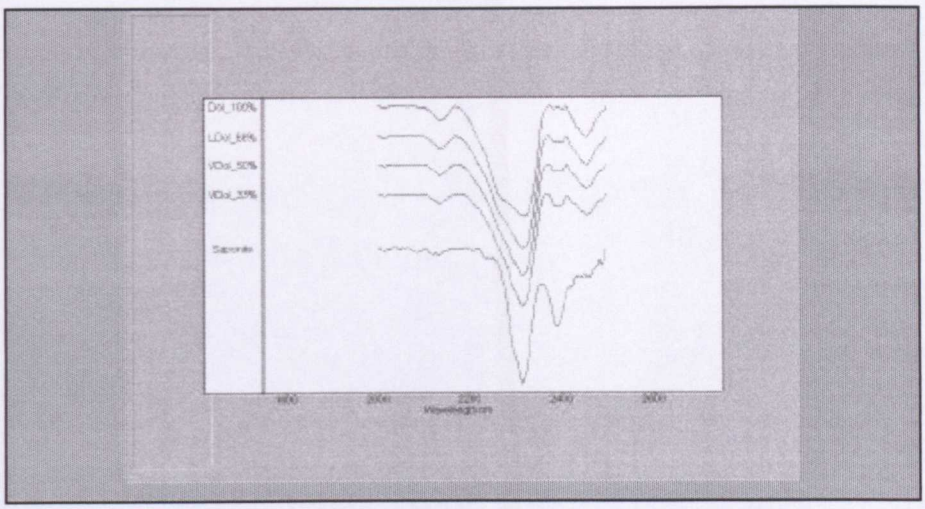

Figure 6.19: Stacked hull quotient of saponite and dolomite spectra for library virtual mixtures. Spectra are offset on the Y-axis by 5 percent for clarity. The Y-axis labels are the spectra file names and indicate the percentages of the end-member in each spectral sample. Note the change in asymmetry in the 2300nm-absorption feature and the shift of its wavelength towards shorter wavelengths

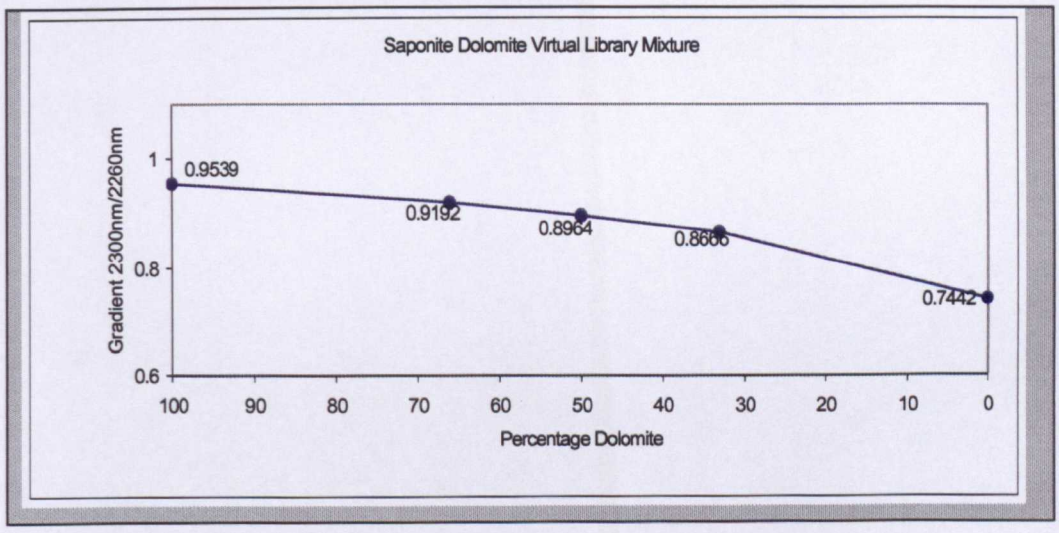

Figure 6.20: Plot of saponite-dolomite library virtual mixture spectra for the gradient values obtained by dividing the hull quotient values at 2300nm and 2269nm.

Comments

The linearity observed between changes in end-member proportions and variations in diagnostic absorption features suggests that in saponite and dolomite mixtures the proportions of these minerals can be determined from parameters obtained from their spectra. This linearity also indicates that it should be possible to discriminate and un-mix these spectrally similar minerals from hyperspectral scanner imagery even though the pure saponite and dolomite are superficially similar with their main absorption feature at >2300nm.

6.5 SAPONITE AND LIMESTONE

Physical Mixture

Figure 6.21 depicts the stacked spectra plot of the saponite-limestone physical mixture. It shows that both the saponite and limestone samples used for this study were contaminated with an Al-OH bearing mineral, indicated by the presence of a distinct absorption feature at 2200nm in all the spectra. Beyond 2300nm there are two distinct absorption features present in the spectra 2312nm for 100 percent saponite and 2342nm for 100 percent limestone. These features combine into one broad feature in the mixed spectra with the absorption minima shifting towards shorter wavelengths as the percentage of saponite increases.

A plot of the depth of the 2312nm was used in this case to determine the linearity of these spectral mixtures. Figure 6.22 is the plot of the 2312nm depth and it shows a linear trend of increasing depth as the proportion of saponite increases.

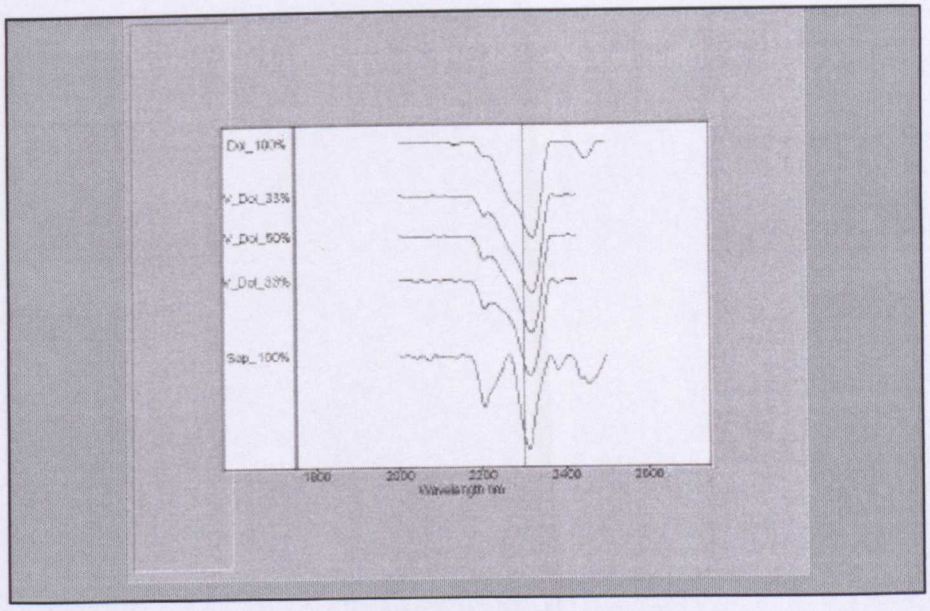

Figure 6.21: Stacked hull quotient spectra of saponite and limestone physical mixture. Spectra are offset on the Y-axis by 5 percent for clarity. The Y-axis labels are the spectra file names and indicate the percentages of the end-member in each spectral sample. Note the merging of absorption feature beyond 2300nm in the mixed spectra and the shift this feature towards shorter wavelengths as the percentage of saponite increases. Vertical bar at 2312nm for reference.

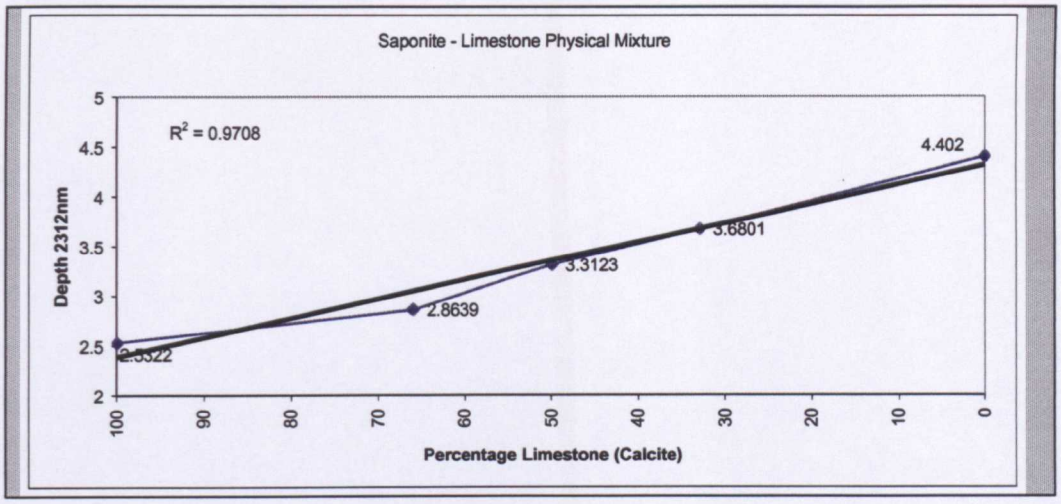

Figure 6.22: Plot of saponite-limestone physical mixture spectra for the depth of the 2312nm absorption feature. Depth determined from hull quotient transformed spectra in Figure 6.21. The trend is linear with depth increasing as the percentage of saponite increases. Regression line darker.

Virtual Mixture

Figure 6.23 is the stacked profile of the virtual saponite-limestone mixture and it is almost identical to the stacked profile for the physical mixture (Figure 6.21).

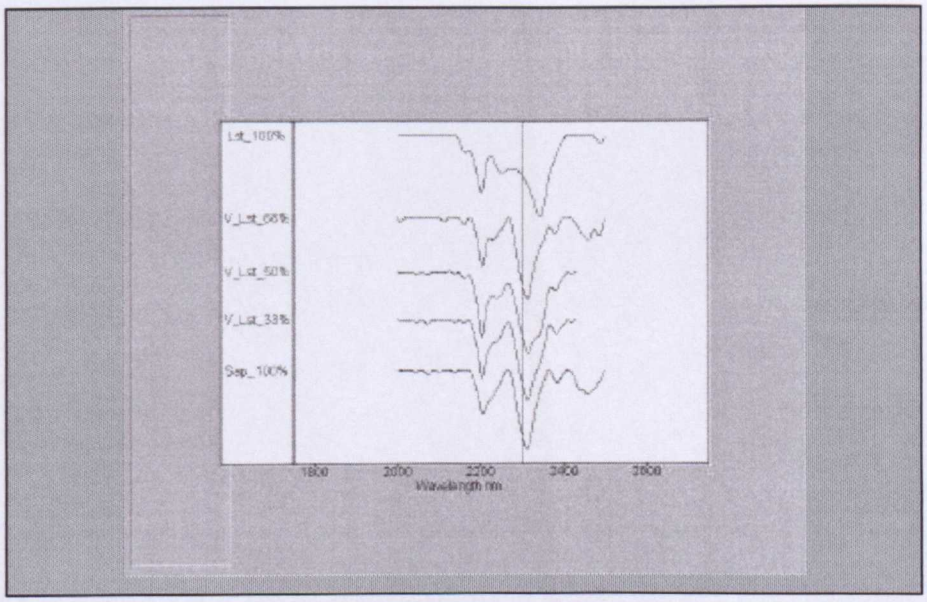

Figure 6.23: Stacked hull quotient spectra for the virtual saponite and limestone mixtures. The spectra are offset on the Y-axis by 5 percent for clarity. The Y-axis labels are the spectra file names and indicate the percentages of the end-member in each spectral sample. Note the merging of absorption feature beyond 2300nm in the mixed spectra and the shift of its wavelength minimum towards shorter wavelengths, as the percentage of saponite increases. Vertical bar at 2312nm.

6.6 SAPONITE AND DRY VEGETATION

Physical Mixtures

In the dry vegetation (crushed pine bark) and saponite mixture (Figure 6.24), the addition of 33 percent saponite dramatically changes the spectral response. The dry vegetation spectra has a marked reduction in the 2130nm, 2260nm and 2360nm features when 33 percent saponite is added. There is no corresponding effect on the Mg-OH 2312nm features of saponite when dry vegetation is mixed with it, though the contaminated 2200nm feature reduces rapidly as the proportion of dry vegetation increases.

Plotting the ratio of the hull quotient depth values for the 2139nm and 2312nm absorption minimum produces a plot (Figure 6.25) that shows a sharp drop in the ratio value from 100 percent dry vegetation to the 33 percent saponite mixture. This reflects the spectral changes that can be observed in Figure 6.24. From 33 percent to 100 percent saponite the decrease in the ratio values is linear.

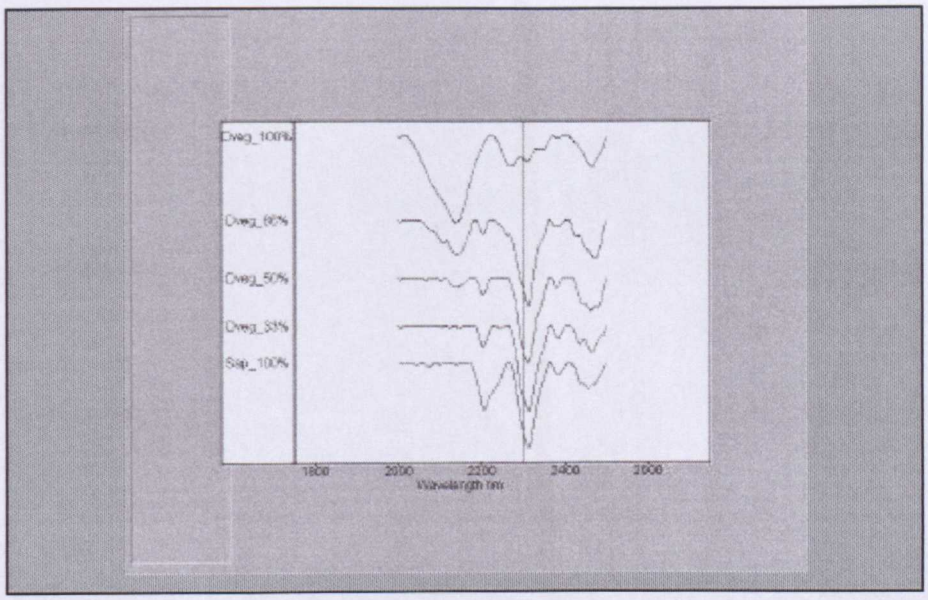

Figure 6.24: Stacked hull quotient spectra for physical mixtures of saponite and dry vegetation. Spectra are offset on the Y-axis by 5 percent for clarity. The Y-axis labels are the spectra file names and indicate the percentages of the end-member in each spectral sample. There is a marked decrease in the depth of the 2139nm feature between the 100 percent and 66 percent dry vegetation spectra. Vertical bar at 2312nm for reference.

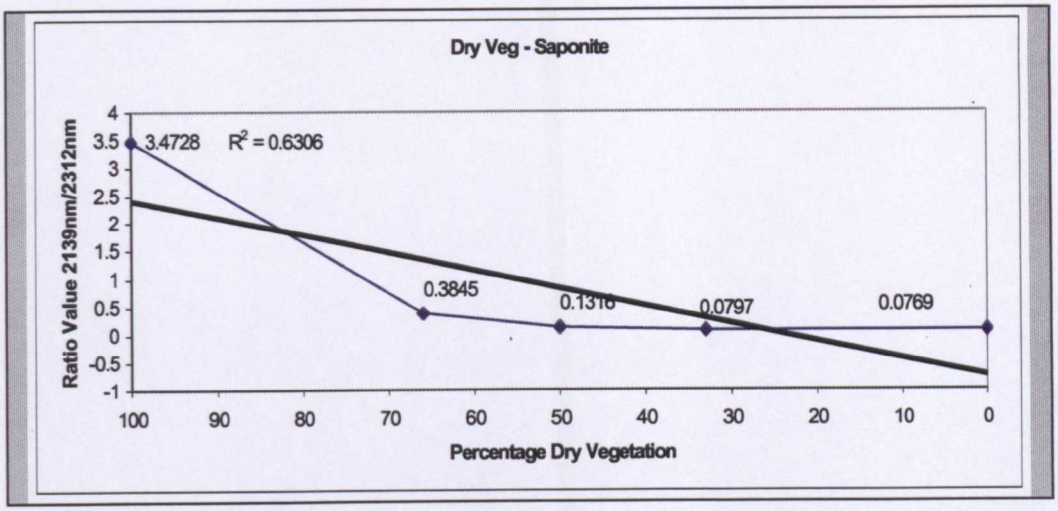

Figure 6.25: Plot of saponite-dry vegetation physical mixtures ratio values obtained by dividing depths of 2139nm by 2312nm absorption features from hull quotient transformed spectra. There is a marked drop in these values between 100 percent and 66 percent dry vegetation content in the mixture. Regression line darker.

Virtual Mixtures

When the stacked profile of spectra obtained from the virtual spectral mixing is examined (Figure 6.26) it shows a more gradual decrease in the depth of 2139nm feature, as the proportion of saponite in the mixture increases, compared to the physical mixture (Figure 6.24).

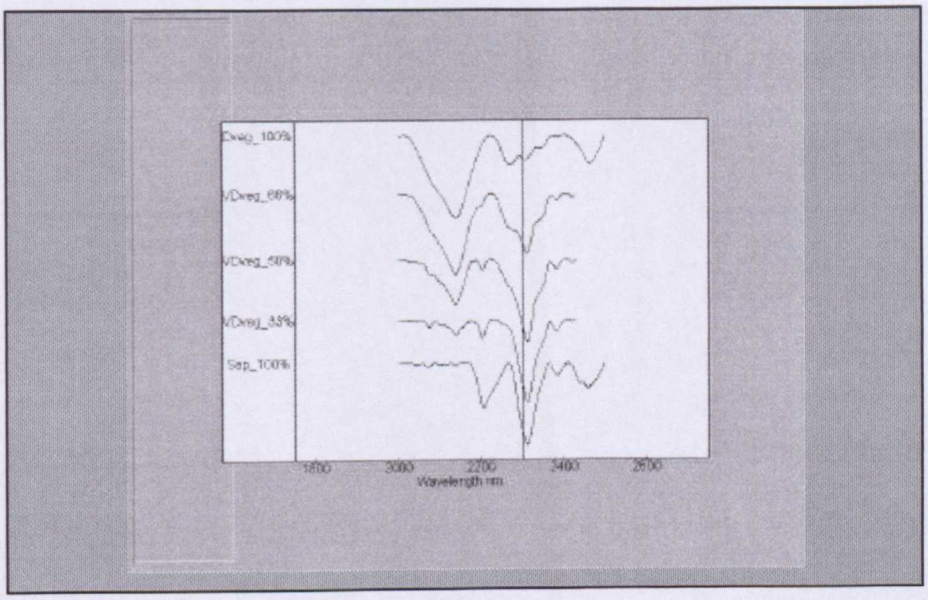

Figure 6.26: Stacked hull quotient spectra of virtual mixtures of saponite and dry vegetation. Spectra are offset on the Y-axis by 5 percent for clarity. The Y-axis labels are the spectra file names and indicate the percentages of the end-member in each spectral sample. Vertical bar at 2312nm for reference.

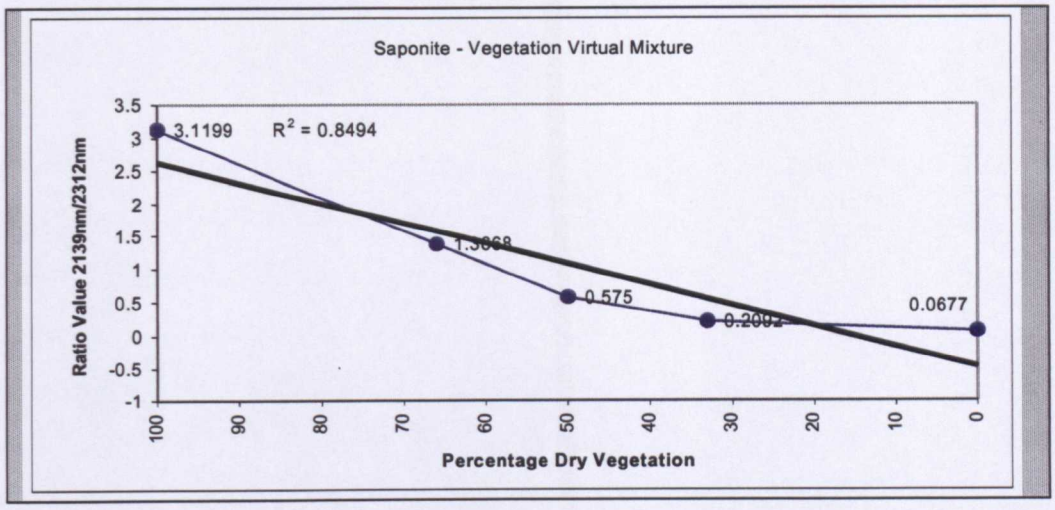

Figure 6.27: Plot of saponite-dry vegetation virtual mixtures ratio values obtained by dividing depths of 2139nm by 2312nm absorption features from hull quotient transformed spectra. The values plot as a convex curve that shows a progressive decrease in the ratio values as the proportion of saponite increases. Regression line darker.

Though the plot of the ratio values derived from these virtual spectral mixtures are convex towards higher proportions of dry vegetation (Figure 6.27) the plot is more linear than for the physical mixture.

Comment

Differences between the physical and virtual results can be explained by the difficulty of achieving uniformity in the physical mixtures coupled with the limited aperture size of the PIMA. If the physical mixture produced is inhomogeneous then the small PIMA aperture may mean spectra measured do not represent the mixture. This problem does not occur with virtual mixtures. This suggests that averaging several spectra from a sample and/or moving the PIMA slightly between readings, may produce a more reliable series of mixed spectra. Operating in field conditions it is quite likely that variations in mineral grain–aggregate size could effect the distribution of minerals in the PIMA field of view analogous to incomplete mixing. This would result in Mg Score values that would not be accurate predictors of mineral proportions. Another solution would be to use a spectrometer with a larger field of view than the PIMA. As spectra derived from scanners are integrated over tens of metres this should not be a problem with their spectra.

6.7 VIRTUAL MIXTURES TO SIMULATE ULTRAMAFIC ROCK SURFACES AND SOIL SPECTRAL EXPRESSION

It would not be practical to produce physical mineral mixtures from all possible combinations of minerals and materials that are likely to be encountered under natural conditions. Furthermore, obtaining pure samples of materials to conduct such experiments is problematic, as the contaminated saponite spectra discussed above indicates Virtual mixtures produced by adding library spectra to simulate spectra of physical mixtures is a solution to this problem. The robustness of this technique has been demonstrated in the previous sections of this chapter. The virtual spectral mixtures produce almost identical spectra to those obtained from measuring physical mixtures. Therefore, the virtual spectral mixtures can be regarded as reliable simulations of the spectra obtained from natural mineral (and other material) mixtures. Under natural conditions the mixtures may consist of more than two end-member minerals that can result in non-linearity as the proportions will vary in more complex ways (Yang and Huntington, 1997). As mentioned previously, at the surface the minerals in ultramafic rocks will weather to saponite and then progressively into kaolinite. As soil forms, other minerals will be introduced of which quartz, in the form of aeolian sand grains, is likely to predominate in arid regions.

Saponite-Quartz Sand Mixtures

In nature quartz sand often contains traces of muscovite the effects of which will be similar to the spectra produced from a mixture of saponite and illite. When the sand is not contaminated its effect on mixing with saponite is to reduce the intensity of the near 2300nm absorption feature by 1.5 percent and (Figure 6.28). In opaline quartz, which may be produced by intense weathering of ultramafic rocks (Chapter 4), there is a broad but shallow absorption feature centred at 2250nm. A mixture of opaline quartz and saponite would give spectra with additional absorption features not seen in a mixed the spectrum of saponite and normal quartz.

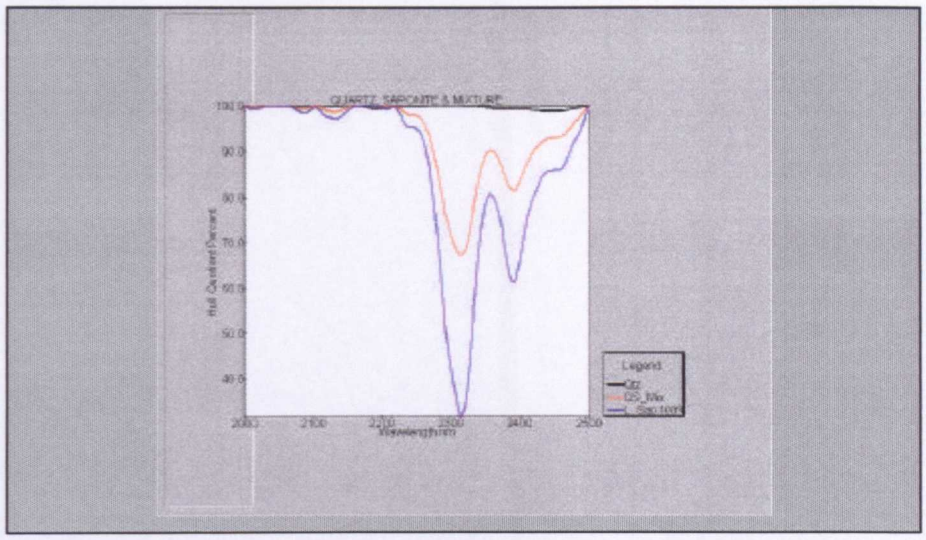

Figure 6.28: Spectra of pure quartz (black), saponite (blue) and a virtual 50 percent-50 percent mixture (red) of both minerals. Note how the quartz has reduced the intensity but not the characteristic form of the saponite spectra. Hull quotient transform has been applied to spectra.

Saponite-Kaolinite-Quartz Mixtures (soil derived from ultramafic rocks)

In Figure 6.29 the spectra of saponite and kaolinite and a virtual library mixture spectrum of these minerals (40 percent each) with 10 percent quartz is shown. In this case the Al-OH absorption at 2200nm is deeper than the 2312nm feature. When the proportion of saponite is increased to 60 percent and kaolinite and quartz set at 20 percent then the 2312nm is the deepest (Figure 6.30). These examples illustrate how spectra that may occur in soils derived from ultramafic rocks, will vary. However, even when quartz and kaolinite are mixed with the Mg-OH minerals the relative depths of the Mg-OH (2312nm) and Al-OH (2200nm) features will still permit recognition of the presence of the Mg-OH minerals and by inference the occurrence of ultramafic rocks.

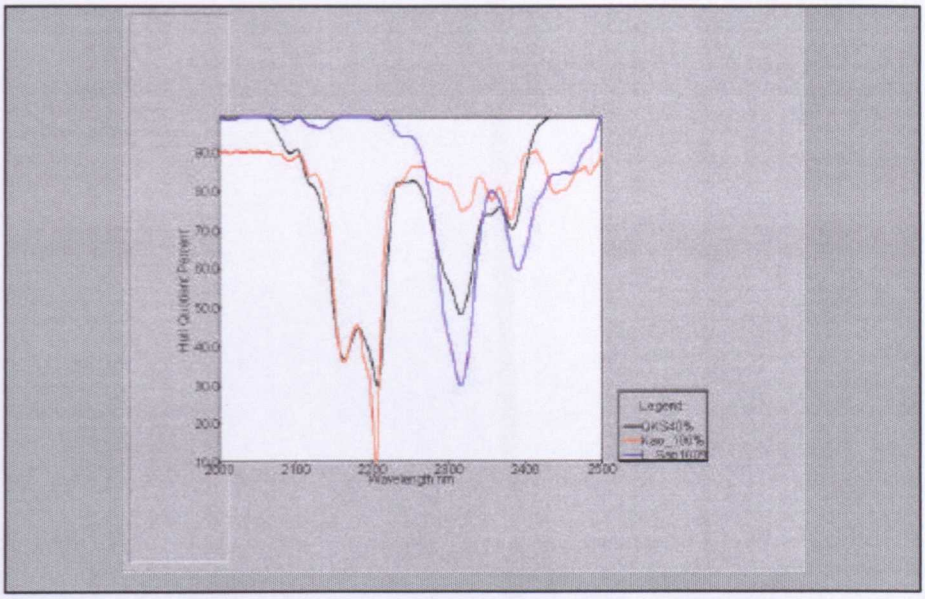

Figure 6.29: Hull quotient transformed spectra of saponite (blue), kaolinite (red) and a virtual mixture of pure quartz, saponite and kaolinite (black) in the ratio 10 percent: 40 percent: 40 percent. In this example the 2200nm Al-OH feature is the deepest in the mixed spectrum.

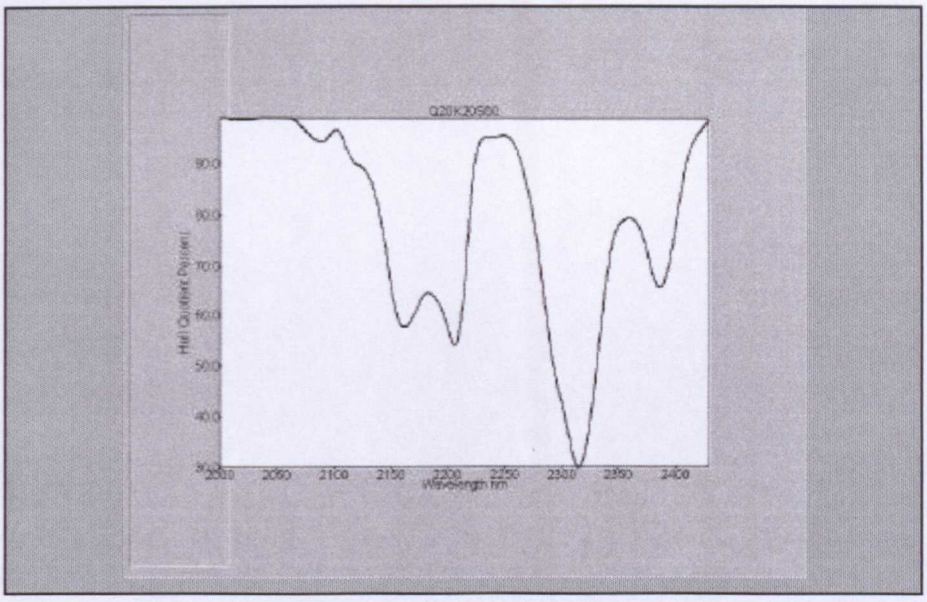

Figure 6.30: Hull quotient transformed virtual mixed spectrum of saponite, kaolinite and quartz, in the ratio 60 percent: 20 percent: 20 percent. In this example the 2312nm Mg-OH feature is the deepest.

6.8 OTHER MINERAL MIXTURES

The virtual 50 percent:50 percent mixed mineral spectrum for saponite-chlorite is compared to chlorite and saponite spectra in Figure 6.31. The mixed spectrum shows as a modified chlorite spectra with a shallower secondary absorption feature at 2250nm and a shift in the main absorption to a shorter wavelength. The mixed spectrum is sufficiently different from the chlorite end-member spectra to indicate that it would be possible to un-mix this spectrum and identify the saponite component when it is in an image pixel. This

indicates it should be possible to identify saponite, and other ultramafic derived Mg-OH minerals, in areas of greenstone, basalt and rocks that are rich in chlorite. Similar virtual mixtures may be constructed to determine which other minerals may be un-mixed from saponite.

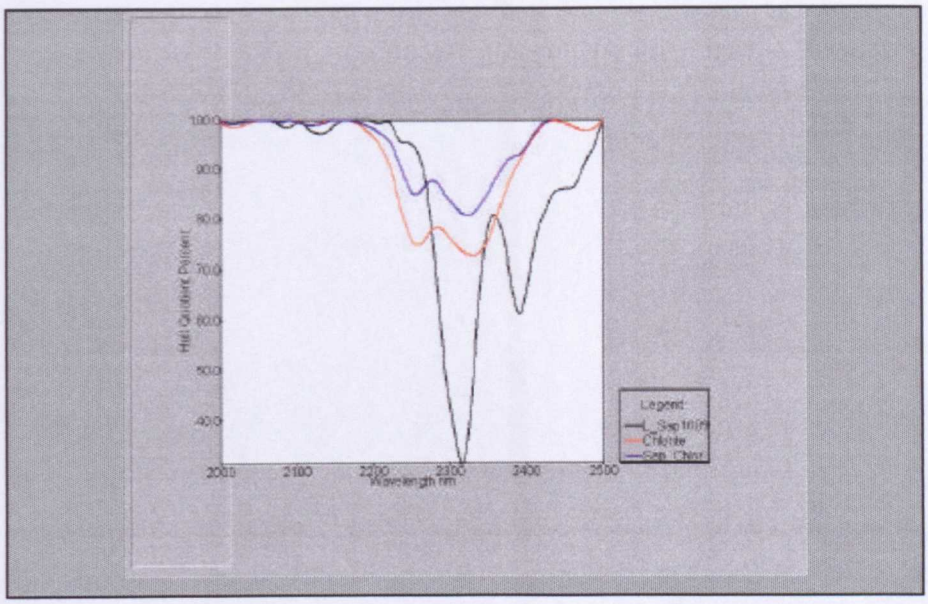

Figure 6.31: Hull quotient transformed virtual 50 percent : 50 percent mixed spectrum of saponite with chlorite (blue) compared to chlorite (red) and saponite (black). Note the differences between the end-member spectra: the saponite lacks the deep feature at 2250nm seen in the chlorite spectra. In the mixture the 2250nm feature becomes smaller and the minimum of the major absorption feature shifts from 2330nm to 2320nm, closer to the 2312nm saponite minimum.

6.9 CONCLUSIONS

This investigation shows that the spectra obtained from the mixing of minerals associated with ultramafic rocks and their weathering products have spectral features that vary in a near linear fashion with the proportions of the end-members present. This linearity has been established in both physical and virtual mixtures, as is reported to be the case in Ramsey and Christensen (1998) and van der Meer (1994). In physical mixtures the degree of linearity may be reduced. This is attributed to a lack of homogeneity in the mixture and is compounded by the small aperture size of the PIMA. This may be rectified by recording several spectra from a mixture and averaging them or using a spectrometer with a wider field of view. However, the fact that linearity has been established means that look-up tables can be constructed by making virtual spectral mixtures from library spectra and plotting the values extracted from the spectra against the proportion of the end-members. This look-up table can then be used to determine the relative proportions of the end-member minerals that have contributed to target spectra. This has applications in logging

variations in mineral assemblages from bore hole samples and surface mapping of mineralogy from grid samples. In this study, the percentage of an Al-OH bearing mineral that contaminated the saponite used as an end-member was determined by this method.

Plotting parameters obtained from the spectra against mineral proportions has indicated linearity in the changes in spectra that result. This linearity indicates that the identity of the end-member minerals can be obtained by un-mixing spectra into their component end-members. These end-member spectra can then be identified. This has obvious implications for the processing of imaged spectral data. It is evident that end-member selection and linear un-mixing can provide a reliable guide to a pixel's constituent minerals and their relative proportions.

Dry vegetation often constitutes a reasonably large proportion of an image pixel area in arid regions. It has a distinct 2300nm absorption feature that can be confused with that obtained from Mg-OH minerals in image data. The fact that the presence of saponite does modify dry vegetation spectra is significant. These mixing experiments reinforce the results obtained from processing image data (see Chapter 8), which suggests dry vegetation can be un-mixed from ultramafic rock signatures in arid areas.

Mixtures of saponite with kaolinite (and quartz) in varying proportions, produce spectra in which the presence of saponite is apparent even at relatively low percentages. Therefore, residual soils weathered from ultramafic rocks should produce a spectral signature that is diagnostic of ultramafic rocks in both field and image spectral data.

CHAPTER 7

7 SPECTRAL CHARACTERISTICS OF REMOTE SENSING SYSTEMS COMPARED TO THE ULTRAMAFIC MODEL AND SIGNAL-TO-NOISE EFFECTS

7.1 INTRODUCTION

There are now more than twelve air and spaceborne multispectral instruments that provide, or will be providing, image data. The ability of these systems to detect the Mg-OH spectral signature that characterises ultramafic rocks with sufficient precision to enable discrimination from background minerals depends on various system specifications. These specifications include the number of bands, their wavelength centre positions and the signal-to-noise ratio (SNR) of the systems. Data from systems that have been classified in this study as multispectral scanners and imaging spectrometers have a limited number of channels and these may or may not be able to make this discrimination. However, systems classified as hyperspectral scanners should have sufficient bands to adequately sample the reflectance spectra of ultramafic rocks so that this discrimination can be achieved. Data from these systems may enable determination of subtle variations in mineralogy and should be able to isolate the Mg-OH spectral signature of minerals, such as saponite, associated with weathered ultramafic rocks in spectrally complex backgrounds. A literature and Internet search has been conducted to determine the characteristics of the various imaging systems that are, have been or will be gathering data now and in the future.

Table 7.1 documents the characteristics of past and current imaging systems that are relevant to the objectives of this thesis. The systems are split into multispectral scanners, imaging spectrometers and hyperspectral scanners. The actual band centres for each of the systems investigated are listed in Appendix 2.

SYSTEM	TYPE	PLAT-FORM	TOTAL NUMBER BANDS	BANDS VNIR 400nm-1200nm	BANDS SWIR1 1200nm-2000nm	BANDS SWIR2 2000nm-2500nm	BANDS TIR 8000nm-12000nm	SNR SWIR2	PIXEL SIZE
SPOT	MSS	SAT	3	3				N/A	20m
LANDSAT MSS	MSS	SAT	4	4				N/A	80m
LANDSAT TM	MSS	SAT	7	4	1	1	1	N/A	30m
DAEDALUS 1268	MSS	HAA	11	8	1	1	1	N/A	15m
JERS OPS OPS	MSS	SAT	7	3	1	3		N/A	24m
ASTER	MSS/IS	SAT	15	3	1	6	5	N/A	15m 30m90m
GEOSCAN MkII	IS	AIR	24+	10	0	8	6	50:1-100:1	7m-15m
GER IS	HS	AIR	63	24	7	32		70:1	5m-20m
GER DIAS	HS	AIR	79	32	8	32	7	B100:1	5m-20m
DAEDALUS MIVIS	HS	HAA	102	20	8	64	10	B100:1	5m
AVIRIS	HS	HAA	224	74	74	74		>400:1	20m
HyMap	HS	AIR	64-128	32	32 optional	32	32 optional	>800:1	5-10m
HyDice	HS	HAA	206	?	?	?		B75:1	3.5m
LEWIS HIS*	HS	SAT	384	128	128	128		N/A	TBD
ARIES	HS	SAT	105	32	41	42		+/-200:1	30m

Table 7.1: System specifications of past and current spectral scanners. For classification of scanner types see Chapter 3. [Abbreviations: MSS-Multispectral Scanner, SAT-Satellite, IS-Imaging Spectrometer, AIR-Airborne, HS-Hyperspectral Scanner, HAA-High Altitude Aircraft] *Failed after launch in 1997, *N/A unable to ascertain reliable information. + Selectable from 32*

7.2 SIMULATED SYSTEM SPECTRA

As discussed in Chapter 5 the spectrum of a mixture of serpentine and saponite is typical of what is obtained from weathered ultramafic rocks. Many other rocks weather to illite and kaolinite and a mixture of their spectra can be considered as typical of the background that is non-ultramafic, in many geological environments. Soils derived from ultramafic rocks typically consist of a mixture of both Mg-OH and Al-OH minerals. Therefore, I have produced fifty-fifty mixtures of saponite and kaolinite spectra to represent soils from ultramafic rocks, saponite and serpentine to represent ultramafic outcrop and kaolinite and illite to represent background soils and lithologies. I have sampled these three spectra to the spectral bands of the main classes of scanners, for the SWIR2 wavelength range, listed in Table 7.1 and the resultant spectra are presented in Figure 7.2 to 7.9. These spectra sampled to model scanner spectra do not show the effects of noise on the data, which is discussed later in this chapter. They have also been hull quotient transformed for clarity but this removes any albedo variation in the spectra.

Figure 7.1 is a plot of the modelled spectra (hull quotient applied) at full PIMA resolution and illustrates the significant spectral differences that occur between these mineral

mixtures. This includes the absence of a 2200nm feature in the serpentine-saponite spectrum (red), which is present in both of the other spectra. However, the kaolinite-illite spectrum (green) does not have a feature at 2310nm but does show absorption at 2350nm. The saponite and kaolinite (blue) mixed spectrum shows both the 2310nm and 2200nm features but none at 2350nm and the 2200nm feature is shallower.

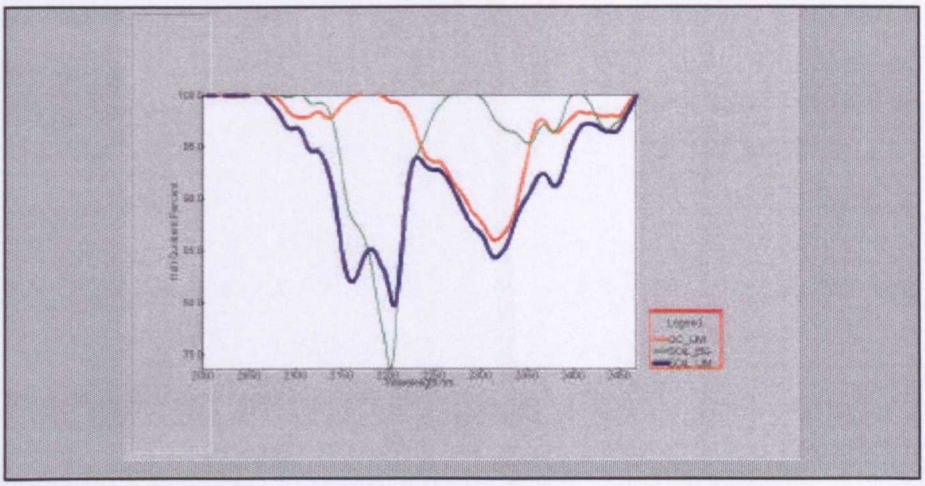

Figure 7.1: Virtual hull quotient spectra that model the ultramafic outcrops (red), background soils and lithologies (green) and soil derived from ultramafic rocks (blue).

Multispectral Scanners

Apart from the JERS OPS scanner members of the multispectral scanner class either have no bands (SPOT) or one band in the SWIR2. Therefore, only the JERS OPS was incorporated into this study. Figure 7.2 shows that it may be possible to discriminate between the exposed ultramafic and background spectra but that the Mg-OH and Al-OH mixed spectrum would be confused with the background spectrum.

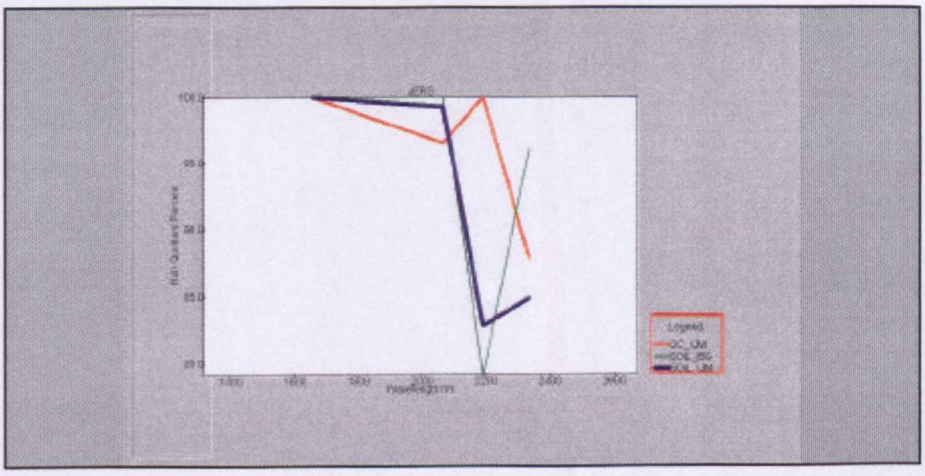

Figure 7.2: JERS OPS sampled SWIR2 hull quotient spectra, colours as per Figure 7.1. Ultramafic and background soils are similar, with 2200nm feature. Exposed ultramafic does have indications of a 2300nm feature. Due to a software bug this spectra was compressed in X axis to force the display of full bandwidth.

Imaging Spectrometers

Figure 7.3 shows that data from the ASTER scanner, which is a borderline imaging spectrometer with six SWIR2 bands, will have a much better chance of detecting the spectral differences between Mg-OH and Al-OH minerals than JERS OPS. It is apparent that both the 2200nm and 2300nm features are resolved. Comparing ASTERs spectra with those of the GEOSCAN MKII (Figure 7.4) shows similarity in the spectral region beyond 2000nm. In Chapter 9 it is demonstrated that GEOSCAN MKII data can be used to detect ultramafic rocks under favourable conditions indicating that ASTER should have similar capabilities. However, in Chapter 11 it is demonstrated that a low signal-to-noise ratio restricts the effectiveness of the GEOSCAN MKII in this respect and this would no doubt apply to data from ASTER.

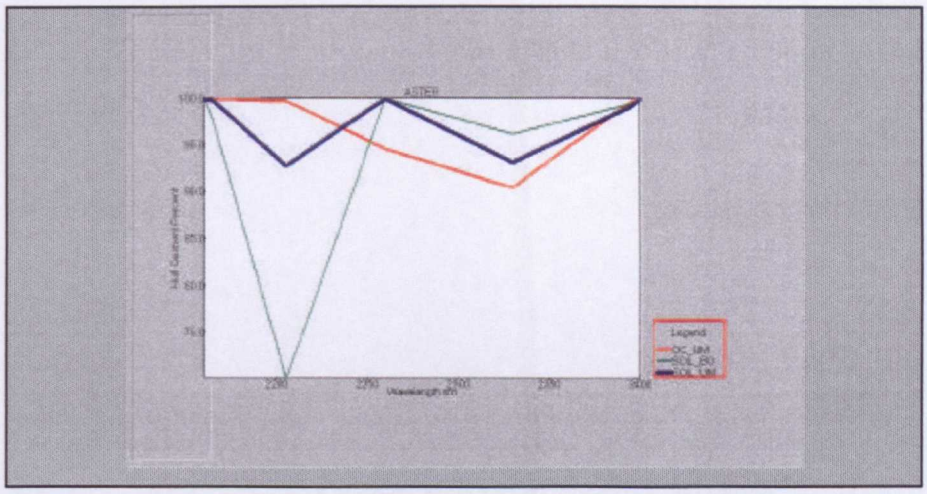

Figure 7.3: ASTER sampled hull quotient SWIR2 spectra, colours as per Figure 7.1. Exposed ultramafic and background soils are similar, with 2200nm feature though 2300nm feature is deeper in soil spectra. Exposed ultramafic rock spectrum has stronger 2300nm feature.

The GEOSCAN MkII imaging spectrometer data shown in Figure 7.4 suggests that with eight bands in the SWIR2 discrimination between these three spectral types will be possible.

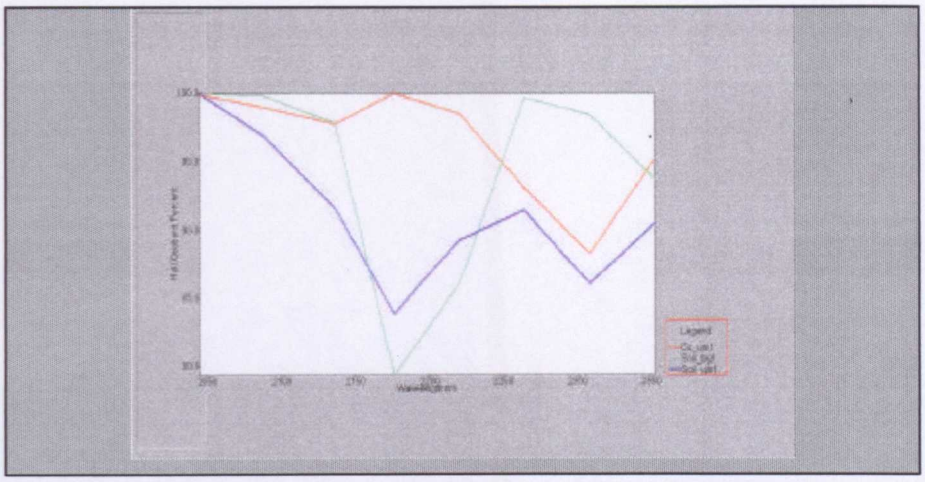

Figure 7.4: GEOSCAN MkII sampled hull quotient SWIR2 spectra, colours as per Figure 7.1. Ultramafic and background soils are similar, with 2200nm feature. However, the modelled ultramafic soil also has a pronounced 2300nm feature, as does exposed ultramafic rock spectrum, not apparent in the background soil spectra.

Hyperspectral Scanners

Figures 7.5 to 7.9 show that the GER IS, GER DIAS, DAEDALUS MIVIS, ARIES and HyMap sampled spectra do not differ significantly from the PIMA spectra, in the SWIR2 (Figure 7.1). This would indicate that any system having more than 32 bands in the SWIR2 should be able to achieve the required spectral discrimination of ultramafic rocks from felsic and possibly other background lithologies, provided the signal-to-noise ratio is sufficiently high.

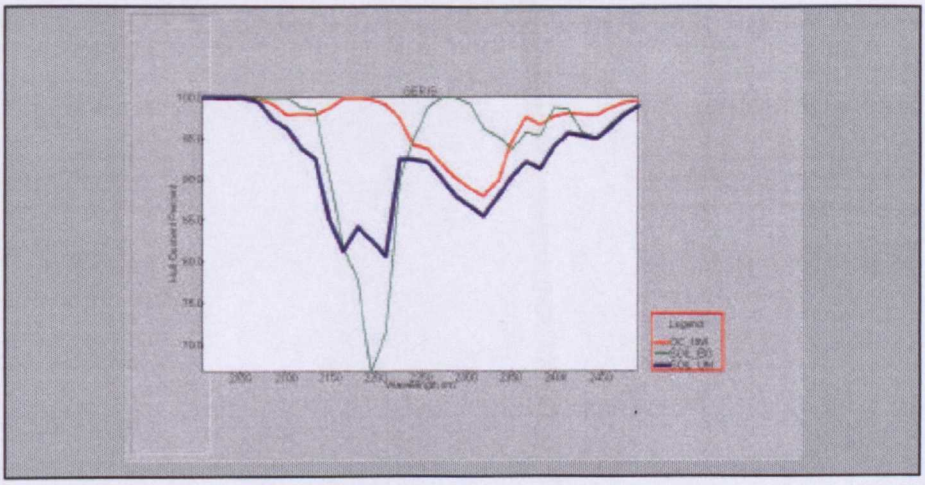

Figure 7.5: GER IS hull quotient sampled spectra SWIR1 and SWIR2 regions, colours as per Figure 7.1.

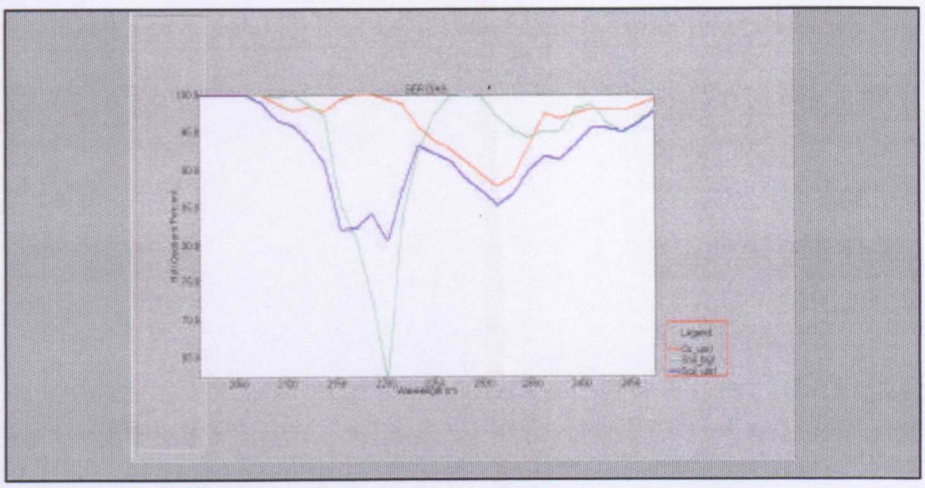

Figure 7.6: GER DIAS hull quotient sampled spectra SWIR1 and SWIR2 regions, colours as per Figure 7.1.

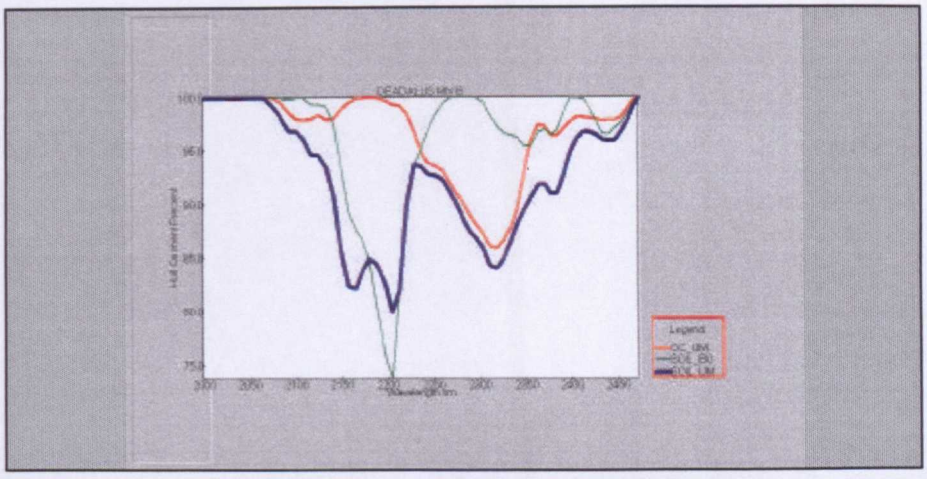

Figure 7.7: DAEDALUS MIVIS hull quotient sampled spectra SWIR1 and SWIR2 regions, colours as per Figure 7.1.

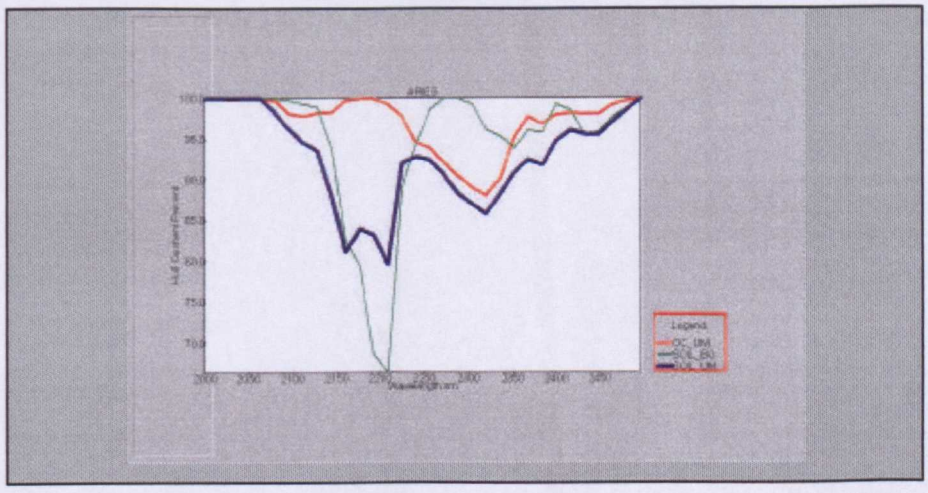

Figure 7.8: ARIES hull quotient sampled spectra SWIR1 and SWIR2 regions, colours as per Figure 7.1.

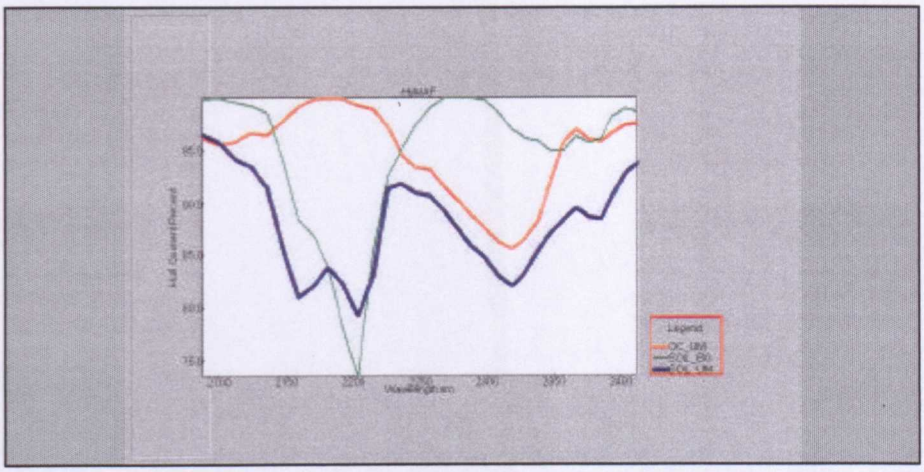

Figure 7.9: HyMap hull quotient sampled spectra SWIR2 region only, colours as per Figure 7.1.

7.3 SIGNAL-TO-NOISE RATIO

The signal-to-noise ratios listed for the scanners in Table 7.1 have been determined from manufacturers specifications and personal communications from various sources. It is evident that this information is not always available and not entirely reliable. Manufacturer's claimed values are often disputed by users of the data. This aspect of system specifications is often poorly defined and confusing. Most manufacturers quote their signal-to-noise ratio as the Spectral Noise Equivalent Radiance Differential (NEΔR), which permits comparison between systems in a technical sense. This has been defined by Barker and Gunther (1983) in Mather (1991) "the signal-to-noise ratio is defined for ... a constant input radiance... as the ratio of the output values (in radiance units) averaged over at least 100 samples to the root mean square (RMS) value of the noise equivalent radiance, which is defined as the RMS of the deviations of the output samples from the average value". To the geological image interpreter, this is not a very meaningful definition nor are figures so quoted very helpful in assessing a system's performance. The system manufacturer usually determines the signal-to-noise ratio of the system with bench tests using a 50 percent target and an artificial light source (Cocks, 1996 pers. comm.). The value an interpreter requires is noise level (N) as a ratio of signal level (S), that is, the S/N. This S/N (the signal-to-noise ratio) value can then be converted into a percentage as shown in Table 7.2.

SNR	NOISE PERCENTAGE
10:1	10
50:1	2
100:1	1
150:1	0.66
200:1	0.5
300:1	0.33
400:1	0.25
500:1	0.2
600:1	0.16
700:1	0.142
800:1	0.125
900:1	0.11
1000:1	0.1
1500:1	0.066
2000:1	0.05

Table 7.2: signal-to-noise ratio levels converted to noise percentages.

Reporting in noise percentage informs the analyst of the detection capabilities of the systems. Examining the spectra presented here shows that if a system's noise levels are greater or of similar magnitude to the depth (deviation from the background spectral curve) of the diagnostic absorption features, such a system will be unable to resolve these features reliably. In other words, increasing the noise in an imaging system reduces the dimensionality of the data it produces (Boardman, 1993). I would consider, from examining the noise spectra shown in Figures 7.10 to 7.13, that an acceptable noise level should not exceed 50 percent of the depth of the absorption features being sought. If the absorption feature of interest has a depth of 0.5 percent reflectance, as is the case with some ultramafic rocks and soils derived from them (see below) then the noise level should not exceed 0.25 percent, which is a signal to noise ratio of 400:1.

The signal-to-noise ratio is not constant across the full width of a spectrometer's bands and when presented as a plot should be shown as a spectrum. Generally, it decreases towards longer wavelengths by a significant amount (Cocks, 1997 pers. comm.). Most geological materials have an albedo between 20 percent and 30 percent in the SWIR2 wavelengths where the diagnostic Mg-OH absorption features occur. This means that quoted signal-to-noise ratios give only an approximate idea of a system's ability to discriminate the features of interest at the wavelengths of interest (2280nm to 2500nm). The general signal-to-noise ratio quoted by manufacturers for their systems is often for the maximum reflectance (near 2100nm in the SWIR2) only. The specifications of the wavelength, reflectance standard and light source used are therefore required if any reliance is to be placed on the signal-to-noise ratio quoted by a manufacturer. A better definition would be: a S/N at Y wavelength for a target albedo of Z percent at A degrees azimuth through a standard modelled

atmosphere (Huntington, 1998, pers. comm.). Even with data presented in this form it will be difficult to determine how the signal-to-noise ratio relates to the ability of a system to spectrally resolve specific spectral targets such as ultramafic rocks. This is because a system operating in an aircraft, rather than on a test bench, is subjected to additional noise sources due to vibrations and electromagnetic induction. The signal may also be reduced in operational conditions by low ground albedo, atmospheric haze and reduction of incident sunlight due to high cloud, time of day, or season.

I have made an analysis of spectral data collected in Australia and South Africa from weathered ultramafic rocks and their derived soils. These analyses indicate that the depth of the diagnostic absorption feature near 2300nm in these spectral ranges are between 7 percent and 0.5 percent. Plots of signal-to noise ratio, such as that shown in Boardman (1995), indicate that there can be a 40 percent reduction in the signal-to-noise ratio between 2200nm and 2300nm due to reduction in radiance intensity. Therefore, I deduce that for a system to achieve the 400:1 signal-to-noise ratio that permits resolution of a 0.5 percent deep absorption feature at 2300nm, associated with ultramafic rocks in some environments, a value of 600:1 is required at 2200nm.

Hook et. al. (1990) pointed out that there are trade-offs between signal-to-noise ratio, pixel size and number of bands (spectral resolution) which further complicate this issue. However, they concluded that signal-to-noise ratio is paramount. From my experience I have found that if the signal-to-noise ratio level can be maintained at a sufficiently high level, then smaller pixels and narrower bands will improve the ability to discriminate between materials at surface. In most airborne instruments the signal-to-noise ratio does not remain constant but varies with time. It may degrade due to instrument fatigue (also true of satellite systems) but it may improve due to ongoing system development. The AVIRIS signal-to-noise ratio was shown by Hook et. al. (1990) to have improved in the SWIR from 10:1 to 50:1 between 1987 and 1990 and Boardman (1995) indicates further improvement to 150:1 at 2200nm for a 40 percent reflectance target by 1994.

In Chapter 8 further considerations of signal-to-noise ratios are discussed where a method of obtaining this value for a system from data acquired under operational conditions is suggested.

To illustrate the effect of noise on multispectral data, the modelled SWIR2 Mg-OH and Al-OH spectra for HyMap and GEOSCAN MkII system band passes have had noise added at

various levels. To add the noise a function was written in Microsoft Excel that added random values, to the scanner band sampled saponite-illite spectrum reflectance values, which ranged up to each percentage noise limit (Appendix 3). As mentioned above, in reality, noise increases with wavelength due to a reduction in radiation energy rather than remaining constant as is the case presented here.

HyMap Spectra

In Figures 7.10 and 7.11, the effects of noise on the sampled PIMA saponite-kaolinite spectra are shown. Figure 7.10, compares all of the reflectance spectra with noise added to a clean spectrum with no noise added. It shows that the 2000:1, 1000:1, 700:1, and 500:1 signal-to-noise ratio spectra only have minor deviations from the clean spectrum, while for 300:1 150:1, 100:1 and 50:1 significant deviations become increasingly apparent.

It should be emphasised that this experiment is directed at the effects of random noise on the data. Systematic noise such that which causes striping and herringbone patterns in the data is not covered in this study. This type of noise is generally the result of equipment failure, insufficient electrical shielding or vibrations and it can be removed by Fast Fourier Transform (FFT) filtering.

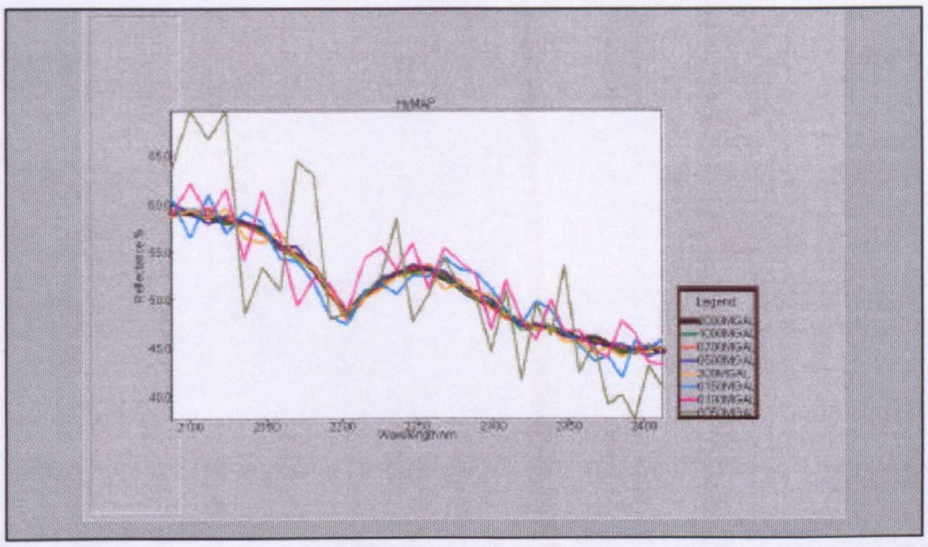

Figure 7.10: PIMA reflectance spectrum sampled to HyMap bands (black) compared to spectra with variable proportions of noise added. Number in the legend is the signal level, for example 1000MGAL indicates a signal-to-noise ratio 1000:1.

Figure 7.11 is a stacked profile that shows the spectra to which noise has been added at various levels of severity. These spectra have had a hull quotient transform applied to them to highlight the differences. The effect of noise on the data is to increase the signal level beyond its true value. This has the effect of introducing spurious peaks and, therefore,

troughs into the spectra that may obliterate actual absorptions and/or introduce spurious features. This will reduce the diagnostic features of the spectrum. In a scanner or spectrometer, these effects are random between measurements (pixels), hence they appear in images as overly bright or dark pixels within a band. This is the so-called salt and pepper noise. In this simulation the effect of noise is shown on a single spectra that would represent one image pixel. Obviously in real data, noise effects between spectra in a sequence (image) will all show different and random effects both in the wavelength bands affected and the level of intensity of the noise. At signal-to-noise ratio levels of 2000:1, 1000:1 and 700:1 the noise spectra are virtually identical and examination of Figure 7.10 shows they almost perfectly match the clean spectrum. This level of noise does not distort the spectra and would not produce salt and pepper effects in imagery. For a signal-to-noise ratio level of 300:1 spurious minor absorption features appear but there is still a strong correspondence to the clean spectra. These spectra show that at these signal-to-noise ratio levels a scanner with thirty-two SWIR2 bands, such as the HyMap, should resolve the spectral signature associated with weathered ultramafic rocks and derived soils.

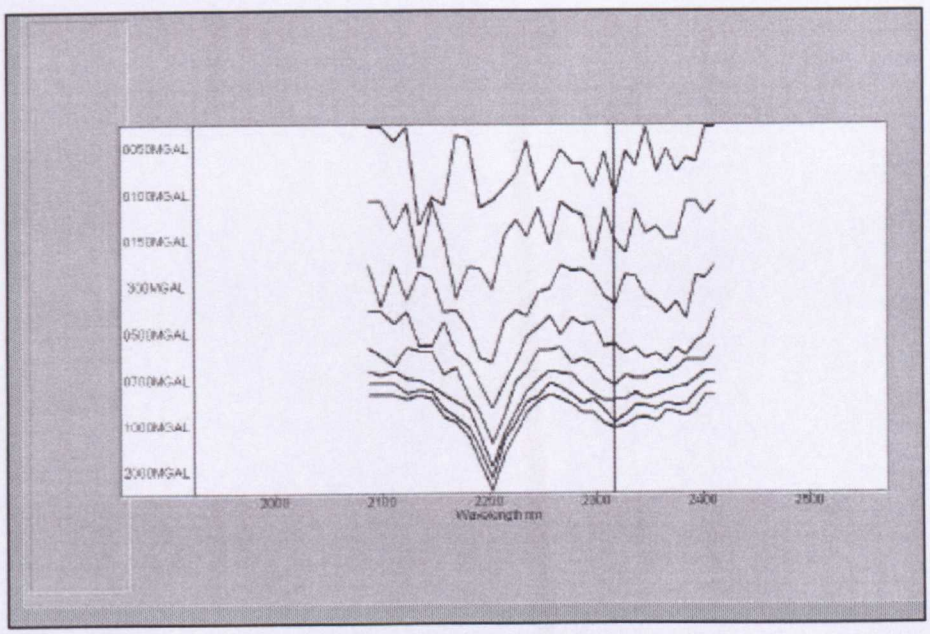

Figure 7.11: PIMA hull quotient stacked spectra sampled to HyMap bands offset for clarity. The Y axis sample names illustrate the noise level, for example 500MGAL indicates a signal-to-noise ratio of 500:1. Vertical line marks 2318nm for reference.

In the signal-to-noise ratio 150:1 spectrum the main absorption feature is still visually discernible but is less anomalous as it occurs in a background characterised by more variation. For example, the absorption feature at 2360nm is spurious but is as deep as the 2318nm feature which is real. In this case noise results in a spectrum that could be confused with a spectrum generated from a mixture of kaolinite-illite rather than saponite and kaolinite, particularly if automated end-member unmixing was being carried out.

When the signal-to-noise ratio reaches 100:1 and 50:1 the spectra show a marked degradation compared to the clean spectrum. In the 100:1 case overall shape of the spectrum is maintained but other spurious features, for example a 2280nm feature that is as large as the 2310nm (which has been shifted to 2320nm), are apparent. While the 100:1 noise spectrum does preserve the form of the clean spectrum only the 2200nm feature can be identified with any degree of confidence. Data that produces spectra such as these would not be reliable in locating diagnostic Mg-OH minerals spectrally. When the signal-to-noise ratio reaches a level of 50:1 the spectrum bares little resemblance to the clean spectra and data with this level of noise would be useless for any type of spectral analysis.

GEOSCAN MkII Spectra

In Figures 7.12 and 7.13 the effects of added noise on GEOSCAN MkII spectra are shown. In Figure 7.12 the comparison of the noise spectra with the clean spectrum shows that at signal-to-noise ratios of 100:1 and 50:1 the overall spectral shape deviates from the clean spectrum.

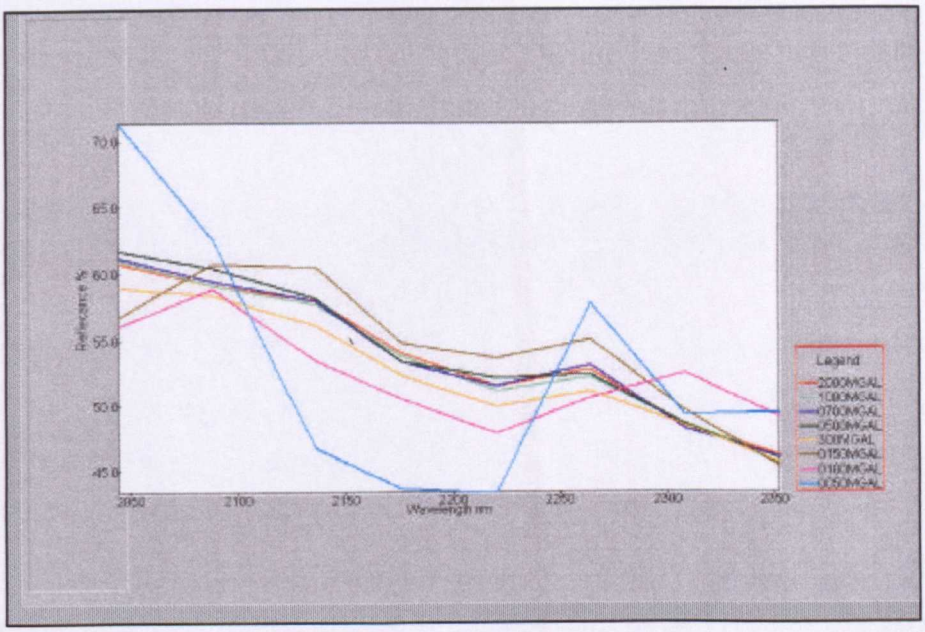

Figure 7.12: PIMA reflectance spectrum sampled to GEOSCAN MKII bands (black) compared to spectra with variable proportions of noise added. Number in the legend indicates the signal-to-noise ratio, for example 1000MGAL indicates a signal-to-noise ratio of 1000: 1.

In Figures 7.12 and 7.13 spectra with signal-to-noise ratios of 2000:1 to 500:1 correlate well with the clean spectra. The sampling effects on the spectra however would make it difficult to recognise visually these spectra as indicative of an ultramafic rock. Whilst the PIMA spectrum is a mixture of saponite and kaolinite, these spectra would probably be

interpreted to be Al-OH bearing mineral such as kaolinite rather than an Mg-OH mineral. At 300:1 all trace of the 2318nm feature is lost. With the under-sampling of the spectra using the GEOSCAN MkII band passes even the low level of noise at 500:1 is enough to shift the 2200nm wavelength and increase the uncertainty in visually interpreting this spectrum. This effect was not observed with the HyMap data. Selecting the optimum wavelength positions for the GEOSCAN MkII scanner has been reported on by Berman (1992).

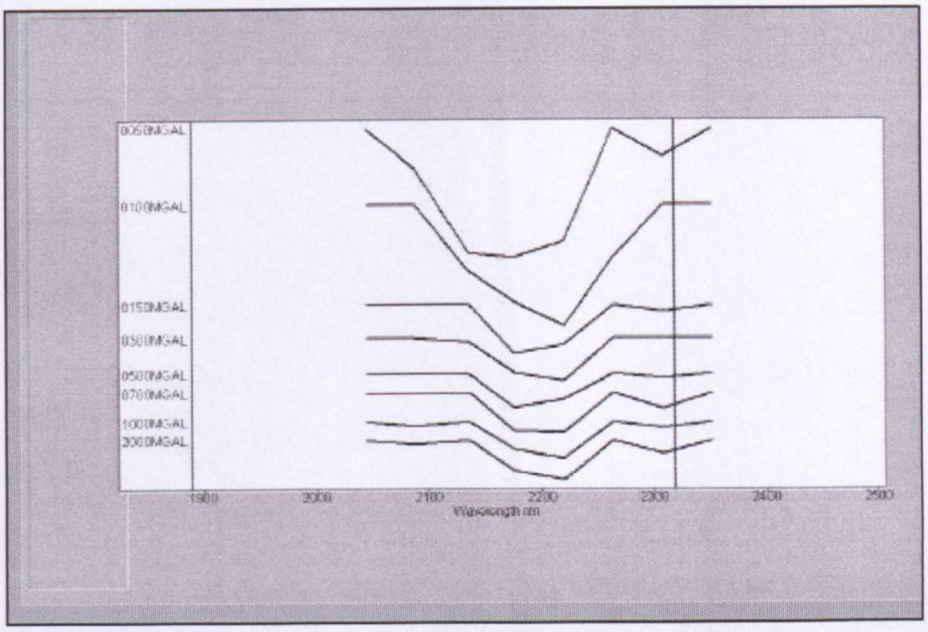

Figure 7.13: PIMA hull quotient stacked spectra sampled to GEOSCAN MKII bands offset for clarity. The Y axis sample names illustrate the signal-to-noise noise level, for example 500MGAL indicates 500:1. Vertical line 2318nm.

Spectra with signal-to-noise ratios of 150:1 and 100:1 show some similarity with the clean spectra in this hull quotient presentation. These spectra would be difficult to identify as having any Mg-OH spectral characteristics. However, in Figure 7.12 these spectra deviate significantly from the clean spectra but, in the hull quotient transformed presentation (Figure 7:13) they do show a general match with the form of the clean spectra. This suggests that in this case the hull quotient is influencing the shape of these under-sampled spectra in a way that is producing a coincidental match. Since noise is random the next pixel in an image would probably show a different spectra, even if derived from a spectrally identical surface, compounding the problem of spectral analysis.

Noise Reduction Filtering

There has been extensive research published on reducing noise in spectral image data and a clear explanation of the subject is given in Huntington et. al. (1994). All techniques

described require interactive processing and are time consuming even on data sets of limited extent.

In Figures 7.14 and 7.15 the effects of a Fast Fourier Transform (FFT) smoothing filter (Gonzalez and Wintz, 1987 and Hlavka, 1986), with a 10 percent weighting, on spectra are shown. Figure 7.14 shows the unfiltered clean spectrum compared to the 150:1, 100:1 and 50:1 noise spectra. Figure 7.15 shows the same spectra with a 10 percent FFT filter applied. The filtering does reduce the spurious absorption features but it does not eliminate them. However, the reduction in the larger spikes that appear throughout these noise spectra does produce a closer match with the clean spectrum. This reduction in noise reduces the ambiguity when attempting to match noisy spectra to known reference spectra. The filtered spectra show some shifts in the position of the absorption minima relative to the clean spectra. At signal-to-noise ratios of 150:1 and 100:1, these shifts do not appear large enough to prevent identification visually. However, the signal-to-noise ratio 50:1 filtered spectrum shows larger shifts and a major spike near 2130nm which is spurious. The fact that all the filtered spectra with noise show both the 2200nm and near 2300nm features proves that applying noise reduction techniques improves the interpretability of noisy spectral data. In this test, the data with noise would be difficult to interpret as representing an Al-OH and Mg-OH mineral mixture, but when filtered this distinction is apparent even if exact mineral identification remains ambiguous.

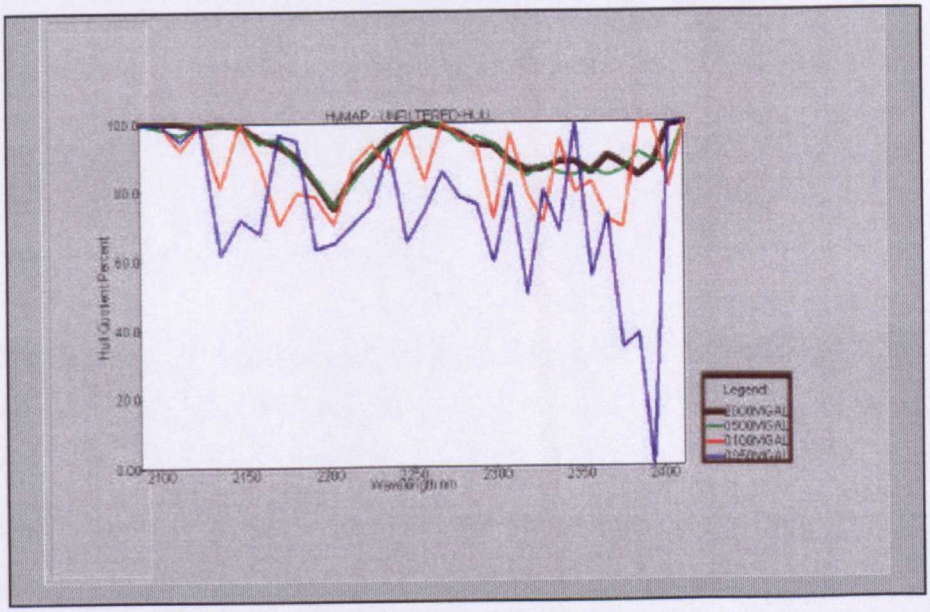

Figure 7.14: Un-filtered PIMA reflectance saponite-kaolinite spectra sampled to HyMap bands. Spectra have had noise added at various levels. Number in the legend indicates the signal-to-noise ratio.

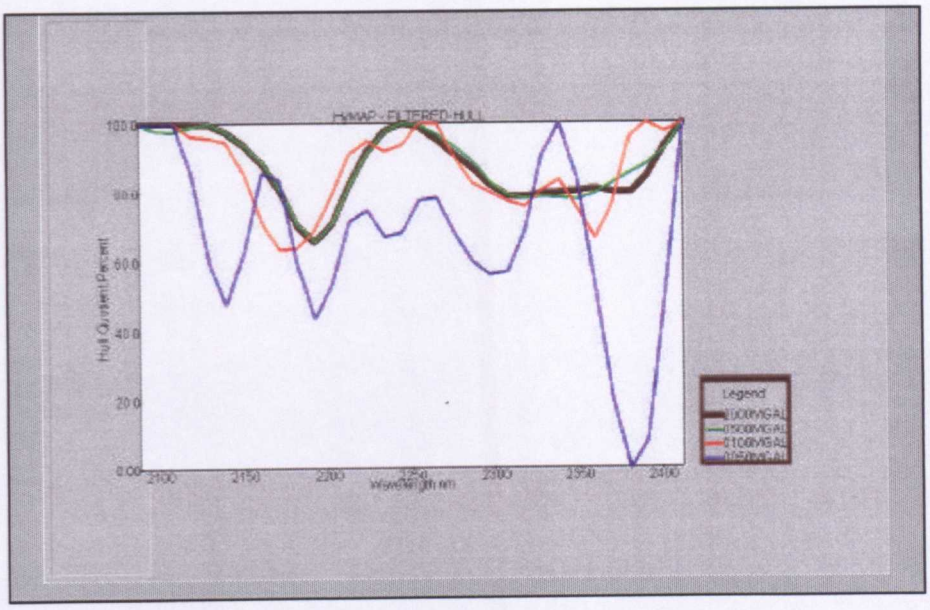

Figure 7.15: FFT filtered PIMA reflectance saponite-kaolinite spectra sampled to HyMap bands. Spectra have had noise added at various levels. Number in the legend indicates the signal-to-noise ratio.

If the data are filtered prior to carrying out processes such as band ratios on imagery or Mg Score ratio on spectra, the effect of filtering on the relative depths of the absorption features needs to be considered. In Figure 7.15, for example, it can be seen that in the 50:1 noise filtered spectrum the depth of the near 2300nm feature has become as deep as the 2200nm feature in the clean spectrum; the 2200nm feature is even deeper. Interpreting the results of band and wavelength ratios after filtering can produce results unrepresentative of the actual spectral composition. In this example, if 50:1 signal-to-noise ratio filtered spectra were being used to detect the presence of ultramafic minerals from the contour plot of Mg Score ratio values, spurious results would produce a random contour pattern. The effects on relative depths would be different for other spectra. This would be the same for image band ratios.

7.4 CONCLUSIONS

It is possible to obtain spectral data from scanners with as few as three bands in the SWIR2, for example JERS OPS (Figure 7.2). However, this study has shown that only when six or more bands are spread across the SWIR2 region can diagnostic information can be extracted from the imagery (compare Figure 7.2 JERS OPS with Figure 7.3 ASTER). In hyperspectral scanners with thirty-two or more bands in the SWIR2, spectra can be extracted from these data that do not differ significantly from spectra that are obtained from the PIMA spectrometer. Therefore, to detect ultramafic rocks hyperspectral instruments such as the currently operational HyMap, AVRIRIS and GER DIAS would be

most suitable. Instruments with fewer bands including the GEOSCAN MkII, and ASTER should be able to provide useful data at a discrimination level and this is shown in Chapter 10. However, a study by Berman (1992) demonstrated that the wavelength location of GEOSCAN MkII scanner bands influences the discrimination of different minerals. This has not been investigated in this study. In this study it is shown that the GEOSCAN MkII, with only eight SWIR2 bands will not locate anomalies/targets as precisely as hyperspectral scanners such as the HyMap. This is especially true when attempting to isolate the mixed spectral response of soils derived from ultramafic rocks from Al-OH mineral backgrounds.

This study has proven that noise is a critical factor in determining the potential of airborne/spaceborne scanners to discriminate ultramafic and other rock types spectrally. When scanner data is obtained for this purpose, I suggest that it should have a signal-to-noise ratio in the SWIR2, of at least 600:1 at 2200nm (400:1 at 2300nm) for a 50 percent reflectance standard to permit the conducting of reliable spectral analysis. It is possible to reduce the impact of noise by filtering, depending on the level and type of noise but this can affect the depth and position of absorption features and may remove smaller diagnostic absorption features. Therefore, I suggest that the degree of filtering applied is kept to a minimum. This is an area requiring additional investigation. Filtering also adds an additional processing stage to data analysis which is time consuming and therefore costly.

As can be seen in Table 7.1 noise estimates for different scanners are not easily obtained. Even when provided by the manufacturer, the signal-to-noise ratio quoted tends to understate the actual noise encountered when instruments are used, particularly in aircraft under operational conditions. The noise figures for AVIRIS and the HyMap instruments tabled may be considered reliable and at the desired levels. However, personal discussions with users of other data suggest that this is not the case for these systems.

If hyperspectral scanners are to be used routinely for geological applications such as those investigated in this thesis, then users of these data must insist that the data supplied has a sufficiently high signal-to-noise ratio. There is a trade-off to a lower signal-to-noise ratio with increased band numbers but with the current technology this is an unacceptable reason for sub-standard data. The value quoted for the instrument should be the signal-to-noise ratio with the test parameters listed and preferably shown as spectra plotted as SNR versus wavelength as in Boardman (1995).

CHAPTER 8

8 EVALUATION OF CONVENTIONIAL IMAGE PROCESSING TECHNIQUES USING SIMULATED SCANNER DATA

8.1 INTRODUCTION

Conventional techniques for image processing of remote sensing data have been applied to all types of scanner imagery since the data became available in the 1970s (Drury, 1993, Mather, 1991, Abrams et. al. 1983 and Rowan et. al., 1977). However, the ability of these techniques to locate ultramafic rocks has not been well documented (see Chapter 2).

These conventional techniques are now being superseded by spectral processing techniques, such as those that are available in the ENVI image processing package (Kruse and Huntington, 1996), for processing hyperspectral scanner data. However, conventional techniques are still widely available and familiar to many geologists. I have conducted the experiments detailed in this chapter to determine how well these conventional techniques discriminate different minerals. The experiments were directed at minerals containing Mg-OH associated with ultramafic rocks and common background minerals (non Mg-OH), using simulated data for multi-spectral scanners, imaging spectrometers and hyperspectral scanners.

Simulated data were chosen as it is easier to access the results of these techniques with such data than by using image data. Unless extensive groundwork has been completed, it is not possible to determine how representative an imaged area (pixel) is of a particular mineral or material. Image data pixels virtually always consist of mineral or mineral and vegetation mixtures of varying proportions.

In conventional image processing there have been two approaches to extracting the information from spectral imagery: classification and spectral feature extraction. The objective of using remote sensing data presented in this thesis has been to locate ultramafic rocks in areas where they are not known but are suspected to occur. As supervised classification techniques require known occurrences of the target being sought, as a training set, this technique does not meet the objectives of this study. In the case of un-supervised techniques the classes identified in an image may not be spectrally unique and it requires careful adjustment of the parameters input to the various routines such as nearest neighbour,

maximum likelihood or parallelepiped (Richards, 1986) before the process identifies the target type sought. Drury (1993) has pointed out that to optimise spectral classification requires selecting the bands that define the absorption features being investigated and carrying out a transform to principal component space of these bands prior to applying the classification procedure. Results of un-supervised classification require checking the targets selected spectrally from the data or in the field and the refining of the classification. The spectral processing techniques discussed in Chapters 9 to 11 produce the desired result, for ultramafic rocks at least, in a more direct manner. Therefore, I have not considered either supervised or un-supervised classification techniques in this study.

Spectral Feature Enhancement

Spectral feature enhancement uses spectral knowledge so that processes applied to the imagery result in output images that can be interpreted in light of this spectral knowledge. These are the techniques that are investigated in this section.

To work consistently these techniques must be applied to imagery that has been converted from radiance to reflectance, that is band-to-band variation is due to spectral variation alone. To convert radiance to reflectance requires corrections that remove atmospheric, topographic and scanner gain and offset effects from the data. This is time consuming and does not always produce consistent results. Therefore, determining the effectiveness of a particular enhancement process can be complicated by not knowing the reliability of the corrections that have been applied to the imagery. A more detailed discussion on conversion of radiance to reflectance data is presented in Chapter 3.

Images that have been converted to reflectance show by variation in grey tone in a single band image the distribution of any diagnostic absorption features at that wavelength. Assigning colours to selected grey levels, ie. density slicing, produces an index image that can highlight the regions of interest within the image. A colour composite produced from several reflectance bands can also be interpreted spectrally. Producing the colour composite from the negative image bands results in a direct correlation of colour intensity with depth of the absorption feature at the band wavelength. Image enhancement techniques can be applied to improve the contrast and enhance the edges of the various spectrally uniform areas within an image. Other standard techniques can be used to extract and enhance spectral differences such as band ratios, directed principal component analysis, Crosta principal component transform

and residual techniques. All rely on knowledge of the spectral response of the materials that are likely to occur in the scene.

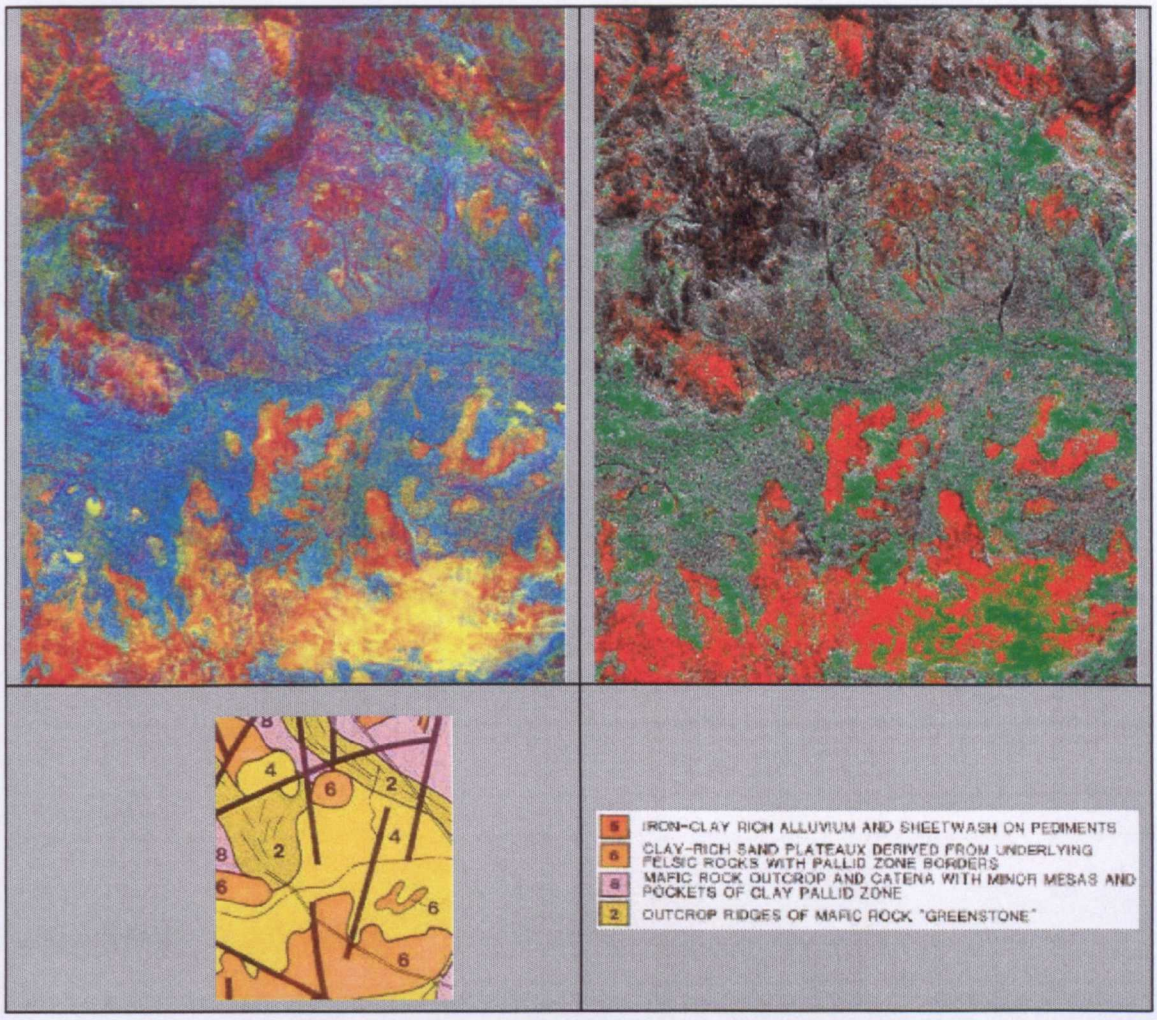

Figure 8.1: Geology and Regolith from Landsat TM imagery. The imagery has been processed to highlight clay, iron and vegetation (RGB) displayed as a Colour Composite (left) and Index Image (right - density sliced for clay and iron only). The regolith - geological interpretation of these images is shown in the map below (Hussey, 1986). Images and map are 10kms east to west, north at top.

In Figure 8.1 an example of a colour composite produced from band ratios and directed principal component analysis applied to TM imagery is shown (Hussey, 1986) together with the equivalent index image.

To establish benchmarks on the reliability of some of the standard classical processing techniques simulated images were produced from spectra measured with the PIMA and obtained from the USGS spectral library that is included with the ENVI processing software. In some imagery, such as GEOSCAN MkII, it is not only necessary to atmospherically correct these data but also remove gains and offsets, introduced into these data during acquisition, prior to converting the data to reflectance. These techniques are also reviewed.

8.2 SIMULATED IMAGERY

To determine the effectiveness of some frequently used digital processing techniques I have produced simulated image data. This simulation was done by simple re-sampling of the spectra to produce Digital Number (DN) values for scanner band wavelengths using the data in Table 8.1.

TM Bands	Wavelength Centres nm	GEOSCAN MkII SWIR Bands	Wavelength Centres nm	GER 32 SWIR2 Bands	Wavelength Centres nm
1	500	11	2044	13	2188
2	560	12	2088	14	2203
3	660	13	2136	15	2218
4	780	14	2176	16	2233
5	1655	15	2220	17	2248
7	2240	16	2264	18	2263
		17	2308	19	2278
		18	2352	20	2293
				21	2308
				22	2323
				23	2338
				24	2353
				25	2368
				26	2383
				27	2398

Table 8.1: Scanner band wavelengths used for simulated images. GER 32 bands highlighted are those used in this study for simulated images.

In this chapter the band numbers rather than wavelengths are used when discussing the application of processes. Though the SWIR2 band of TM is referred to by convention as Band 7, in this study it is referred to as Band 6 as this maintains the sequence of the bands.

The DN values obtained from the spectra of various minerals were entered into a program, written at my request by Dr A. Becker, which produced multi-band images of specified size (100 X 100 pixels for example). This program can also add noise to the image determined as random percentages using a DN value as a mean. The simulated TM images also had constants added to each image band to simulate atmospheric scattering offsets and scanner effects (values derived from actual TM imagery, Crippen, 1986). Division of the image bands by constants was carried out to simulate brightness (radiance) variation. The resulting radiance images were then used to determine how effective various atmospheric and radiance corrections performed were in correcting the imagery back to reflectance.

The images simulated were from spectra of the following materials and minerals:

- TM Imagery (Bands 1,2,3,4,5,6) – iron oxide (goethite + hematite), goethite, hematite, calcite, kaolinite mixed with iron oxide, kaolinite mixed with green vegetation, kaolinite, saponite, quartz, muscovite, dry vegetation, green vegetation.
- GEOSCAN MkII (SWIR2 Bands 11-18) – kaolinite, muscovite, quartz, goethite, green vegetation, serpentine, saponite, dolomite, calcite, dry vegetation
- GER 32 (Bands proposed in 1993 for DIAS SWIR2) – same minerals and materials as GEOSCAN MkII.

Field Examples

Images were also constructed from spectra measured with a PIMA from a grid of soil samples collected over the Meredith melnoite (a rock name used by those involved in kimberlite studies for a magnesium rich melilite-bearing basalt) located in the Brisbane Ranges west of Melbourne. These spectra were re-sampled to simulate GEOSCAN MkII and GER 32 images. In the case of the GEOSCAN MkII the simulated image data was produced without noise and with 2 percent noise (SNR 50:1) added. In the case of the GER 32 image experiments were done with varying noise levels.

8.3 ATMOSPHERIC CORRECTION

Methods

There are a number of methods used to atmospherically correct scanner imagery. These remove the effects of additional radiation that is back scattered from the atmosphere and have the effect of increasing the brightness to above that reflected from the ground. This atmospheric effect reduces as the radiation wavelength increases above aerosol particle size. Crippen (1987) reviewed the main methods that have been applied as part of his paper on the regression intersection method for atmospheric correction. These techniques are:

Dark Pixel Subtraction (DPS) (Chavez, 1977)

This technique is based on locating a pixel in the image that is the darkest in all bands. It is based on the assumption that such pixels should in fact be of zero reflectance. Therefore, the value of this darkest pixel, for each band, is the atmospheric offset for each band.

Regression Method (RM) (Potter, 1977)

In this technique a regression line is determined from scattergrams produced from each band versus the longest wavelength band, in the case of TM bands 1-5 versus 6. In this case it is assumed that there is a minimal offset in band 6, which fits with the atmospheric modelling of less atmospheric scattering at longer wavelengths. Since TM band 6 is located in the SWIR region where atmospheric scattering is minimal, this is not an unreasonable assumption.

Covariance Matrix Method (Switzer) (Switzer 1981)

This method is an extension of the RM but is based on using covariance matrices.

Regression Intersection Method –RIM (Crippen, 1986)

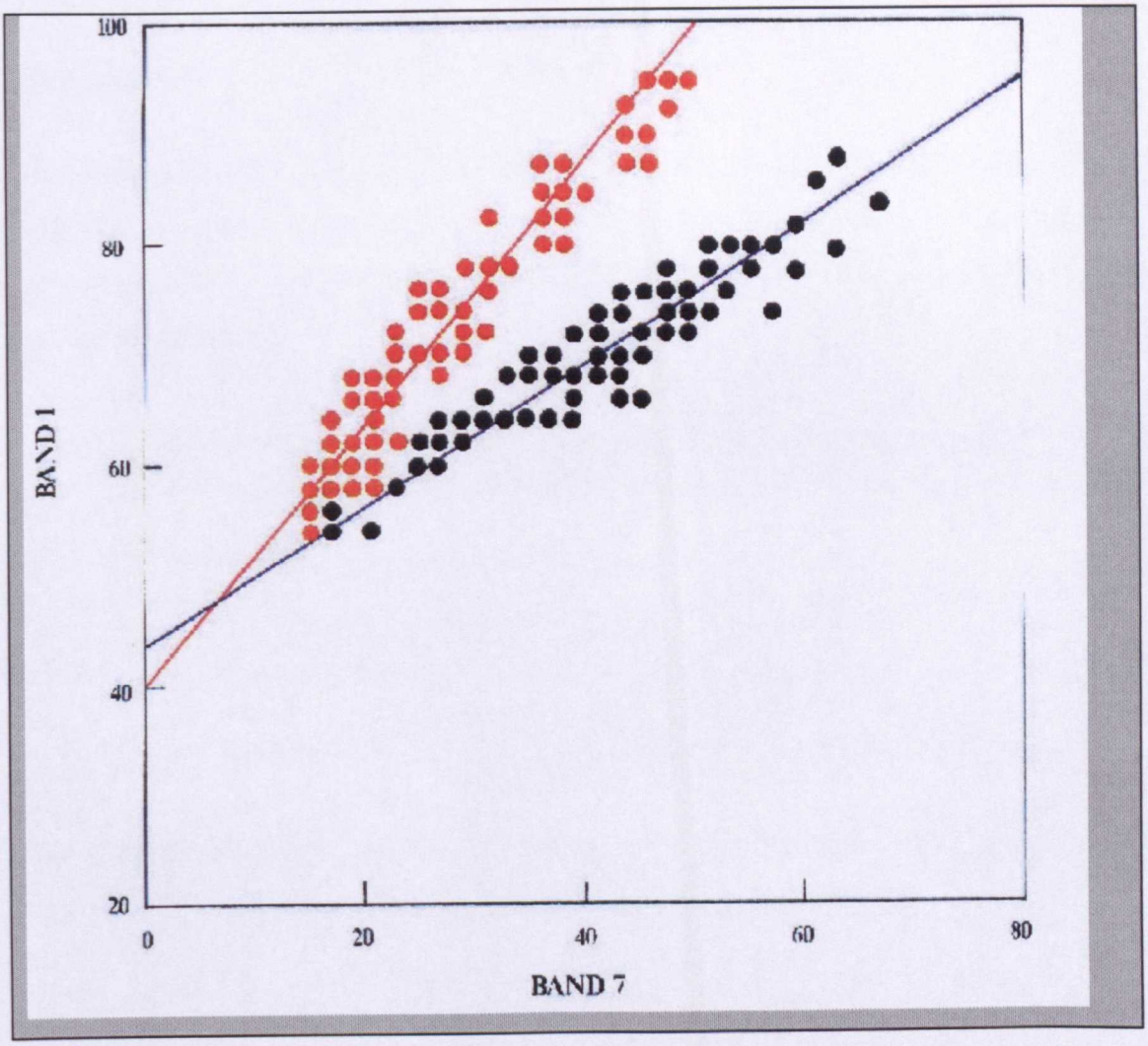

Figure 8.2: RIM - scattergram plot of pixels DNs of two sites from TM imagery for bands 1 and 6(7). The extrapolated intersection of regression lines is used to obtain atmospheric offsets as DN for bands 1 and 6(7). In this example offsets are 48 (band 1) and 8 (band 6).

In this technique scattergrams are plotted for each band against the longest wavelength band for pairs of sample sites and the X axis value of the intersection of their regression lines determines the offset for that band (Figure 8.2). In Crippen (1987), it is stated that test sites need to be bright with varying albedo (intensity) but constant hue and saturation. This means locating areas in the scene that are spectrally homogenous but with high surface radiance variation due to shadowing, this requires terrain with topographic variation.

My experience with atmospheric correction in TM imagery has shown that the DPS method gives consistent results but if different sub-scenes from the same image are examined, differing values are determined for the offsets. Hence, the assumption of a zero reflectance pixel in every sub-scene in every image is probably not valid. Using the DPS method, the larger the area of an image that is examined, consequently increasing the amount of variation in the DN values, the more likely it is that the correct atmospheric offset value will be obtained.

Test Results

To produce simulated imagery the spectra of dolomite, calcite, goethite, quartz, muscovite, saponite and green vegetation were convolved to the TM wavelengths and then used to seed the production of square pixel blocks of 100 by 100 pixels. The simulated imagery was processed as follows:

- 100 by100 pixel images created for each material, no noise added.
- Images were then divided by 0.5 and 0.7 to simulate shadow-radiance variations.
- Combination of these images into an mosaic.
- Addition of atmospheric offsets taken from Crippen (1986) (40, 20, 10, 5, 2, 0) were added to bands 1-6 to mosaic image.
- Random percentage values added to each pixel for each image in all bands to simulate instrument noise and ground radiance variations.
- Combination of images with noise added into another mosaic image.

The various atmospheric corrections were then applied to the mosaic image and on individual material blocks within it and the results obtained are shown in Table 8.2.

	TM B 1	TM B2	TM B3	TM B4	TM B5	TM B6
Offsets added	40	20	10	5	2	0
Total image						
DPS	40	20	10	5	2	20*
RM	52	37	26	64	46	0
Switzer	-82	-108	-125	-64	20	0
Dolomite						
DPS	40	20	10	5	2	53*
RM	38	19	8	3	0	0
Switzer	39	19	8	3	1	0
Muscovite						
DPS	40	20	10	5	2	25*
RM	39	20	9	5	1	0
Switzer	39	20	9	5	1	0
Goethite						
DPS	40	20	10	5	2	76*
RM	40	20	9	4	2	0
Switzer	40	20	9	4	2	0
Wet vegetation						
DPS	40	20	10	5	2	20*
RM	39	20	10	5	2	0
Switzer	39	20	10	5	2	0

*Table 8.2: Results of testing various atmospheric correction techniques on simulated TM imagery. The values obtained from each process should be compared to the values in the Offsets added row. TM B1, B2 etc. refers to TM Band 1, Band 2. For * see text.*

Band 6 had no offset added because the minimum pixel value is not considered to be due to atmospheric effects at these wavelengths. Hence in the case of the DPS the value for band 6 is the minimum pixel value in the band and should be ignored (values flagged with an * in Table 8.2). These results demonstrate that when applying atmospheric corrections, other than DPS, it is best to look at small spectrally homogenous areas. The composition of the material is not overly significant in selecting reference sites but the more correlation there is between bands the better. It is interesting that green vegetation and goethite both produce better results than muscovite and dolomite. As iron rich and vegetated areas are easily identified in the imagery, such areas could be ideally suited as atmospheric reference correction targets.

8.4 GEOSCAN MkII OFFSETS.

Huntington et. al. (1992) reported that the Switzer technique (Switzer, 1981) can be used to remove the offsets introduced into GEOSCAN MK II imagery during surveys. If these offsets are additive they can be regarded in the same way in which atmospheric scattering effects the imagery. However, if these offsets are of mixed sign across bands this technique will not be reliable, i.e. all offsets should be additive and one band must have its lowest DN set above zero ground reflectance. This means that the data should not be clipped at random offset levels during the data acquisition.

To investigate this procedure kaolinite spectra were convolved into GEOSCAN MkII SWIR bands and two versions of the offsets calculated. In one case the offsets added were all positive (AT1) with one band having no offset added. In the other case the offsets added were both positive and negative (AT2). The spreadsheet used to calculate the offsets is presented in Table 8.3 and the results obtained are shown in Table 8.4.

	B11	B12	B13	B14	B15	B16	B17	B18	Comment
Byte DN	108	93	77	45	50	58	48	44	Image DN byte values.
Offset AT1	10	15	20	7	10	12	2	0	Positive offset values
Offset AT2	10	-7	15	-5	2	8	20	0	Positive and negative offset values
Output AT1 DN	118	108	97	52	60	70	50	44	Image DN byte value plus AT1
OutputAT2 DN	118	86	92	40	52	66	68	44	Image DN byte value plus AT2

Table 8.3: Spreadsheet showing calculation of the DN values for kaolinite for simulated GEOSCAN MkII image with offsets introduced.

The offsets obtained from processing of the simulated output AT1 and AT2 data values with the RM and Switzer techniques are shown in Table 8.4. In Table 8.4 the results for the Switzer technique were produced using Band 18 as a reference band, the result of using other bands as the reference band is shown in Table 8.5, AT1 offset only.

Method	B11	B12	B13	B14	B15	B16	B17	B18	Comment
AT1 Offset	10	15	20	7	10	12	2	0	Offset from Table 8.6
AT2 Offset	10	-7	15	-5	2	8	20	0	Offset from Table 8.6
RM AT1	9	15	21	7	10	11	1	0	Good match with AT1 Offset
RM AT2	9	2	16	4	2	7	19	0	Good match with AT1 Offset
Switzer AT1	10	15	21	8	10	12	1	0	Good match with AT1 Offset
Switzer AT2	10	-5	16	3	2	8	19	0	Good match with AT1 Offset

Table 8.4: Results of processing the output AT1 and AT2 simulated kaolinite GEOSCAN MkII data with RM and Switzer techniques.

Reference Band	B11	B12	B13	B14	B15	B16	B17	B18
Offset AT1	10	15	20	7	10	12	2	0
Ref. B11	10	15	21	7	10	11	1	0
Ref B14	7	13	19	7	9	10	0	0
Ref B15	9	15	21	7	10	11	1	0
Ref B17	10	16	21	8	10	12	2	0

Table 8.5: Results of calculating the AT1 offsets using the simulated data from Table 8.3 with the Switzer techniques using different bands (Ref. B#) as reference bands. Band 17 and B11 both produce closest matches with the introduced offsets.

High levels of noise may degrade the reliability of these techniques for offset determination. This study does indicate that if instrument offsets introduced during the survey do not clip the data at the low DN range it is possible to remove them from GEOSCAN MkII imagery. Offset removal can be carried out using either the RM or Switzer techniques. It will depend, however, on locating spectrally homogenous test sites in the survey area with strong intensity contrast.

Now the GEOSCAN MkII scanner has been upgraded to record the radiance values as integer rather than byte values introduced offsets will no longer be a problem with these data. There is, however, still a large volume of data that is commercially available that was recorded as byte which does require the removal of offsets if it is to be processed in a spectrally meaningful way.

8.5 LANDSAT TM PROCESSING

These experiments were conducted to determine if it is possible to produce images from TM data that can discriminate the following materials: iron oxide (goethite + hematite), goethite,

hematite, calcite, kaolinite mixed with iron oxide, kaolinite mixed with green vegetation, kaolinite, saponite, quartz, muscovite, dry vegetation and green vegetation.

To discriminate these materials using TM imagery the following was considered:

- The spectral response of clay is bright in all channels except TM band 6, while vegetation, though varying in brightness at shorter wavelengths, is also darker in band 6. This can cause problems in producing enhancements to discriminate these materials.
- The similarity of goethite and hematite spectra (Fraser, 1985) means that processing to emphasise one of these iron oxides will usually highlight the other.

There are a number of techniques that partially resolve these ambiguities but they are not unmixing because they do not determine the percentage of each component material within a pixel's area. However, they can be used to classify pixels as, for example, containing some clay or mainly vegetation.

In presenting the image results two levels of density slicing have been applied to the images 149DN (mean 128DN plus one standard deviation) and 170DN (mean 128 plus two standard deviation), based on byte DN range of 0 to 255, with standard deviation of 21.

Band Ratios

Both arithmetic and normalised pixel components were tested for this simulation. Normalised pixel components takes the second principal component of the two bands to be ratioed as the equivalent of an arithmetic ratio; this is implemented by adding the two bands weighted by 0.707 and -0.707.

The results of some of the arithmetic ratioed images produced are presented in Figure 8.3. The grey scale output of the two band ratios images are density sliced so that values greater than the mean plus two standard deviations (>DN170 - DN128 plus DN42) are highlighted in light-tones. Ratios density sliced at >DN149 (DN128 plus DN21), that is, mean plus one standard deviation were also produced.

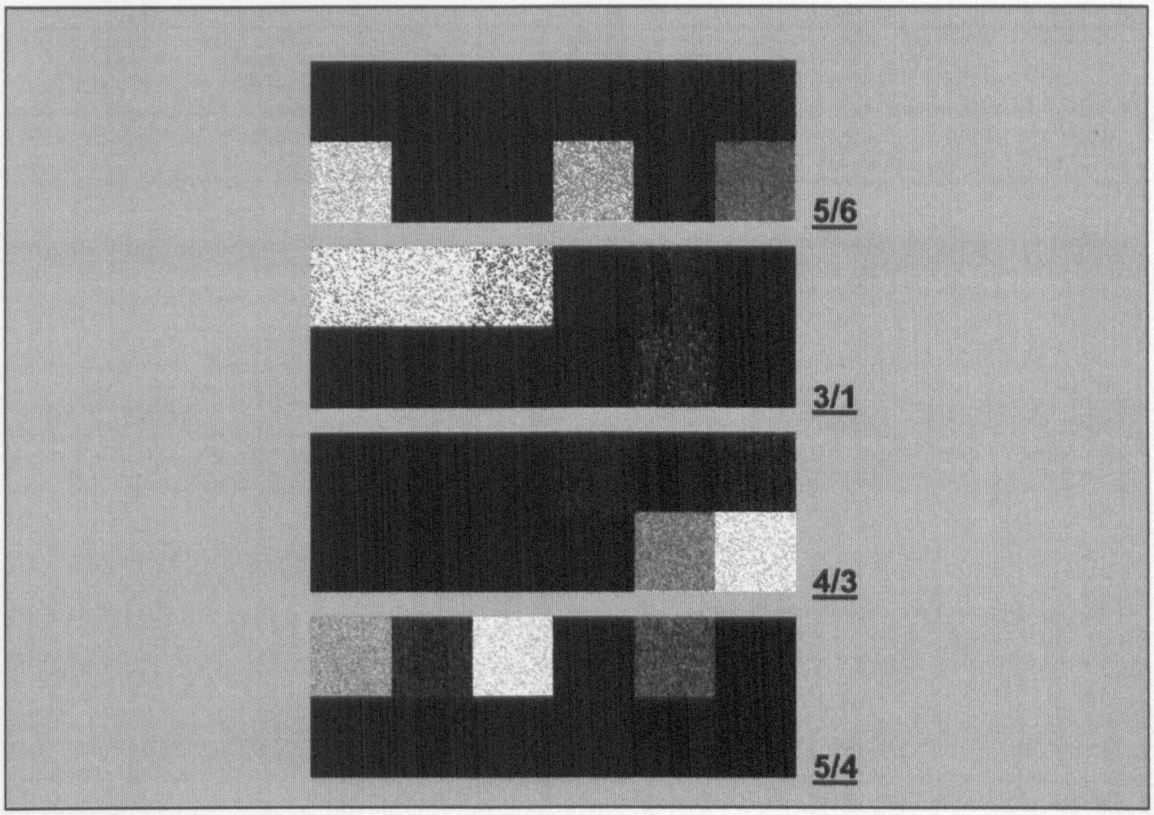

Iron	Goethite	Hematite	Calcite	Kaolinite + Iron	Kaolinite + Veg.
Kaolinite	Saponite	Quartz	Muscovite	Dry Vegetation	Green Vegetation

Figure 8.3: Arithmetic ratio images that have been clipped so that values >DN 170, are highlighted in light tones. The bands ratioed are shown to the right of the image. Legend below figure shows distribution of materials in image blocks.

Discriminations achieved for minerals by density slicing at >170DN (image mean plus twice the standard deviation) shown in Figure 8.3 are as follows:

- Ratio 5/6 >170 highlights kaolinite and muscovite.
- Ratio 3/1 >170 highlights iron, goethite and hematite.
- Ratio 4/3 >170 highlights green and dry vegetation.
- Ratio 5/4>170 highlights iron, hematite and kaolinite mixed with iron

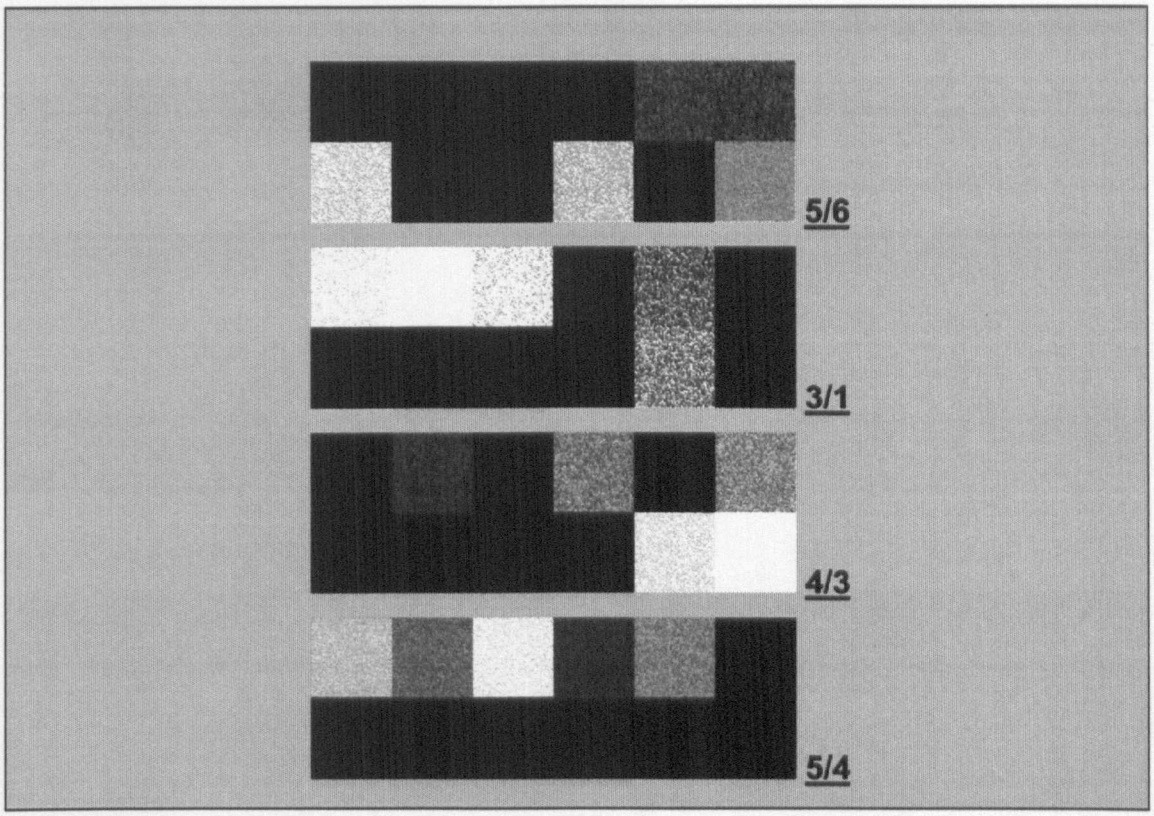

Iron	Goethite	Hematite	Calcite	Kaolinite + Iron	Kaolinite + Veg.
Kaolinite	Saponite	Quartz	Muscovite	Dry Vegetation	Green Vegetation

Figure 8.4: Arithmetic ratio images that have been clipped so that values > DN 149, are highlighted in light tones. The bands ratioed are shown to the right of the image. Legend below figure shows distribution of materials in image blocks.

Discrimination of minerals achieved by band ratios tested with the 140DN density slice shown in Figure 8.4 are:

- Ratio 5/6 >149 DN highlights kaolinite, muscovite, green vegetation, kaolinite+iron and kaolinite+vegetation
- Ratio 3/1>149 DN highlights iron-goethite-hematite, dry vegetation and kaolinite + iron.
- Ratio 4/3>149 DN highlights green vegetation, dry vegetation, calcite and kaolinite + vegetation
- Ratio 5/4 >149DN highlights iron-goethite-hematite and kaolinite+iron

From these results it can be deduced that discrimination particularly between clay and vegetation and the iron minerals is not distinct at the lower clip level though this is improved by clipping with twice the standard deviation.

A colour composite (Figure 8.5) where red displays ratio 5/6 (clay), green displays ratio 3/1 (iron) and blue displays ratio 4/3 (vegetation) has been produced. This image is displayed as a

raw result and after histogram modification using histogram equalisation, which improves the colour saturation.

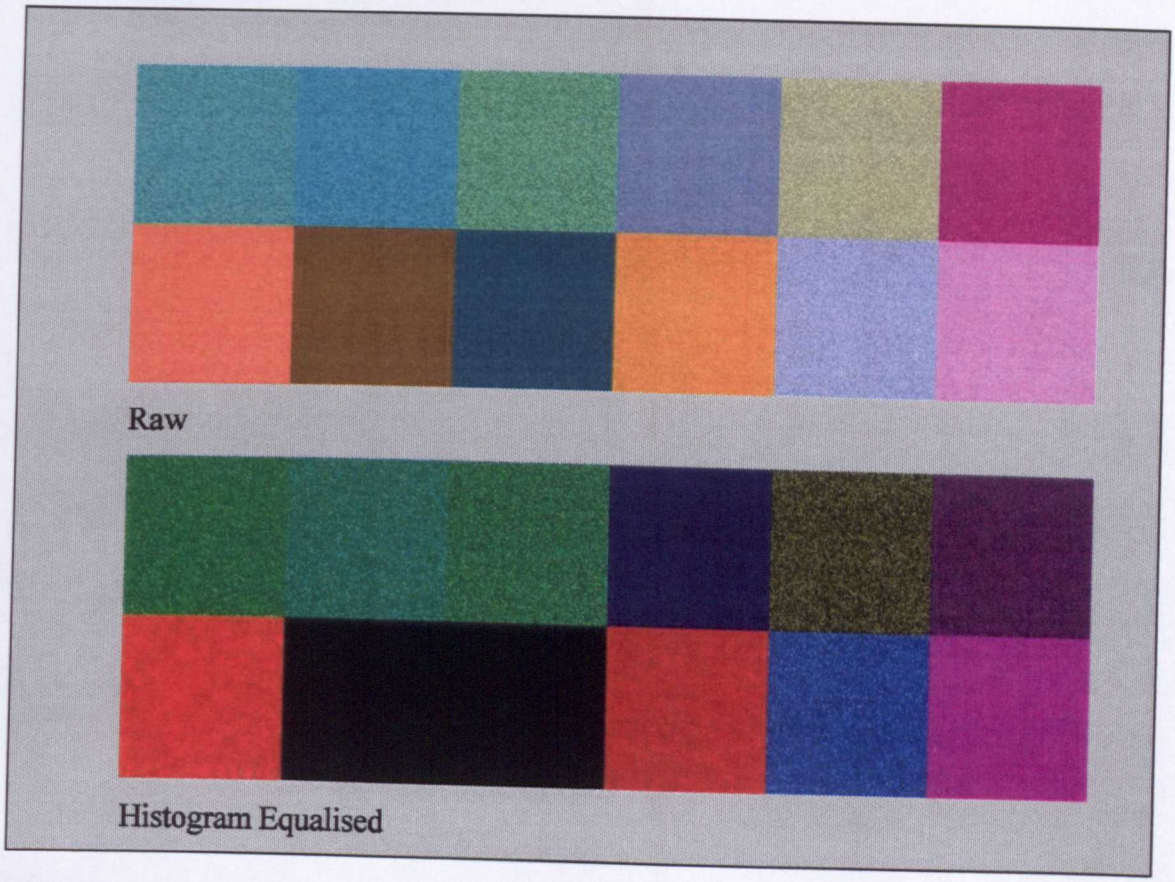

Iron	Goethite	Hematite	Calcite	Kaolinite + Iron	Kaolinite + Veg.
Kaolinite	Saponite	Quartz	Muscovite	Dry Vegetation	Vegetation

Figure 8.5: Arithmetic ratio colour composite of TM band ratios 5/6(7), 3/1 and 4/3 displayed in red, green and blue images. Upper image is raw and lower has been histogram equalised.

In the more saturated histogram-equalised colour ratio composite image iron minerals are green, red hues highlight kaolinite and muscovite and blue-purple hues highlight vegetation, kaolinite + vegetation and dry vegetation; saponite, quartz and calcite are dark grey. In the raw un-stretched image these colours are somewhat less distinct This test indicates that applying band ratios to TM data will not discriminate Mg-OH minerals, such as saponite, from other clays and carbonates to assist with the identification of ultramafic rocks. However, the discrimination achieved with the iron minerals might be useful in areas where the ultramafic rocks are exposed in an iron-poor background. The fact that the vegetation shows in purple rather than a blue hue means that in actual images there may be some ambiguity between the red of kaolinite and purple of vegetation, this can be overcome be re-assigning the colours, such as 4/3 to green and 3/1 to blue.

Using the principal component normalised ratios does not change the discrimination achieved. Hence, there is no advantage to using second PC ratios over arithmetic ratios.

Clay Prediction Techniques

Anomaly Residual Prediction Technique (Pendock and Lamb, 1989).

Applying this technique (Pendock and Lamb, 1989), to the simulated TM data produced the results shown as density sliced images in Figure 8.6.

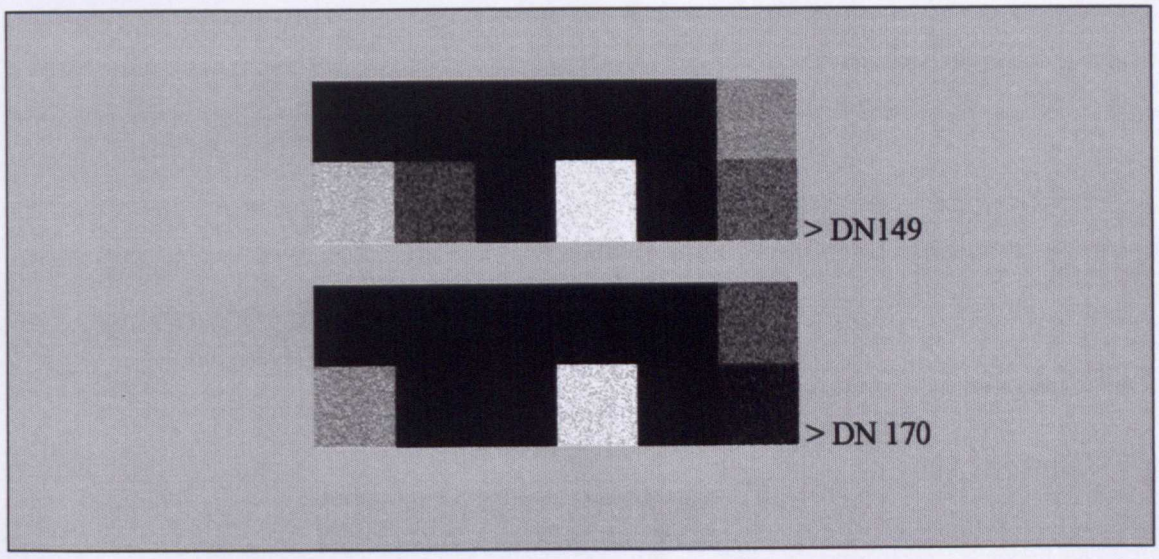

Iron	Goethite	Hematite	Calcite	Kaolinite + Iron	Kaolinite + Veg.
Kaolinite	Saponite	Quartz	Muscovite	Dry Vegetation	Vegetation

Figure 8.6 Anomaly Residual Prediction TM Band 6 image density sliced at >DN149 (lower) and >DN170 (upper). Legend below figure shows distribution of materials in image blocks.

The results of this prediction of Band 6 from the other bands when density sliced are as follows:

- >DN149 highlights kaolinite, muscovite, kaolinite+vegetation (and saponite, vegetation faintly)
- >DN170 highlights kaolinite and muscovite.

This technique does not confuse kaolinite and green vegetation, as does the 5/6 ratio.

Directed Principal Components (using ratios 4/3 and 5/6)

Figure 8.7, was produced from the second principal component of an image produced by the combined ratios 4/3 and 5/6 (in this order). The ratios were produce by adding the bands weighted by 0.707, -0.707; normalised principal component ratios.

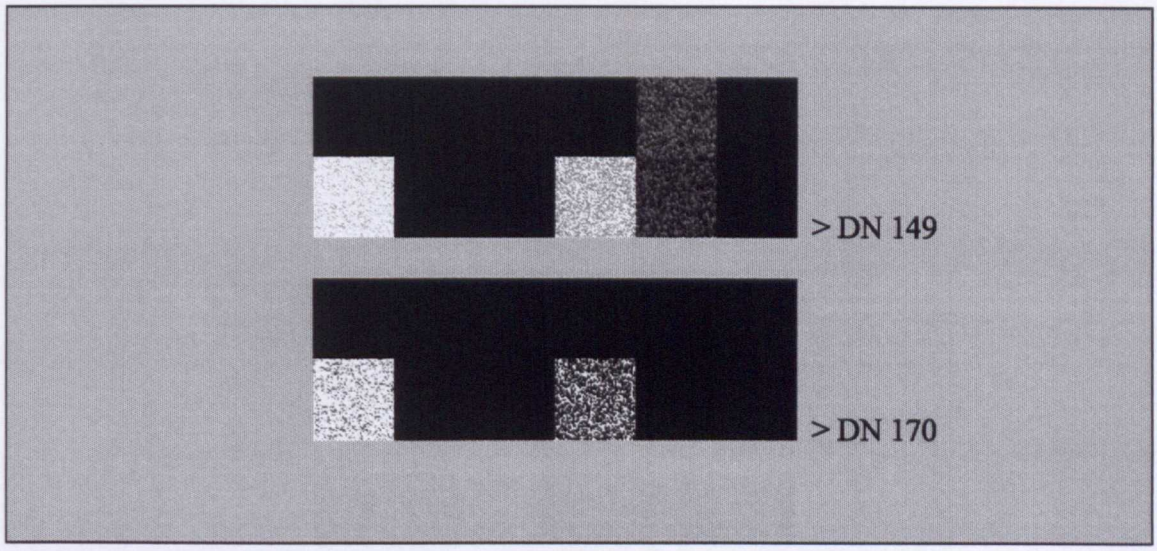

Iron	Goethite	Hematite	Calcite	Kaolinite + Iron	Kaolinite + Veg.
Kaolinite	Saponite	Quartz	Muscovite	Dry Vegetation	Vegetation

Figure 8.7 TM directed principal components using ratios (4/3 and 5/6) density sliced at >DN 149 and >DN 170. Legend below figure shows distribution of materials in image blocks.

The negative of the resultant image band then discriminates:

- >DN149 highlights kaolinite-saponite and muscovite (kaolinite + iron and dry vegetation faintly)
- >DN170 highlights kaolinite and muscovite

The directed principal component technique produces an image similar to that produced by the anomaly residual prediction technique. However, the anomaly residual prediction (LsFit) technique is simpler to use in practice.

Quick Residual Processing

The quick residual processing is similar to the log residual processing described by Craig and Green (1985) but uses normal arithmetic rather than geometric (log) means.

A kwik residual image should maximise the gains for each band by removing the common features between and within bands. Images of bands produced with this technique should show materials with absorption as dark grey tones, inverting the bands will result in absorptions highlighted in lighter tones. This is illustrated by the display of the results of applying this technique to the simulated TM images shown in Figure 8.8.

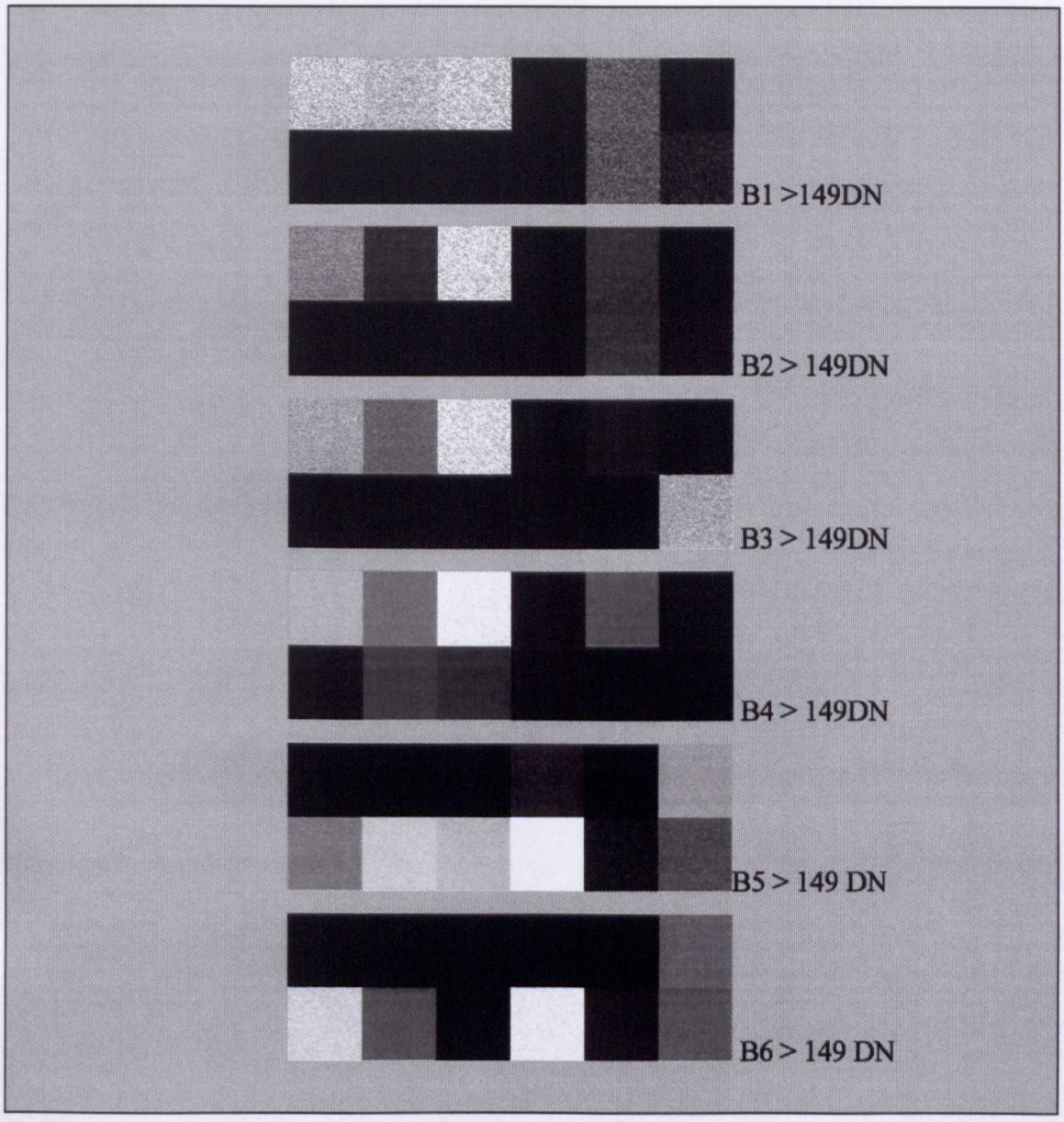

Iron	Goethite	Hematite	Calcite	Kaolinite + Iron	Kaolinite + Veg.
Kaolinite	Saponite	Quartz	Muscovite	Dry Vegetation	Vegetation

Figure 8.8: Kwik residual image (negative) of Bands 1-6. Absorptions are highlighted in light tones. Legend below figure shows distribution of materials in image blocks.

The kwik residual band images highlight the materials as follows:

- Band 1- Iron, goethite, hematite (kaolinite + iron and dry vegetation faintly)
- Band 2 - Iron and hematite
- Band 3 - Iron, goethite hematite and vegetation
- Band 4 - Iron, hematite and kaolinite + iron
- Band 5 - Kaolinite, saponite, quartz, muscovite, kaolinite + vegetation and vegetation
- Band 6 - Kaolinite, muscovite, (kaolinite + vegetation and vegetation faintly)

As the presence of a mineral is indicated by an absorption feature the negative image colour composite produced will highlight the mineral in the colour assigned to its diagnostic band. The simulated colour composite image shown in Figure 8.9 has the kwik residual bands 6,1,3 displayed in red, green and blue respectively.

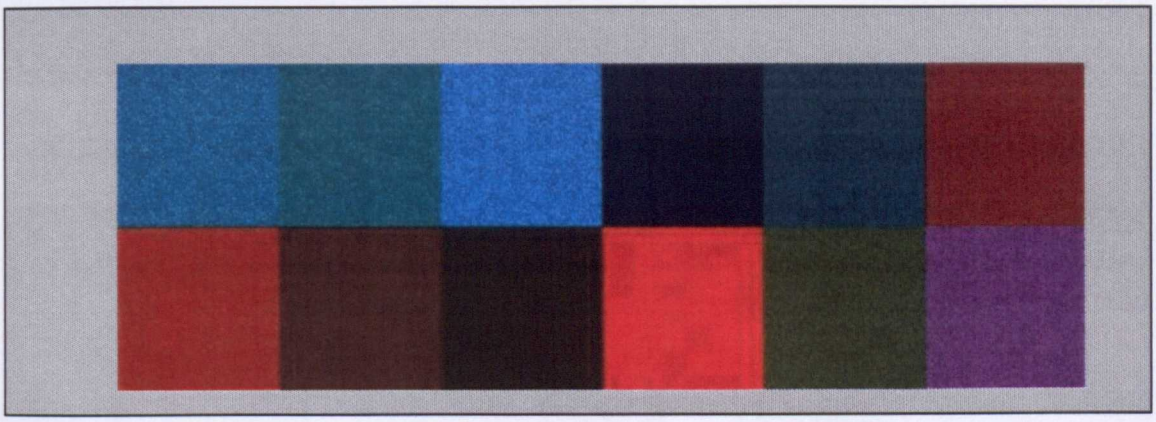

Iron	Goethite	Hematite	Calcite	Kaolinite + Iron	Kaolinite + Veg.
Kaolinite	Saponite	Quartz	Muscovite	Dry Vegetation	Vegetation

Figure 8.9: Kwik Residual Colour Composite simulated TM Bands 6,1,3 displayed in red, green and blue. Legend below figure shows distribution of materials in image blocks.

The kwik residual colour composite image shows kaolinite, saponite, muscovite and kaolinite+vegetation in red-orange, iron minerals and dry vegetation in green/cyan and vegetation in blue-purple hues.

Crosta Principal Component Transform (Crosta Technique)

According to Loughlin (1991) it is possible to map iron oxide and hydroxyl minerals from TM imagery using Crosta principal component transform analysis based on consideration of the eigen matrices for four of the bands:

- Bands 1, 4, 5 and 7- hydroxyl minerals.
- Bands 1, 3, 4 and 5- iron oxide minerals.

The eigen matrices for these four bands are checked to determine which principal component has the diagnostic bands (5 and 7 for clay and 1 and 3 for iron) with near equal magnitude but opposite sign. Examination of the image band obtained from these eigen vectors is then made to determine if it requires negation to ensure that the brightest tones highlight the materials of interest. In this study it was been found that the best contrast for iron oxide minerals occurs when bands 1,2,3,5 are used. For the simulated TM image the hydroxyl eigen vector weights in principal component band 3 are:

TM BAND	**1**	**4**	**5**	**6**
PC3	0.146	-0.562	-0.554	**0.596**

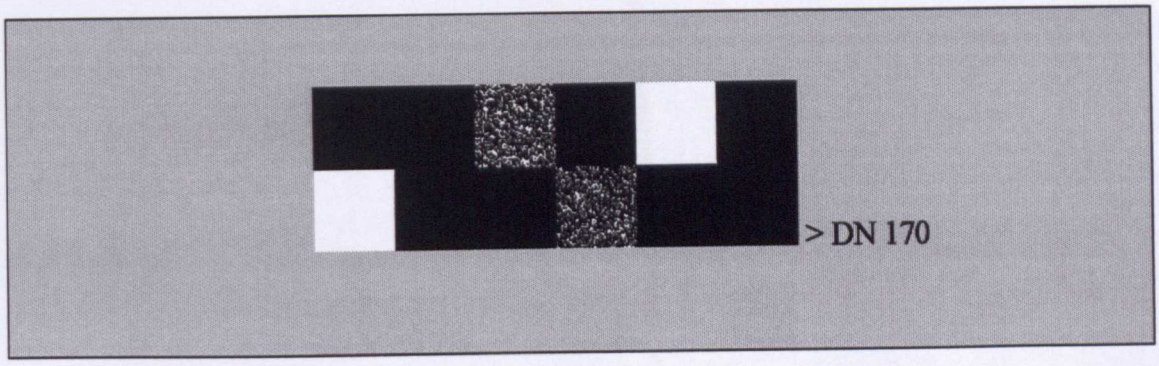

Iron	Goethite	Hematite	Calcite	Kaolinite + Iron	Kaolinite + Veg.
Kaolinite	Saponite	Quartz	Muscovite	Dry Vegetation	Vegetation

Figure 8.10 Hydroxyl Crosta principal component three density sliced >DN 170. Legend below figure shows distribution of materials in image blocks.

The eigen vectors show the most marked negative/positive contrast between bands 6 and the other bands in PC3. The negative of PC3 highlights in lighter tones kaolinite, kaolinite + iron, muscovite and hematite, Figure 8.10.

For iron oxide minerals the eigen vector for the bands 1,2,3,5 has a strong contrast between band 3 and the other channels in PC1. In the image of the Crosta PC1 for bands 1,2,3,5 the iron oxide minerals and kaolinite + iron are highlighted in lighter tones, Figure 8.11

TM BAND	1	2	3	5
PC1	-0.642	-0.279	**0.712**	-.902

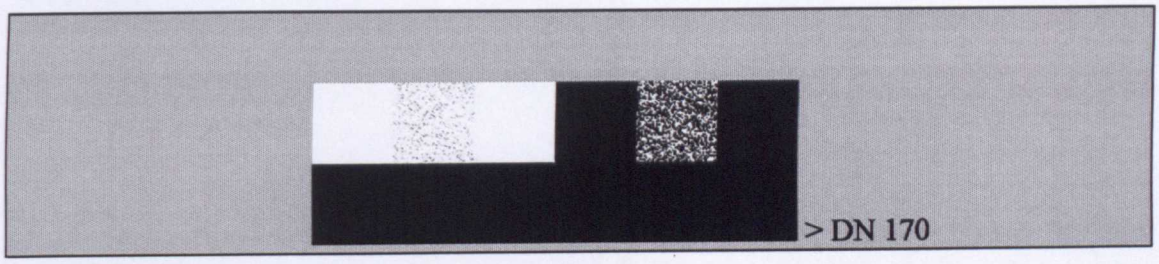

Iron	Goethite	Hematite	Calcite	Kaolinite + Iron	Kaolinite + Veg.
Kaolinite	Saponite	Quartz	Muscovite	Dry Vegetation	Vegetation

Figure 8.11: Iron mineral Crosta principal component one density sliced >DN 170. Legend below figure shows distribution of materials in image blocks.

Mixed Composite Images

To produce an image that will segregate clay (hydroxyl minerals) from iron and vegetation a colour composite (Figure 8.12) can be produced as follows:

- Band prediction (Band 6) displayed in red.
- Crosta 1,2,3,5 PC1 displayed in green.
- Ratio 4/3 displayed in blue.

This is a mixed composite technique and other combinations of processing can be combined to distinguish other minerals and materials. The mineral discrimination possible with this image is detailed in the caption to Figure 8.12.

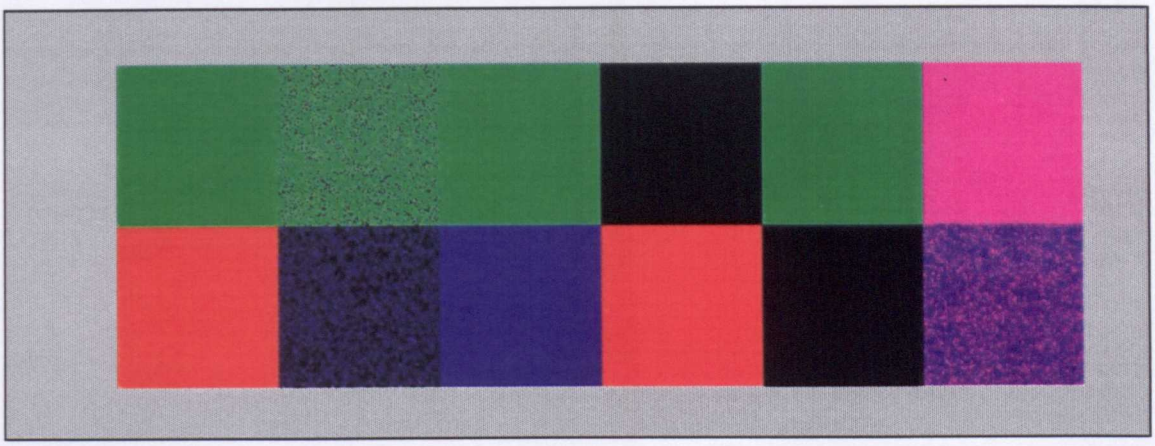

Iron	Goethite	Hematite	Calcite	Kaolinite + Iron	Kaolinite + Veg.
Kaolinite	Saponite	Quartz	Muscovite	Dry Vegetation	Vegetation

Figure 8.12: Mixed colour composite of band prediction in red, Crosta 1,2,3,5 PC one in green and ratio 4/3 in blue. Red highlights kaolinite and muscovite. Green highlights iron, goethite, hematite and kaolinite + iron. Blue/purple highlights green vegetation. Other minerals are black, that is not highlighted. Image has been contrast modified by histogram equalisation. Legend below figure shows distribution of materials in image blocks.

Comments

Colour composite images produced by combining the results of these techniques to discriminate clay/iron/vegetation and the clay/iron oxides appear to be the limits of mineral discrimination that can be achieved by processing of TM imagery with the techniques discussed.

In practice it is better to highlight the >170DN level in the separate image bands and combine these as colour overlays onto a black and white background image to produce an index image. Such index images can highlight the distinctly anomalous concentrations of clay, iron, (goethite, hematite) and vegetation within an area.

From the viewpoint of detecting the spectral signature of minerals that are associated with ultramafic rocks these tests show that Mg-OH clays cannot be isolated uniquely from TM imagery. This is not because the techniques are failing but because Landsat TM does not have enough bands in the SWIR2 to permit such discrimination. However, iron minerals can be discriminated with the techniques, which can be important in some locations for locating ultramafic rocks (see Chapter 2).

8.6 GEOSCAN MkII PROCESSING

For the GEOSCAN MK II scanner the convolved spectra for the SWIR2 bands were made into an image in the order shown in the legend below Figure 8.13.

As the bands are narrower in the GEOSCAN MkII imagery than in TM, specific absorptions are resolved and it should be possible to discriminate minerals using quick residual images alone, either as single band index images or colour composites. However, the concept of using Crosta processing was also tested on the imagery. This was recommended in Loughlin's (1991) paper because actual scanner data noise levels may reduce the spectral variability between bands (Chapter 7).

Quick Residual Processing

The negative colour composite of the kwik residual image (Figure 8.13) for bands 17,14,12 clearly shows the difference between the Mg-OH and carbonate minerals in red/pink and the Al-OH minerals in green with quartz, vegetation, dry vegetation and goethite in pale blue.

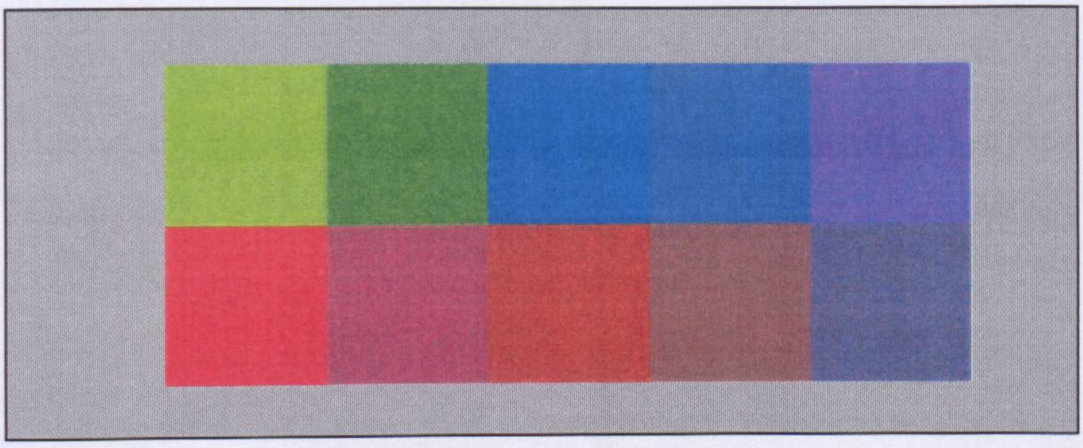

Kaolinite	Muscovite	Quartz	Goethite	Vegetation
Serpentine	Saponite	Dolomite	Calcite	Dry Vegetation

Figure 8.13: GEOSCAN MkII SWIR2 quick residual colour composite image. The negative image is shown with bands 17, 14, 12 displayed in red, green and blue.

Crosta Principal Component Transform

Examination of the spectra (Chapter 7) show that in GEOSCAN MkII data bands 15 and 17 differentiate most between Al-OH and Mg-OH minerals while bands 11 and 18 are at similar levels for both these materials. The eigen matrix obtained from the simulated is:

	B11	**B18**	**B15**	**B17**
PC1	-0.345	-0.549	-0.550	0.526
PC2	0.912	-0.102	-0.104	-0.384
PC3	0.210	-0.190	**0.632**	**-0.721**
PC4	0.071	-0.808	-0.536	-0.236

This eigen matrix shows that PC3 should discriminate the Mg-OH and Al-OH minerals and Figure 8.14 confirms this. However, this image also highlights carbonates but this might be expected as these minerals also have an absorption feature located near 2300nm.

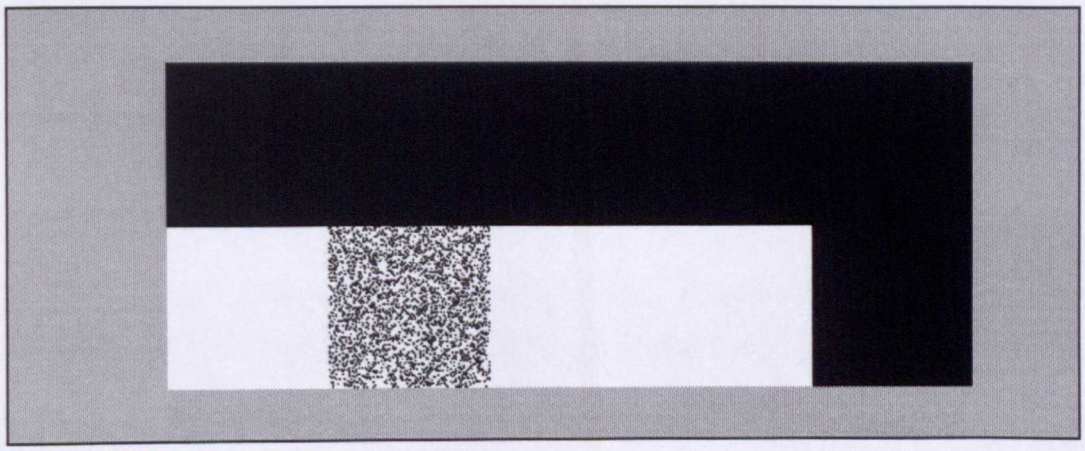

Kaolinite	Muscovite	Quartz	Goethite	Vegetation
Serpentine	Saponite	Dolomite	Calcite	Dry Vegetation

Figure 8.14: GEOSCAN MkII Crosta technique index image of principal component three from bands 11,18,15,17. Serpentine, saponite and dry vegetation blocks are all highlighted in lighter tones >DN170.

Effects of Noise on Crosta Technique

With 2 percent noise added to the imagery, the eigen matrix from this noise image for bands 11, 18, 15,17 is:

	B11	**B18**	**B15**	**B17**
PC1	-0.346	-0.549	-0.550	0.526
PC2	0.912	-0.102	-0.105	-0.384
PC3	0.210	-0.109	**0.632**	**-0.722**
PC4	0.071	-0.808	-0.538	-0.236

This matrix has weighting values that are virtually identical to the values obtained from the noise free data and this indicates that the Crosta technique may produce useful discrimination even from noisy images.

8.7 GER 32 BAND (SWIR2) PROCESSING

Using the spectra of the Al-OH and Mg-OH minerals together with iron, vegetation and calcite, a 32-band image was produced using the GER 32 wavelengths listed in Table 8.1. Due to the limited buffer size of the I^2S processing package used in these experiments, this image was sub-banded into a fifteen band image using the highlighted bands shown in Table 8.1. The distribution of the mineral blocks in this simulated image is the same as used for the Geoscan MkII data.

Quick Residual Processing

In the case of the Geoscan MkII imagery it was shown that quick residual processing of the data allows production of colour composites of three bands that adequately discriminate minerals of interest, that is, Mg-OH from Al-OH minerals. Examination of the convolved spectra in Chapter 7 indicates that taking the negative of the quick residual bands, 21, 14 and 16 and displaying these in red, green and blue respectively should achieve this segregation. This band combination is shown in Figure 8.15 and shows that the Mg-OH and carbonate minerals with near 2300nm absorptions are discriminated from the Al-OH minerals (near 2200 absorptions).

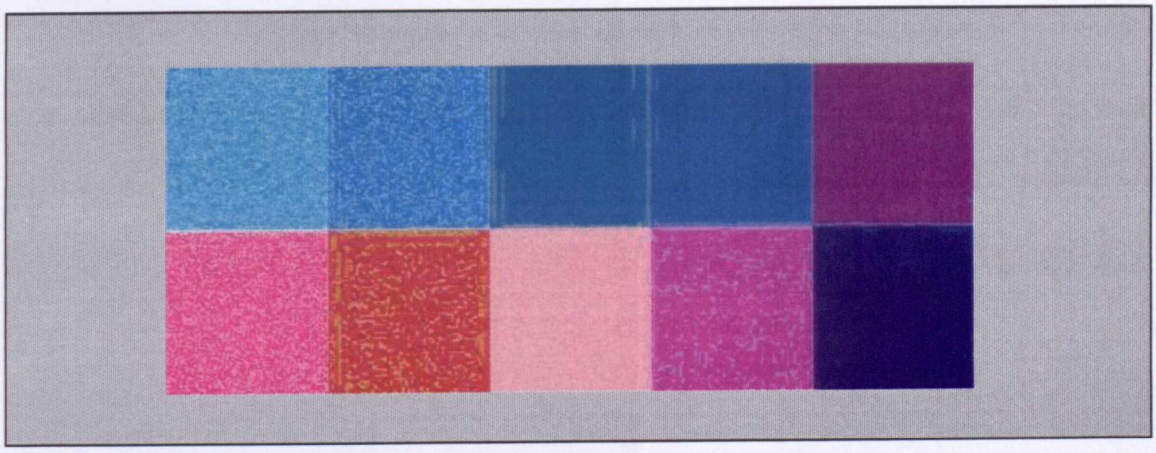

Kaolinite	Muscovite	Quartz	Goethite	Green Vegetation
Serpentine	Saponite	Dolomite	Calcite	Dry Vegetation

Figure 8.15: GER 32 Band kwik residual colour composite. Mg-OH minerals (saponite and serpentine) and carbonates are highlighted in red-pink hues, Al-OH minerals (kaolinite and muscovite) are green/cyan and other minerals and vegetation show as blue and grey.

Crosta Principal Component Transform.

Examining the spectra it appears that using bands 16, 17, 14 and 21 should allow discrimination between Al-OH and Mg-OH minerals using the Crosta technique on this GER 32 Band simulated image. The eigen matrix for this sub-banded image is:

	B14	**B16**	**B17**	**B21**
PC1	-0.551	-0.484	-0.468	0.493
PC2	0.673	-0.099	-0.136	-0.72
PC3	0.47	-0.478	**-0.565**	**0.481**
PC4	-0.149	0.726	-0.655	0.086

The differences between Mg-OH and Al-OH should then be concentrated in PC3. This is shown in the level sliced image of PC3 (Figure 8.16) where the data range DN127-DN255 is set to white (255DN) highlighting the Mg-OH minerals and where the DN1-DN126 is set to white (255DN), highlighting the Al-OH minerals and goethite (faintly).

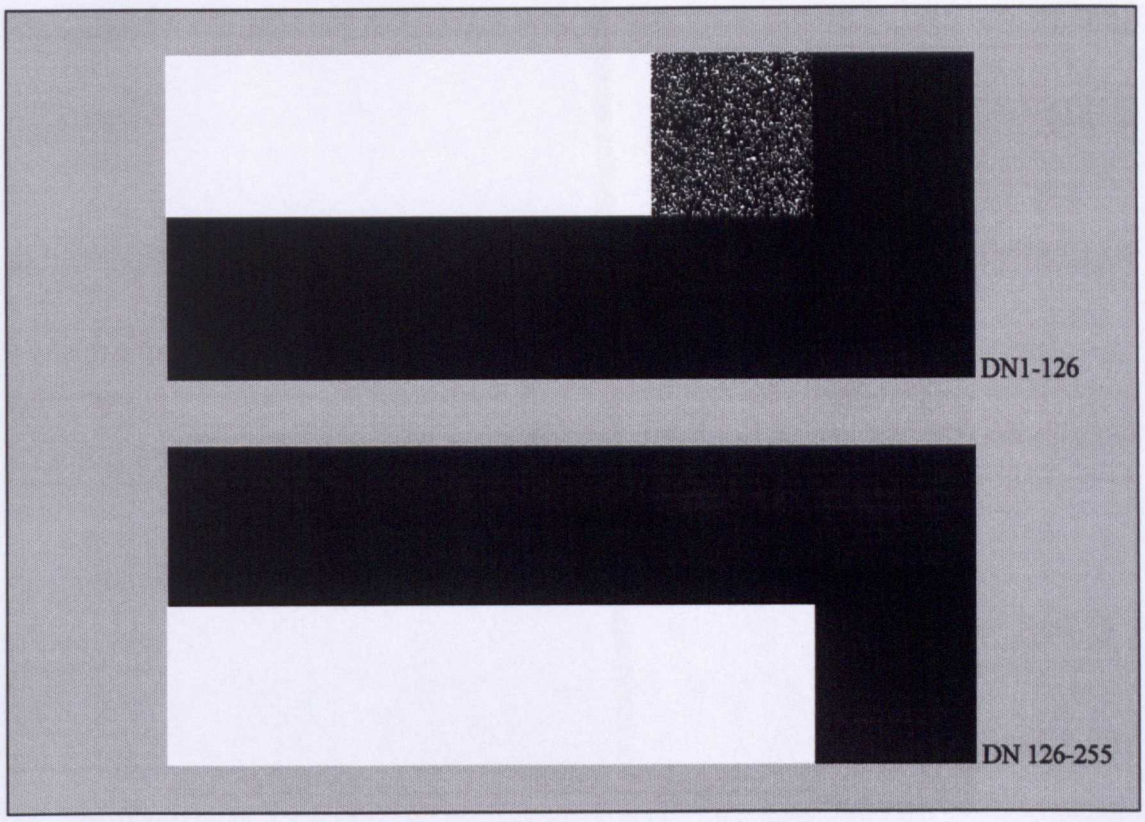

Kaolinite	Muscovite	Quartz	Goethite	Vegetation
Serpentine	Saponite	Dolomite	Calcite	Dry Vegetation

Figure 8.16 GER 32 Crosta 14_16_17_21 PC3 index image, DN level 0-124 highlights Al-OH minerals white and 129-255 highlights the Mg-OH/CO_3 minerals white.

The advantage of the Crosta technique is that the contrast between Al-OH and Mg-OH minerals can be presented in a single band that can be density sliced to reveal these differences directly.

8.8 MEREDITH DATA

The spectra used in this simulation were collected with the PIMA spectrometer from samples taken in the field. Figure 8.17 shows the project location, the Mg Score ratio contour plot derived from spectra and the contact mapped between the melnoite and country rock when the samples were collected.

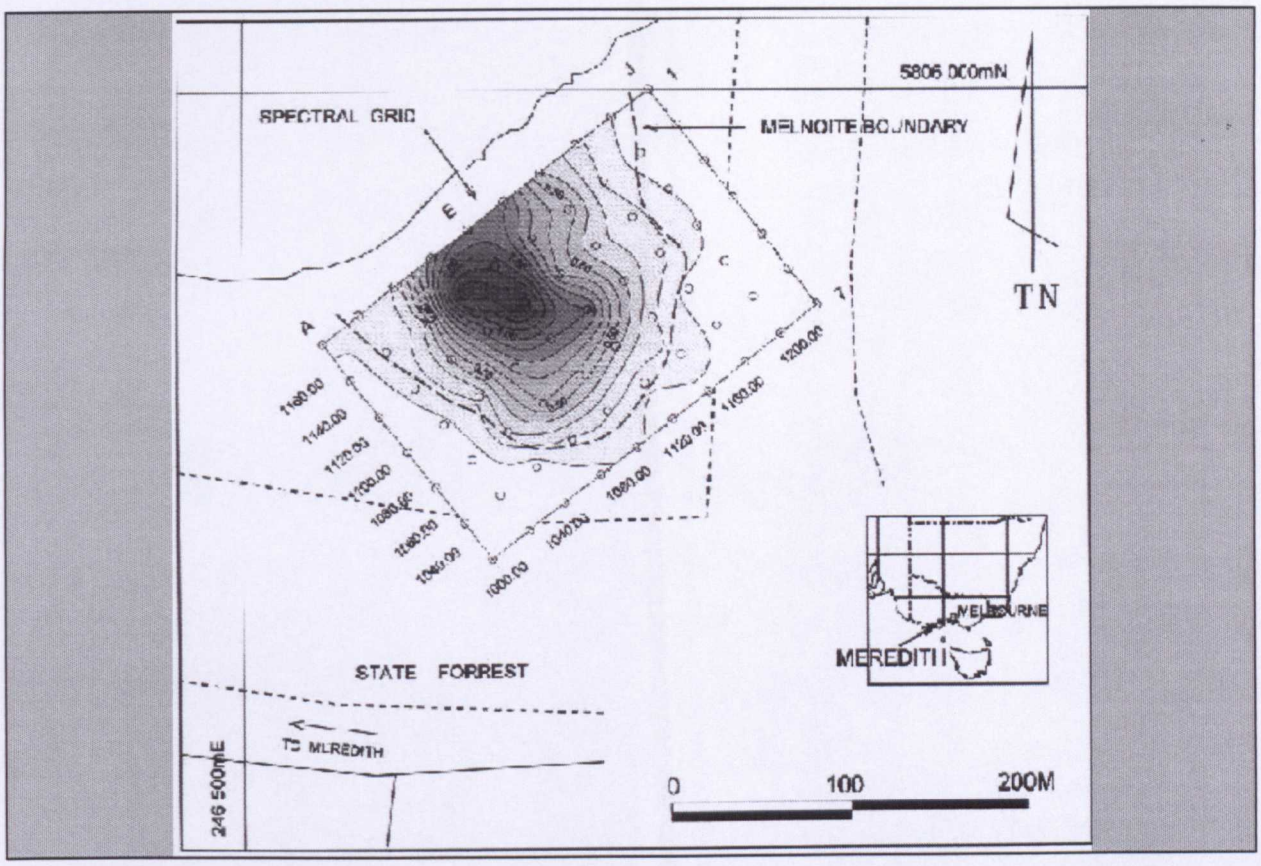

Figure 8.17: Meredith melnoite grid MgScore ratio showing the Melnoite contact and location map. The location of column E 1-7 (1180-1000) referred to in the text is indicated.

Figure 8.18 shows the SWIR2 spectra plots for column E rows 1-7 as both raw and hull quotient transformed spectra.

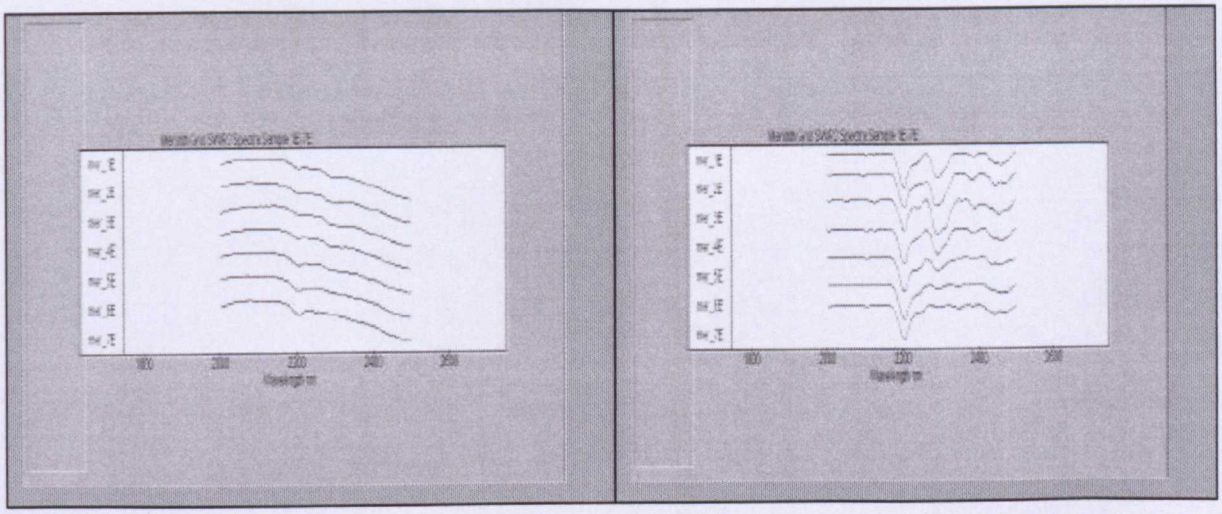

Figure 8.18: Meredith melnoite grid PIMA Spectra collected on column E rows 1-7). Left image is raw reflectance and the right is hull quotient transformed. Note the decrease in the depth of the 2300nm feature from sample 1E to 7E.

The convolved values for each scanner band from each grid spectrum were converted to a 100 by 100 pixel image and sampled to simulate GEOSCAN MkII and GER 32 Band SWIR2

scanner images. These image blocks were combined into an image that geometrically equates to Figure 8.16. Each sample block of pixels had their spectra offset to different random levels to emulate topographic variation. Similarly another set of images was created for the GER 32 data with random noise added to them between 10 percent to 0.1 percent (SNR 10:1 to 1000:1).

GEOSCAN MkII Simulated Image

Kwik Residual Colour Composite

The kwik residual program was applied to the GEOSCAN MkII gridded image. Taking the negative of bands 17, 14, and 11 and displaying them in red, green and blue produces an image (Figure 8.19) in which the melnoite body is highlighted in red, orange and brown. The background areas appear blue, cyan and grey.

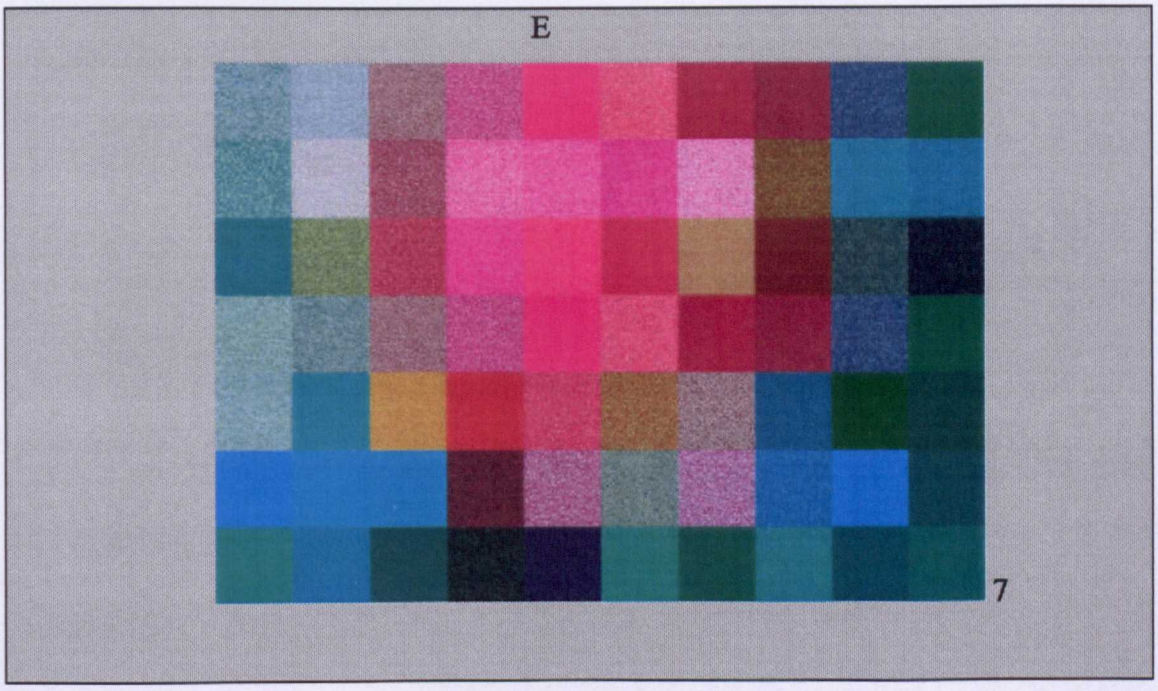

Figure 8.19: Meredith melnoite grid GEOSCAN MkII simulated image. Kwik residual colour composite of band 17, 14 and 11 in red, green and blue. Samples 1E-7E flagged. The melnoite is highlighted by the red hues.

Crosta Principal Component Transform

To increase the spectral differences the Crosta technique was applied using GEOSCAN MkII bands 11, 12, 15, and 17 after they had been transformed using the kwik residuals. This produced the following eigen matrix:

	B11	B12	B15	B17
PC1	0.587	0.501	0.573	0.275
PC2	0.223	0.447	**-0.245**	**0.828**
PC3	0.385	-0.668	0.729	-0.121
PC4	0.771	-0.321	-0.282	-0.473

In this case, the PC2 eigen vector shows the most contrast between band 17 and band 15. Figure 8.20 shows that the melnoite area is highlighted in the second principal component image as a lighter tone, which has been emphasised by slicing at >DN170 level.

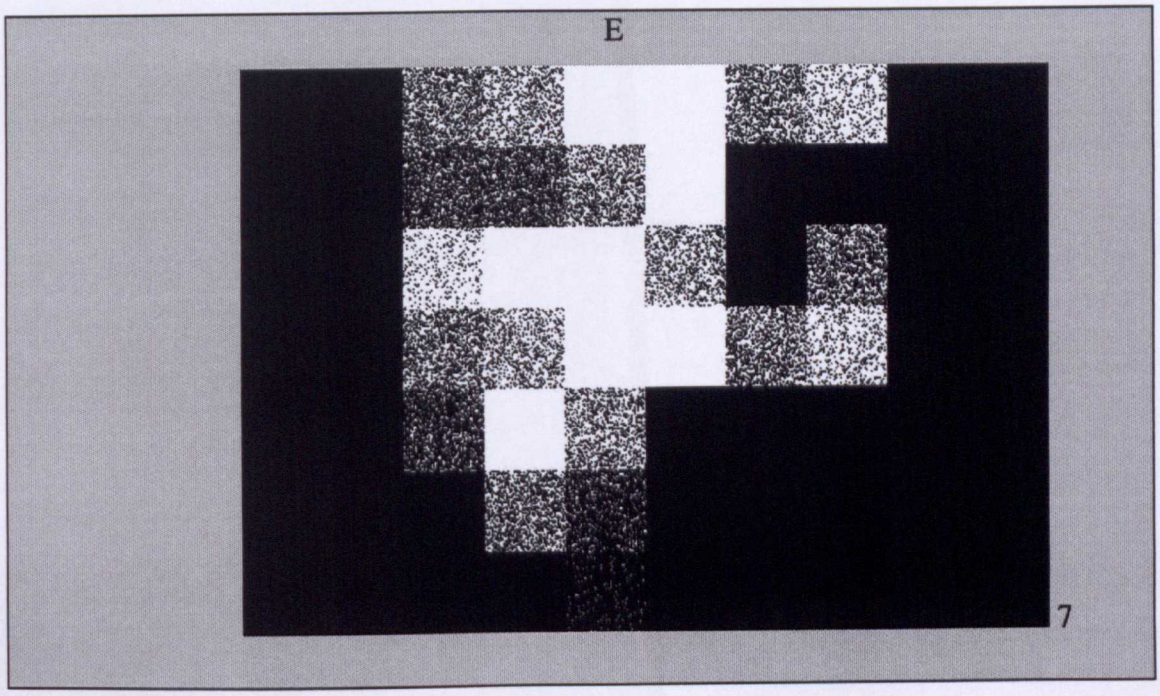

Figure 8.20: Meredith melnoite grid GEOSCAN MkII simulated image. Crosta 11-12-15-17 principal component 3 image. Melnoite area is highlighted as the lighter toned area sliced at >DN170.

GER 32 Band Simulated Images

Kwik Residual Colour Composite GER 32 Band

The negative of a quick residual transform colour composite for a simulated image of these data was produced by placing bands 21, 14 and 24 in red, green and blue. This image also highlights the melnoite in red hues, Figure 8.21.

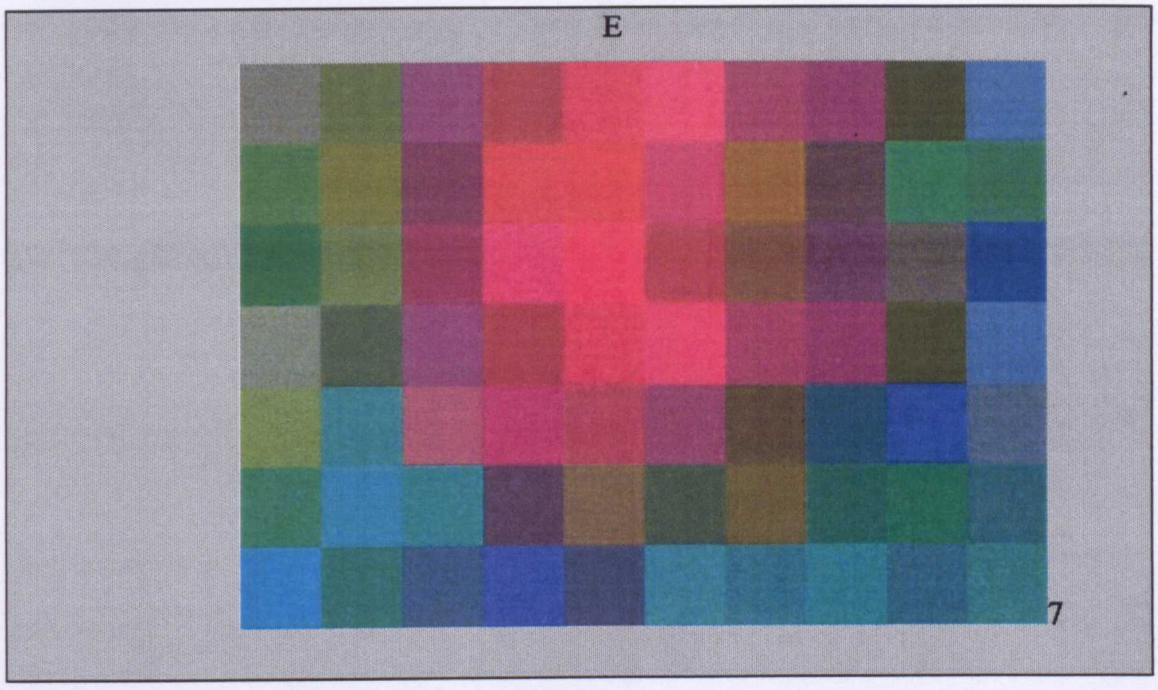

Figure 8.21: Meredith melnoite grid GER 32 Band simulated image. Quick residual colour composite of bands 21, 14 and 24 in red, green and blue. The melnoite is highlighted by the red hues.

Crosta Principal Component Transform

The Crosta Principal Component transform of the GER 32 image was derived from bands 14, 17, 21, 24. The eigen vector for PC3 shows band 21 weighted against the other bands:

	B14	**B17**	**B21**	**B24**
PC3	-0.501	0.060	**0.688**	-0.521

The image of PC3 derived from this Crosta principal component transform is shown in Figure 8.22. In this case the data have not been sliced but a histogram equalisation contrast stretch was applied. The area of Mg-OH samples show in lighter tones.

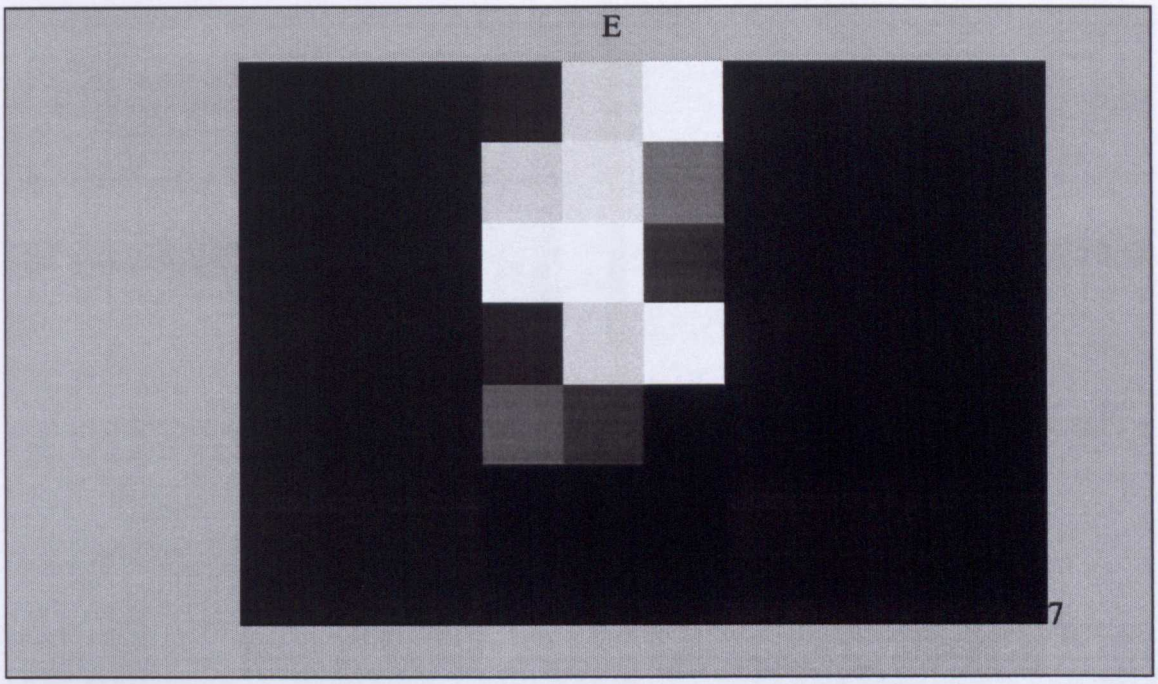

Figure 8.22: Meredith melnoite grid GER 32 Band simulated image. Crosta 14-17-21-24 principal component three image. Melnoite area is highlighted by the lighter toned area.

Noise was added to this GER 32 image at the following levels:

- 10 percent equal to a signal to noise ratio of 10:1
- 8 percent equal to a signal to noise ratio of 20:1
- 6 percent equal to a signal to noise ratio of 20:1
- 2 percent equal to a signal to noise ratio of 50:1
- 1 percent equal to a signal to noise ratio of 100:1
- 0.5 percent equal to a signal to noise ratio of 200:1
- 0.2 percent equal to a signal to noise ratio of 500:1
- 0.1 percent equal to a signal to noise ratio of 1000:1

Images were then produced and examined and they (Figure 8.23) showed that when the noise level exceeds 2 percent (SNR 50:1) the Mg-OH area cannot be discriminated. A one percent (SNR 100:1) noise level is marginal; only when the noise is at or below 0.5 percent (SNR 200:1) is the boundary of Mg-OH region completely distinct and easily interpretable.

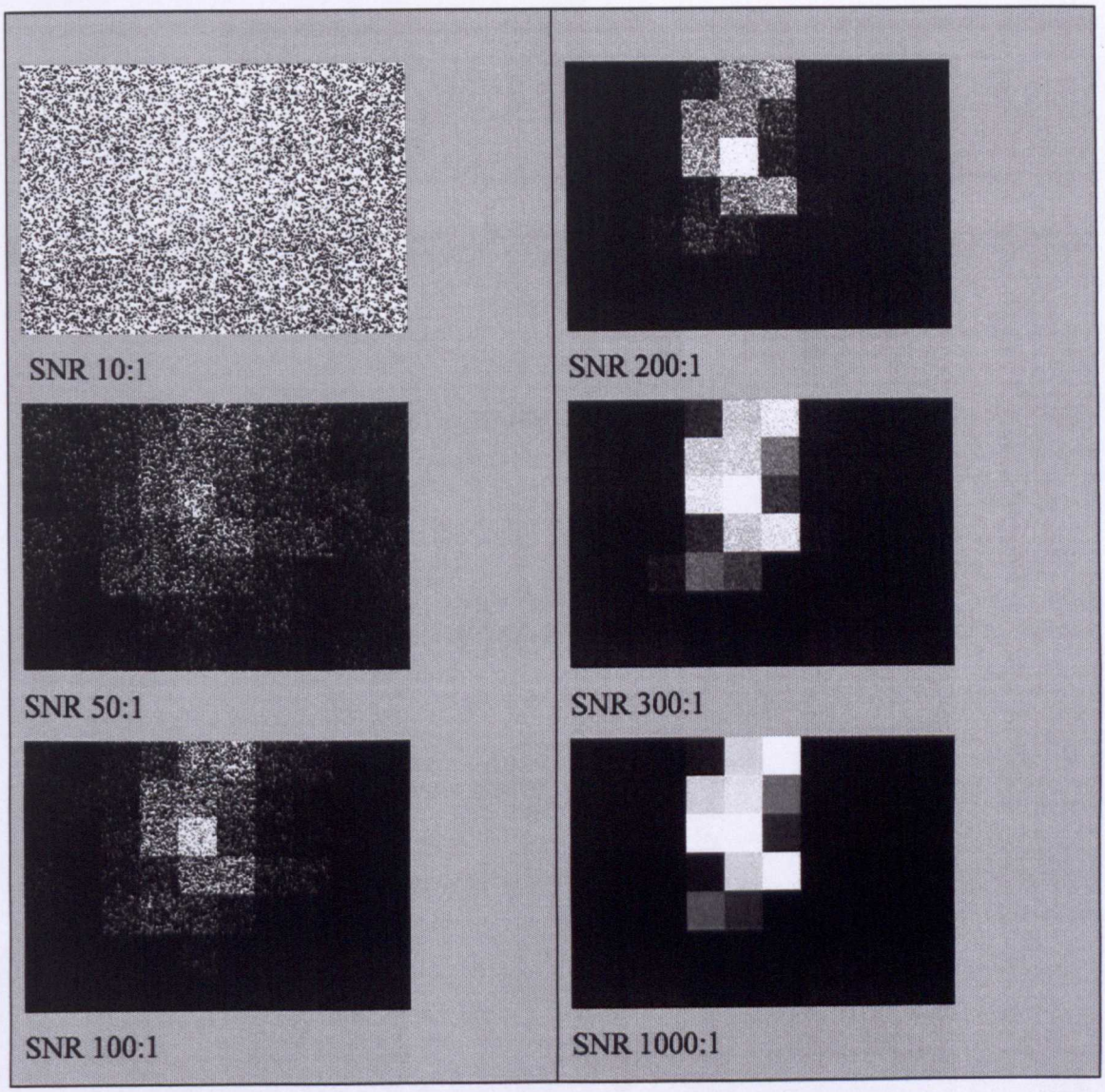

Figure 8.23: Meredith melnoite grid GER 32 Band quick image showing the effects of adding various levels of noise.

It has been stated (Hook et al, 1991) that the standard deviation derived from an area of homogeneous material in an image can be used to determine the SNR of the data. To test this the standard deviations derived from a 99 by 99 pixel block contained in sample pixel block 1E were calculated for each noise level image. These standard deviation values were then plotted against the noise level (Figure 8.24). This plot shows a linear relationship between noise level and the standard deviation. Therefore, checking the actual noise level in scanner data (after it has been acquired) could be achieved by selecting a region of pixels that represent a topographically flat and spectrally homogeneous area and determining their standard deviation. Figure 8.25 can then be used as a look-up-table to obtain the noise value.

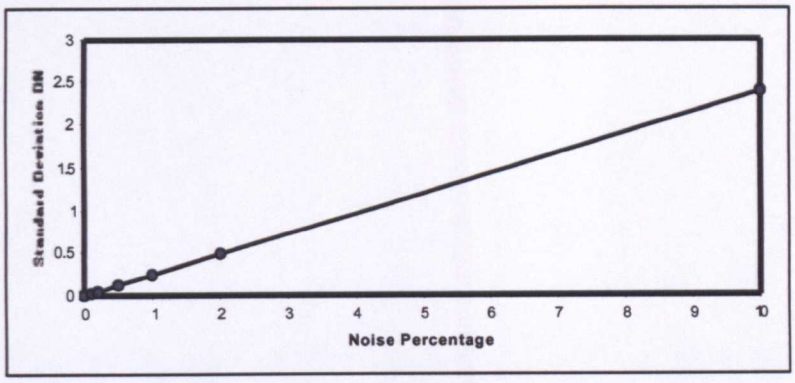

Figure 8.24: Plot of noise versus standard deviation derived from sample pixel block E1 with noise added. This plot could be used as a look-up-table to estimate the noise levels in scanner data, if spectrally homogeneous topographically uniform areas can be located within the image from which to determine the standard deviation.

8.9 CONCLUSIONS

This study indicates that as the number of bands decrease and the bandwidths broaden, the amount of image processing required to produce images that permit the requisite discrimination increases while the overall reliability of this discrimination is reduced. This study has indicted that Landsat TM, and other scanners with limited SWIR2 bands, are unable to reliably discriminate ultramafic rocks. This statement can be qualified when considering areas where anomalous levels of iron minerals are produced from ultramafic rocks; then data such as Landsat TM may be of use (Pontual 1990).

When data is obtained from scanners with the number of SWIR2 bands equal to or greater than the GEOSCAN MkII, then the processing techniques investigated can be used for mapping the minerals that spectrally identify ultramafic rocks. Specifically the quick or log residual transform and Crosta techniques showed promising results. This, of course, is dependent on the signal-to-noise ratio of the data. If the signal-to-noise ratio is below 150:1 then the ability to process the image so that spectrally meaningful results can be obtained, is limited.